Title
Tectonic and Aqueous Processes in the Formation of Mass-wasting Features on Mars and Earth

Author
Watkins, Jessica Andrea

Publication Date
2015

Peer reviewed|Thesis/dissertation

UNIVERSITY OF CALIFORNIA

Los Angeles

Tectonic and Aqueous Processes in the Formation of Mass-wasting Features on Mars and Earth

A dissertation submitted in partial satisfaction of the requirements for the degree Doctor of Philosophy in Geology

by

Jessica Watkins

2015

ABSTRACT OF THE DISSERTATION

Tectonic and Aqueous Processes in the Formation of Mass-wasting Features on Mars and Earth

by

Jessica Watkins

Doctor of Philosophy in Geology

University of California, Los Angeles, 2015

Professor An Yin, Chair

Fundamental to the advancement of planetary geology is an understanding of the interaction between tectonic and aqueous processes on planetary surfaces. This dissertation examines this interaction within two geomorphologic processes: landslide emplacement, on Mars and on Earth, and the formation of seasonal slope features on Mars.

Long-runout landsliding in equatorial Valles Marineris, Mars is among the most prominent geomorphic occurrences shaping the canyon. However, the mechanism of landslide long-distance transport, and the highly debated role of water therein, remains elusive. Through systematic mapping of high-resolution satellite images, integrated with spectral analysis, we show that hydrated silicates played a decisive role in facilitating landslide transport by lubricating the basal sliding zone. This conclusion implies that clay minerals, generated by ancient water-rock interactions, exert a long-lasting influence on Mars surface processes.

The Eureka Valley (EV) landslide is an unexamined, well-preserved long-runout landslide in arid southeast Eureka Valley, California. The field, photogeologic, spectral, and luminescence dating investigation presented here support initiation as a result of fault-generated

fracture during the mid to early Holocene at minimum, and transport lubricated by the presence of basal clays, characterized by 3-D internal deformation, as the most likely EV landslide emplacement mechanism. This geomorphological characterization may be applied to long-runout landslides on Earth and other planetary surfaces, suggesting that their emplacement likely does not require the participation of water.

Recurring slope lineae (RSL) are seasonal, narrow, low-albedo features extending down steep, equator-facing Mars slopes. RSL formation has been largely attributed to the seepage of near-surface water, though its source is not well understood. Through detailed analysis of high-resolution satellite images of RSL geologic contexts, we quantify the significant spatial correlation between RSL source regions and fractures in several geologic settings, indicating that fractures may act as conduits for fluid flow in the formation of RSL. This work provides insight into the hydrological cycle and the potential presence of habitable conditions on present-day Mars.

This new understanding of the formation processes of these planetary surface features implicates the persistent role of aqueous and tectonic processes in the formation of geomorphic features on widespread planetary surfaces throughout geologic time.

The dissertation of Jessica Watkins is approved.

David A. Paige

David Clifford Jewitt

Scott Joseph Brandenberg

An Yin, Committee Chair

University of California, Los Angeles

2015

TABLE OF CONTENTS

LIST OF FIGURES

LIST OF TABLES

ACKNOWLEDGEMENTS

There are many people I would like to thank for their invaluable assistance and support during the doctoral research process. I am grateful to my advisor, An Yin, not only for his insight, creativity, and guidance over the course of my graduate career, but also for the freedom he gave me to learn to think critically and do independent research. I am also indebted to Bethany Ehlmann, who graciously gave of her time to teach me how to analyze CRISM data with a skeptical approach. Her instruction and discussion of interpretations were absolutely crucial to the rigor of the work presented in Chapters 2 and 3, as well as to my development as a scientist. Discussions with each of my committee members have been instrumental in guiding this research as well.

Much of the field observation and analysis presented in Chapter 4 was conducted in collaboration with Jennifer Scully. Michael Lawson aided in collecting and prepared the field samples for OSL dating described in Chapter 4, and Edward Rhodes performed the measurement at the University of Sheffield. I would also like to acknowledge the National Park Service for access to their resources to conduct field work in Eureka Valley, and Lujendra Ojha for providing assistance in obtaining the results presented in Chapter 5. This research was conducted with support from a National Science Foundation Graduate Research Fellowship to Jessica A. Watkins.

Chapter 1 of this dissertation contains a version of published entries “slide” and “mass wasting” contributed to

Watkins, J.A. (*contributor*), eds. Hargitai, H., and A. Kereszturi (2015), Encyclopedia of Planetary Landforms, New York: Springer-Verlag New York Inc.

Chapter 2 is a version of an article published in *Geology* as

Watkins, J.A., Ehlmann, B.L., Yin, A. (2015), Long-runout landslides and the long-lasting effects of early water activity on Mars, *Geology, 43*, 107-110.

Chapter 3 is based on a manuscript to be submitted to *Icarus*:

Watkins, J.A., Ehlmann, B.E., Yin, A. Spatiotemporal evolution, mineralogical composition, and transport mechanisms of long-runout landslides in Valles Marineris, Mars. In prep.

Chapter 4 is based on a manuscript in preparation for submission:

Watkins, J.A., Scully, J.E.C., Lawson, M., Rhodes, E., Yin, A. Emplacement mechanisms and spatiotemporal evolution of the long-runout Quaternary Eureka Valley landslide, Eastern California. In prep.

Chapter 5 is also based on a manuscript in preparation for submission:

Watkins, J.A., Ojha, L., Yin, A. Structurally controlled subsurface fluid flow as a mechanism for the formation of recurring slope lineae. In prep.

VITA

Education

2014	Candidate in Philosophy, University of California, Los Angeles
2010	B.S. in Geological and Environmental Sciences, Stanford University - Minor in African and African American Studies

Selected Awards and Honors

2014	University of Tennessee Future Faculty Program Invitee
2012	UCLA Department of Earth and Space Sciences Harold and Mayla Sullwold Scholarship for Academic Excellence and Outstanding Original Research
2012	National Science Foundation Graduate Research Fellowship in Geosciences
2012	NASA Earth and Space Science Fellowship in Planetary Science (declined)
2011	Geological Society of America Diversity in the Geosciences Minority Research Grant Award
2010	UCLA Chancellor's Prize Award
2008- 2010	Stanford University Dean's Award for Academic Excellence

Selected Research and Professional Experience

2011- present	Graduate student researcher (advisor: Dr. An Yin), UCLA
2013- 2014	JPL Minority Initiatives Intern (PI: Dr. Charles Budney), NASA Jet Propulsion Laboratory
2013	JPL Minority Initiatives Intern (PI: Dr. Ashwin Vasavada)
2011	JPL Summer Internship Program participant (PI: Dr. Amy Mainzer)
2010-2012	Teaching Assistant, Dept. of Earth, Planetary and Space Sciences, UCLA
2009-2010	Research Assistant (PIs: Dr. Carol Stoker, Dr. John Marshall, SETI), NASA Ames Research Center
2008	Education Associate Program Research Intern (PI: Dr. Carol Stoker), Ames
2008	Undergraduate Researcher in Geological and Environmental Sciences (advisor: Dr. Donald Lowe), Stanford University

Peer-reviewed publications

Watkins, J., Ehlmann, B.E., Yin, A. (2015), Long-runout landslides and the long-lasting effects of water activities on Mars, *Geology, 43,* 107-110.

Bauer, J. et al. (co-author) (2013), Centaurs and scattered disk objects in the thermal infrared: Analysis of WISE/NEOWISE observations, *The Astrophysical Journal, 773,* 22.

Bauer, J. et al. (co-author) (2012), WISE/NEOWISE observations of active bodies in the Main Belt, *The Astrophysical Journal, 747,* 49.

Mainzer, A. et al. (co-author) (2011), NEOWISE studies of asteroids with Sloan photometry: Preliminary results, *The Astrophysical Journal, 745*, 7.

Mainzer, A. et al. (co-author) (2011), NEOWISE observations of Near-Earth Objects: Preliminary results, *The Astrophysical Journal, 743*, 156.

Mainzer, A. et al. (co-author) (2011), NEOWISE studies of spectrophotometrically classified asteroids: Preliminary results, *The Astrophysical Journal, 741,* 90.

Selected presentations

Watkins, J.**,** Ehlmann, B., Yin, A., 2015, Role of hydrated silicates in long-distance transport of landslides in Valles Marineris, Mars, Lunar and Planetary Science Conference XLVI, Abstract 1030.

Watkins, J., Ojha, L., Chojnacki, M., Reith, R., Yin, A., 2014, Structurally controlled subsurface fluid flow as a mechanism for the formation of recurring slope lineae, Lunar and Planetary Science Conference XLV, Abstract 2911 (*oral presentation*).

Watkins, J., 2013, Role of clay minerals in long-distance (> 10s of km) transport of Martian landslides, JPL Mars Seminar, NASA Jet Propulsion Laboratory *(invited oral)*.

Watkins, J., Yin, A., 2012, Progressive evolution of the Valles Marineris fault zone and its role in controlling interior layered deposits and outflow channels, American Geophysical Union Fall Meeting, Abstract 1502196.

Watkins, J., Ehlmann, B.E., Yin, A., 2012, Correlating contrasting morphology of landslides in Valles Marineris with hydrated minerals: New insights from detailed morphological mapping and CRISM spectral analysis, Geological Society of America Annual Meeting, Abstract 213419 (*oral presentation*).

Watkins, J., Scully, J.E.C., Yin, A., 2012, Emplacement and subsequent modification of the Quaternary Eureka Valley landslide, Eastern California, Geological Society of America Annual Meeting, Abstract 213448.

Watkins, J., Yin, A., 2011, Spatial and temporal relationships of landslides in Valles Marineris, Mars: Constraints on their triggering mechanisms, AGU Fall Meeting, Abstract 1200637.

CHAPTER 1

Introduction

1.1 Motivation

The interaction between tectonics and water on planetary surfaces is fundamental to a planet's geologic history and the geomorphologic processes shaping its landscape. Examples of the interaction between tectonic and aqueous processes are ubiquitous on Earth. Canyons, geysers, waterfalls, and landslides are all indicative of the key interplay between water and tectonic activity on Earth. The role of such an interaction has also been intensely examined on Mars since spacecraft first began observing its surface (e.g., Masursky, 1973). The widespread tectonic overprinting observed on the Martian surface, including that related to impact and to internal stresses, implies that tectonic processes have been vital to its geologic history (Banerdt et al., 1992). The presence and influence of water have been observed across the surface of Mars in numerous datasets, including high-resolution imagery of fluvial, deltaic, and lacustrine morphologies (e.g., Baker, 2001), spectral identification of hydrated minerals (e.g., Mustard et al., 2008), and in-situ rover detections of fluvio-lacustrine conditions (Grotzinger et al., 2014) and near-surface water ice (Smith et al., 2009). These observations suggest that the interaction of aqueous and tectonic processes has had a key impact on the surface of Mars throughout its history.

Comparison to terrestrial examples facilitates understanding of observations of Mars surface features. Though features on Mars are often much larger than their terrestrial counterparts, Earth provides an excellent analog for geologic processes observed on Mars. Analysis of terrestrial examples constrains the viability of various geologic processes on rocky bodies, enabling acquisition of a ground-truth of hypotheses made based on planetary orbital

data. Variations in environment, including surface and subsurface temperatures, precipitation, climate cycles, wind, dust cover, atmospheric conditions, mineralogical composition, and gravity, can significantly influence the formation and modification of geologic features exposed on the surface, and must be taken into account in comparative study. In this way, the fundamental principles governing the mechanics and kinematics of features observed on Earth can be applied to observations of Mars and other planetary surfaces to investigate their geologic history, as well as to add insight into terrestrial processes.

In order to further understanding of the interaction between tectonics and water on both planets, with potential implications for the surfaces of other rocky bodies, this thesis examines two specific geomorphologic processes related to mass wasting: the emplacement of landslides, on Mars and on Earth as an analog, and the formation of seasonal slope features on Mars.

1.2 Background on mass wasting

1.2.1 Definition

Mass wasting is a broad class of features formed on Earth, Mars, and other rocky bodies by the movement of rock or debris downslope controlled by gravity. Transport of rock or debris by a transporting medium such as wind (e.g., aeolian activity), water (e.g., fluvial deposition), or ice (e.g., glacial activity) is not included, but flows with high fluid content where the pore-fluid mediates (but does not completely dominate) grain-to-grain interactions are included in this category. A slide is a broad term that can include (and has been applied towards) landslides, slumps, avalanches, debris flows, and other features formed through the destabilization of a slope and movement due to gravity of a coherent or semi-coherent body of rock or soil along a surface of rupture. Mass-wasting feature morphology can most simply be divided into a source region

(zone of erosion) and a deposit (zone of accumulation), and can include (**Fig. 1.1**) (Highland and Bobrowsky, 2008; WPWLI, 1993):

Accumulation: The volume of the displaced material lying above the original ground surface.

Crown: The undisplaced material adjacent to the highest parts of the main scarp (scarp crest).

Depletion: The volume bounded by the main scarp, the depleted mass, and the original ground surface.

Depleted mass: The volume of the displaced material, overlying the rupture surface but underlying the original surface.

Displaced material: Material displaced from its original position (i.e., the depleted mass and the accumulation).

Flank: The undisplaced material adjacent to the sides of the rupture surface. They can be identified by compass directions or by relative directions as viewed from the crown.

Foot: The portion of the landslide that has moved beyond the toe of the rupture surface and overlies the original surface.

Head: The upper parts of the landslide along the contact between the displaced material and the main scarp.

Main body: Displaced material overlying the rupture surface between the main scarp and the toe of the rupture surface.

Main scarp (breakaway scarp): The visible, steep part of the rupture surface on the undisturbed ground at the upper edge of the landslide, from which material was displaced, caused by movement of displaced material away from undisturbed ground.

Minor scarp: A steep surface on the displaced material that overlies the surface of rupture between the main scarp and the toe of the surface of rupture, and is produced by its differential movements.

Original ground surface: The surface of the slope that existed before the landslide took place.

Surface of separation: The part of the original ground surface overlain by the foot of the landslide.

Surface of rupture (sliding surface): The surface that forms (or which has formed) the lower boundary of the displaced material below the original ground surface.

Slip surface: The mechanical idealization of the surface of rupture.

Tip: The point of the toe farthest from the top of the landslide.

Toe: The lower, usually curved margin of the displaced material that is the most distant from the main scarp.

Top: The highest point of contact between the displaced material and the main scarp.

Toe of surface of rupture: The (usually buried) intersection between the lower part of the rupture surface and the original ground surface.

Zone of accumulation (accumulation zone): The area where the displaced material lies above the original ground surface.

Zone of depletion (depletion zone): The area where the displaced material lies below the original ground surface.

These morphological characteristics are exhibited by landslides on Mars (**Fig. 1.2**) as well Earth, though Martian landslides are much larger in volume and extent. These similarities imply that they are formed by similar mechanisms, which are investigated in detail in this dissertation.

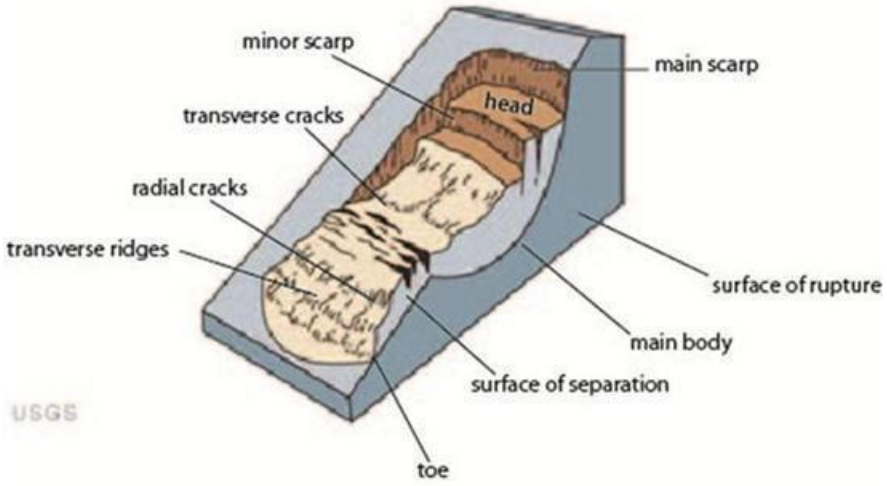

Figure 1.1. Basic morphological elements of a rotational landslide, including the breakaway scarp, which is the surface expression of the surface of rupture, minor scarps produced by differential movement of the landslide downslope, the head, and the toe.

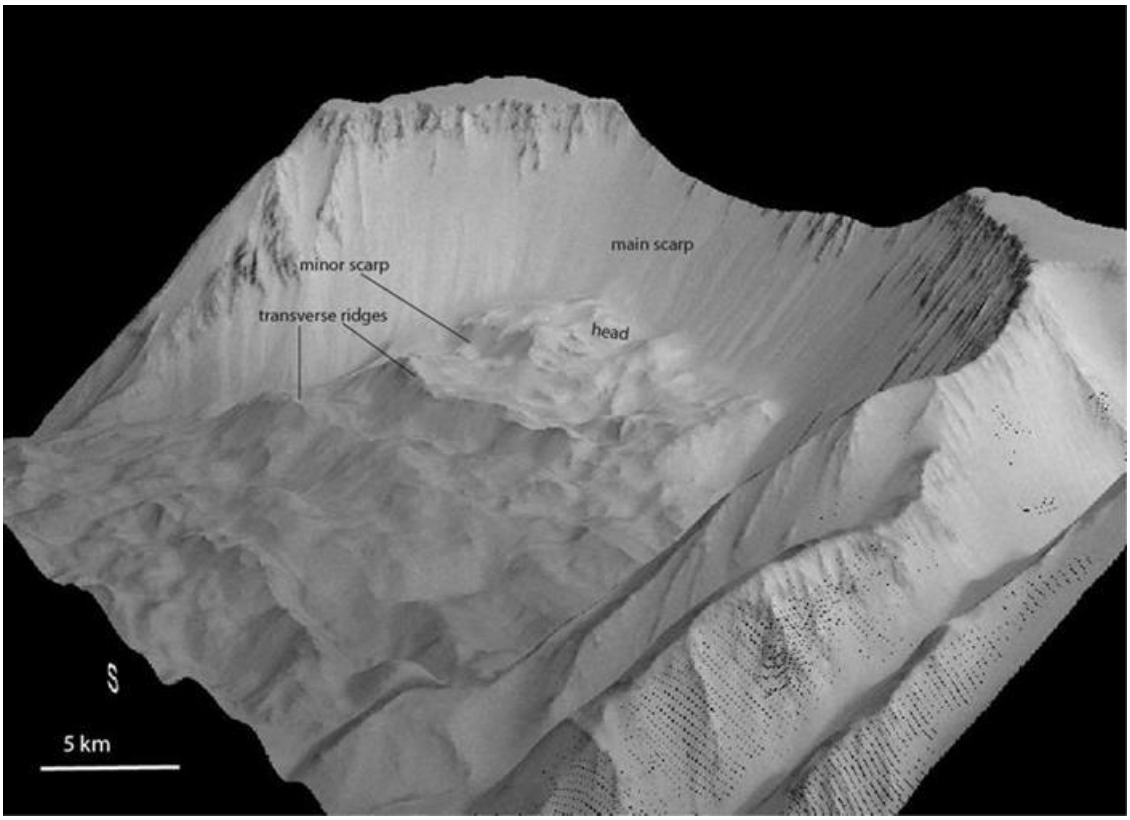

Figure 1.2. High Resolution Stereo Camera image (Neukum and Jaumann, 2004) overlain on Mars Orbiter Laser Altimeter (MOLA) topographic data (Zuber et al., 1992) displaying three-dimensional perspective of the head portion of a long-runout landslide in Ius Chasma in Valles Marineris, Mars. Observable morphological characteristics of rotational landslides, including multiple rotational blocks, are labeled. Vertical exaggeration is 3x.

1.2.2 Subtypes

Mass-wasting features can be classified according to: (1) the material(s) involved, (2) the movement type, and (3) the movement velocity (Varnes, 1978) (**Fig. 1.3**). A mass-wasting feature can also be classified based on movement geometry, the volume moved, and the fluid in which it occurs. Classifications of landslides are associated with specific mechanics and properties of slope failure, and the material involved, which will influence the characteristics of the mass-wasting body, such as the coherence, standard grain/body size, porosity and fluid (water or air) content. These properties will determine the potential speed of movement, volume of displacement, and runout distance of the landslide (e.g., Hewitt et al., 2008; Iverson, 1997; 2006).

The basic materials that may be involved in mass wasting events include (Varnes, 1978): (1) bedrock or rock, (2) debris (coarse-grained), defined as < 80% sand and finer particles < 2 mm diameter, and (3) earth (sediment, fine-grained), defined as > 80% sand and finer particles < 2 mm diameter. Landslides consist of rock (mass that was intact before initiation of movement), soil (aggregate of solid particles that was either transported or was formed by the weathering of rock in place), or a combination thereof, and can have a range of moisture contents (from dry to very wet).

The basic movement mechanisms or kinematic types of mass wasting events include (Varnes, 1978): (1) fall, (2) topple, (3) spread (lateral spread), (4) flow (e.g., debris flow, rock avalanche, creep, solifluction), and (5) slide. Landslides are characterized by two main categories of movement. In rotational landslides (slump), slide movement occurs on a deep-seated rupture surface that is curved concave upward. Movement is more or less rotational about an axis that is parallel to the contour of the slope. The upper surface of the displaced material may tilt

backwards toward the scarp. Rotational landslides typically occur in homogeneous materials. In translational landslides (planar slides or block slides), material moves down and outward along a relatively shallow, planar surface of rupture, often broadly channel-shaped in cross-section, with little rotational movement or backward tilting. Subtypes of translational landslides include rock or wedge slides, in which sliding is of one single bedrock unit or few closely related bedrock units as a relatively coherent mass, debris slides, in which sliding is of relatively dry, predominantly coarse soil or regolith on a planar surface parallel with the ground, earth slides, in which sliding is of predominantly fine soil or sediment on a planar surface, and skinflows, or active layer detachment slides, which involve slope failure that occurs when the thawed or thawing portion of a shallow permafrost active layer detaches from and flows rapidly on the underlying permanently frozen soil.

The movement velocity of mass wasting events can vary significantly, and are divided into seven classes (**Table 1.1**; Cruden and Varnes, 1996): (1) extremely slow ($< 5x10^{-10}$ m/sec), (2) very slow ($5x10^{-10}$ m/sec), (3) slow ($5x10^{-8}$ m/sec), (4) moderate ($5x10^{-6}$ m/sec), (5) rapid ($5x10^{-4}$ m/sec), (6) very rapid (0.05 m/sec), and (7) extremely rapid ($\geq$ 5 m/sec). Velocities of long-runout landslides (sturzstroms) and some flows (e.g., rock avalanches) on Earth and extraterrestrial surfaces may considerably exceed typical "extremely rapid" values as a result of decreased basal friction (e.g., Hungr et al., 2001). In addition to velocity, landslides can also be categorized by state. Active landslides are those that are currently moving. Inactive landslides are those that last moved more than one annual cycle of seasons ago. Landslides that remain visible in the landscape for thousands of years after becoming inactive are called ancient or paleolandslides. Paleolandslides that have been covered by other deposits are called buried landslides. Landslides that have clearly developed under different geomorphic or climatic

Velocity class	(m/sec)	Typical velocity
(1) Extremely Slow	$< 5x10^{-10}$	< 15 mm/year
(2) Very Slow	$5x10^{-10}$	15 mm/year
(3) Slow	$5x10^{-8}$	1.6 m/year
(4) Moderate	$5x10^{-6}$	13 m/month
(5) Rapid	$5x10^{-4}$	1.8 m/hr
(6) Very Rapid	0.05	3 m/min
(7) Extremely Rapid	≥ 5	≥ 5 m/sec

Table 1.1. Velocity classifications of mass movements (Cruden and Varnes, 1996).

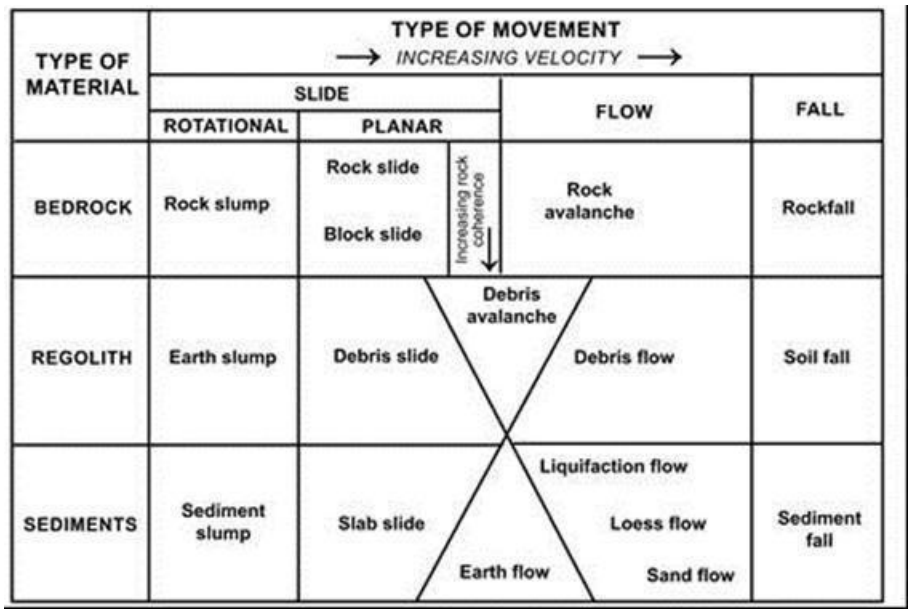

Figure 1.3. Classification of mass movements based on type of material and type of movement (after Malin, 1992).

conditions are relict (WPWLI, 1993). No active large landslides have been observed on other planets.

Mass wasting events can also be classified based on the fluid in which it occurs: (1) subaerial and (2) subaqueous. Submarine events are the subset of subaqueous events which occur across the continental shelf and into the deep ocean. Sublacustrine events are those which occur within lacustrine depositional settings. Subaqueous deposits tend to be much larger than subaerial features, likely a result of reduced friction at the base (e.g., hydroplaning; Mohrig, 1998), and share morphological characteristics with long-runout landslides.

The volume moved in a mass wasting event influences the type of feature morphology created and the runout distance, defined as the distance between the toe of the source and the toe of the deposit (Fell et al., 2000). Within mass-wasting features involving a small number of particles, individual bodies do not generally interact with each other during their movement (e.g., boulder tracks on Mars). Mass-wasting features involving enough particles so that body-collisions influence movement exhibit effective coefficients of friction consistent with "grain-to-grain" interactions, and can be explained with simple sliding models (e.g., rock avalanches). Mass-wasting features with a large number of particles and/or involving a fluid exhibit much lower coefficients of friction and achieve unusually long runout distances due to pore-fluid mediating collisions, or "fluidization" processes.

Mass movement can occur along a range of depths as well (Sidle and Dhakal, 2002): (1) shallow, rapid failures (e.g., debris flows, rock avalanches), (2) extremely slow to rapid, deep seated failures (e.g., slumps, creep, earthflows), and (3) surficial mass wasting. The initial (pre-movement), final (post-movement), and rupture surface slope also contribute to the mass movement geometry. Additionally, a single mass-wasting feature may form through more than

one movement (occurring in parallel or in sequence) (WPWLI, 1993). Features are classified as complex when they exhibit at least two types of movement in sequence, composite when they exhibit at least two types of movement simultaneously in different parts, and successive when it is of the same type as a deposit nearby but does not share displaced material or rupture surface with it. A single event involves a single movement of displaced material, and multiple events show repeated development of the same type of movement.

1.2.3 Morphometry

On Earth, rotational landslides are associated with slopes ranging from 20-40°. The surface of rupture generally has a depth-to-length ratio between 0.3 and 0.1. Mass wasting on steeper slopes produces rock falls, topples, and flows as aspect ratio increases and bedrock loses coherence. Translational landslides are generally shallower, and their surfaces of rupture have depth-to-length ratios of < 0.1. They range from small to very large failures (e.g., Blackhawk landslide deposit has a deposit area of ~24 km^2; Shreve, 1959). The efficiency of landslides is estimated by their mobility (runout length/vertical drop) (Heim, 1882). Large rock slides can exhibit much greater mobility than predicted by frictional models for dry rock fragments and thus have much longer runout distances (Hungr et al., 2001), with maximum values of 5-10 times the total rock fall height (Hewitt et al., 2008). Eyewitness and morphological evidence of terrestrial rock avalanches (sturzstroms) suggest that large avalanche motion is high-velocity, "fluidized", and "flow-like" (Heim, 1882; Hsu, 1975; Hewitt et al., 2008).

On Mars, large long-runout landslides have been identified in Valles Marineris, where the average slopes of the canyon walls are 20-30°. These features are one order of magnitude larger in volume than terrestrial ones. They are 36 km long and 32 km wide on average, dropping ~6

km in height, and have deposit areas that range from 50 to 5000 km^3 (Quantin et al., 2004; Lucchitta, 1978; 1979; McEwen, 1989). Their surfaces of rupture have a depth-to-length ratio between ~0.6 and 0.1. Mobility of landslides in Valles Marineris ranges from 1.8-12 (Quantin et al., 2004).

1.2.4 Formation

Accumulations of debris (interpreted as talus) and rock at the bases of scarps and slopes, likely at or near the angle of repose, are interpreted to be largely derived from materials immediately above and to have been deposited due to mass-wasting processes. The build-up of preconditional factors that make a slope prone to failure (e.g., fracturing, compositional weakness, climatic variation) can occur over long time scales. The timescale of formation can be very rapid (e.g., a rock avalanche) or can occur more gradually (e.g., a slump).

Landslides occur when shear stresses within a slope exceed the shear strength (resistance to shearing) of the materials that form the slope. Several physical triggers can contribute to landslide initiation (Cruden and Varnes, 1996; Highland and Bobrowsky, 2008). Water, in the form of intense or sustained rainfall, rapid snowmelt, rapid drawdown (of floods and tides) or filling, can lead to increased groundwater levels, erosion at the base of slopes, and saturation within the slide, causing significant decrease in rock strength (**Fig. 1.4**). Earthquake/impact shaking exerts influence on landslide initiation in that landslide surfaces of rupture often occur near adjacent normal fault traces and are nucleated upslope of the faults. Additionally, through liquefaction, saturated material shaken loose by an earthquake may liquefy and then flow, transporting masses of overlying drier material with it. Volcanic eruption and mechanical

weathering, including thawing, freeze-and-thaw weathering, and shrink-and-swell weathering, can all also facilitate landslide initiation.

Preexisting natural conditions also participate in landslide initiation (Cruden and Varnes, 1996; Highland and Bobrowsky, 2008). Geologically weak materials, such as some volcanic slopes or unconsolidated marine sediments, for example, weathered materials (see **Fig. 1.4**), sheared materials, jointed or fissured materials, and regions of contrast in permeability or rigidity can be of sufficiently low strength to initiate failure. Translational landslides often fail along geologic discontinuities such as faults, joints, bedding surfaces, schistosity, the contact between rock and residual or transported soils, or a permafrost layer. Morphological conditions, including the formation of oversteepened slopes by tectonic or volcanic uplift, glacial rebound following removal of buttresses (**Fig. 1.5**), glacial meltwater outburst, fluvial erosion of the base of the slope, wave erosion of the base of the slope; glacial erosion of the slope, erosion of lateral margins, subterranean erosion, deposition loading of the slope or its crest, and vegetation removal (by forest fire or drought) may also produce slope instability.

Models often consider the material within the slide as a coherent or semi-coherent body that moves with bulk inertia properties and deforms over a low-friction sliding surface (e.g., Iverson, 2006) (**Fig. 1.6**). The failure and resulting movement of small slides can generally be well explained by considering a standard coefficient of internal friction (typically 0.6-1 for most geological materials). Some slides (i.e., large rock avalanches) show substantially greater mobility than small granular flows, suggesting that the effective coefficient of friction for such flows is < 0.2 (Lajeunesse et al., 2006; Lucas and Mangeney, 2007). Several theories have been proposed to explain the low apparent coefficient of friction exhibited by long-runout landslides,

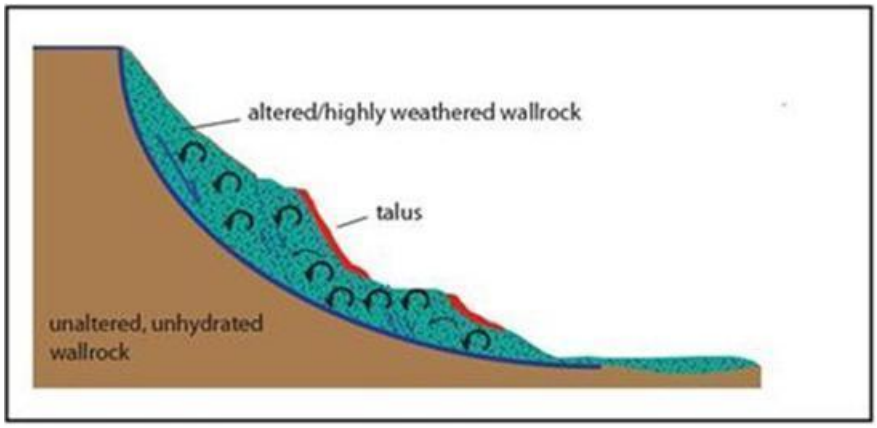

Figure 1.4. Local concentration of fluids can alter and weather bedrock, decreasing the rock strength and leading to landslide initiation.

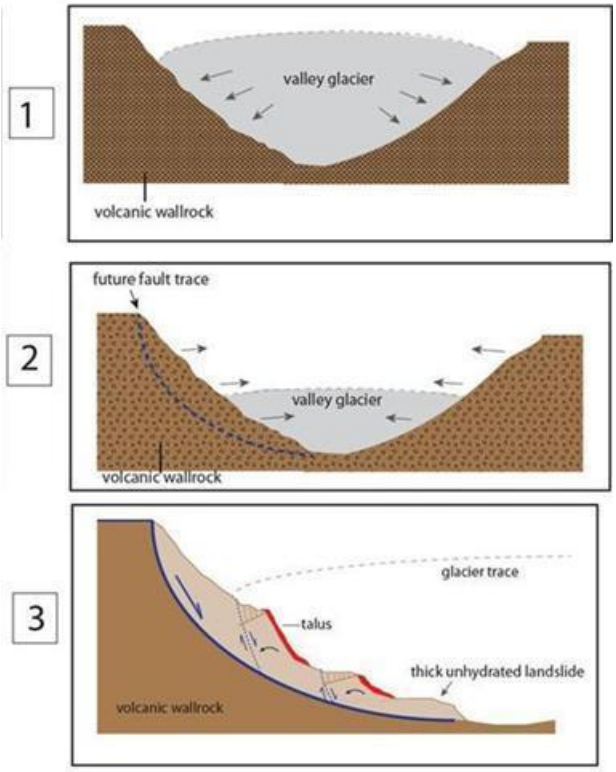

Figure 1.5. Glacial oversteepening in landslide initiation: (1) Glacier flow fills valley and steepens wall slopes on either side of canyon, (2) Removal of glaciers leads to slope instability and re-equilibrium of paraglacial topography, (3) Failure of oversteepened slope initiates landsliding.

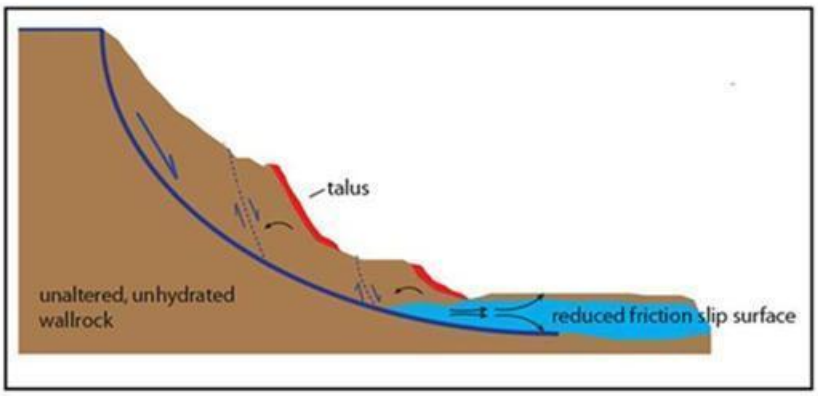

Figure 1.6. Basal lubrication by high pore fluid pressure, air cushion, or presence of weak materials (e.g., hydrated minerals) may facilitate landslide transport.

but none is universally accepted. Hypotheses for this transport mechanism are outlined and investigated in detail in Chapter 2.

1.2.5 Distribution

On Earth, landslides can occur virtually anywhere, but can be linked to natural patterns of elevation gradient, climate and weather, river courses, and anthropological disturbance. Landslides that are exposed on the surface and exhibit characteristic morphology are generally Quaternary in age (1.8 Ma to present) (e.g., Hewitt et al., 2008).

On planetary surfaces, mass-wasting features generally occur where impact craters form. Inward sliding of material is an integral part of the modification stage of impact crater development, occurring as the transient cavity wall collapses. In complex craters, landslides typically form terraced crater walls. Planetary landslides have also been observed along the steep slopes of canyons and volcanoes. In addition to Mars and Earth, planetary examples of mass wasting have been found on Venus (Malin, 1992), Callisto (Chuang and Greeley, 2000; Moore et al., 2004), Europa (Moore et al., 1999), and Io (Schenk and Bulmer, 1998), Iapetus (Singer et al., 2012), the Moon (Howard, 1973; Bart, 2007), Itokawa (Miyamoto et al., 2007), Phobos (Shingareva and Kuzmin, 2001), and other small bodies.

1.2.6 Significance

On Earth, landslides pose a significant hazard (Varnes, 1984). Often, they cause long-term economic disruption, population displacement, negative effects on the natural environment, and are responsible for thousands of deaths and injuries each year. Throughout the Solar System, an understanding of landslide formation mechanisms may shed light on planetary surface formation

histories and potentially expose processes at work in the subsurface of planetary bodies. The possible involvement of fluids, including water, or volatiles in mass wasting processes/landslide formation on planetary bodies could have astrobiological implications, indicating a potentially habitable climate, possibly in the relatively recent past.

1.3 Dissertation structure

In this dissertation, multiple techniques will be utilized in combination to investigate the emplacement mechanisms of mass wasting features on Mars and on Earth. Photogeologic mapping of high resolution satellite imagery of the surface, analysis of high resolution digital topographic surfaces, near-infrared spectroscopy, comparative field-based observation and geologic mapping, and optically stimulated luminescence dating were all conducted in order to constrain the interaction between tectonics and water on both planets.

The second chapter of this dissertation is an analysis of the emplacement processes of a long-runout landslide in Ius Chasma in Valles Marineris, Mars, and the third chapter describes the results of the application of this model on a regional scale. We examined the mineralogic composition of landslide-related units through spectral reflectance analysis, geologic mapping, and morphometric analysis of high-resolution Mars Reconnaissance Orbiter imagery data in order to determine whether hydrated minerals are present within and/or at the base of long-runout landslides throughout the canyon. Our survey reveals a distinct correlation in Valles Marineris between landslide transport distance, lateral spreading, low mass-independent basal coefficient of friction, and the presence of hydrated silicates in the sliding zone, as well as a distinct spatial relationship between hydrated-silicate-bearing trough-floor deposits and landslide mobility. Our results favor lubrication through the presence of liquefied, entrained hydrated-

silicate-bearing trough-floor deposits in the basal sliding zones as the transport mechanism of long-runout landslides in Valles Marineris.

The fourth chapter of this dissertation is an examination of the mechanisms of emplacement and subsequent modification of a long-runout landslide in the arid Mars analog environment of Eureka Valley, California. Integrated field, photogeologic, spectral, and luminescence dating investigation of the geomorphology of the extremely well-preserved EV landslide deposit has permitted constraint of its initiation as a result of fault-generated fracture, transport by lubrication of the fluidized landslide mass through the presence of basal clays, resulting in 3-D simple shear internal deformation, and post-emplacement fluvial modification and rotation. We determine a minimum landslide emplacement age and a maximum age of post-emplacement rotation of mid to early Holocene.

The fifth chapter of this dissertation is an investigation of the role of groundwater and conduit faults in the formation of recurring slope lineae (RSL). We conduct detailed mapping of geologic context and quantification of the spatial relationships between the source regions of these seasonal features and their surrounding regions using high-resolution satellite images to enable constraint on RSL formation mechanisms related to the seepage and downslope transport of near-surface water-based liquid. Our results reveal a distinct spatial correlation between RSL source regions and fractures in all RSL geologic environments, supporting the key role of fracture-controlled flow in facilitating RSL formation.

This dissertation represents a significant contribution to the study of aqueous and tectonic processes on planetary surfaces by constraining the formation mechanisms of various hillslope geomorphic features and the involvement of water, hydrated materials, and tectonic activity therein throughout geologic time.

1.4 References

Baker, V.R. (2001), Water and the Martian landscape, *Nature, 412*, 228-236.

Banerdt, W.B., Golombek, M.P., Tanaka, K.L. (1992), Stress and tectonics on Mars, *Mars, 1*, 249-297.

Bart, G.D. (2007), Comparison of small lunar landslides and martian gullies, *Icarus, 187*, 417-421.

Chuang, F.C. and R. Greeley (2000), Large mass movements on Callisto, *J. Geophys. Res., 105*, 20,227–20,244.

Cruden, D.M. and D.J. Varnes (1996), Landslide types and processes, In: Turner, A.T., Schuster, R.L. (eds) Chapter 3: Landslide Types and Processes; Landslides - Investigation and Mitigation, Transportation Research Board Special Report No. 247, National Academy Press, Washington DC, 36-75.

Fell, R., Hungr, O., Leroueil, S., Riemer, W. (2000), Geotechnical engineering of the stability of natural slopes and cuts and fills in soil, Procs., GeoEng2000, International Conference on Geotechnical and Geological Engineering in Melbourne, Australia, November.

Grotzinger et al. (2014), A habitable fluvio-lacustrine environment at Yellowknife Bay, Gale Crater, Mars, *Science, 343*, 1242777.

Heim, A. (1882), Der bergsturz von elm, *Zeitschrift der Deutschen Geologischen Gesellschaft, 34*, 74–115.

Hewitt, K., Clague, J.J., Orwin, J.F. (2008), Legacies of catastrophic rock slope failures in mountain landscapes, *Earth-Science Reviews, 87*, 1-38.

Highland, L.M. and P. Bobrowsky (2008), The Landslide Handbook— A Guide to Understanding Landslides, USGS Circular 1325: Reston, Virginia.

Hsü, K.J. (1975), Catastrophic debris streams (sturzstroms) generated by rockfalls, *Geological Society of America Bulletin, 86*, 129–140.

Hungr, O., Evans, S.G., Bovis, M., Hutchinson, J.N. (2001), Review of the classification of landslides of the flow type, Environmental and Engineering Geoscience VII, 221-238.

Iverson, R.M. (1997), The Physics of Debris Flows, *Reviews of Geophysics, 35*, 245–296.

Iverson, R.M. (2006), Forecasting Runout of Rock and Debris Avalanches, In: Evans, S.G. et al. (ed) Landslides from Massive Rock Slope Failure, 197-209.

Howard, K.A. (1973), Avalanche Mode of Motion: Implications From Lunar Examples, *Science, 180*, 1052-1055.

Lajeunesse, E., Quantin, C., Allemand, P., Delacourt, C. (2006), New insights on the runout of large landslides in the Valles Marineris canyons, Mars, *Geophys. Res. Lett*., 33, L04403.

Lucas, A. and A. Mangeney (2007), Mobility and topographic effects for large Valles Marineris landslides on Mars, *Geophys. Res. Lett*., *34*, L10201.

Lucchitta, B.K. (1978), A large landslide on Mars, *GSA Bulletin*, *89*, 1601-1609.

Lucchitta, B.K. (1979), Landslides in Valles Marineris, Mars, *J. Geophys. Res.*, *84*, 8097.

Malin, M.C. (1992), Mass movements on Venus: Preliminary results from Magellan cycle 1 observations, *JGR*, 97,16337-16352.

Masursky, H. (1973), An overview of geological results from Mariner 9, *J. Geophys. Res.*, *78*, 4009-4030.

McEwen, A.S. (1989), Mobility of large rock avalanches: Evidence from Valles Marineris, Mars, *Geology*, *17*, 1111-1114.

Miyamoto et al. (2007), Regolith Migration and Sorting on Asteroid Itokawa, *Science, 316*, 1011.

Moore et al. (1999), Mass Movement and Landform Degradation on the Icy Galilean Satellites: Results of the Galileo Nominal Mission, *Icarus, 140,* 294–312.

Moore et al. (2004), Callisto, *Jupiter. The Planet, Satellites and Magnetosphere 1*, 397-426.

Mustard et al. (2008), Hydrated silicate minerals on Mars observed by the Mars Reconnaissance Orbiter CRISM instrument, *Nature, 454*, 305-309.

Neukum, G. and R. Jaumann (2004), The High Resolution Stereo Camera of Mars Express, In (eds.) A. Wilson and A. Chicarro, Mars Express: The Scientific Payload, pp. 17-35, ESA SP-1240, Noordwijk, The Netherlands.

Quantin, C., Allemand, P., Delacourt, C. (2004), Morphology and geometry of Valles Marineris landslides, *Planetary and Space Science, 52,* 1011–1022.

Schenk, P.M. and M.H. Bulmer (1998), Origin of mountains on Io by thrust faulting and large-scale mass movements, *Science, 279,* 1514-1517.

Shingareva, T.V. and R.O. Kuzmin (2001), Downslope Movement of Surface Material on Phobos, LPSC XXXII #1453.

Shreve, R.L. (1959), Geology and mechanics of the Blackhawk landslide, Lucerne Valley, California, Dissertation (Ph.D.), California Institute of Technology.

Sidle, R.C. and A.S. Dakhal (2002), Potential Effects of Environmental Change on Landslide Hazards in Forest Environments, In: Slide, R.C. (ed) Environmental Change and Geomorphic Hazards in Forests, CABI Publishing.

Singer, K.N., McKinnon, W.B., Schenk, P.M., Moore, J.M. (2012), Massive ice avalanches on Iapetus mobilized by friction reduction during flash heating, *Nature Geoscience, 5*, 574-578.

Smith et al. (2009), H_2O at the Phoenix landing site, *Science, 325*, 58-61.

Varnes, D.J. (1978), Slope movement types and processes, In: Schuster, R.L., Krizek, R.J. (eds), Landslides: Analysis and Control, Special Report, Transp. Res. Board, Nat. Acad. Sci. 176, National Academy of Sciences, Washington, DC, 11 – 33.

WPWLI (1993), Multilingual landslide glossary, UNESCO Working Party for World Landslide Inventory; The Canadian Geotechnical Society, BiTech Publishers Ltd: Richmond BC Canada.

Zuber et al. (1992), The Mars Observer Laser Altimeter Investigation, *J. Geophys. Res.*, *97*, 7781-7797.

CHAPTER 2

Long-runout landslides and the long-lasting effects of early water activity on Mars

2.1 Introduction

Although landsliding is among the most prominent processes shaping the surfaces of solar-system bodies, its emplacement mechanisms both on Earth (e.g., Erismann, 1979; Legros, 2002) and other planets (e.g., Melosh, 1987) remain contentious. An example is the debate over the transport mechanisms of long-runout (> 50 km) landslides in the ≤ 700-km-wide and ≤ 7-km-deep Valles Marineris (VM) trough system on Mars. Current hypotheses appeal variously to basal lubrication by water, trapped air, ice, snow, evaporates, and dry granular flow (e.g., Lucchitta, 1978; Harrison and Grimm, 2003; McEwen, 1989). Because landslides with shared morphologies occurred widely and nearly continuously from 3 Ga to 50 Ma (Quantin et al., 2004) (**Figs. 2.1A and 2.1B**), resolving the mechanisms of their emplacement may have several important implications for past Mars surface conditions. For example, the involvement of ice (Lucchitta, 1978; De Blasio, 2011) or water (Harrison and Grimm, 2003) at the base of VM landslides could correlate landsliding with wetter, cold or warm climates, respectively, whereas dry granular flow requires no such correlation (McEwen, 1989; Soukhovitskaya and Manga, 2006).

Thus far, efforts in differentiating the competing hypotheses have focused on the geometric properties of VM landslides. These include (1) the ratio of landslide volume to transport distance (McEwen, 1989; Soukhovitskaya and Manga, 2006), (2) multidimensional simulations of landform generation in longitudinal and map-view geometry (Harrison and Grimm, 2003; Lucas et al., 2011), (3) surface morphology comparisons to long-runout terrestrial

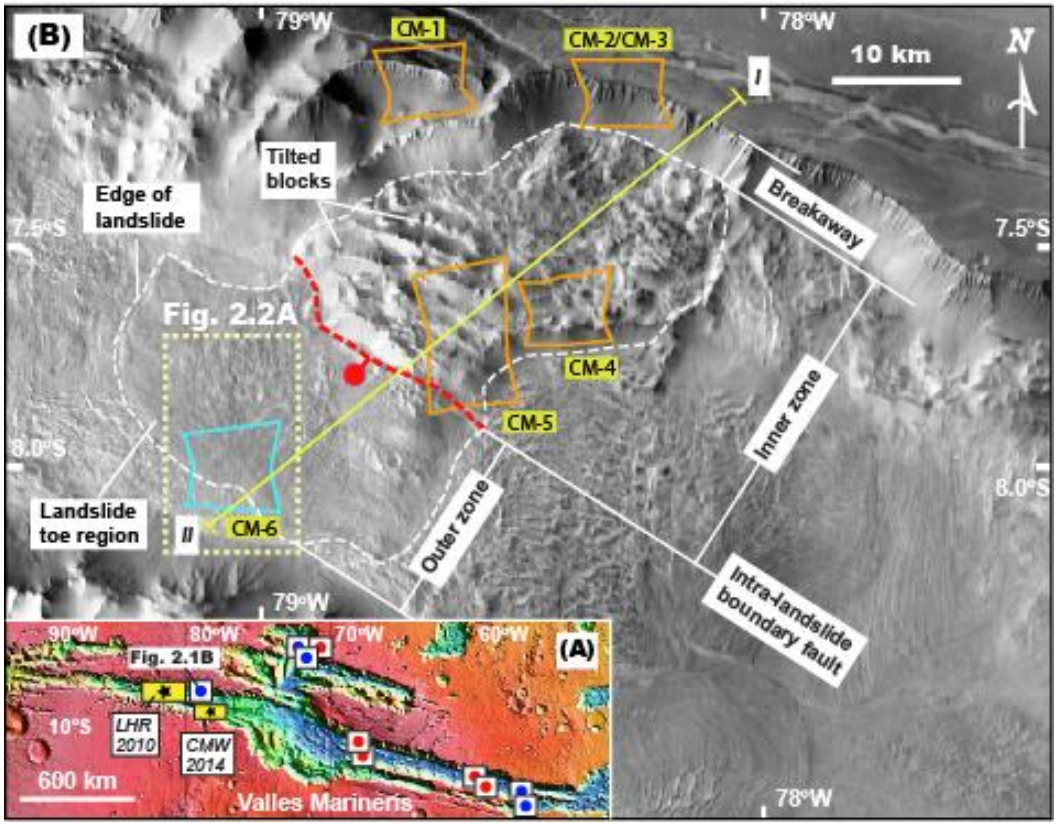

Figure 2.1. (A) Valles Marineris, Mars, with locations of B, study area of Roach et al. (2010) labeled as LHR 2010, and study area of Weitz et al. (2014) labeled as CMW 2014. Blue circles indicate clays detected in Valles Marineris long-runout landslides; red, hydrated minerals not detected in landslide. (B) Thermal Emission Imaging System (THEMIS) mosaic displaying Ius Labes landslide and locations of cross-section in D and Fig. 2.2A. Blue box indicates hydrated mineral detection; orange, no detectable hydrated minerals.

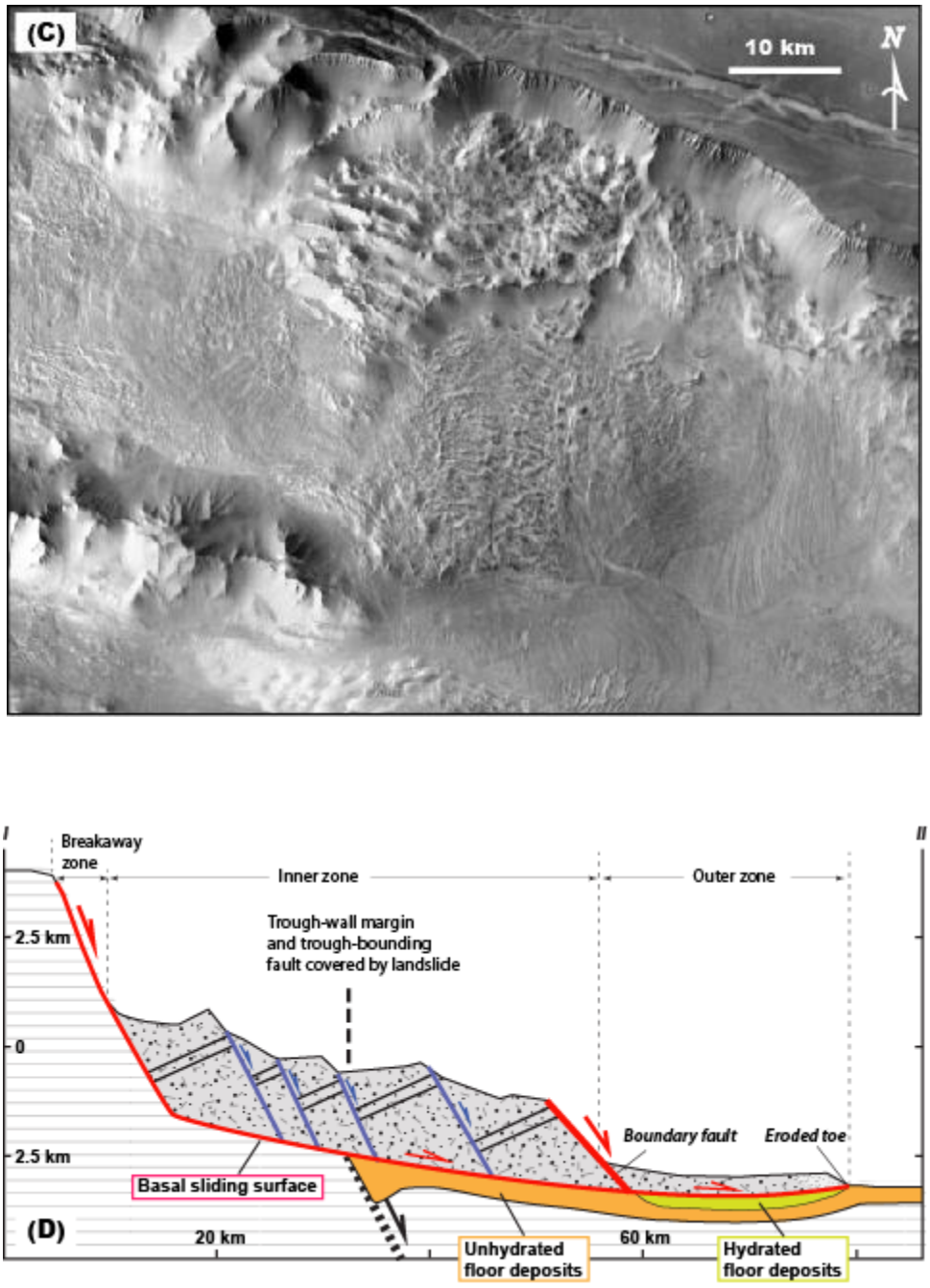

Figure 2.1, cont. (C) Unmarked THEMIS mosaic in B. (D) Geologic cross section with topographic profile derived from Mars Orbiter Laser Altimeter (MOLA) data.

analogs (Lucchitta, 1978; De Blasio, 2011), and (4) the slope and relief of the source (Lajeunesse et al., 2006). These geometric observations have been used to support both dry and wet models. However, the mineralogic composition of the basal sliding layers of VM landslides has never been directly examined with spectral data. In this study, we survey the mineralogy of long-runout landslides in VM and then determine the structural relationships and mineral composition of the best-exposed and best-imaged basal section of a long-runout (>75 km) VM landslide (**Fig. 2.1B**) using integrated CRISM (Compact Reconnaissance Imaging Spectrometer for Mars) (Murchie et al., 2007), THEMIS (Thermal Emission Imaging System) (Christensen et al., 2004), CTX (Context Camera) (Malin et al., 2007), and HiRISE (High Resolution Science Imaging Experiment) (McEwen et al., 2007) data. Our results suggest that transport was facilitated by hydrated silicates in the basal sliding zone, documenting the effects of clay minerals in shaping the morphology of Mars.

2.1.1 Data and Methods

Spatial resolutions of satellite images analyzed in this work are as following: (1) ~18 m/pixel for THEMIS images (Christensen et al., 2004), (2) ~5.2 m/pixel for CTX images (Malin et al., 2007), and (3) ~30 cm/pixel for HiRISE images (McEwen et al., 2007). Following the procedure of Schultz et al. (2010) and Yin (2012a,b), we conducted systematic mapping of landslides and their spatial relations with surrounding rocks directly on satellite images.

Composition of exposed rocks was determined using the CRISM hyperspectral imaging spectrometer, which takes targeted observations in 544 6.55-nm-wide channels in the visible to near-infrared (VNIR) (Murchie et al., 2007). "L" detector Targeted Reduced Data Record (TRDR) observations in the 1.0-4.0 μm wavelengths were analyzed to identify the presence of

hydrated minerals. Water in minerals is characterized by vibrational absorptions between 1.91 and 1.95 μm from H_2O and between 1.40 and 1.45 μm induced by OH and H_2O (Clark et al., 1990).

In the regional survey of VM long-runout landslides (**Fig. 2.1A**), CRISM images examined include FRT0000B939 (see **Fig. 2.1B**), FRT000093E3, HRL0000A8F6, HRL0000A432, and HRL0000508A (clays detected- blue circles in **Fig. 2.1A**), as well as FRT0001672B, FRT0000B510, FRT0001892B and FRT000195E8, FRT00009D64 and HRL00019803, and HRL00019505 (no detectable hydrated minerals- red circles in **Fig. 2.1A**). For the landslide studied in detail (**Fig. 2.1B**), CRISM images analyzed include FRT0000BDF1 (CM-1), FRT0000D243 and FRT0001883A (overlapping CM-2 and CM-3), FRT0000A834 (CM-4), and HRL00007AA5 (CM-5) (no detectable hydrated minerals- orange boxes in **Fig. 2.1B**), as well as FRT0000B939 (CM-6) (with hydrated minerals- blue box in **Fig. 2.1B**).

Using the CRISM Analysis Toolkit (CAT) produced by the CRISM Science Team (Murchie et al., 2009b), standard CRISM photometric and atmospheric corrections of the raw data were applied to each image by dividing each pixel by the cosine of the incidence angle and by a scaled atmospheric transmission spectrum derived from observations of Olympus Mons (e.g., Mustard et al., 2008). Spectra of interest were generated by averaging signals in an area of 7x7 pixels. The signals were then normalized by dividing the spectra of interest by the spectrum of a spectrally neutral or unremarkable region (usually corresponding to Mars dust) in roughly the same detector column. This procedure enhances spectral differences among areas of different geologic units and removes residual atmospheric and instrument artifacts (e.g., Roach et al., 2010). These ratioed spectra were then compared to RELAB and USGS library laboratory

reflectance spectra within the wavelengths of CRISM data for potential matches in diagnostic absorption band locations and spectral shapes.

2.1.2 Regional context

A characteristic surface morphology is exhibited by many long-runout VM landslides of diverse ages (Lucchitta, 1978; Quantin et al., 2004). For example, Ius Labes, dated as 100 Ma by crater counting estimate (Quantin et al., 2004), consists of a breakaway zone, an inner zone with tilted blocks (~4 km wide), and an outer zone with a fan-shaped lobe marked by surficial longitudinal grooves (**Figs. 2.1B and 2.1C**). The width of the unconfined outer zone (~43 km) is nearly double that of the inner zone (~28 km, similar to that of the breakaway escarpment), thus requiring significant lateral spreading during landslide runout and an unusual transport mechanism (e.g., Legros, 2002).

Approximately 30 characteristic long-runout landslides occur in VM and of these, ten had CRISM coverage (**Fig. 2.1A**). Among them, five clearly show the presence of clay minerals in materials entrained in their long-runout portions, where dust cover is low and erosion has exposed entrained material at the surface (**Fig. 2.1A**). Structural relationships between CRISM-detected clay minerals and slide units are rarely discernible due to the concealing nature of later-emplaced stratigraphic units. However, one landslide- Ius Labes (**Figs. 2.1B and 2.1C**), had exemplary exposure of pristine slide deposits due to erosion, and several CRISM full-resolution target (FRT) data covering multiple portions of the deposit permit detailed, coupled structural-mineralogic analysis.

2.2 Geologic and mineral mapping

We mapped the following geomorphic features and geologic units at the eroded landslide toe and its neighboring region (**Figs. 2.1B and 2.2A**): (1) a landslide deposit with a lumpy surface (unit 1 in **Fig. 2.2B**), (2) a layered and mesa-forming unit (feature a in **Fig. 2.2B**) mostly covered by dust and sand dunes, (3) a layered unit with high-albedo patches (feature b), cross-cut by discontinuous (feature c; see **Fig. 2.2C**) and degraded (feature d ; see **Fig. 2.2C**) longitudinal grooves, linear and curvilinear scarps, and narrow troughs sub-perpendicular to the grooves (feature e; see **Fig 2.2C**), (4) a low-albedo layered unit characterized and cross-cut by continuous and well-preserved longitudinal grooves (feature f; see **Fig. 2.2C**), and transverse extensional cracks (feature g; see **Fig. 2.2C**), (5) talus deposits from the southern wall, and (6) a young debris-flow sheet overriding the talus deposits. The high- and low-albedo grooved units (i.e., units 3 and 4 in **Fig. 2.2B**) are parts of the Ius Labes outer zone; the former (unit 3) is thrust over unit 2 as indicated by a truncated crater basin (feature h in **Fig. 2.2B**) below the contact. A HiRISE image shows that low-albedo unit 4 is a sub-horizontal sheet and overlies high-albedo unit 3 (white arrow in **Fig. 2.2D** points to contact). A CTX digital terrain model with MOLA topographic data displays the topographic relief between the two units (**Fig. 2.2E**). Pervasive parallel grooves, interpreted as stretching lineations, and linear fissures, interpreted as tension gashes (**Figs. 2.2A-2.2D**), in units 3 and 4 are indicative of shared differential shear and lateral spreading at high velocities (> 50 m/s for terrestrial examples) during landslide emplacement (McEwen, 1989). The contact and cross-cutting relationships between the mapped units are summarized in **Fig. 2.2F**.

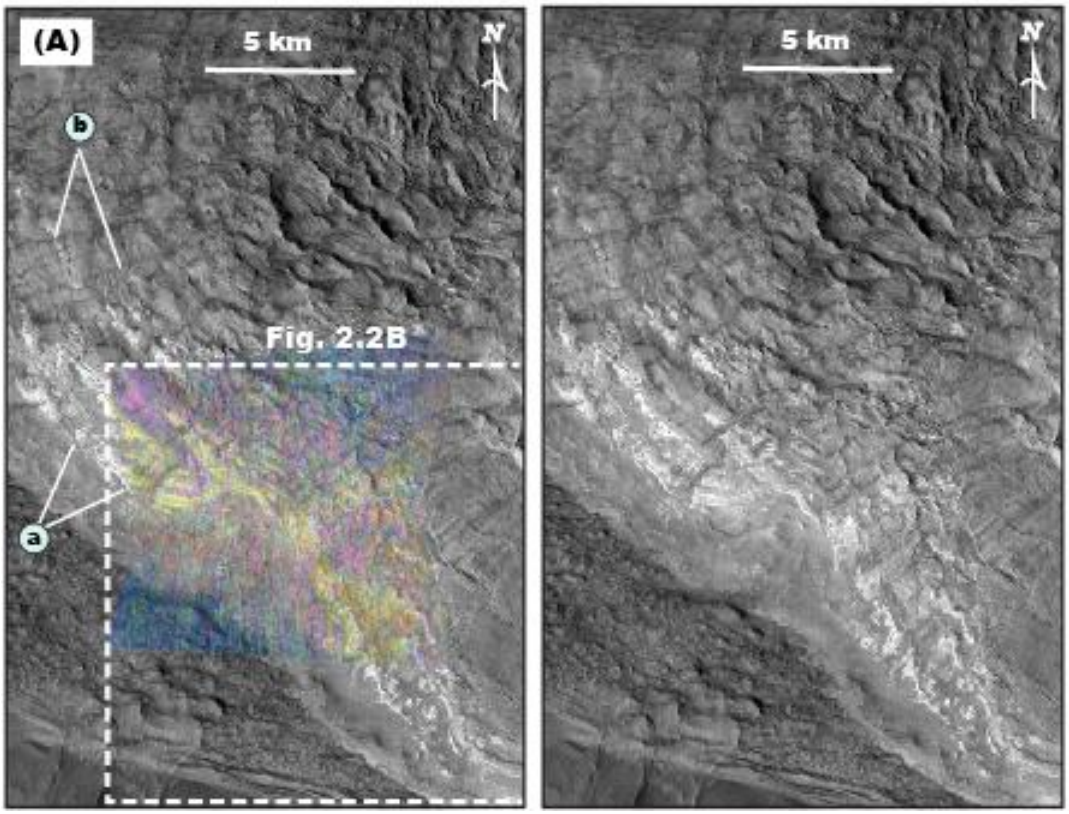

Figure 2.2. (A) Summary spectral parameter map of Compact Reconnaissance Imaging Spectrometer for Mars (CRISM) image FRT0000B939 (R: BD1900, G: Doub2200, B: D2300), where Fe/Mg smectites are magenta; doublet hydrated material is yellow-green; anhydrous materials are dark blue, overlain on Context Camera (CTX) image P07_003606_1727_XN_07S079W (see Fig. 2.1B for location; unmarked image shown on right). Feature (a), outer rim of the landslide; feature (b), longitudinal ridges and grooves. Location of B is also shown.

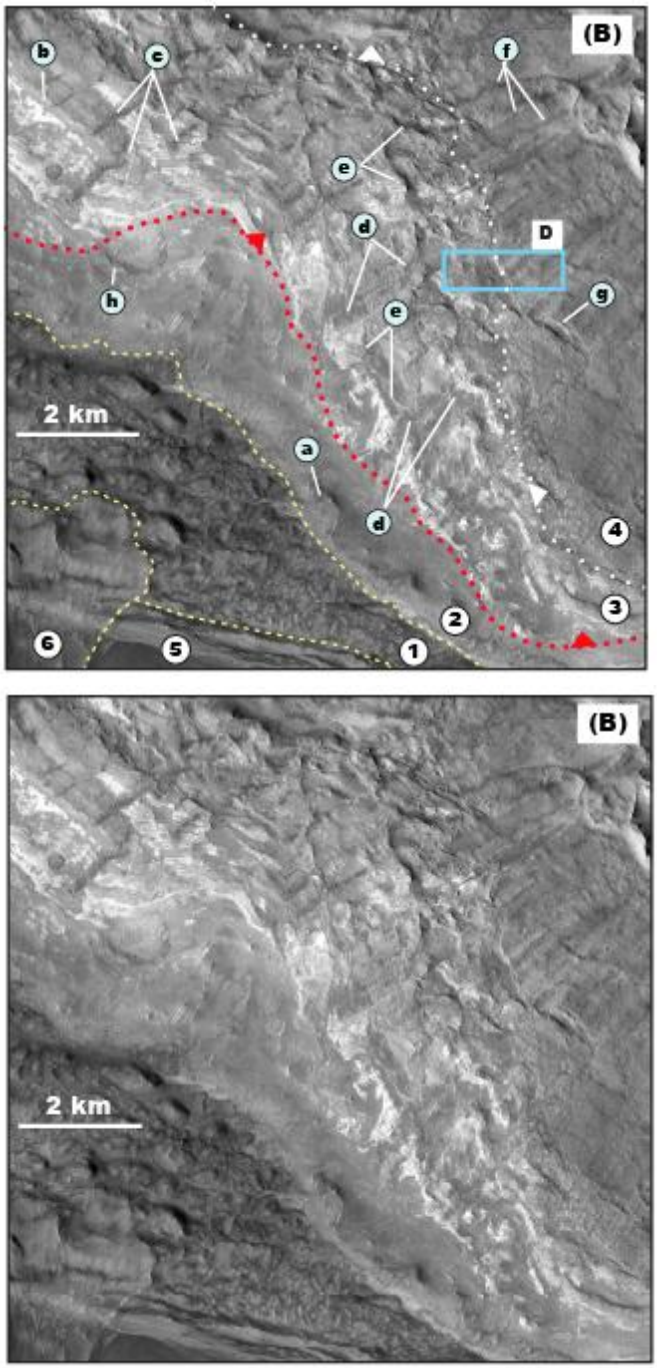

Figure 2.2, cont. (B) Interpreted geologic map of a basal section of the landslide based on CTX image in A (unmarked image shown below). Numbers and letters indicate lithologic units discussed in the text (see C for unmarked zoom-ins of features). Dashed red line is trace of basal sliding surface with triangles on overriding plate; dashed white line is trace of an intra-landslide sliding surface separating light-toned unit 3 below from dark-toned unit 4 above; yellow lines are geologic contacts unrelated to emplacement of the studied landslide. Blue box shows location of D.

C

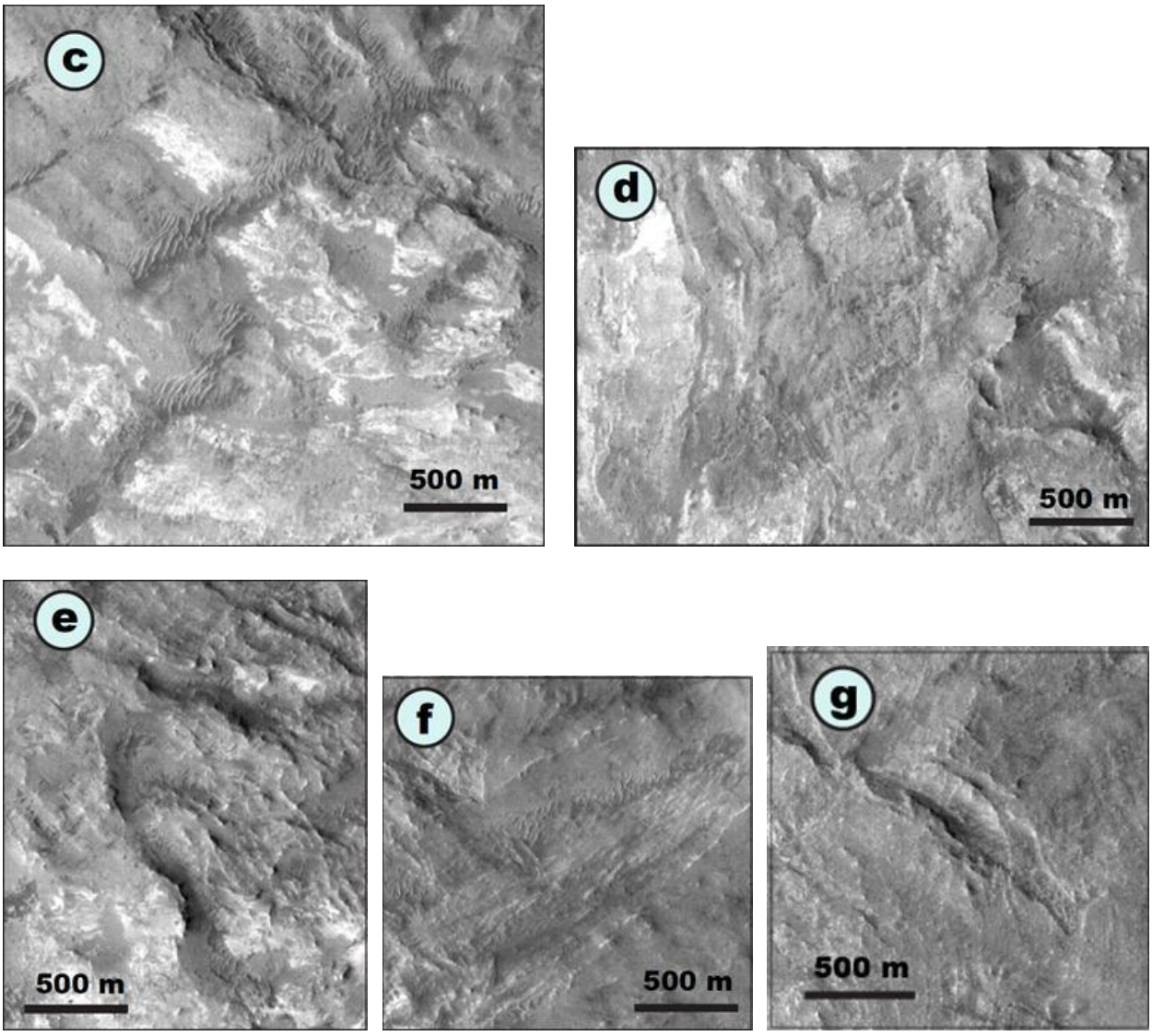

Figure 2.2, cont. (C) Unmarked zoom-ins of features *c, d, e, f,* and *g* in B.

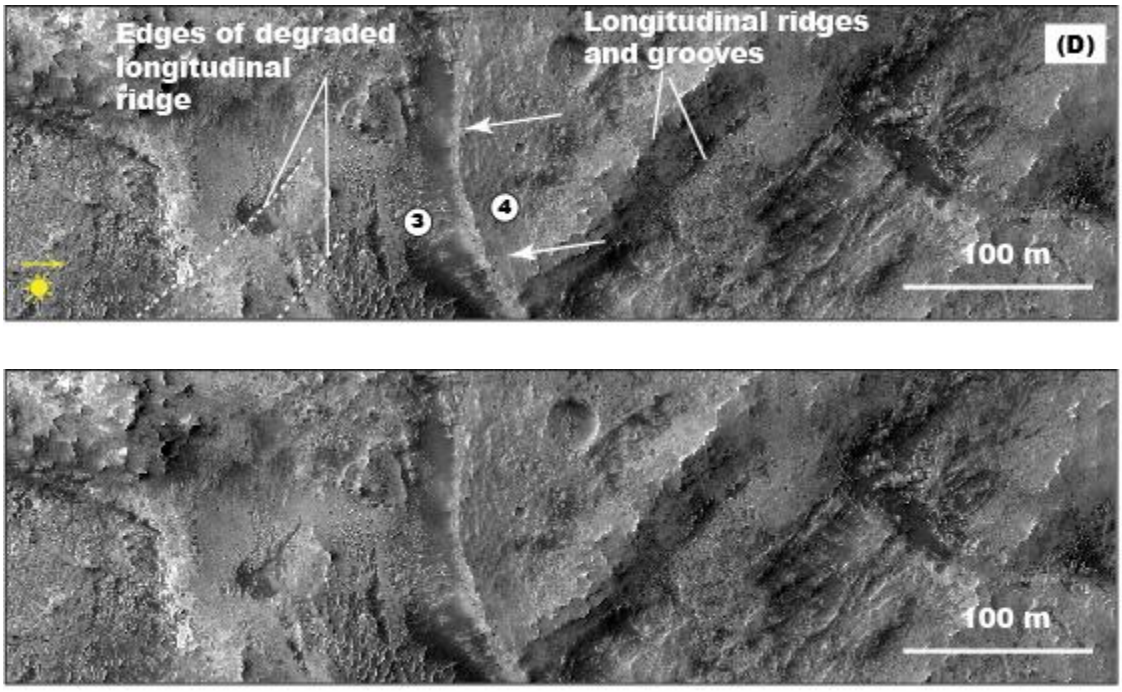

Figure 2.2, cont. (D) High Resolution Science Imaging Experiment (HiRISE) image (ESP_016172_1720; unmarked image shown below) showing that unit 4 lies above unit 3; sun illumination direction (yellow arrow).

E

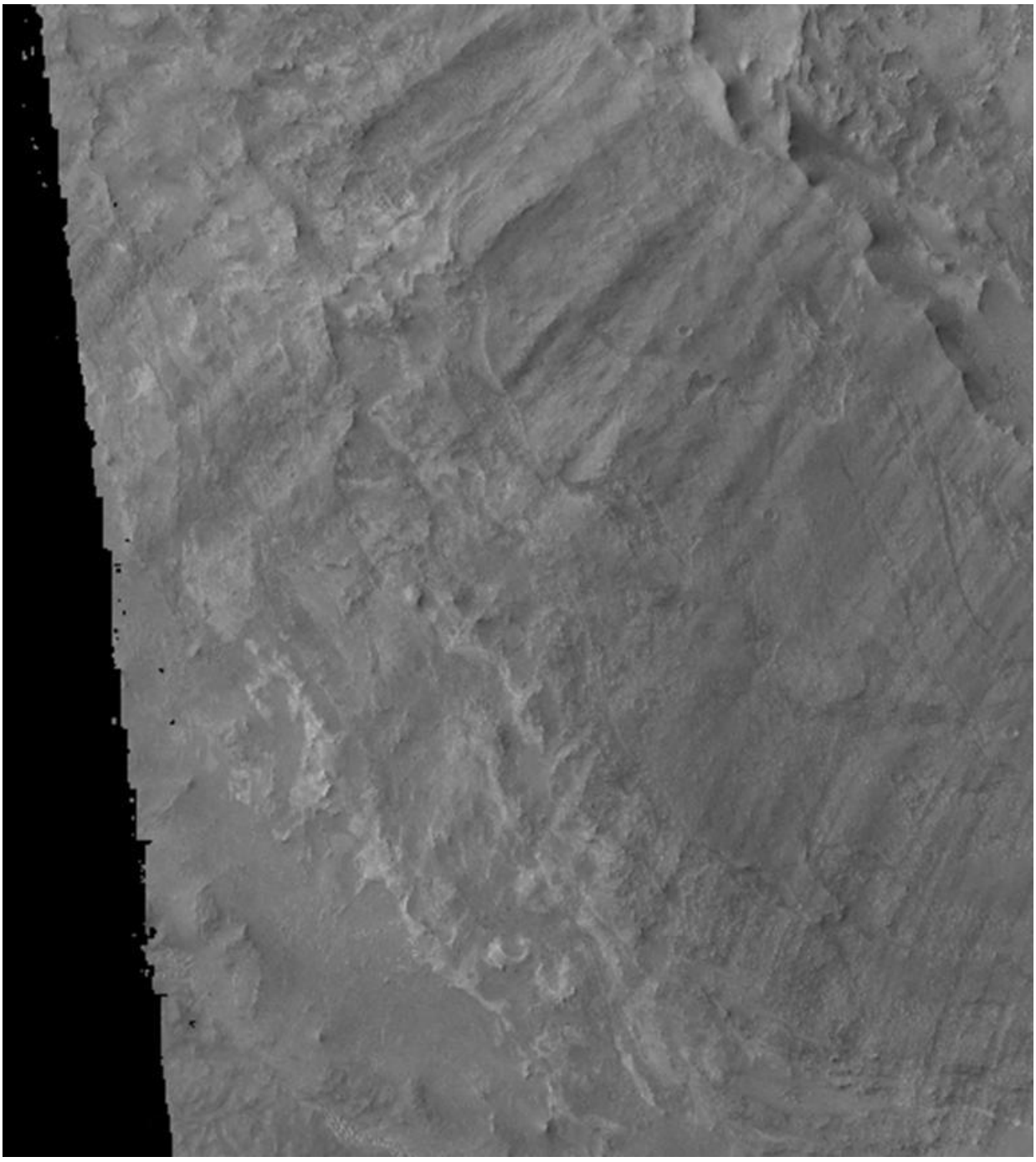

Figure 2.2, cont. (E) Portion of CTX DTM expressing the topographic relief along the contact between units 3 and 4 visible in the HiRISE image in D.

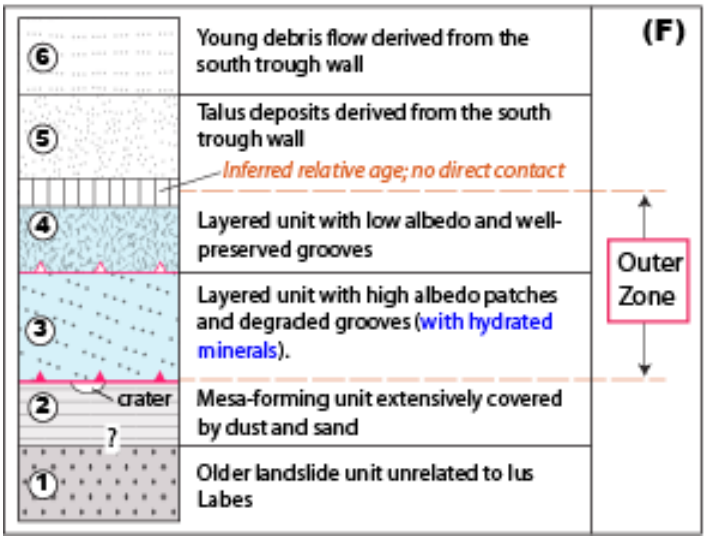

Figure 2.2, cont. (F) Summary of geologic units and their contact relationships as shown in B.

Our analysis of the six available CRISM images reveals no hydrated minerals in the trough-wall breakaway zone, the inner zone, most of the outer zone, and a small outcrop of trough-floor sediments (i.e., unit 2) (**Figs. 2.1B, 2.2A. and 2.2G**). In contrast, unit 3 in the landslide basal layer contains hydrated minerals, indicated by absorption bands at 1.4 and 1.9 μm (e.g., Roach et al., 2010). CRISM data from some patches display a sharp doublet, with minima around 2.21 and 2.278 μm, and an inflection near 2.4 μm (**Fig. 2.2H**), consistent with a hydrated silicate material previously identified at other sites in VM, likely representing a mixture of hydrated silica, Fe-smectite, and/or jarosite (Roach et al., 2010; Weitz et al., 2014; Thollot et al., 2012). Other patches also show absorptions at 2.3 μm (**Fig. 2.2H**), characteristic of Fe/Mg-OH in phyllosilicates, which have also been found in VM (Murchie et al., 2009a; Roach et al., 2010; Weitz et al., 2014; Thollot et al., 2012) and elsewhere on Mars (Ehlmann et al., 2011). The longitudinal grooves in unit 3 (feature c in **Fig. 2.2B**) cross-cut both high-albedo hydrated silicate patches and low-albedo phyllosilicate patches.

2.3 Discussion and conclusions

The longitudinal grooves on the Ius Labes surface are similar to the morphology of exceptional terrestrial landslides, as well as fluidized crater ejecta, potentially lubricated at the base by low-friction ice or snow (Peulvast et al., 2001; De Blasio, 2011; Lucchitta, 1978). Thus, it is conceivable that Ius Labes may have ridden over a layer of ice. However, the lack of compelling morphologic features related to near-surface ice or a periglacial environment, e.g., pingos, or polygonal patterned ground (e.g., Soare et al., 2005), does not uniquely implicate this hypothesis. Had Ius Labes instead rode on top of a water-saturated bed, the landslide would have

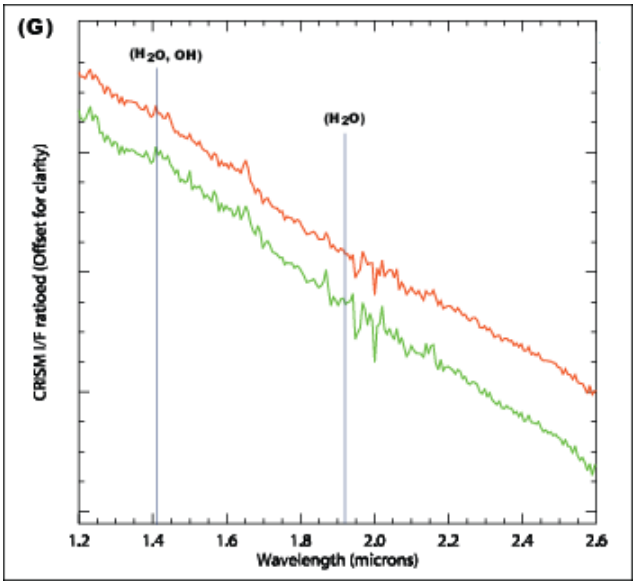

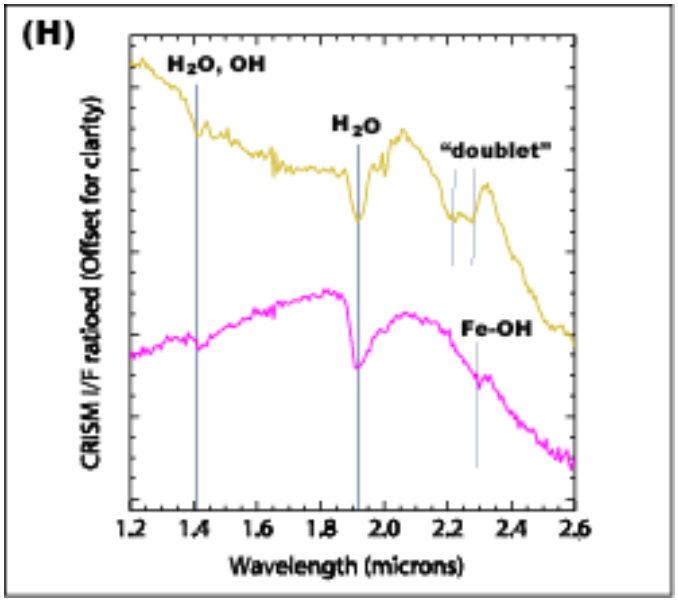

Figure 2.2, cont. (G) Example ratioed spectra from unhydrated portion of the landslide, CM-5, which show no absorptions related to OH or H_2O. (H) In contrast, ratioed CRISM spectra for image FRT0000B939 with spectra colors corresponding to mapped units in A, showing hydrated signature.

bulldozed soft materials near its rim outward and created a small-scale fold-and-thrust belt at the landslide front (Dahlen, 1990), which is not observed.

Instead, the presence of hydrated silicates in the basal layer of this and other landslides suggests that clay minerals may have played a key role in the formation of long-runout landslide morphologies. One such mechanism is lowering the basal friction and thus facilitating long-distance transport. For example, smectite clay absorbs water into its layered crystal structure and can have a friction coefficient that is lower by a factor of three versus that of dry rocks (Saffer and Marone, 2003; Byerlee, 1978). The coefficient of friction is fundamentally dependent on the normal stress on the sliding surface (Byerlee, 1978). In order to estimate the normal stress initially exerted at the landslide base, we assume: (1) a maximum density of 2500 kg/m^3 (i.e., for fractured basalt) for the landslide material (e.g., Hungr and Evans, 2004), (2) a maximum landslide thickness of 1800 m, and (3) a surface gravitational acceleration of 3.71 m/s^2. This results in a normal stress of ~15 MPa, yielding a low coefficient of friction of ~0.25 for smectite (Saffer and Marone, 2003), as compared to ~0.85 for igneous rock (Byerlee, 1978). This smectite friction coefficient is consistent with those previously determined for VM landslides (McEwen, 1989). Based on the observed CRISM absorption band strengths, smectite is likely to comprise far less than half of the basal layer's bulk composition. However, as shown by Collettini et al. (2009), even 10% smectite in a mixture under high shear strain yields a similar bulk friction coefficient to smectite alone. This is because high shear strain creates interconnected networks of smectite-bearing, low-friction slippage surfaces that bound the high-friction material, facilitating long runout. Though the composition of the basal layer surface can only be directly examined at the toe, we expect that mechanically significant hydrated materials are present at the base of most of the landslide mass based on along-strike projection of regional geology. Directly west

and southeast of our study area, Roach et al. (2010) and Weitz et al. (2014), respectively, documented trough-floor deposits that contain the same smectite and smectite-jarosite-silica mixture as found in the basal unit of Ius Labes (yellow boxes in **Fig. 2.1A**). This particular floor unit (Witbeck et al., 1991) is located directly below the Ius Labes landslide complex.

Based on the above arguments, in conjunction with previous understanding of Ius Chasma wall rock stratigraphy and geologic history (e.g., Murchie et al., 2009a; Roach et al., 2010), we propose the following sequence of events to form long-runout landslides: (1) partial alteration of VM wallrock to clay minerals (Murchie et al., 2009a) and the later formation of talus slopes and trough-floor deposits with hydrated silicates during the Noachian and Hesperian (Roach et al., 2010; Weitz et al., 2014) (**Fig. 2.3A**); (2) Slope failure and rotational sliding of the trough-wall rock downslope as a landslide, which was broken into several large, highly-fractured blocks and initially traveled over a high-friction, unhydrated surface (**Fig. 2.3B**); (3) Concurrently, the frontal landslide mass overrode and entrained the hydrated-silicate-bearing floor deposits, causing further loss of coherence and permitting the landslide outer zone to spread laterally while moving forward over the low-friction surface (Dahlen, 1990) (**Fig. 2.3C**). Other VM landslides with detected clay minerals have similar morphology and mobility (e.g., Lajeunesse et al., 2006; Lucas and Mangeney, 2007), suggesting they may have been generated by a similar process. The non-detection of clay minerals in the others may be explained by incomplete CRISM coverage of the landslides and lack of exposure combined with relatively small amounts of clay (e.g., ~20% smectite in units traversed by the Curiosity rover was not detected from orbit (Vaniman et al., 2014)). The first possibility can be tested by future studies as orbital acquisition continues.

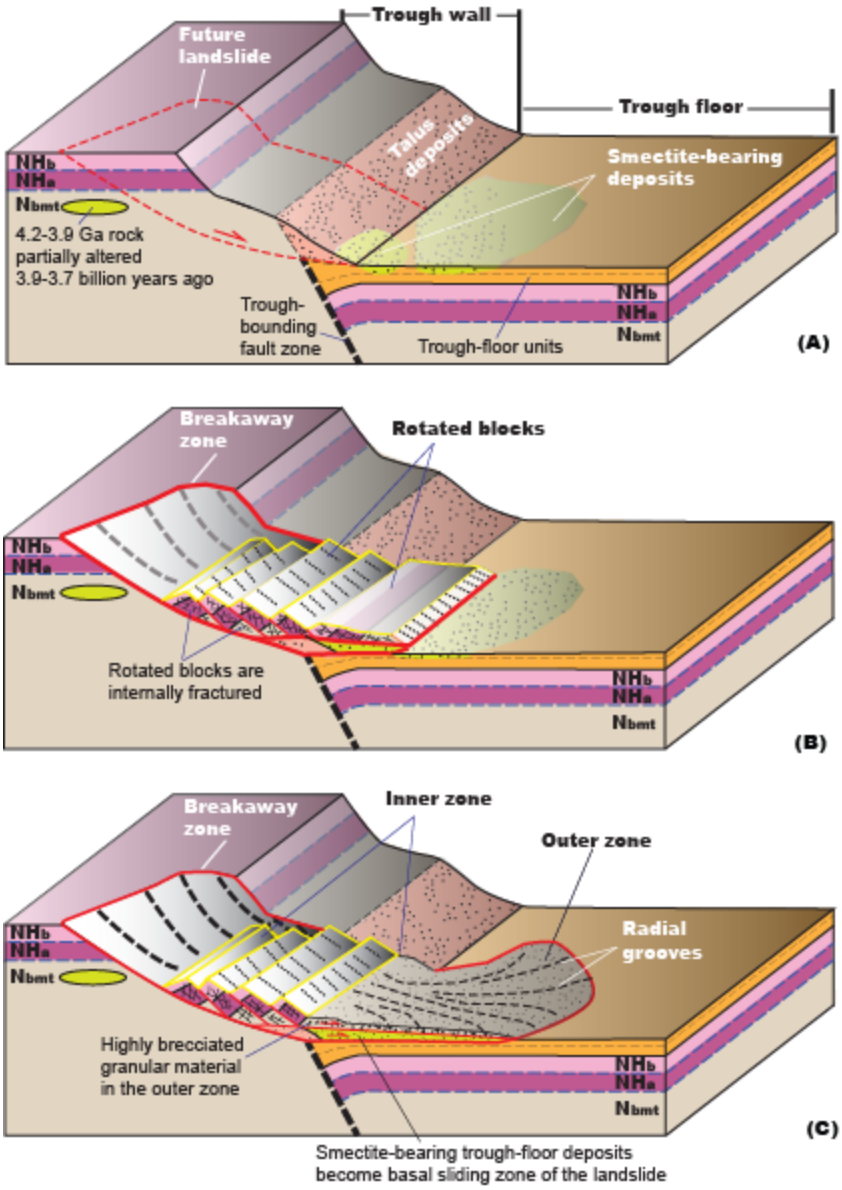

Figure 2.3. (A) Idealized model illustrating clay minerals such as smectite were produced by alteration of trough-wall rocks, and hydrated detritus was later transported to the trough floor. Trough-wall geologic units after Witbeck et al. (1991): Nbmt are Noachian basement rocks, locally altered to smectite-bearing hydrated material (Murchie et al., 2009a); NHa and NHb are Late Noachian and Hesperian volcanic flows that postdate the Noachian alteration event. (B) Failed trough-wall rock slides downslope as a landslide. (C) Frontal landslide mass rides over low-friction clay-bearing deposits, facilitating long-distance transport.

Our climate-independent clay-lubrication model (**Fig. 2.3**) is consistent with the interpretation of Quantin et al. (2004) that the nearly continuous occurrence of VM landslides from 3.5 Ga through 50 Ma has been independent of changing climate conditions. It also implies that, although hydrated silicate minerals were created mostly in the Noachian (4.1- 3.7 Ga) on Mars as a result of intense early water-rock interactions (Bibring et al., 2006; Murchie et al., 2009a; Ehlmann et al., 2011), the effects of early water are long-lasting, manifested in the participation of clay minerals in large-scale geomorphic processes shaping Mars' surface even at present.

2.4 References

Bibring et al. (2006), Global Mineralogical and Aqueous Mars History Derived from OMEGA/Mars Express Data, *Science, 312*, 400–404, doi:10.1126/science.1122659.

Byerlee, J. (1978), Friction of rocks, *Pure and Applied Geophysics, 116*, 615–626, doi:10.1007/BF00876528.

Christensen et al. (2004), The Thermal Emission Imaging System (THEMIS) for the Mars 2001 Odyssey Mission, *Space Science Reviews, 110*, 85–130, doi:10.1023/B:SPAC.0000021008.16305.94.

Clark, R.N., Gallagher, A.J., and Swayze, G.A. (1990), Material absorption band depth mapping of imaging spectrometer data using a complete band shape least-squares fit with library reference spectra, In: Proceedings of the Second Airborne Visible/Infrared Imaging Spectrometer (AVIRIS) Workshop, 2, 4-5.

Collettini, C., Niemeijer, A., Viti, C., Marone, C. (2009), Fault zone fabric and fault weakness, *Nature, 462*, 907–910, doi:10.1038/nature08585.

Dahlen, F.A. (1990), Critical taper model of fold-and-thrust belts and accretionary wedges, *Annual Review of Earth and Planetary Sciences, 18*, 55–99, doi:10.1146/annurev.ea.18.050190.000415.

De Blasio, F.V. (2011), Landslides in Valles Marineris (Mars): A possible role of basal lubrication sub-surface ice, *Planetary and Space Science, 59*, 1384–1392, doi:10.1016/j.pss.2011.04.015.

Ehlmann, B.L., Mustard, J.F., Murchie, S.L., Bibring, J.-P., Meunier, A., Fraeman, A.A., Langevin, Y. (2011), Subsurface water and clay mineral formation on early Mars, *Nature, 479*, 53–60, doi:10.1038/nature10582.

Erismann, T.H. (1979), Mechanisms of large landslides, *Rock Mechanics, 12*, 15–46, doi:10.1007/BF01241087.

Harrison, K.P. and R.E. Grimm (2003), Rheological constraints on Martian landslides, *Icarus, 163*, 347–362, doi:10.1016/S0019-1035(03)00045-9.

Hungr, O. and S.G. Evans (2004), Entrainment of debris in rock avalanches: An analysis of a long run-out mechanism, *Geological Society of America Bulletin, 116*, 1240–1252, doi:10.1130/B25362.1.

Lajeunesse, E., Quantin, C., Allemand, P., Delacourt, C. (2006), New insights on the runout of large landslides in the Valles Marineris canyons, Mars, *Geophysical Research Letters, 33*, L04403, doi:10.1029/2005GL025168.

Legros, F. (2002), The mobility of long-runout landslides, *Engineering Geology, 63*, 301–331, doi:10.1016/S0013-7952(01)00090-4.

Lucas, A. and A. Mangeney (2007), Mobility and topographic effects for large Valles Marineris landslides on Mars, *Geophysical Research Letters, 34*, L10201,

doi:10.1029/2007GL029835.

Lucas, A., Mangeney, A., Mege, D., Bouchut, F. (2011), Influence of the scar geometry on landslide dynamics and deposits: Application to Martian landslides, *Journal of Geophysical Research, 116*, E10001, doi:10.1029/2011JE003803.

Lucchitta, B.K. (1978), A large landslide on Mars, *Geological Society of America Bulletin, 89*, 1601–1609, doi:10.1130/0016-7606(1978)89<1601:ALLOM>2.0.CO;2.

Malin et al. (2007), Context Camera Investigation on board the Mars Reconnaissance Orbiter, *Journal of Geophysical Research, 112*, E05S04, doi:10.1029/2006JE002808.

McEwen, A.S. (1989), Mobility of large rock avalanches: Evidence from Valles Marineris, Mars, *Geology, 17*, 1111–1114, doi:10.1130/0091-7613(1989)017<1111:MOLRAE>2.3.CO;2.

McEwen et al. (2007), Mars reconnaissance orbiter's high resolution imaging science experiment (HiRISE), *Journal of Geophysical Research, 112*, E5S02, doi:10.1029/2005JE002605.

Melosh, H.J., 1987, The mechanics of large rock avalanches: Reviews in Engineering Geology, v. 7, p. 41–50, doi:10.1130/REG7-p41.

Murchie et al. (2007), Compact Reconnaissance Imaging Spectrometer for Mars (CRISM) on Mars Reconnaissance Orbiter (MRO), *Journal of Geophysical Research, 112*, E05S03, doi:10.1029/2006JE002682.

Murchie et al. (2009a), A synthesis of Martian aqueous mineralogy after 1 Mars year of observations from the Mars Reconnaissance Orbiter, *Journal of Geophysical Research, 114*, E00D06, doi:10.1029/2009JE003342.

Murchie et al. (2009b), Compact Reconnaissance Imaging Spectrometer for Mars investigation

and data set from the Mars Reconnaissance Orbiter's primary science phase, *J. Geophys. Res., 114*, E00D07.

Mustard et al. (2008), Hydrated silicate minerals on Mars observed by the Mars Reconnaissance Orbiter CRISM instrument, *Nature, 454*, 305-309.

Peulvast, J.P., Mege, D., Chiciak, J., Costard, F., Masson, P.L. (2001), Morphology, evolution and tectonics of Valles Marineris wallslopes (Mars), *Geomorphology, 37*, 329–352, doi:10.1016/S0169-555X(00)00085-4.

Quantin, C., Allemand, P., Mangold, N., Delacourt, C. (2004), Ages of Valles Marineris (Mars) landslides and implications for canyon history, *Icarus, 172*, 555–572, doi:10.1016/j.icarus.2004.06.013.

Roach, L.H., Mustard, J.F., Swayze, G., Milliken, R.E., Bishop, J.L., Murchie, S.L., Lichtenberg, K. (2010), Hydrated mineral stratigraphy of Ius Chasma, Valles Marineris, *Icarus, 206*, 253–268, doi:10.1016/j.icarus.2009.09.003.

Saffer, D.M. and C. Marone (2003), Comparison of smectite-and illite-rich gouge frictional properties: Application to the updip limit of the seismogenic zone along subduction megathrust, *Earth and Planetary Science Letters, 215*, 219–235, doi:10.1016/S0012-821X(03)00424-2.

Schultz, R. A., Hauber, E., Kattenhorn, S. A., Okubo, C. H., Watters, T. R. (2010), Interpretation and analysis of planetary structures, *Journal of Structural Geology, 32*, 855-875.

Soare, R.J., Burr, D.M., Wan Bun Tseung, J.M. (2005), Possible pingos and a periglacial landscape in northwest Utopia Planitia, *Icarus, 174*, 373–382, doi:10.1016/j.icarus.2004.11.013.

Soukhovitskaya, V. and M. Manga (2006), Martian landslides in Valles Marineris: Wet or dry?,

Icarus, 180, 348–352, doi:10.1016/j.icarus.2005.09.008.

Thollot et al. (2012), Most Mars minerals in a nutshell: Various alteration phases formed in a single environment in Noctis Labyrinthus, *Journal of Geophysical Research, 117*, doi:10.1029/2011JE004028.

Vaniman et al. (2014), Mineralogy of a mudstone at Yellowknife Bay, Gale crater, Mars, *Science, 343*, doi:10.1126/science.1243480.

Weitz, C.M., Dobrea, E.N., Wray, J.J. (2014), Mixtures of clays and sulfates within deposits in western Melas Chasma, Mars, Icarus, doi:10.1016/j.icarus.2014.04.009, (in press).

Witbeck, N.E., Tanaka, K.L., Scott, D.H. (1991), Geologic map of the Valles Marineris region, Mars: U.S. Geological Survey Miscellaneous Investigation Series Map I-2010, scale 1:2,000,000.

Yin, A. (2012a), Structural analysis of the Valles Marineris fault zone: Possible evidence for large-scale strike-slip faulting on Mars, *Lithosphere, 4*, 286-330.

Yin, A. (2012b), An episodic slab-rollback model for the origin of the Tharsis rise on Mars: Implications for initiation of local plate subduction and final unification of a kinematically linked global plate-tectonic network on Earth, *Lithosphere, 4*, 553-593.

CHAPTER 3

Spatiotemporal evolution, mineralogical composition, and transport mechanisms of long-runout landslides in Valles Marineris, Mars

3.1 Introduction

Long-runout landsliding is among the most prominent and enigmatic geomorphic processes sculpting the landscape of Mars, occurring nearly continuously in time over the past 3.5 billion years in the 4500-km-long, up to 700-km-wide, and 7-km-deep equatorial Valles Marineris (VM) trough system (Blasius et al., 1977; Lucchitta, 1979; McEwen, 1989; Witbeck et al., 1991; Quantin et al., 2004a,b) (**Fig. 3.1**). Mass wasting processes, in addition to fluvial incision and interior deposition, modify the morphology of VM, which is predominantly shaped by tectonics (e.g., Schultz, 1998; Yin, 2012a; Quantin et al., 2004b; cf. Sharp, 1973; McKenzie and Nimmo, 1999). VM lies along the crest of a regionally extensive highland, extending eastward from the Tharsis Montes and Syria Planum of the Central Tharsis Rise. The Tharsis Rise is the youngest tectonic feature on Mars and its origin has been attributed to a rising plume (Carr, 1973), impact-induced mantle upwelling and volcanism (e.g., Solomon and Head, 1982; Reese et al., 2004), migrating plume activity (Zhong, 2009), or slab-rollback subduction (Yin, 2012b). Despite decades of research, the origin and geologic history of the VM trough system remain contentious. The opening of the VM troughs may have started in the late Noachian (e.g., Dohm et al., 2009) and lasted after the end of the Hesperian (Schultz, 1998) or as late as the late Amazonian (Witbeck et al., 1991). The presence of pristine fault scarps has led some workers to suggest that the trough-bounding faults remain active today (Blasius et al., 1977; Yin, 2012a). The formation of this long trough system has been related to: (1) rifting (e.g., Blasius et al.,

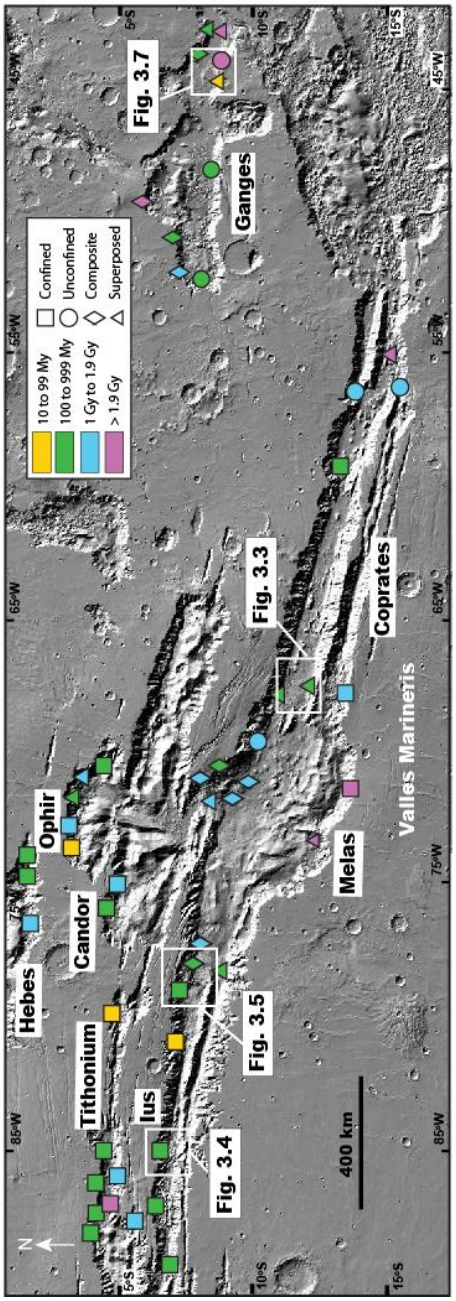

Figure 3.1. **Distribution of long-runout landslides in Valles Marineris.** Landslide locations, ages, and classifications (after Quantin et al., 2004). Landslides are classified as confined (squares) if transport of the outer zone was impeded by a topographic barrier, composite (diamonds) if multiple landslide outer zone lobes source from the same breakaway scarp, superposed (triangles) if the outer zone was deposited on the surface of a younger landslide debris apron, and unconfined (circles) if otherwise. Colors correspond to landslide surface ages with warmer colors representing younger deposits. The locations of Figs. 3.3, 3.4, 3.5, and 3.6 are also noted.

1977; Lucchitta et al., 1994; Peulvast and Masson, 1993; Schultz, 1998; Schultz and Lin, 2001; Mège and Masson, 1996; Mège et al., 2003; Masson, 1985; Golombek and Phillips, 2010), (2) subsurface removal of dissolvable materials or magmatic withdraw (e.g., Spencer and Fanale, 1990; Adams et al., 2009), (3) massive dike emplacement causing ground-ice melting and thus catastrophic formation of outflow channels (e.g., McKenzie and Nimmo, 1999), (4) the interaction between Tharsis-driven activity and an ancient Europe-sized basin (Dohm et al., 2001), (5) lava flow channels (Leverington, 2004; 2009), and (6) large-scale left-slip faulting related to plate tectonics, lateral extrusion, or continental-scale mega-landslide emplacement (Purucker et al., 2000; Anguita et al., 2001; Montgomery et al., 2009; Yin, 2012a). Some combination of the above processes and the role of pre-existing weakness in controlling its developmental history have also been proposed (Lucchitta et al., 1994; Schultz, 1998; Dohm et al., 2009; Andrews-Hanna, 2012a; 2012b; 2012c).

Due to their exceptional exposure and complete to nearly complete preservation of surface morphology, the emplacement processes of VM landslides have been intensely studied since they were first documented by investigations using images obtained by the Mariner 9 and Viking-1 spacecrafts (e.g., Blasius et al., 1977; Lucchitta, 1978; 1979; 1987; McEwen, 1989; Shaller, 1991; Peulvast et al., 2001; Schultz, 2002; Quantin et al., 2004a,b; Neuffer and Schultz, 2006; Soukhovitskaya and Manga, 2006; Bigot-Cormier and Montgomery, 2007; Lucas and Mangeney, 2007; De Blasio, 2011; Lucas et al., 2011; Legros, 2002; Mege and Bourgeois, 2010; Metz et al., 2010; Roach et al., 2010b; Watkins et al., 2015). These in-depth studies have led to a wide range of competing models for the mechanisms of long-distance landslide transport. Current hypotheses include (1) basal lubrication of the landslide mass by water, air cushion, or soft/weak materials (e.g., clay, ice, snow) (Shaller, 1991; Shreve, 1968; Watkins et al., 2015; De

Blasio, 2011) , and (2) fluidization of landslide materials with (Harrison and Grimm, 2003; Lucchitta, 1979; 1987; Quantin et al., 2004; Legros, 2002) and without (Melosh, 1979; 1987; McEwen, 1989; Soukhovitskaya and Manga, 2006; Hsu, 1975) the presence of water and volatiles.

With one exception (Watkins et al., 2015), the existing efforts are limited by the lack of constraints on the mineralogical composition of VM landslides, their source rock, and the underlying trough-floor material on which the landslides were transported. Thus, key questions such as whether water was involved in landslide transport and whether morphologic differences among VM landslides are controlled by differences in source and/or basal rock lithology remain uncertain. This work addresses this issue by conducting detailed geologic mapping of contact relationships and analysis of morphometric properties of landslides and their surrounding regions using high-resolution THEMIS (Thermal Emission Imaging System) satellite images obtained by Mars Odyssey (Christensen et al., 2004), CTX (Context Camera) (Malin et al., 2007) and HiRISE (High Resolution Science Imaging Experiment) images obtained by MRO (Mars Reconnaissance Orbiter) (McEwen et al., 2007), and HRSC (High Resolution Stereo Camera) images obtained by Mars Express (Neukum and Jaumann, 2004) in combination with topographic data from the Mars Orbiter Laser Altimeter (MOLA) on the MGS spacecraft (Zuber et al., 1992). Photogeologic mapping based on image analysis is coupled with examination of mineralogical composition of VM landslides and their surrounding regions using CRISM (Compact Reconnaissance Imaging Spectrometer for Mars) near-infrared spectral data collected by MRO (Murchie et al., 2007). Because landslide emplacement has occurred widely in space and continuously in time in VM throughout much of Mars' history (Quantin et al., 2004b),

resolving the underlying mechanisms of VM landslide transport would provide insight into past Mars surficial conditions and climate variability.

3.2 Background

3.2.1 Geologic setting

An understanding of the initial conditions within the canyon and trough floor is vital to determining the mechanical origin of VM landslides. Following its formation, early Noachian mafic basement rocks were partially altered to Fe/Mg phyllosilicates, including smectites and chlorites (Murchie et al., 2009). Subsequently, flood basalts accumulated as late Noachian and early Hesperian flat-lying layers exposed along the VM trough walls (McEwen et al., 1999). The layered rocks are locally intruded by plutons at the eastern end of the trough zone (Williams et al., 2003; Yin, 2012a). After the initial opening of the canyon, the walls of VM were extensively modified by fluvial erosion, mass wasting, and continued normal faulting- forming prevalent spur-and-gully morphology, triangular facets, sapping channels, and landslide scars (e.g., Peulvast et al., 2001). Based on analysis of a well-exposed, relatively continuous section in eastern Coprates Chasma with consistent mineralogical occurrences at comparable elevations throughout the canyon, VM wall rock stratigraphy consists of massive to layered pyroxene and olivine-rich erosion-resistant material in the lowermost wall near -4 km elevation, weakly layered, blocky chlorite-bearing material moving up in section near -2 km elevation, several kilometers of layered pyroxene-rich erosion-resistant material consistent with basalt, massive to blocky wind-eroded Fe/Mg smectite and Al-smectite in the uppermost portion of the wall near +3 km elevation, and an overlying layer of friable pyroxene-rich material at the top of the section (Murchie et al., 2009). Additionally, overlapping talus deposits blanket the lower portions of the

wall as a result of erosion and mass wasting of fine-grained materials, and these sometimes contain hydrated silicates (Roach et al., 2010). The steep scarps at the base of VM trough walls have been proposed to be induced by tectonic movement along trough-bounding faults (e.g., Lucchitta, 1979) and/or by glaciation (Mege and Bourgeois, 2010).

Following VM formation in the late Hesperian, continuous mass wasting associated with the opening of the chasma transported altered wall rock containing Fe/Mg smectites as sedimentary fines and breccia blocks. The mobilized fine-grained material constitutes layered deposits on the trough floor. The layered sedimentary Fe/Mg smectite was subsequently eroded by multiple fluvial and/or aeolian processes. As a result of the change in surface water geochemistry to more acidic conditions, hydrated silicate was then unconformably deposited on top of the layered sedimentary Fe/Mg smectite and deposits of sulfate precipitated from evaporating brines at the lowest elevations, and as matrix material cementing megabreccia (Roach et al., 2010). It has been proposed that large volumes of groundwater were discharged into VM and that ponding of this water in the Hesperian led to the formation of a large lake within the canyon (e.g., Harrison and Chapman, 2008; Nedell et al., 1987; Lucchitta et al., 1994). Massive and enigmatic interior layered deposits (ILDs) within the canyon have been interpreted as sedimentary mounds, likely formed in a lacustrine depositional environment (e.g., Nedell et al., 1987; Carr, 2012; Carr and Head, 2010; Harrison and Chapman, 2008). Near-surface ice has also been postulated within the chasmata (e.g., Lucchitta, 1987; Nedell et al., 1987; Peulvast and Masson, 1993). Metz et al. (2010) document the presence of prevalent soft-sediment structures in trough-floor deposits in Melas Chasma, and attribute deformation to the potentially rapid deposition and shallow burial of liquefied, homogenous fine-grained landslide sediments, rather than induced by tectonics. A

similar conclusion was also reached by Okubo (2010) in his study in southwestern Candor Chasma.

Other factors may also influence the transport distance and morphology of landslide emplacement. For example, the initial and underlying topography and the geometry of landslide breakaway surfaces may be related to trough-bounding seismic activity and may play a critical role in controlling the mobility of landslides (Lucas and Mangeney, 2007; Lucas et al., 2011). Landslide-related deformation may be induced by ground shaking from either Mars quakes or impacts. Landslide occurrences in VM exhibit a distinct spatial correlation with normal faults, implying that ground shaking from Mars quakes causes preferential concentration of landslide breakaway zones along trough-bounding faults (Blasius et al., 1977; Mege and Masson, 1996; Peulvast et al., 2001; Peulvast and Masson, 1993; Quantin et al., 2004a,b). In contrast, weak spatial correlation exists between landslides and craters large enough to have generated sufficient magnitude shaking to have triggered them (Akers et al., 2012).

3.2.2 Distribution of long-runout landslides in VM

Witbeck et al. (1991) were the first to systematically map the distribution and age of VM long-runout landslides based on Viking satellite images. Their map shows that the majority of the landslides in the trough walls and on the trough floors are Amazonian in age. More detailed work was conducted based on higher resolution images from Mars Orbiter Camera (MOC) and from THEMIS by Quantin et al. (2004a). These authors examined a total of 56 long-runout landslides and determined their emplacement ages to be between 3.5 Gy and 50 My by surface crater-counting estimate (see **Fig. 3.1**). These dates are supported by the lack of spur-and-gully morphology on the slopes of landslide scarps, implying landslide emplacement after the opening

of the canyon and formation of the morphology in the early Hesperian. As all the investigated landslides share characteristic morphologic features (e.g., Lajeunesse et al., 2006; Lucas and Mangeney, 2007) despite their occurrence over a widespread period of time, Quantin et al. (2004a) suggests that the landslides developed under similar conditions, and that they were emplaced by the same mechanism(s) regardless of their age and location in VM. Figure 3.1 shows the spatial distribution of these landslides. While there does not appear to be an observable correlation between landslide location and age within VM, there is an evident paucity of landslide occurrences in Coprates Chasma and at the eastern outlet of the canyon. This may be due to recent fluvial erosion in the downstream portion of the trough system as a result of regional slope, as exemplified by catastrophic flooding to form the circum-Chryse outflow channels (e.g., Warner et al., 2013; Harrison and Chapman, 2008).

3.2.3 Current hypotheses for long-runout landslide mobility

Landslide transport on Earth and Mars is fundamentally governed by the basic laws of physics that can be used to explore the mechanics of landslide motion. Assuming the gravitational energy released by landslide initiation is balanced by frictional resistance (i.e., ignoring heat loss) (Iverson, 1997), a simple relation can be obtained.

$$\boldsymbol{E = W} \qquad (1)$$

where $\boldsymbol{E = mgh}$ is gravitational potential energy of the landslide before it was launched and $\boldsymbol{W = \mu mgL}$ is work consumed by frictional transport of the landslide; m is mass, g is gravitational acceleration, h is the elevation drop of the landslide, μ is coefficient of basal friction, and L is the distance of landslide runout. This leads to the simple relationship between the coefficient of basal friction μ and the ratio of h/L. Because the exceptional runout distance of

long-runout landslides cannot be sufficiently explained solely by scaling for initial relief, a special mechanism of reducing the coefficient of friction during transport is required to achieve these extended lengths (e.g., Legros, 2002).

The above relationship may not be complete as additional kinetic energy also contributes to landslide motion at high speed, which may cause the landslide to leave the ground at a sudden steepening of slope (Shreve, 1968b). In this way, μ in Equation 1 is a maximum value for static friction rather than a lower, more relevant velocity-dependent kinematic friction (Di Toro et al., 2004). In addition, this approximation falsely treats the slide as a single block and landslide transport as a purely frictional-sliding process, whereas in actuality it transitions from behavior dominated by Coulomb friction to turbulent flow controlled by high shear stress in a viscous layer as a result of the exchange of momentum between the failing rock mass and the material entrained along the path (Harrison and Grimm, 2003; De Blasio and Elverhoi, 2008; Hungr and Evans, 2004). Equation 1 also neglects the heat produced by the slide. The characteristic total energy dissipation per unit mass at the beginning of a slide event, given as gh by Iverson (1997), for h = 2.5- 9.7 km in VM (Quantin et al., 2004), equates to 9.3- 36 kJ/kg. Given a specific heat of 0.84 kJ/kg°C for basalt, this would produce an average rise in temperature at the base of a typical VM slide of about 27° C, if all potential energy went into heating.

An additional effect of the gravitational potential energy is to spread the landslide sheet laterally, which occurs when it transports out of a narrow valley and meets a flat and open area; the landslide sheet then widens in the direction perpendicular to the main flow, as a consequence of the lateral pressure gradient (De Blasio, 2011). When the basal friction coefficient of the flat surface is negligibly small compared to the internal friction coefficient of the flowing mass, ϕ, a condition satisfied when sliding occurs on a very smooth base or if the base of the flow is

lubricated by a weak layer, such as a thin layer of liquefied saturated soil (Hungr, 2008), the earth-pressure force causing the granular avalanche to spread on a broader area can be calculated as $\boldsymbol{F_{LAT} \approx -\frac{1}{2}\rho g K_{EP} \delta L D^2}$, where K_{EP} is the earth-pressure coefficient for a strongly deformed granular material, and is dependent on the sign of longitudinal strain, δL is the element of landslide length along the direction of flow, and *D* is the slide height or thickness (De Blasio, 2011). According to Rankine's theory of frictional-plastic stress states, while K_{EP} is greater than 1.0, the material is in the "passive state" and is under compression. When K_{EP} drops below 1.0, the "active state" prevails and the material begins to expand (Hungr, 2008). *L* and *D* would change with time as the landslide stretches, maintaining the product *LD* constant (De Blasio, 2011).

i. Previously proposed models for terrestrial long-runout examples

Constraints on the mechanism(s) of long-runout landslide transport even in terrestrial examples have remained elusive. Debate over whether landslide transport involves viscous flow or frictional sliding has occurred over the past several decades (Hungr, 1995; Melosh, 1987; Shreve, 1968; Hsu, 1975; McSaveney, 1978). Several models have been proposed to explain the low coefficient of friction exhibited by these slides, but none is universally accepted. Early hypotheses about specific terrestrial deposits, including Elm landslide in Switzerland, Blackhawk landslide in California, and Sherman landslide in Alaska, assumed that interstitial surface or near-surface fluids allowed the slides to move as "fluid" flows (where the pore fluid mediates grain-grain interactions and lubricates flow), thus increasing the runout distance (e.g., Hungr and Evans, 2004). Proposed sources of this fluid include air-layer lubrication (Shreve, 1968), melted ice (McSaveney, 1978), and melt generation (Erismann, 1979). Proposed dry dynamic

weakening mechanisms include turbulent dispersive grain flow (Hsu, 1975; Bagnold, 1956), acoustic fluidization (Melosh, 1979; Collins and Melosh, 2003), mechanical fluidization (Davies, 1982), and dynamic rock fragmentation (Davies and McSaveney, 2009). These dry mechanisms each explain the apparent reduction in coefficient of friction by a temporary lowering of the normal stress between fragments. In these previously proposed models, this is achieved via the inelastic collision of particles, via elastic (sound) waves generated by the flow of and scattering through the avalanche, and via localized pressure drops resulting from the release of elastic strain energy as individual grains fail, respectively.

An additional complication not mentioned in the existing models is that the compositional properties of the landslide material itself may be favorable for long-distance transport. For example, a landslide mass penetratively cut by dense fracture networks and filled with hydrated minerals could be transported over a long distance due to self-lubrication. One model for this mechanism involves landslide initiation along a fault where altered fault-zone rocks are exhumed in the wall and provide the source material for self-lubricating transport. Blackhawk landslide provides a terrestrial example of the conditions required by this model, including pervasive faulting and hydrated material (Furnace limestone) in the source region, as well as fractured source region rocks exposed at the base of the long-runout portion of the landslide deposit (Shreve, 1959).

ii. Previously proposed models for VM long-runout landslides

Though long-runout landslides in VM have been studied in depth by various authors, and it is generally agreed that their initiation was triggered by Mars quakes along trough-bounding faults and that they were transported at high speeds (> 100 km/hour) (Lucchitta, 1979; Schultz, 2002;

Metz et al., 2010; Yin, 2012a; Peulvast et al., 2001), their mobility remains controversial. In particular, the role of fluids in VM landslide transport has long been debated. Two types of models have been proposed for emplacement of long-runout landslides in VM: (1) mechanisms that assist basal lubrication, and (2) mechanisms that promote fluidization and self-lubrication of landslide material itself during transport (see review by Legros, 2002). Basal lubrication may be achieved by (a) generation of high pore-fluid pressure at the base of a landslide due to released groundwater (Lucchitta, 1987), (b) sliding on a weak layer such as ice, snow, wet debris, mud, or clays (Lucchitta, 1987; De Blasio, 2011; Watkins et al., 2015), and (c) melt layers generated by frictional heating (De Blasio and Elverhøi, 2008; Weidinger and Korup, 2009). Basal lubrication hypotheses predict the observation of a correlation between landslide outer zone mobility and the presence of hydrated materials in the sliding zone. In contrast, proponents of fluidization for landslide transport invoke (a) the lubrication effect of fine-grained particles that ease motion of coarse-grained particles, i.e., dry granular flow (Hsu, 1975; Shaller, 1991) and (b) seismic shaking during landslide transport causing the gliding zones or the whole landslide bodies to act as fluid (Melosh, 1979). Fluidization mechanisms predict observation of correlation between landslide outer zone and source region composition. The self-lubrication of fault-zone rock model proposed in section (i) may also be particularly relevant to the VM long-runout landslides as they are initiated along trough-bounding fault scarps where possible localized hydrothermal alteration (controlled by the availability of water) may have occurred along fractures in fault zones prior to exhumation of the fault-zone rocks (**Fig. 3.2**). It is important to note that the proposed fluidization mechanisms do not require the presence of water or fluids at the time of landslide occurrence (Harrison and Grimm, 2003, cf. McEwen, 1989).

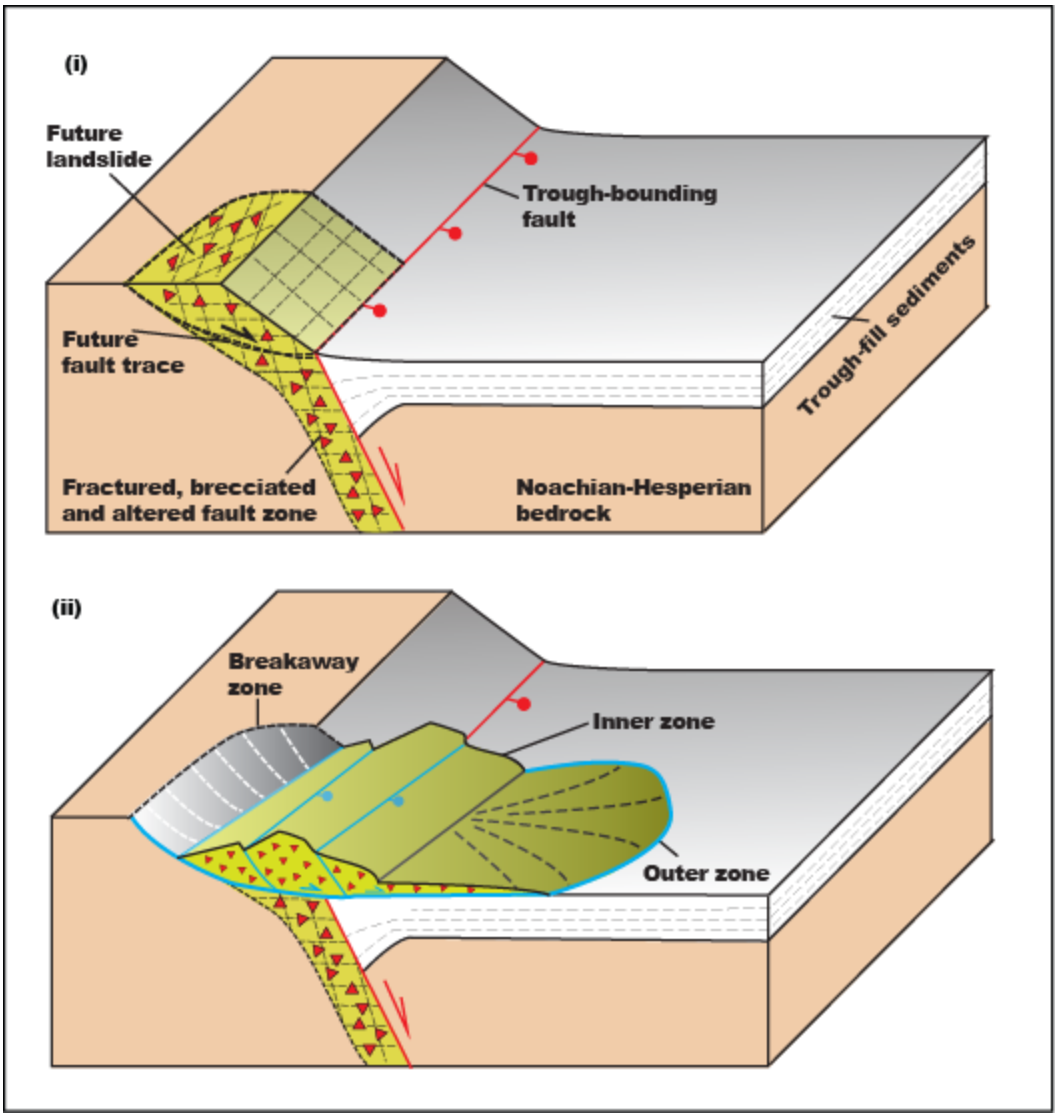

Figure 3.2. **Self-lubrication transport mechanism**. Model of mechanism: (i) pre-landsliding initial condition where fault-zone rocks have been locally altered and exhumed; (ii) landslide emplacement along a semi-circular breakaway scarp through self-lubrication of altered fault-zone rocks.

The preceding models not only bear significant implications for the mechanics of long-runout landslide transport in VM, but they also make specific predictions that have important implications for our understanding of Martian volatile history, past atmospheric conditions and fluctuations, and surface processes. For example, the potential contribution of water in VM landslide transport would indicate episodic water availability through recent time periods, and the possible involvement of ice in VM landslide activity would require the endurance of cold climate conditions at the surface of equatorial Mars. Dry granular flow, on the other hand, predicts no correlation between climate and landslide occurrence. Lubrication by hydrated minerals depends only on mineral formation at some point and then transport of detrital materials to the landslide region.

Much of the previous efforts in distinguishing between the competing formation hypotheses has focused mainly on the morphometric properties of the landslide deposits and source regions (e.g., Lucchitta, 1978; 1979; 1987; De Blasio, 2011; Harrison and Grimm, 2003; Soukhovitskaya and Manga, 2006; Lucas et al., 2011; McEwen, 1989; Quantin et al., 2004; Schultz, 2002; Bigot-Cormier and Montgomery, 2007; Roche et al., 2011; Brunetti et al., 2014). While morphology can be an important indicator of the relevant transport process(es), its ambiguity and variability have led to application of the same morphologic observations in support of opposing models for the role of water in landslide emplacement. Exclusive focus on morphometric analysis is insufficient for constraint of landslide transport mechanism(s) because the basal resistance that controls runout distance is dependent on multiple variables, including slide deposit internal friction and viscosity, cohesive strength, pore-fluid pressure, and composition, as well as the friction coefficient, cohesive strength, pore-fluid pressure, and composition of the basal sliding surface. Watkins et al. (2015) addressed this by investigating the mineralogical composition of a

landslide in Ius Chasma. Their clay-lubrication model for VM long-runout landslide transport is consistent with observations of a single example; in this study we combine morphological investigation with spectral analysis of sliding zone materials of long-runout landslides throughout VM, in order to examine the viability of this model on a regional scale.

3.3 Datasets

3.3.1 Satellite image and topographic data

Each orbital imager utilized by this study provides various advantages for investigating landslide morphology. HiRISE acquires very high resolution (up to 25 cm/pixel) imagery, useful in analyzing very detailed stratigraphic relationships and morphologic features (McEwen et al., 2007). CTX images are ~6 m/pixel and ~30 km across, well-suited for compiling high spatial resolution mosaics covering large areas and thus useful in detailed analysis of larger regions (Malin et al., 2007). THEMIS images are ~18 m/pixel in resolution and can be stitched together in a mosaic to create high resolution base maps of entire landslide regions, facilitating the correlation of unit morphologies across vast distances (Christensen et al., 2004). HRSC images are ~12 m/pixel (Neukum and Jaumann, 2004), and can be used along with MOLA topographic data (Zuber et al., 1992) to image the surface in three dimensions. Higher resolution CTX image mosaics can be constructed and registered to HRSC digital terrain models (DTMs) in order to more accurately identify layers for attitude calculation (e.g., Fueten et al., 2008). These capabilities are especially vital in a study region with drastic changes in topography because it enables the creation of stratigraphic cross-sections.

3.3.2 CRISM data

The CRISM instrument is a visible-infrared hyperspectral imaging spectrometer, with targeted observations taken in 544 channels in the visible to near-infrared (VNIR) (Murchie et al., 2007). It is capable of acquiring observations in both ~20 m/pixel targeted and 100–200 m/pixel mapping modes. The "S" detector covers the 0.4- 1.0 micron wavelengths in the VNIR and the "L" detector covers the 1.0-4.0 micron wavelengths. This study analyzes "L" detector Targeted Reduced Data Record (TRDR) observations in order to understand the contribution of surficial water to the mineralogical signature and composition of exposed rocks as evidenced by the detection of electronic transition absorptions from iron, and vibrational overtones and combination tones such as OH and H_20 in minerals (Burns, 1993; Clark et al., 1990). CRISM's high spatial resolution reduces spatial mixing of spectra, making it ideal for the collection of robust spectra of discrete units within a deposit (Roach et al., 2010a). CRISM mineral maps can be overlain on morphologic datasets.

3.4 Methods

3.4.1 Mapping methods

Two lines of research were conducted in this work in order to investigate the observable predictions of the basal lubrication and fluidization hypotheses for VM long-runout landslide transport: (1) systematic mapping and quantified analysis of landslide morphology and relationships to nearby geologic features and (2) correlation of landslide morphology to mineralogic compositions. The first task was completed based on analysis of THEMIS, CTX, HiRISE, and HRSC imagery data; the second by analyzing CRISM near-infrared spectral data from the same landslide systems documented by photogeologic investigations.

Following the procedure of Schultz et al. (2010) and Yin (2012a,b), we conducted detailed mapping of landslides and their spatial relations with surrounding rocks directly on satellite images. Bedding and sliding-surface attitudes were calculated using DTMs constructed with ORION software available from Pangaea Scientific (e.g., Fueten et al., 2005). Geometric properties of landslide outer zones were measured on mosaicked satellite images overlain on MOLA topographic data in JMARS (Java Mission-planning and Analysis for Remote Sensing).

i. Morphometric parameters of VM long-runout landslides

A landslide is broadly defined as the movement of a mass of rock, debris, or earth (soil) down a slope (IAEG, 1990). Mass-wasting features can be classified according to the materials involved, the movement type, and the movement velocity (Varnes, 1978). The first two are discernible after the fact from remote sensing data. Many types of mass-wasting features occur within VM, including small debris flows (e.g., Lucchitta, 1979), rockfalls (e.g., Bulmer and Zimmerman, 2005), and long-runout landslides. Debris flows are distinct from landslides mainly in that they consist of non-cohesive, poorly sorted, water-saturated material flowing rapidly down a channel (e.g., Iverson, 1997). The resulting morphological features observable in VM from orbit include a narrow and shallow main scarp, a relatively small area and volume (as compared to that of landslides), a channel-shaped depletion zone, and a fan-shaped depositional zone with variable roughness, indicative of variation in grain size within the material (Brunetti et al., 2014). Long-runout landslides, however, are the most dominant in aerial extent within VM and the focus of this work. The morphology of a landslide provides an indication of its rheology, including whether its transport was dry or fluid-enhanced. At least two different end-member zones (in addition to a semi-circular breakaway zone (or deflection zone; see Schultz, 2002))

occurring within single landslide systems of diverse ages (Quantin et al., 2004) have been identified in long-runout landslides in VM based on their characteristic surface morphology: a thick-skinned inner zone and thin-skinned outer zone (see Watkins et al., 2015) (**Fig. 3.3A**). This two-zone morphology is common in VM, but this key observation has not been considered by most existing models, and may be crucial to our understanding of VM long-runout landslide emplacement mechanisms. A distinction between these two landslide zones is implied by the morphological variance and the differing behavior of the two materials during landslide transport: discrete brittle deformation in inner zones compared to deformation of outer zones by flow. As shown in the study detailed below, this fundamental difference may be due to different emplacement processes, transport mechanisms, or composition of landslides or underlying rocks.

The internal structure of thick-skinned VM landslide inner zones is very coherent and structured in comparison to the thin outer zones. The inner zones are characterized by fault-bounded, tilted toreva slump blocks that dip back towards the head, bounded by minor intra-landslide fault scarps, with < 10 km transport distances from their source regions (feature *a* in **Figs. 3.3A and 3.3B**). The landslide inner zones exhibit a similar width to that of the breakaway scarp, implying that they did not spread laterally while moving. This morphology is characteristic of rotational landslides (Cruden and Varnes, 1996), which are nucleated upslope of a normal fault trace, where curvature occurs due to circular failure combined with rotational sliding along the curved basal slip surface (Highland and Bobrowsky, 2008). This curved surface of rupture and tilted block morphology is shown schematically in cross section of VM long-runout landslides (**Fig. 3.3C**). On Earth, rotational slides involve mechanically homogenous slope rocks that retain the stratigraphy of the breakaway source region and occur adjacent to trough-bounding normal fault scarps. The style of landslide initiation in VM can be inferred from

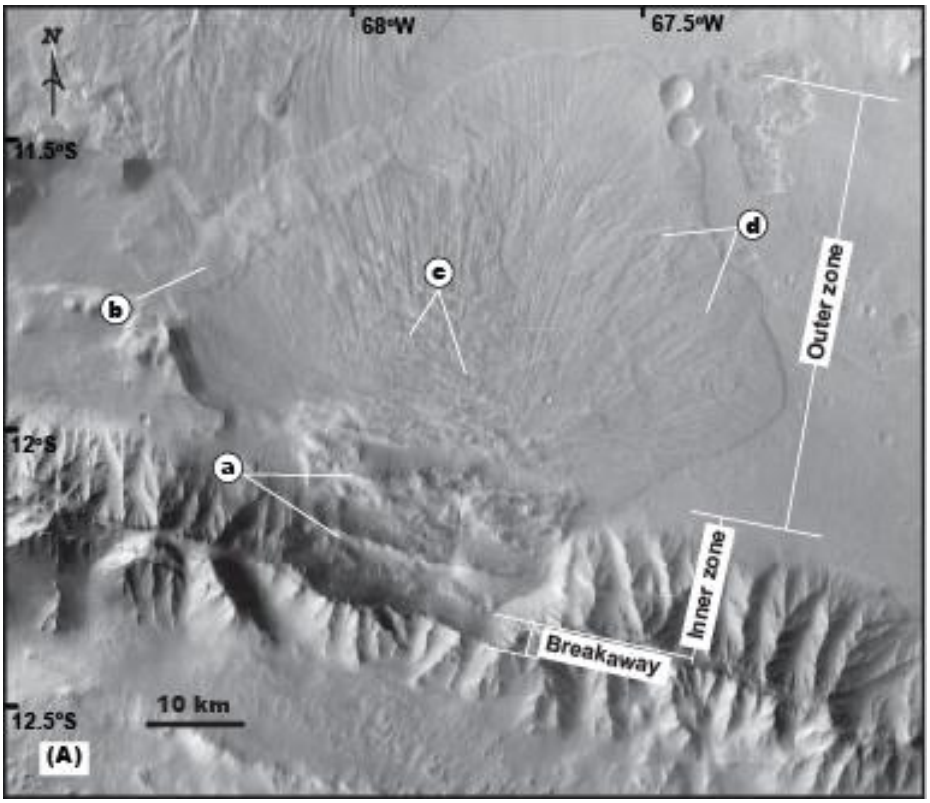

Figure 3.3. **VM long-runout landslide morphological structure.** (A) THEMIS mosaic of unconfined VM long-runout landslide example in Coprates Chasma, indicating morphological features *a*, tilted blocks, *b*, thinness of the deposit at the toe, evident where the younger landslide deposit is visibly superposed on the apron of an older slide, *c*, radial fractures, and *d*, longitudinal ridges and grooves, as well as the inner, outer, and breakaway zones.

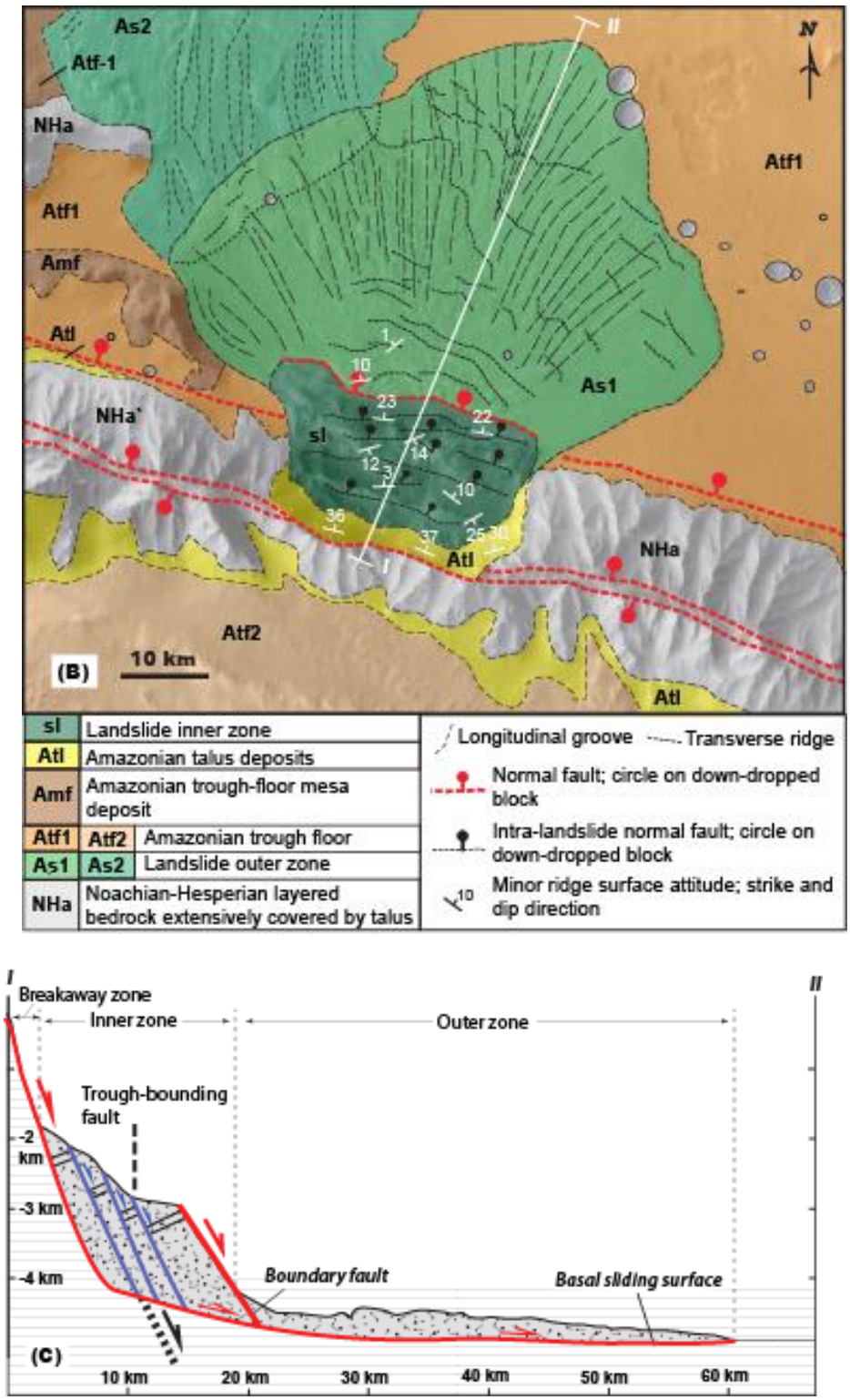

Figure 3.3, cont. (B) Detailed geologic map of units and features in A. Red dashed line follows trace of trough-bounding and intra-landslide normal faults. Circles are on the down-dropped block. (C) Interpreted cross-section through geologic map in B using MOLA topographic data.

the topography of the source regions. Some landslides were launched from the upper section of the trough wall, as suggested by the presence of steep trough-wall scarps directly below amphitheater-shaped alcoves. The basal surfaces of other landslides cut all the way down to the base of the trough wall, causing the evacuation of landslide materials from the entire trough-wall section. The general morphology of the landslide systems initiated from the upper versus whole sections of the trough walls is similar.

VM landslide outer zones, on the other hand, are separated from the inner zones by a bounding major intra-landslide fault, expressed by a prominent down-slope-facing scarp, and are characterized by thin, fan-shaped lobe sheets (feature *b* in **Fig. 3.3A**) spreading over 10s of km across the trough floor. They have highly chaotic and brecciated internal structures, indicative of loss of coherence, and their surfaces exhibit convex-forward transverse (feature *c* in **Figs. 3.3A and 3.3B**) and longitudinal ridges (feature *d* in **Figs. 3.3A and 3.3B**) in a vast debris apron radiating from the source region. These longitudinal ridges are separated by V-shaped grooves, where the ridges have diverged into the fan and locally curved to form distinguishable lobes. The ridges have been thought to be preserved shear surfaces between loosely consolidated debris (Christensen et al., 2003) (as compared to the resistant cap rock of the slump blocks), moving forward at variable speeds during landslide emplacement (e.g., Lucchitta, 1979). At the toe, material piles up and either transverse ridges (e.g., Lucchitta, 1979) or soft-sediment deformation (Metz et al., 2010) dominates. Lastly, outer zone lobe deposits are commonly much wider than the landslide inner zone, implying significant lateral spreading during landslide runout. The debris aprons of slide outer zones are also highly elongated as compared to slide inner zones on Mars and all landslides on Earth. These observations largely agree with the observations of landslide morphology made by Lucchitta (1978), (1979), and (1987).

Because ice lubrication models have been proposed, we specifically searched for morphologies that may resemble pingos or polygonal patterned ground, which are typically related to the presence of near-surface ice (e.g., MacKay, 1973; Soare et al., 2005), basic landforms characteristic of a glacial landscape, e.g., eskers, drumlins, kettles, and kames, or the symmetrical trimlines required by a paraglacial environment (Mege and Bourgeois, 2010). However, our efforts yield no convincing results indicating their presence. Dominant trough floor features are mesas and buttes that are likely remnants of ILDs.

In order to characterize the frictional forces that control VM landslide long-distance transport and extensive lateral spreading, we measured and analyzed in detail several morphometric parameters for all 26 VM long-runout landslide systems with unobstructed characteristic morphology. The morphometric properties measured for each landslide system include maximum runout length (L), maximum outer zone spreading width (sp), breakaway scarp width (W_0) as a proxy for initial volume, and minimum outer zone spreading angle (α) as a mass-independent measure of coefficient of friction (μ) (**Figs. 3.3D and 3.3E**). We define L as the maximum distance in the direction of transport from the prominent intra-landslide boundary fault scarp to the edge of the outer zone toe. We define sp as the maximum exposed width of the outer zone perpendicular to the direction of transport. L and sp in combination represent overall landslide mobility. We define W_0 as the width of the main scarp perpendicular to the transport direction of a given lobe, that is, the steep, visible part of the rupture surface on the undisturbed ground at the upper edge of the landslide, from which material was displaced. This value provides an approximation of an initial bounding condition for the volume of mobilized material. We define α based on application of fundamentals of glacier flow, whereby yield stress is compensated by the basal drag (Paterson, 1994):

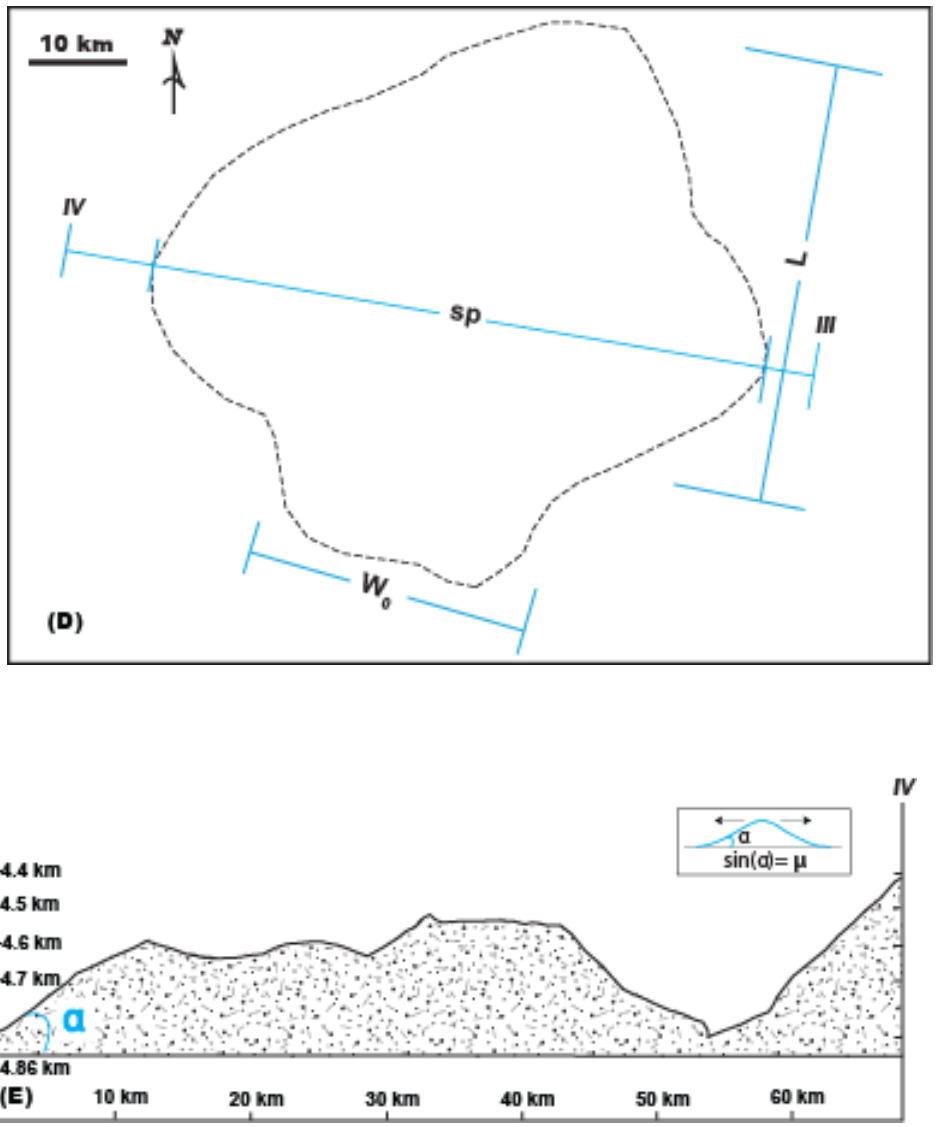

Figure 3.3, cont. (D) Landslide outline with definitions of measured VM long-runout landslide geometric parameters in plan view: *sp*, spreading width, *L*, runout length, W_0, breakaway scarp width. (E) Landslide cross-section with topographic profile derived from MOLA data, with definitions of measured VM long-runout landslide geometric parameters in cross-sectional view: α, spreading angle, μ, coefficient of friction.

$$\boldsymbol{\tau = \mu \sigma_N} \qquad (2)$$

where $\boldsymbol{\tau = \rho g H sin\alpha}$, $\boldsymbol{\sigma_N = \rho g H}$, τ is shear stress at the base, σ_N is normal stress at the base, ρ is density, H is thickness of the flow, and α is the angle of the deposit cross section on the horizontal trough floor. Using Equation 2, the spreading angle value α can be used to calculate a mass-independent value for the minimum coefficient of friction at the base of the landslide. Where possible, α was measured at the intersection of the widest portion of the lobe, where it is spread the thinnest, and the underlying trough floor sliding surface, in order to obtain the minimum coefficient of friction of the lobe (**Fig. 3.3E**). These parameters were then used in analysis of landslide mechanics.

ii. Classification of VM long-runout landslides

VM long-runout landslides can be categorized into four morphological classifications, which express distinct kinematics: unconfined, confined, composite, and superposed. Despite variation in classification, VM long-runout landslides share the characteristic morphologic features outlined in section (i), suggesting that they were all emplaced by a similar mechanism. We define an *unconfined landslide* as one in which the transport of the outer zone, following emplacement of the inner zone, was unimpeded by any topographic barrier within the valley during runout (circles in **Fig. 3.1**). That is, the only governing parameters in stopping landslide motion (and runout length *L* as a result) are internal and sliding surface resisting forces. A landslide example in Coprates Chasma (**Fig. 3.3**), whose features were discussed in section (i), provides an example of an unconfined landslide.

We define a *confined landslide* as one that is juxtaposed with a topographic barrier in the valley, suggesting that its original transport was interrupted due to external obstacle(s) (squares

in **Fig. 3.1; Fig. 3.4**). That is, the inner zone reached a barrier prior to outer zone emplacement, deflecting subsequent transport of the outer zone perpendicular down the canyon. Because of this, the runout length *L* in this case is limited and not solely dependent on the work done by basal friction. In order to isolate and characterize the frictional forces that control landslide runout distance, therefore, confined landslides are not included in the compiled morphometric analyses of VM landslides to follow in section 3.5.1.

We define a *composite landslide* as one in which more than one overlapping debris apron (including an inner and/or outer zone) sources from the same breakaway scarp (diamonds in **Fig. 3.1**; **Fig. 3.5**). While the transport direction of each of these debris aprons, inferred from the lobe shape of the deposit, may differ, they likely still represent a singular emplacement event comprised of multiple pulses or surges, as occurs invariably within debris flows (Iverson, 1997) and is the case for the multiple lobes emplaced during the Mount La Perouse ice and rock avalanche in Alaska in 2014 (**Fig. 3.6**). Composite landslides may be confined or unconfined. In order to quantify the frictional force that governs the runout of each debris apron, all morphometric parameters of unconfined composite landslides were measured for each individual lobe separately, including outer zone spreading width (*sp*) to the degree that it is unconcealed and thus discernible, and spreading angle (α) at the intersection of the widest portion of the lobe and the trough floor rather than an underlying lobe, where possible.

Lastly, we define a *superposed landslide* as one whose outer zone surface lies in any part on top of and overprints the surface of another outer zone deposit, which sources from a different breakaway scarp (triangles in **Fig. 3.1; Fig. 3.7**). This cross-cutting relationship implies that both the inner and outer zones of the superposed landslide were emplaced in succession subsequently to the inner and outer zones of the underlying landslide. Superposed landslides may also be

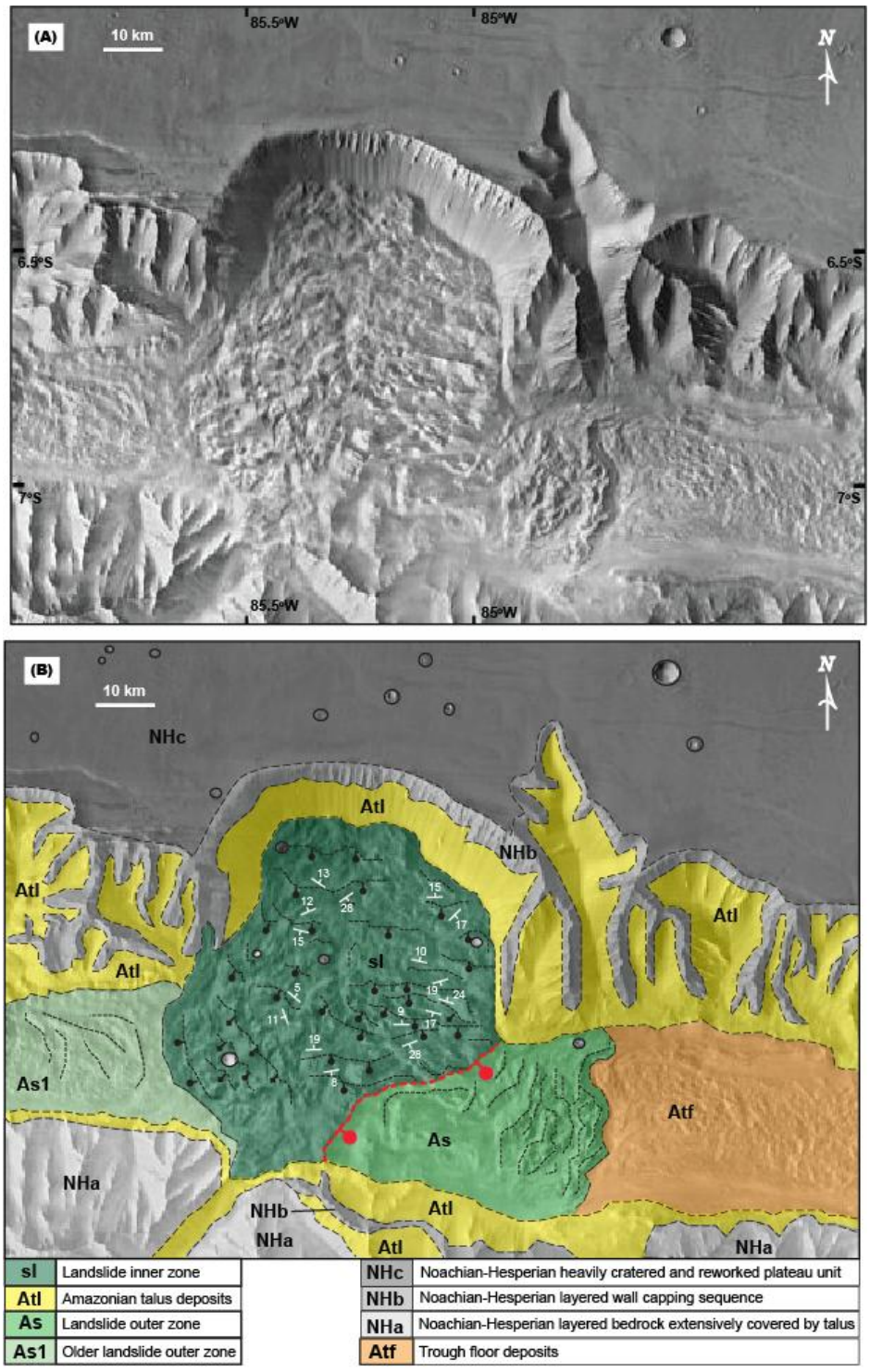

Figure 3.4. C**onfined VM long-runout landslide classification example**. (A) Confined type in Ius Chasma (THEMIS mosaic). (B) Geologic map of landslide in A. Red dashed lines indicate main intra-landslide boundary fault scarp; black dashed lines indicate minor scarps and ridges. Circles on down-dropped block. Long-dashed lines indicate longitudinal grooves.

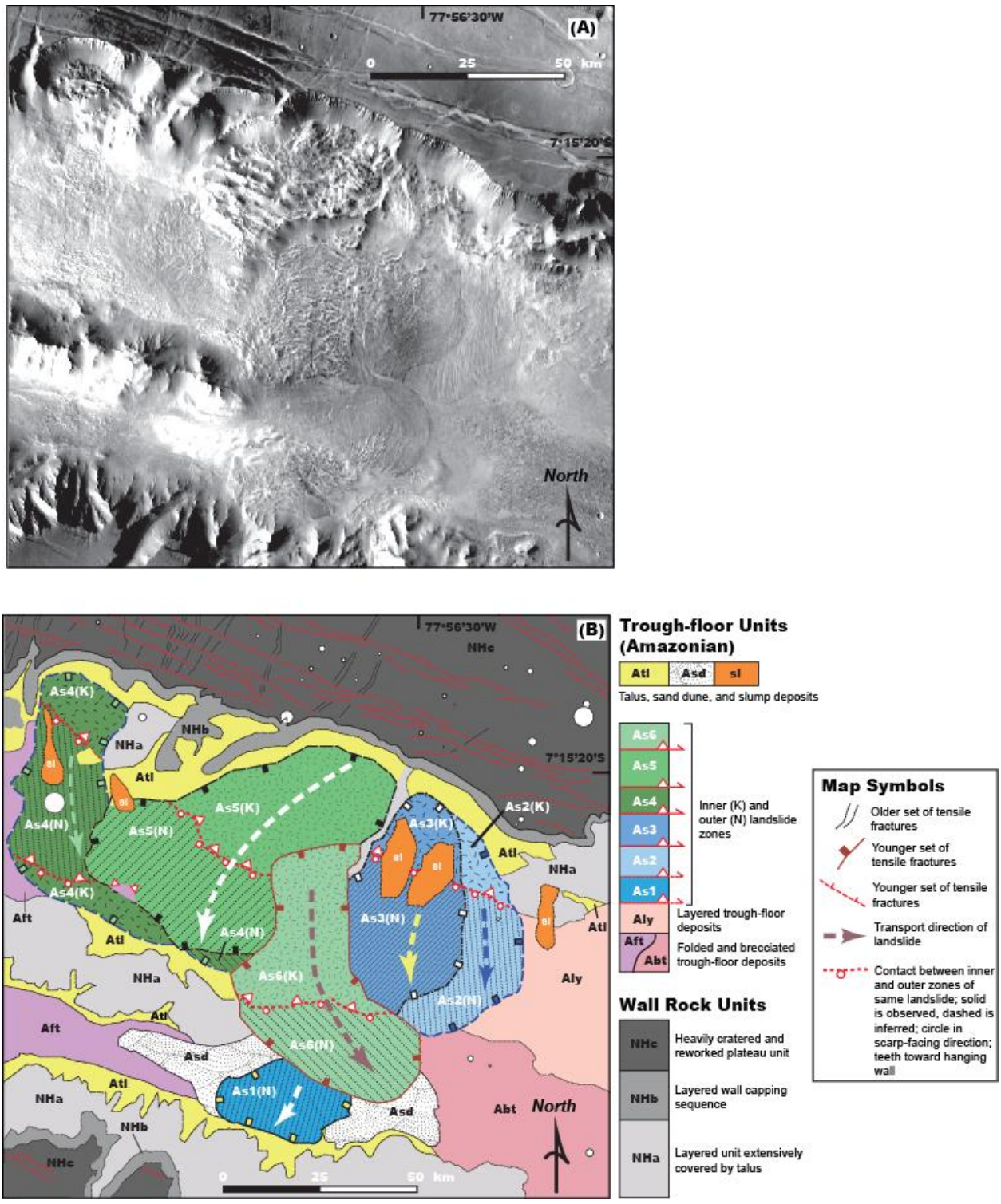

Figure 3.5. Composite VM long-runout landslide classification example. (A) Composite type in eastern Ius Chasma (THEMIS mosaic). (B) Geologic map of landslide complex in A.

Figure 3.6. **Mount La Perouse rock avalanche, Alaska**. (A) Spread of the landslide toe and emplacement of multiple long-runout lobes within the single event. Note also the longitudinal grooved morphology which resembles that of VM long-runout landslides, implying a similar transport mechanism. Location of B also shown. (Photo used with permission from Drake Olson.) (B) Constituent materials at the landslide toe, consisting of ice and snow, suggesting that the landslide entrained a large amount of snow and ice as it travelled downslope. While morphologic evidence of ice is not observed in VM, VM long-runout landslides are proposed to similarly entrain clay-bearing material during emplacement. (Photo used with permission from Drake Olson.)

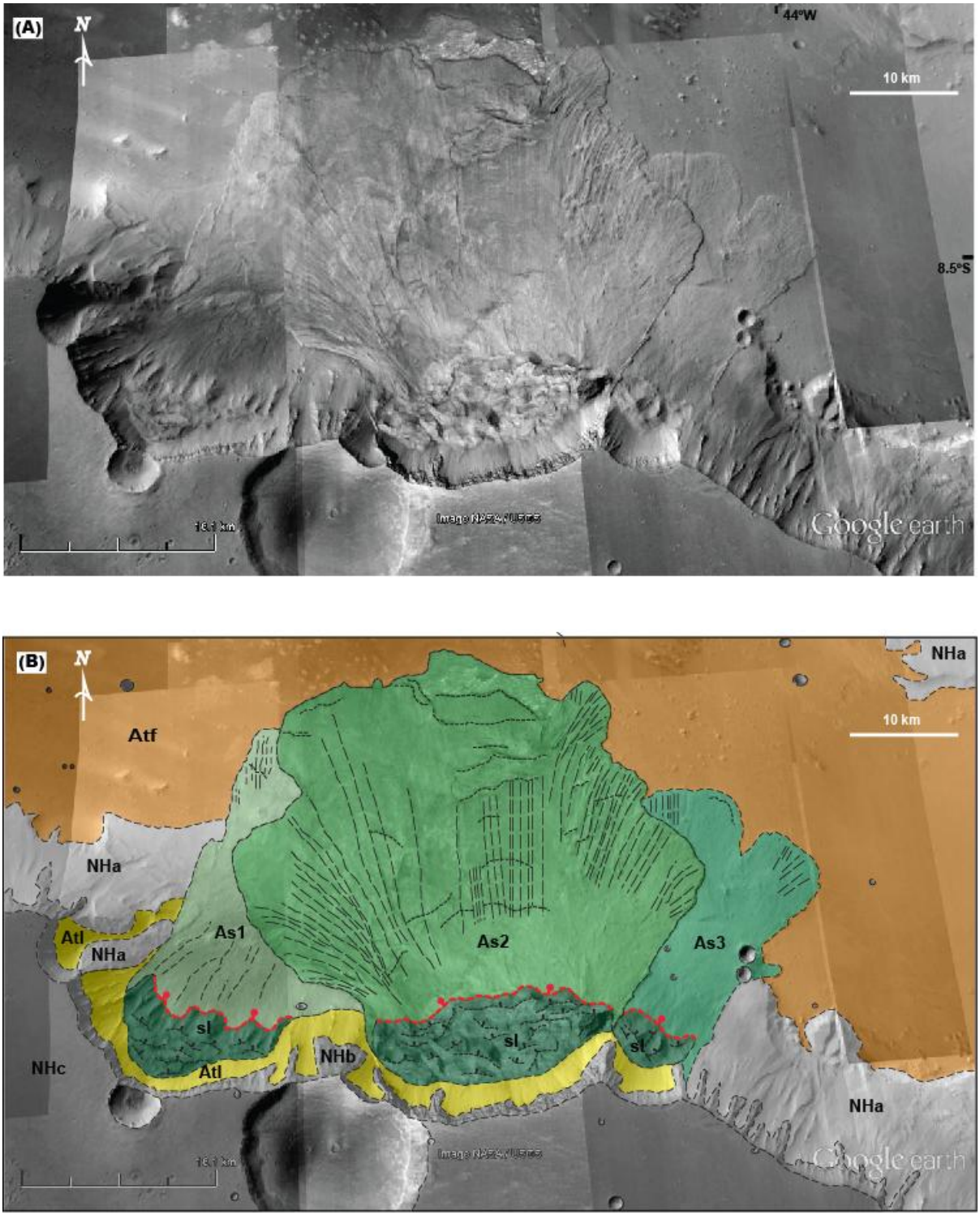

Figure 3.7. **Superposed VM long-runout landslide classification example**. (A) Superposed type in Ganges Chasma (CTX mosaic). (B) Geologic map of landslide in A. Despite variation in classification, VM long-runout landslides share characteristic morphologic features.

confined or unconfined. Again, where possible, the outer zone spreading angle (α) of unconfined superposed landslides was measured at the intersection of the widest portion of the debris apron and the trough floor, where motion was not impeded by an underlying lobe. Given that the pre-landsliding potential energy contribution to landslide transport is on the order of 20 times that introduced by the topographic obstacle presented by the average pre-existing outer zone deposit, we consider the kinematic effects of the interaction of a superposed landslide with an underlying lobe to be negligible in our analysis.

3.4.2 CRISM methods

In order to establish whether a correlation between VM long-runout landslides and basal hydrated silicates exists on a regional scale or is an anomaly, a survey of VM landslide outer zone compositions was completed. Morphologic end members in each image, defined based on analysis of the geologic context in corresponding satellite images, were investigated using CRISM data to search for hydrated minerals. Sites where landslide outer zones and their surrounding regions are well exposed and for which CRISM full-resolution target (FRT) or half-resolution long observation (HRL) images exist were selected for spectral study. 51 total CRISM images were examined, exhausting the available long-wavelength channel CRISM coverage of long-runout landslides and their immediate vicinities in VM. 40 images covering landslides were examined, 36 of which cover the outer zones of 14 landslide systems. 12 images covering trough floor in the region surrounding 8 landslide outer zones were also examined. Images were examined using the CRISM procedures outlined in Chapter 2.

Specific hydrated minerals possess unique and characteristic spectral signatures. Water in mineral structures has an absorption between 1.91 and 1.95 μm due to H_2O vibration that is

observed and mapped in CRISM data. In VM, also commonly observed is a weaker absorption between 1.40 and 1.45 μm, also due to H_2O vibration. A sharp doublet, with minima near 2.21 μm and 2.278 μm (due to metal-OH vibrations) and an inflection around 2.4 μm are spectral signatures consistent with the presence of a class of hydrated silicate material previously identified in Ius, Coprates, and Melas Chasmata and Noctis Labyrinthus (Roach et al., 2010b; Metz et al., 2010; Weitz et al., 2011; 2014). This "doublet material" does not show a good spectral match to any single library spectra, and is thought to contain some mixture of hydrated silica, Fe-smectite, possibly partially altered, and jarosite (Thollot et al., 2012). A broad absorption between 2.20 μm and 2.26 μm indicates the presence of structural H_2O, a hydrated signature evident in the library reflectance spectra of hydrated minerals such as monohydrated sulfates (kieserite), also found in VM (Roach et al., 2010b). An absorption at 2.3 μm is a spectral signature of Fe/Mg-OH, such as in Fe/Mg phyllosilicates previously found at the foothills of Ius Chasma (Roach et al., 2010a), in dark boulders and associated dusty talus in the mid to lower walls of western Valles Marineris (Flahaut et al., 2012), in troughs and a closed depression in Noctis Labyrinthus (Thollot et al., 2012; Weitz et al., 2011), in lower parts of Coprates Chasma walls and landslides (Murchie et al., 2009), and in globally widespread exposures of Noachian bedrock, associated with impact craters, in paleolakes and fluvial basins, and in stratigraphy in high-standing topography (Ehlmann et al., 2011; 2013).

Spectral summary parameters were calculated from diagnostic absorptions to distinguish between these minerals and facilitate preliminary identification and mapping of distinct geologic regions within a CRISM image (e.g., Pelkey et al., 2007). Summary parameters used in this study include the 1.9 μm band depth, due to combinations of H_2O bending and stretching vibrations (BD1900); the 2.21–2.27 μm band depth (BD2200), and the 2.3 μm band depth

(D2300), both due to metal-OH vibrations (e.g., Roach et al., 2010b), and are configured to highlight spectral end members distinguished mostly by water content. Map-projected composition data were integrated with geologic maps created by interpreting CTX, HiRISE, THEMIS, and HRSC orbital imagery. Geologically defined end member units based on the relationships in both the satellite images and summary parameter images were mapped. Morphological indicators of CRISM-defined spectral units were used for geologic mapping outside the extent of CRISM observations.

3.5 Results

3.5.1 Quantification of landslide morphology

The map-view shape of 26 VM landslide outer zone lobes was analyzed in detail in order to understand the mechanisms specific to their long-distance transport. These outer zones exhibit exceptionally high mobility compared to rare terrestrial examples that share morphological similarities with Martian long-runout examples (e.g., Blackhawk, Sherman, and Elm landslides; Lucchitta, 1978), and to debris flows in VM (**Fig. 3.8A**). Based on the fundamental governing equations outlined in section 2.3, the differences in initial drop height between these examples account in part but not in totality for this disparity in mobility. Across these outer zones, spreading width generally increases with runout length, with lateral spreading occurring at ~1.4 times the rate of runout (**Fig. 3.8A**). In comparison, a steeper trend amongst VM debris flows implies debris flow runout increases faster than debris flow lateral spreading (**Fig. 3.8B**).

On the whole, spreading width normalized with runout length increases with breakaway scarp width, as a proxy for initial volume of the incipient landslide mass in the canyon (**Fig. 3.8C**). This relationship expresses a broad mass dependence of outer zone mobility, whereby the

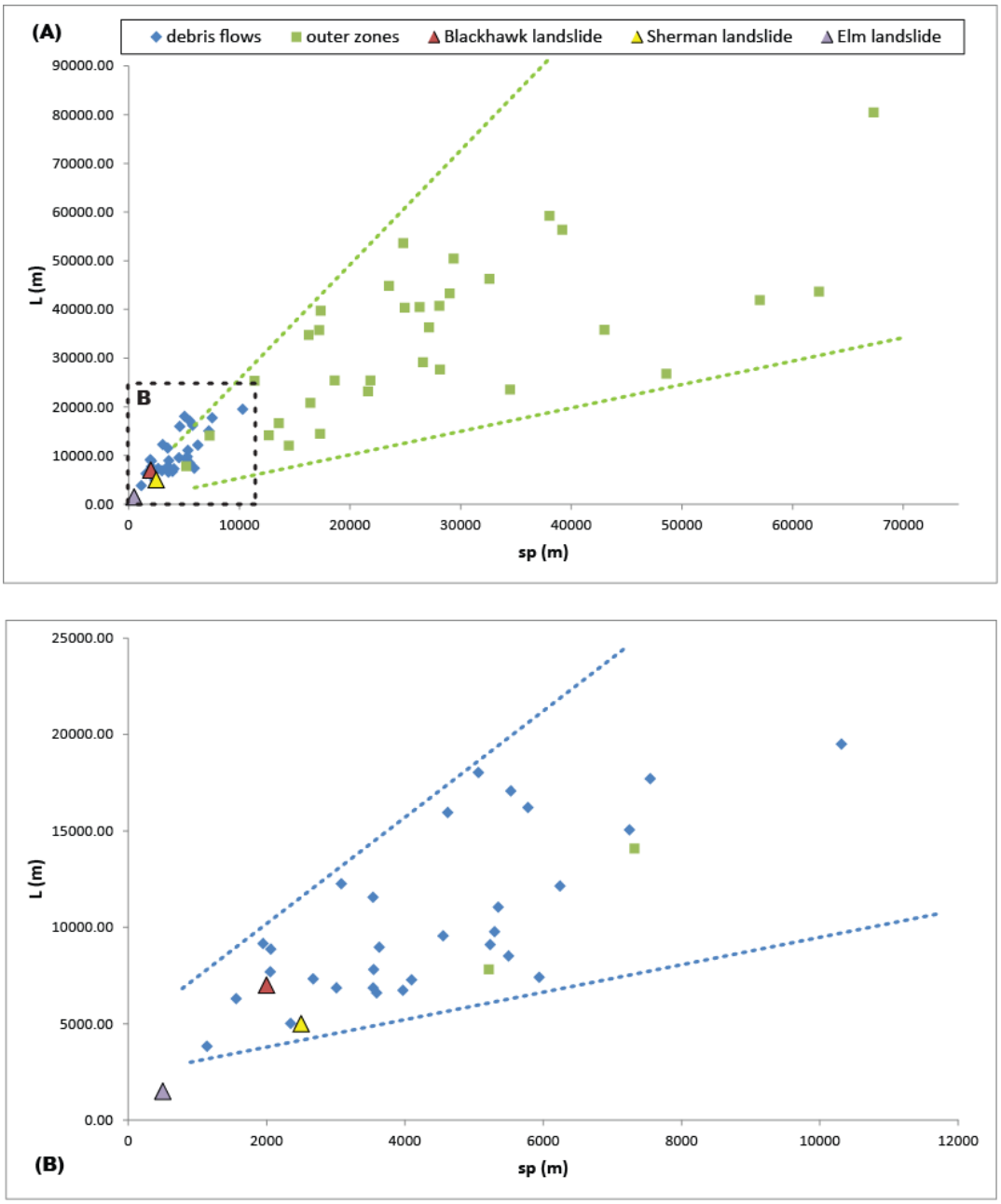

Figure 3.8. Plots of VM landslide morphometry. (A) Plot of landslide runout versus spreading, for VM landslide outer zones and debris flows. Also plotted are the values for the Blackhawk landslide in California, the Sherman landslide in Alaska, and the Elm landslide in Switzerland, illustrating the exceptionally high mobility of VM long-runout landslides compared to terrestrial long-runout examples. Dashed lines represent approximate upper and lower bounds for the data. Note the ~1.5 factor increase in outer zone lateral spreading with runout during landslide emplacement in comparison to that of debris flows. (B) Enlargement of A for VM debris flows, which follow a steeper trend, implying that debris flow runout increases faster than debris flow lateral spreading. Dashed lines represent approximate upper and lower bounds for the data.

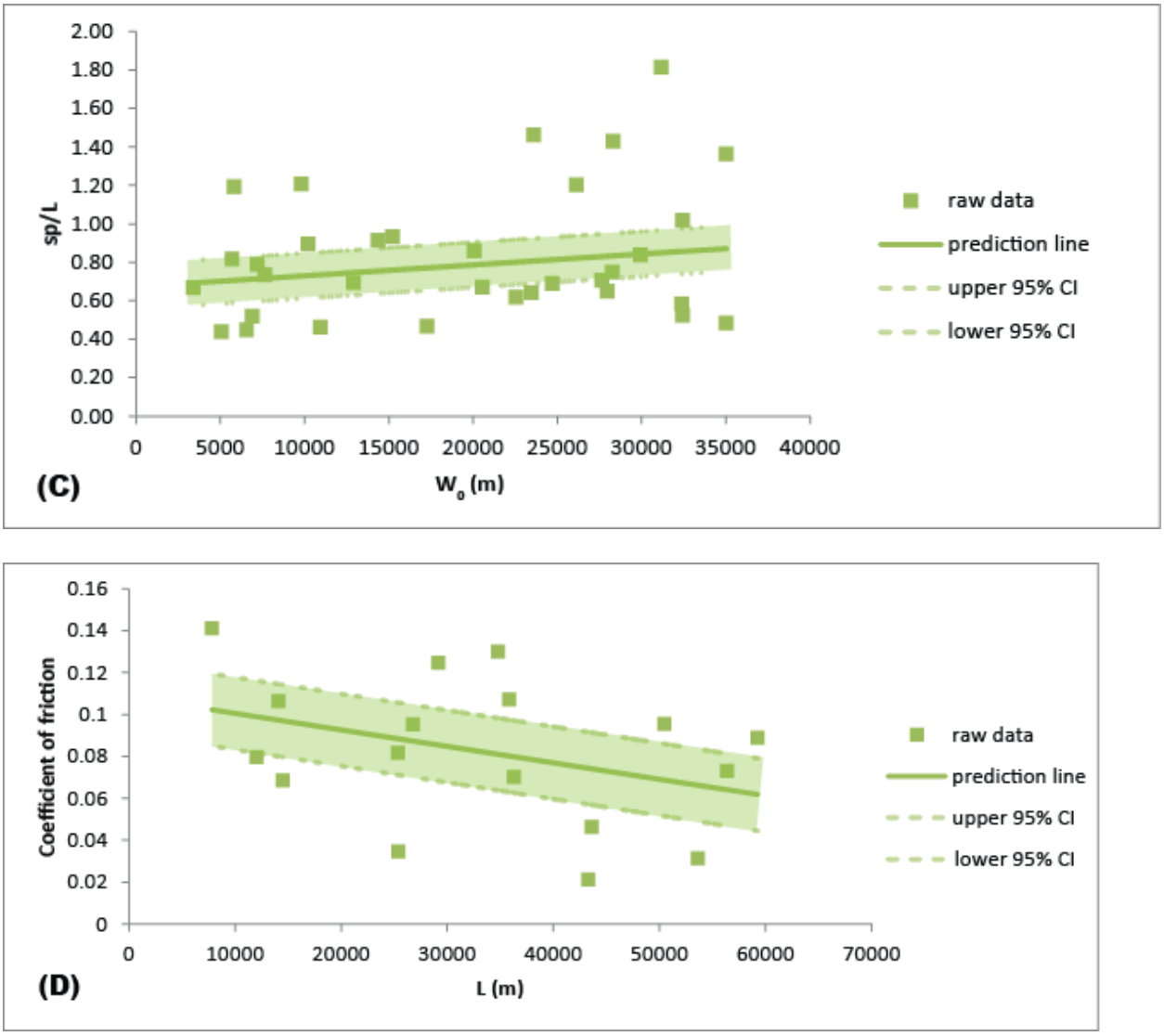

Figure 3.8, cont. (C) Plot of spreading normalized with runout distance versus breakaway width. Dashed lines represent 95% confidence intervals for the linear regression. Note the increasing trend of $W_{0,}$ a proxy for initial volume of the landslide mass in the canyon, with aspect ratio, suggesting that landslide transport is broadly mass dependent. However, the high degree of scatter represented by the high number of landslides that plot outside of the 95% confidence intervals shows this mass dependence is significantly variable. (D) Plot of coefficient of friction, measured as a function of spreading angle, versus runout distance. Note the general trend of decreasing coefficient of friction with increasing runout, suggesting that mass-independent basal friction plays a role in VM long-runout landslide length. 95% confidence intervals for the linear regression (dashed lines) provide reasonable bounds for this trend.

aspect ratio increases with breakaway scarp width, suggesting that the degree of spreading is largely dependent on flux of original volume of landslide mass in the canyon wall (also see Lucas et al., 2011). This association is corroborated by the observed relative lack of lateral spreading of smaller volume debris flows. However, the trend is very gradual and substantial variability exists. In investigation of controls on this variance, coefficient of friction (as a function of measured spreading angle) decreases with increasing runout length (**Fig. 3.8D**). This trend suggests that mass-independent basal friction plays a role in outer zone runout. Landslide spreading normalized with breakaway width to remove mass dependency, as a function of runout, also normalized with breakaway width, lacks a significant correlation with age (**Fig. 3.8E**). Regional slope also does not prove to be a control on aspect ratio (all VM long-runout landslides occur along regional slopes of < 3°).

3.5.2 Results of compositional analysis

In the spectral and structural analysis of a well-exposed VM long-runout landslide in Chapter 2 of this dissertation (Watkins et al., 2015), no hydrated minerals were detected in the source trough-wall rocks and inner zone, and a high-albedo stratigraphic unit in the basal layer of its toe was found to contain hydrated minerals with absorption signatures consistent with the presence of hydrated silicates and Fe/Mg phyllosilicates. Structural relationships at the toe suggest that the basal layered units that contain the hydrated silicates experienced shared deformation during emplacement, and consequently comprise the sliding zone. This observation led to the hypothesis that hydrated silicates within the sliding zone lower the coefficient of friction and thereby enable long-runout landslide emplacement (Watkins et al., 2015).

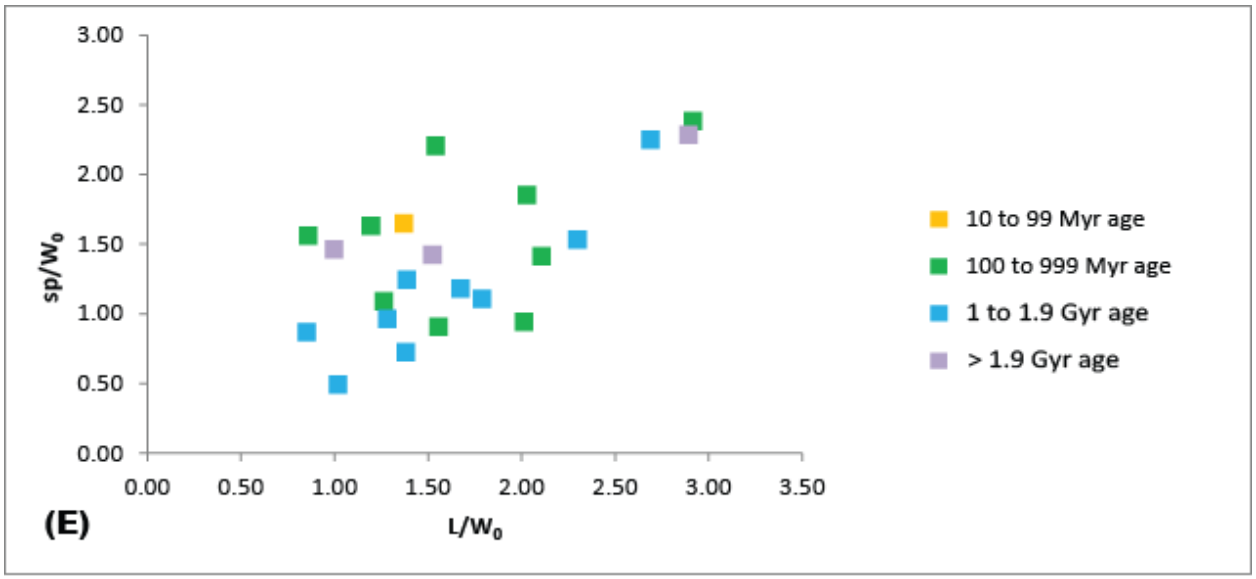

Figure 3.8, cont. (E) Plot of landslide spreading normalized with breakaway width versus runout also normalized with breakaway width, as a function of age (Quantin et al., 2004). Note the lack of significant correlation, excluding age as a contributing factor in landslide morphological variance.

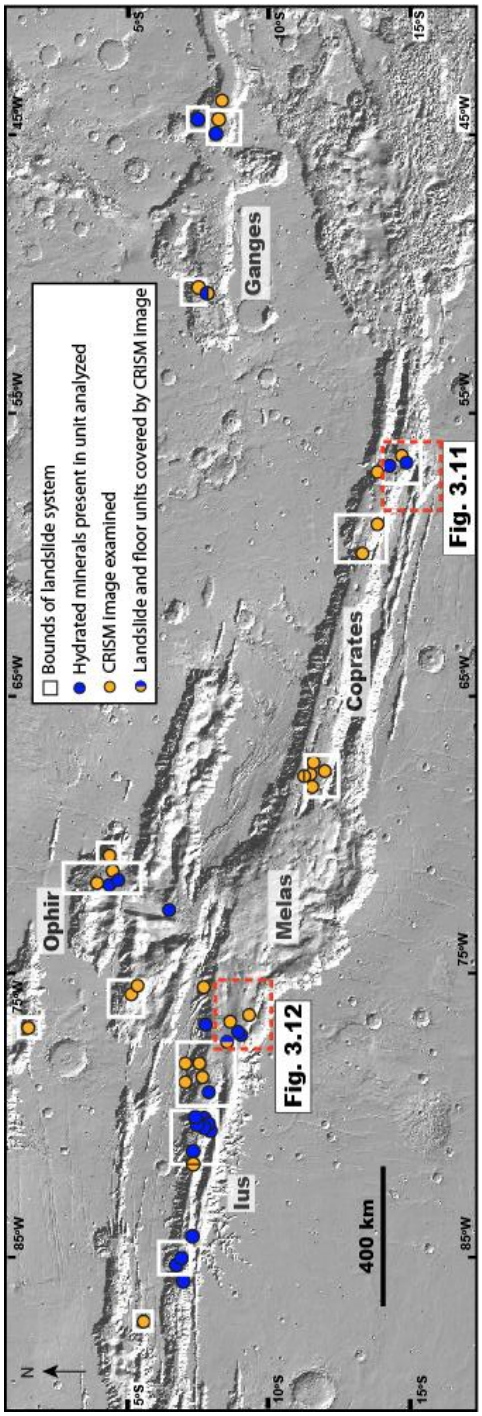

Figure 3.9. **Distribution of hydrated minerals associated with landslides in VM.** White boxes delineate individual landslide complexes. Blue circles within boxes indicate hydrated minerals present in outer zone; blue circles outside of boxes indicate hydrated minerals present on the trough floor in the immediate vicinity. Orange circles indicate landslide/trough floor materials in CRISM image examined. Images that cover both landslide deposit and trough floor materials are denoted with a split circle across the landslide complex boundary. Locations of Figs. 3.11 and 3.12 are also shown.

Of the analyzed 14 landslide systems with outer zone CRISM coverage, 8 landslides were found to exhibit the presence of hydrated silicate minerals in their long-runout sections (**Fig. 3.9**). Hydrated minerals are present in at least one example of each landslide classification. In western Ius Chasma, hydrated silicate and smectite were detected in the outer zone of a confined landslide (**Fig. 3.4**) in CRISM images 13EDE, 8FF0, and 88FC, consistent with the mapping of this unit as hydrated material by Roach et al. (2010). In central Ius Chasma, hydrated silicate and potential smectite, with a weak absorption at 2.3 μm, were detected in the outer zone of another confined landslide in CRISM images 1E247, 27E2, 905B, A396, C119, D740, and 18FD5. These observations of hydrated landslide material are also consistent with those of Roach et al. (2010). In eastern Ius Chasma, Watkins et al. (2015) found composite landslide Ius Labes (**Fig. 3.5**) to contain hydrated silicate and smectite. In eastern Coprates Chasma, kieserite, a monohydrated sulfate, was detected in the outer zone of an unconfined landslide in CRISM image 93E3. In western Ganges Chasma, likely smectite with persistent but weak 1.4 and 1.9 μm absorptions and a step at 2.3 μm was detected in the outer zone of a composite landslide in CRISM image B48A. In northeastern Ganges Chasma, likely smectite with a 1.9 μm absorption and a step at 2.3 μm that persists weakly with a non-neutral denominator was detected in the outer zone of a composite landslide in CRISM image 1693A. Hydrated minerals were also detected in the outer zones of a superposed landslide in southeastern Ganges Chasma (CRISM image 136CF; **Fig. 3.7**) and a composite landslide in Ophir Chasma (CRISM images A432 and 508A).

In order to determine whether composition affects the parameters examined in morphometric analyses, runout length normalized with spreading is plotted against breakaway width and categorized by the detection of clay minerals in landslide outer zones. Outer zones with hydrated minerals runout further at smaller initial volumes and spread laterally more at larger initial

volumes as compared to the consistent aspect ratio of those without hydrated mineral detections (**Fig. 3.10**).

In order to understand whether the hydrated minerals in the studied landslides source from the wall rock or the trough floor, each of which would have implications for the transport mechanism, the composition of the walls and floor in the immediate vicinity of the landslides was analyzed. CRISM data covers the trough floor surrounding 8 landslide outer zones. Upon compositional analysis of each of those trough floor regions, the presence of hydrated minerals was detected near 4 landslides (**Fig. 3.9**). While most pristine breakaway and inner zone material is obscured by talus and dust cover, hydrated silicate and Fe/Mg smectite (previously identified as Fe-rich allophane/opal and saponite in this location; Weitz et al., 2014) were detected in the upper layers of the inner zone of a superposed landslide in eastern Coprates Chasma, exposed along the intra-landslide boundary fault scarp and within a small channel (**Fig. 3.11**). This landslide also contains hydrated minerals in its outer zone.

Inherent in the hydrated mineral distribution is the irregular erosional exposure of outer zone basal layers, pristine trough floor deposits, and source wall rock at the surface for unobstructed detection by CRISM. As a result, the lack of detection of clay minerals in some locations may, in addition to absence, be explained by dust or talus cover, or burial of entrained materials by overriding units and incomplete CRISM coverage of landslide and trough floor surfaces, in combination with relatively low abundances of clay (e.g., Vaniman et al., 2014). Thinner landslide deposits with higher degrees of lateral spreading may permit exposure of an underlying basal clay layer; consistent morphology across outer zones with and without a hydrated signature suggests that all outer zones share a common emplacement mechanism.

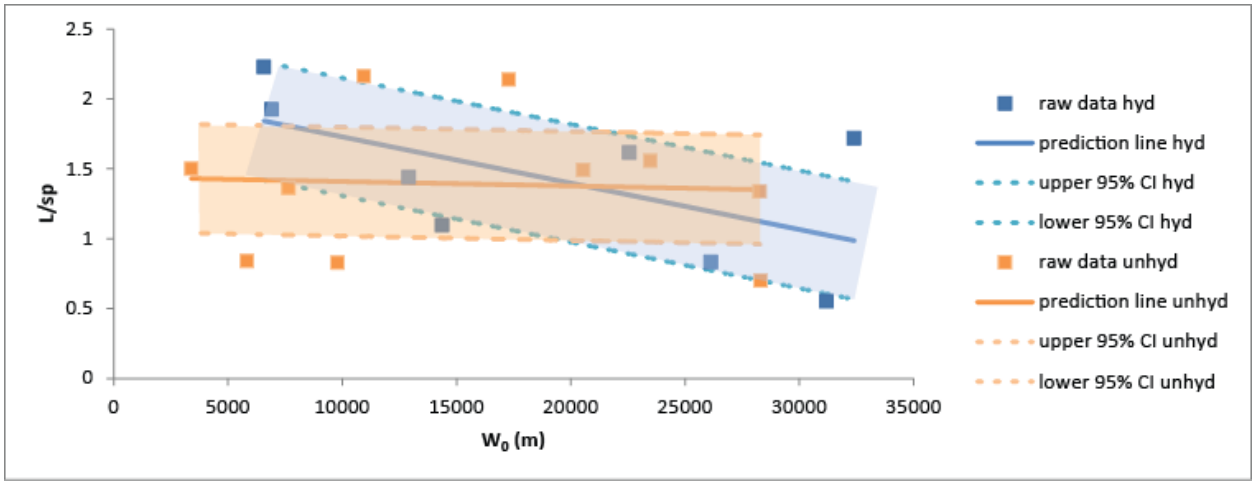

Figure 3.10. VM outer zone mobility by hydration. Plot of runout length normalized with spreading versus breakaway width categorized by the detection of clay minerals in landslide outer zones. The equation for the linear regression for unhydrated outer zones is $y = -3 * 10^{-6}x + 1.4411$, with an R^2 value of 0.0034. The equation for hydrated outer zones is $y = -3 * 10^{-5}x + 2.0603$, and $R^2 = 0.3675$. 95% confidence intervals for the linear regressions (dashed lines) provide reasonable bounds for these trends. Hydrated outer zones exhibit longer runout and increased lateral spreading as compared to unhydrated outer zones. In this way, composition may explain low friction, long runout, high spreading, and variance in mass dependence.

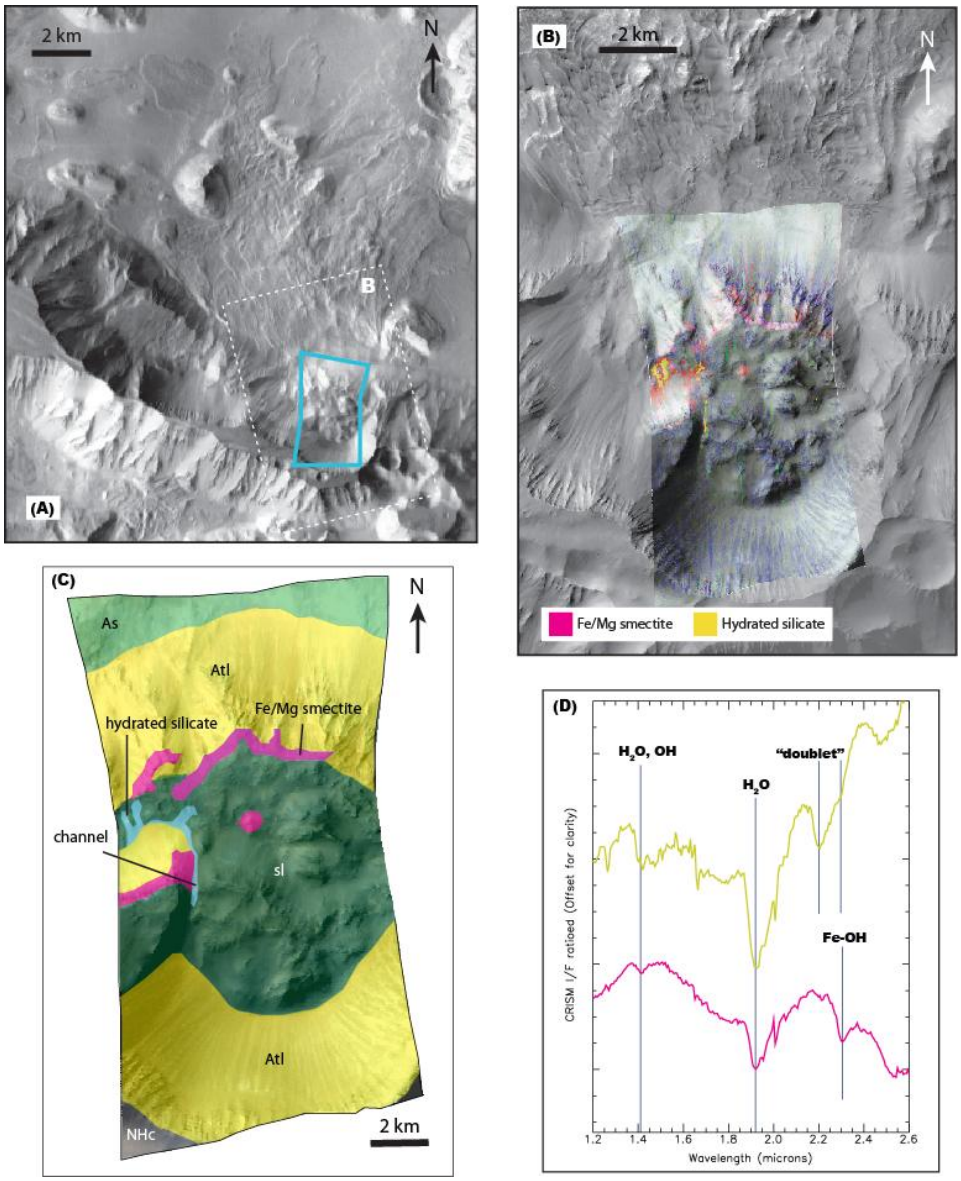

Figure 3.11. (A) THEMIS mosaic context map of landslide in Coprates Chasma (see Fig. 3.9 for location). Location of B is also shown; blue box outlines the location of CRISM image analyzed in B, C, and D. (B) Summary spectral parameters map of CRISM image HRL0000A8F6 highlighting the presence of hydrated minerals (R: BD1900R, G: Doub2200, B: D2300) overlain on CTX image P18_008141_1647_XN_15S056W. Fe/Mg smectites are magenta, hydrated silicate material is yellow-green, and anhydrous materials are dark blue. Most of the landslide inner zone (lower half of parameter map) is unhydrated, but hydrated units are exposed near and along the intra-landslide boundary fault scarp (upper half of parameter map; see C for unit mapping). (C) Geomorphological mapping of landslide units covered by CRISM image A8F6 based on photogeologic analysis of corresponding satellite images. (D) Ratioed CRISM spectra for image A8F6. The yellow spectra corresponds to the yellow-green, hydrated silicate units in the summary parameters maps; the magenta corresponds to the magenta, Fe-Mg phyllosilicate units. Note the absorption at 1.9 µm, indicative of the presence of hydrated minerals.

3.6 Discussion

The main morphological observations of this work include (1) the characteristic two-zone landslide morphology, which persists throughout VM despite variability in age, location, classification (i.e., kinematics), and height of initiation, (2) the lack of persuasive evidence for the presence of morphologies related to near-surface ice, and (3) that mass-independent basal friction decreases with increasing outer zone runout length. The main compositional observations made in this study include the presence of hydrated silicates in 8 out of 14 landslide outer zones and in 4 out of 8 trough-floor regions surrounding outer zones, the increase in runout and lateral spreading of outer zones with hydrated mineral detections compared to those without, and the detection of hydrated minerals in one landslide inner zone. Below we discuss two fundamental questions:

(1) whether prior localized alteration (e.g., Viviano-Beck and Murchie, 2014) has prepared VM fault-zone rocks for self-lubricating outer zone transport, and

(2) whether the trough floor contains prevalent clay minerals, providing a lubricant for overriding outer zones (Watkins et al., 2015).

3.6.1 Morphological implications

The lack of predicted morphological and structural observations precludes several previously proposed transport mechanism hypotheses. First, there is insufficient morphologic evidence related to the presence of postulated ice at or near the surface in VM to imply that ice or snow played a role in long-runout landslide emplacement (Shreve, 1966; Lucchitta, 1987; De Blasio, 2011). We also dismiss the possibility that VM landslides rode on top of a lacustrine bed, as the morphology characteristic of this type of lubrication mechanism as evidenced by terrestrial

examples is discordant with that of VM long-runout landslides. Though they are geometrically similar to VM landslides and often exhibit long runout distances, landslides falling on shallow coasts produce much more extensive deformation directly adjacent to their rims (Frey-Martinez et al., 2006), and do not exhibit longitudinal grooves (De Blasio, 2011). The persistent preservation of these grooves in VM long-runout landslides, especially on the surface of the underlying lobe of a superposed landslide system (e.g., **Fig. 3.3**), suggests that they experienced a lesser degree of reworking during emplacement than would be expected as a result of lubrication by a shallow water layer.

Regional morphometric analysis of landslide outer zones reveals that low mass-independent basal coefficient of friction is a control on mobility of the outer zones. In addition to the observed inversely proportional relationship between friction coefficient and runout, the observed transition from transport dominated by runout to transport dominated by lateral spreading in hydrated VM outer zones is likely indicative of gradual transition from the passive to the active stress state, causing expansion of the material (Hungr, 2008). Because $\mu << \phi$ is required in order for lateral normal stress to be exerted, this transition corroborates basal coefficient of friction as a control on outer zone mobility. This basal resistance force may also represent apparent viscosity of the fluidized basal layer, which exhibits control on the exceptional runout lengths and significant lateral spreading of the initial outer zone mass. In addition, morphometric relationships exclude both age and regional slope as contributing factors in outer zone morphological variance, though the low values observed for regional slope also indicate the flat environment generally required for lateral spreads. Moreover, since the total cross-sectional area of the outer zone debris apron (*LD*) is largely maintained, the decrease in area caused by pervasive extensional failure during transport must be compensated by a high

entrainment rate of weaker, lubricating materials along its runout path across the trough floor (Harrison and Grimm, 2003), which may contribute to reduction of the basal friction coefficient (e.g., Hungr and Evans, 2004; Iverson et al., 2011). All morphometric observations suggest time-independent basal lubrication was the cause of high spreading, extended runout, and variance in mass dependence of VM landslide outer zones.

This reduced basal friction may either be the result of lubrication by landslide material itself, as suggested by the self-lubrication model, or by material entrained at the base, as suggested by the clay-lubrication model. Based on breakaway zone morphology, it is clear that the development of the two-zone morphology in individual long-runout landslides is independent of the launch height in the trough walls, and thereby, the original composition of the landslide source materials in the wall rock. This inference is based on existing analysis of combined CRISM and morphological data, which indicates the presence of a consistent, vertically variable stratigraphy at comparable elevations within the trough walls of VM, whereby landslides launched from the upper section of the trough wall would have involved friable and eroded sand and clays, and landslides initiated from a whole section of the trough wall would have largely involved layered, resistant, pyroxene-rich material (Murchie et al., 2009; Ehlmann et al., 2011; Flahaut et al., 2012). This implies that outer zone emplacement by self-lubrication of altered fault-zone rock is unlikely. Moreover, the observed association in VM between dust-covered slope deposits at the base of trough walls and mass wasting suggests that the lack of slump blocks in landslide outer zones and their fine surface texture are the results of mobilized fine-grained surficial deposits rather than fragmented trough-wall bedrock as speculated earlier (Lucchitta, 1979; De Blasio, 2011).

3.6.2 Compositional implications

Synthesis of the local and surrounding regional geologic context of VM long-runout landslides suggests that hydrated outer zones are not anomalous within the canyon. Detection of hydrated minerals in over half of VM landslide outer zones implies a discernible correlation between debris apron mobility and the presence of clay minerals and other hydrated silicates, which suggests that the presence of hydrated minerals in basal sliding zones is a key control on mass-independent coefficient of friction and resultant outer zone mobility in unconfined landslides. Though compositional data covering the basal layer of every landslide is not available for examination, hydrated materials may be present below most of the landslides based on the strong correlation amongst those which are well-exposed, as well as projection of documented regional geology, which involves widespread hydrated silicates on the VM trough floor (Roach et al., 2010b; Weitz et al., 2015; Witbeck et al., 1991).

Given the correlation between clay mineral presence and mobility in outer zones, it is necessary to determine whether clay minerals originate from either (a) the landslide source material, as in a model that appeals to the participation of locally altered, exhumed fault-zone rock in self-lubricated landslide transport, or (b) the trough floor, as proposed by the clay lubrication model of Watkins et al. (2015). Regional correlation between wall rock and landslide outer zone composition, as required by the self-lubrication model, yields ambiguous results within the limitations of the available datasets. While hydrated minerals are detected in one landslide inner zone, this correlation is only observed at a single site in VM, and regional morphological inferences preclude such a correlation. In contrast, the detection of hydrated minerals in half of trough-floor materials in the immediate vicinity of long-runout landslides in VM favors the

interpretation that clay minerals present in patches on the trough floor prior to landslide occurrence played a key role in landslide emplacement.

The clay-bearing deposits pre-date emplacement of the landslides based on contextual relationships (Murchie et al., 2009; Roach et al., 2010b) and stratigraphic analysis where the outer zone basal sliding layer is uniquely exposed in Ius Chasma (Watkins et al., 2015). At Ius Labes (see **Fig. 3.5**), the toe of the example hydrated landslide outer zone is juxtaposed over the clay-bearing broken-bed unit (Abt) of trough-floor deposits (**Fig. 3.12**). Previous identification of nontronite in Melas Chasma trough floor units by Weitz et al. (2015) corroborates this detection. This further indicates both that deposition of hydrated minerals preceded landslide emplacement, and that these hydrated trough-floor materials may be incorporated into outer zones during transport. Within this framework, however, it is permissible that the clay can be recycled and subsequently re-deposited on top of the landslides, as is the case in southwestern Candor Chasma and common in VM (Okubo, 2010).

3.6.3 Role of hydrated silicates

A constraint on the role of hydrated silicates in the formation of long-runout landslide morphologies is whether clay could viably lubricate landslides to produce the long-distance transport observed in VM (see Chapter 2; Watkins et al., 2015; references therein). The hydrated silicates found beneath several long-runout landslides may have a mechanically significant component of smectite clay. Even at abundances as low as 10% smectite within a bulk composition, which is reasonable to assume detection to imply particularly given the exceptional dust cover in VM, the low frictional strength of smectite weakens the surface beneath the landslide mass (Collettini et al., 2009), facilitating slip of clay-rich materials (Shaller, 1991) and

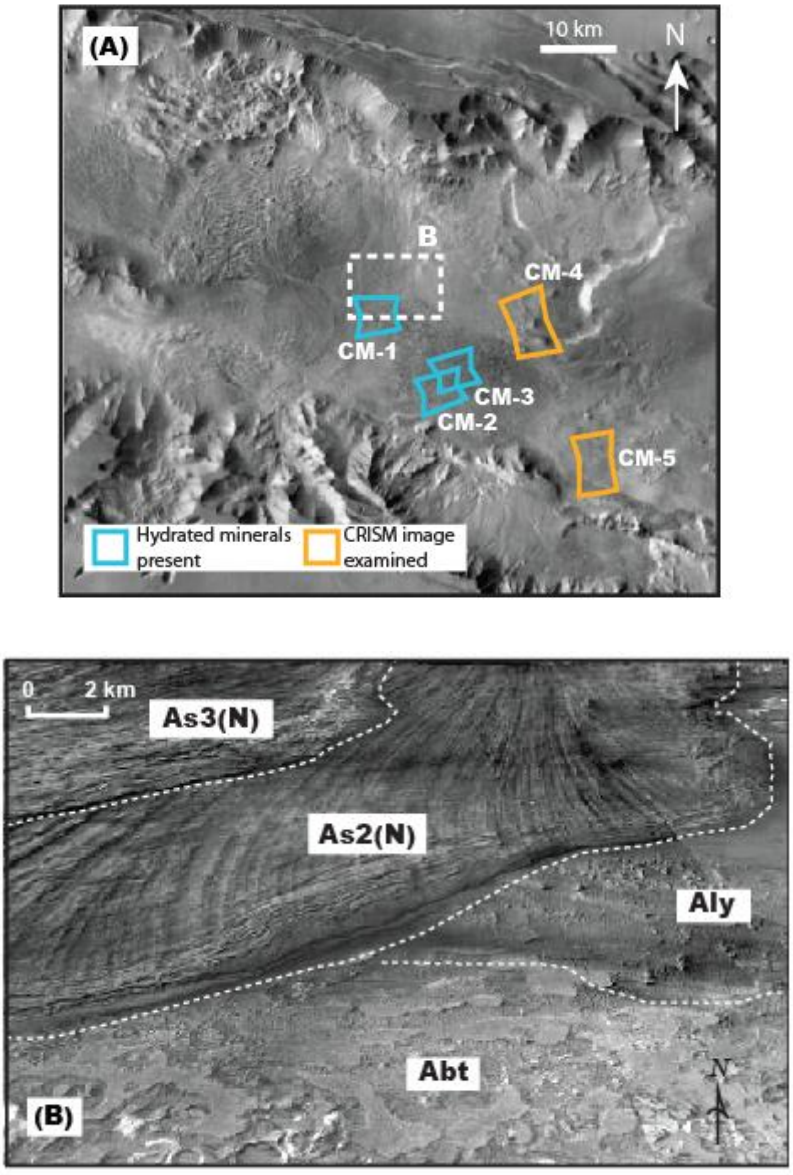

Figure 3.12. Field relationships on western Melas Chasma floor. (A) THEMIS mosaic context map of the western Melas Chasma trough floor in the immediate vicinity of the Ius Labes landslide (see Fig. 3.9 for location), with the locations of CRISM images analyzed, as well as B. CRISM image CM-1 is analyzed in C and D. Blue boxes indicate hydrated minerals present in trough floor materials; orange boxes indicate CRISM image examined. (B) Map of geologic field relationships from perspective view of CTX mosaic. The contact between the landslide outer zone toe and the trough floor is delineated.

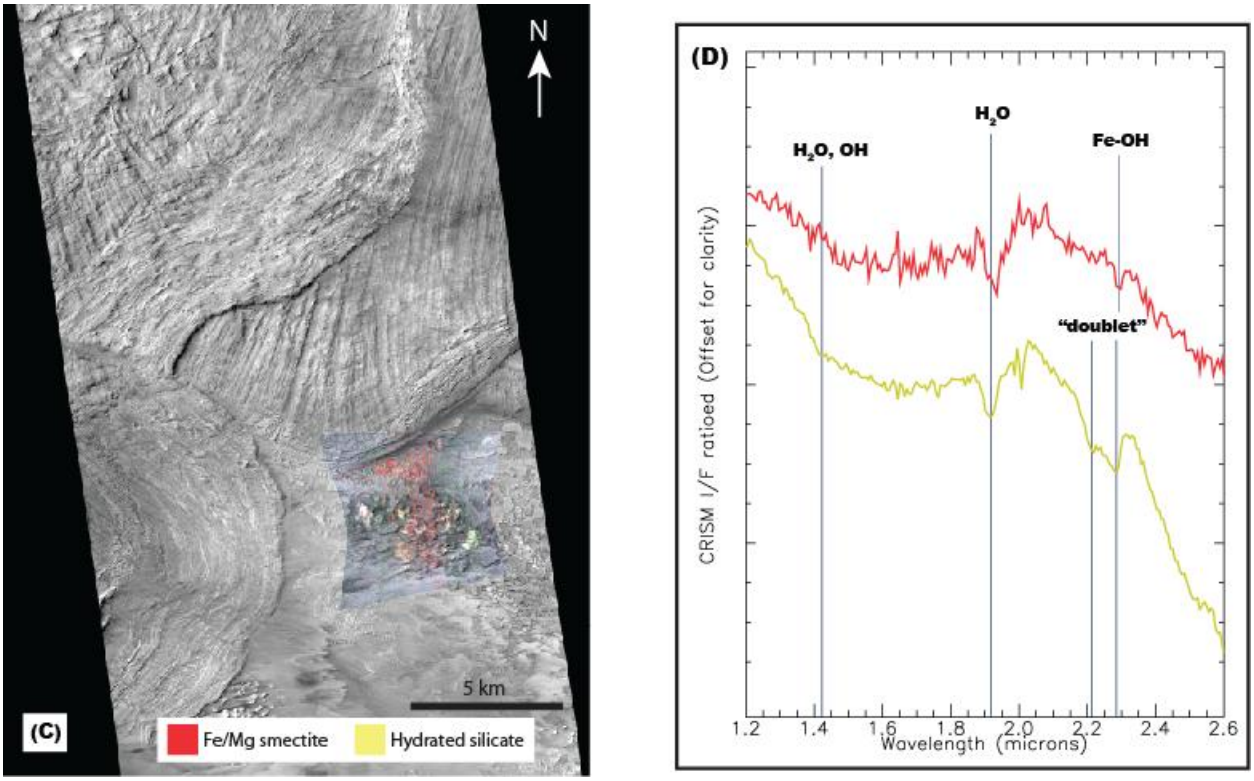

Figure 3.12, cont. (C) Summary spectral parameters map of CRISM image FRT00016B12 highlighting the presence of hydrated minerals (R: BD1900R, G: Doub2200, B: D2300) overlain on CTX image G03_019218_1728_XN_07S078W. Fe/Mg smectites are red, hydrated silicate material is yellow, and anhydrous materials are dark blue. The toe of the landslide is visible in the top left corner of the image, and is unhydrated. The proximity and superposition of the landslide deposit to these hydrated-silicate-bearing trough floor materials suggests clays played a key role in landslide emplacement. (D) Ratioed CRISM spectra for image FRT00016B12. The yellow spectrum corresponds to the yellow units in the summary parameters map; the red corresponds to the red units. Note the absorption at 1.9 µm, indicative of the presence of hydrated minerals.

making it an ideal lubricant. We would also expect apparent viscosity of the sliding surface to decrease with increased clay content (Harrison and Grimm, 2003) as well as increased sliding speed (Saffer and Marone, 2003). High basal shear stresses along a weak substrate (e.g., ice, snow, mud, soil), have also been observed to fluidize debris along the bases of notable long-runout landslides on Earth, including Blackhawk (Johnson, 1978; Shaller, 1991) and Sherman (De Blasio, 2011; Shaller, 1991) landslides.

One tenable mechanism of clay facilitation of VM long-runout landslide lubrication and transport may be the involvement of thixotropic clays. Thixotropic clays behave rigidly at low shear stresses, but when subjected to sufficiently high shear stresses, they liquefy upon loss of strength and flow with low viscosity. Failure of thixotropic clays characteristically occurs as a result of liquefaction, the process by which saturated, metastable, loosely packed, cohesionless sediments are transformed from a solid to a liquid state. On Earth, this process is often triggered by seismic shaking due to large earthquakes, causing deformation which initiates sediment strength loss and continues at an accelerating rate during failure (e.g., Lovie, 1975). During fluidization, the basal portions or whole bodies of landslides experience penetrative deformation and behave as laterally spreading granular flow materials consisting of highly broken and rotated rock fragments. Terrestrial thixotropic clays commonly form long-runout earthflows that involve saturated fine-grained slope material that liquefies and runs out downslope with substantial internal deformation (Baum et al., 2003).

3.6.4 Clay-lubrication model

Of the models proposed in this work for transport of landslide outer zones in VM, the data best fit basal lubrication through the entrainment of clay minerals in trough-floor materials. We

propose that during emplacement, the highly fractured landslides became moving critical Coulomb wedges downslope (Dahlen, 1990) and seismic shaking upon initiation reduced the strength of proximal thixotropic clays. The frontal wedges that form the inner zone overrode and entrained the liquefied, low-friction hydrated-silicate-bearing trough-floor sediments into the turbulent, fluidized mixture of fine grains in the basal layers, lubricating the sliding zones and propelling the liquefied debris forward. This may have led to drastic shallowing of the wedge-surface slope, which may have been accommodated by further loss of coherence due to continued fracturing and frictional sliding, permitting granular flow and lateral spreading of the sliding outer zone mass over the reduced-friction surface (Dahlen, 1990). As it became fluidized upon transport, landslide-induced heating likely further reduced the viscosity of the thin basal lubricating clay layer (De Blasio and Elverhoi, 2008), allowing it to behave as a viscous flow (Harrison and Grimm, 2003).

Within this model, the outer zones likely represent long-runout earthflows, producing the observed characteristic morphology including longitudinal grooves, transverse ridges, lateral spreading, and soft sediment deformation at the toe. In this way, the landslide morphology is controlled by its provenance and heterogeneities in rheology: inner zones originate from the downslope movement of wall rock, sourcing from alcoves that cut deep into the trough wall, reaching to the plateau margin, while outer zones are derived from mobilization of fine-grained trough-floor material containing clay minerals, sourcing from frontal floor deposits at the base of the trough walls.

The resemblance of VM long-runout landslide morphological features to those of lobate crater ejecta deposits on the plateau suggests that they share kinematic similarities and that comparison may provide insight into landslide evolution. These fluidized ejecta blankets exhibit

radial groove morphology in their distal portions similar to that of VM landslide outer zones (Weiss and Head, 2013), and terraced structure indicative of outward slumping of the rim region resembling the slump blocks and scarp-like features of VM landslide inner zones (Barnouin-Jha et al., 2005). Near-rim ejecta are typically emplaced with less velocity than distal ejecta (Barnouin-Jha et al., 2005), which have initial sliding velocities of up to ~70 m/s for a comparable volume of displaced material to VM long-runout landslides (Weiss and Head, 2014). Additionally, the persistence of linear, longitudinal grooves orthogonal to the direction of transport in the outer zone is indicative of rapid emplacement (Lucchitta, 1979; McEwen et al., 1989, Brunetti et al., 2014; De Blasio, 2011), and an emplacement speed within the range of those of large, catastrophic terrestrial landslides has been calculated for the VM long-runout landslide in Ganges Chasma shown in Fig. 3.7 (Lucchitta, 1978). This may indicate that VM long-runout landslide evolution includes slow emplacement of the inner zone following initiation, and subsequent rapid emplacement of the outer zone.

The Portuguese Bend landslide in Palos Verdes, CA may provide a terrestrial analogue for outer zone emplacement (**Fig. 3.13**). This earthflow was emplaced on bentonite-lubricated slip planes in which fine-grained debris and bentonite underwent plastic flow. This clay (altered tuff) is rich in Ca-montmorillonite of the smectite group, and is highly thixotropic, causing a dramatic reduction of shear strength and viscosity of the sheared clays (Kerr and Drew, 1967). The Portuguese Bend landslide and most other terrestrial clay-assisted landslides differ from VM long-runout landslides in a few ways: terrestrial examples were (1) initiated on a basal clay layer, (2) transported by fluidization of original landslide material itself upon saturation of clay, and (3) emplaced slowly rather than quickly. However, a similar mechanism can be applied to the rapid earthflows in VM, which entrain the facilitative clay, similar to the entrainment of ice and snow

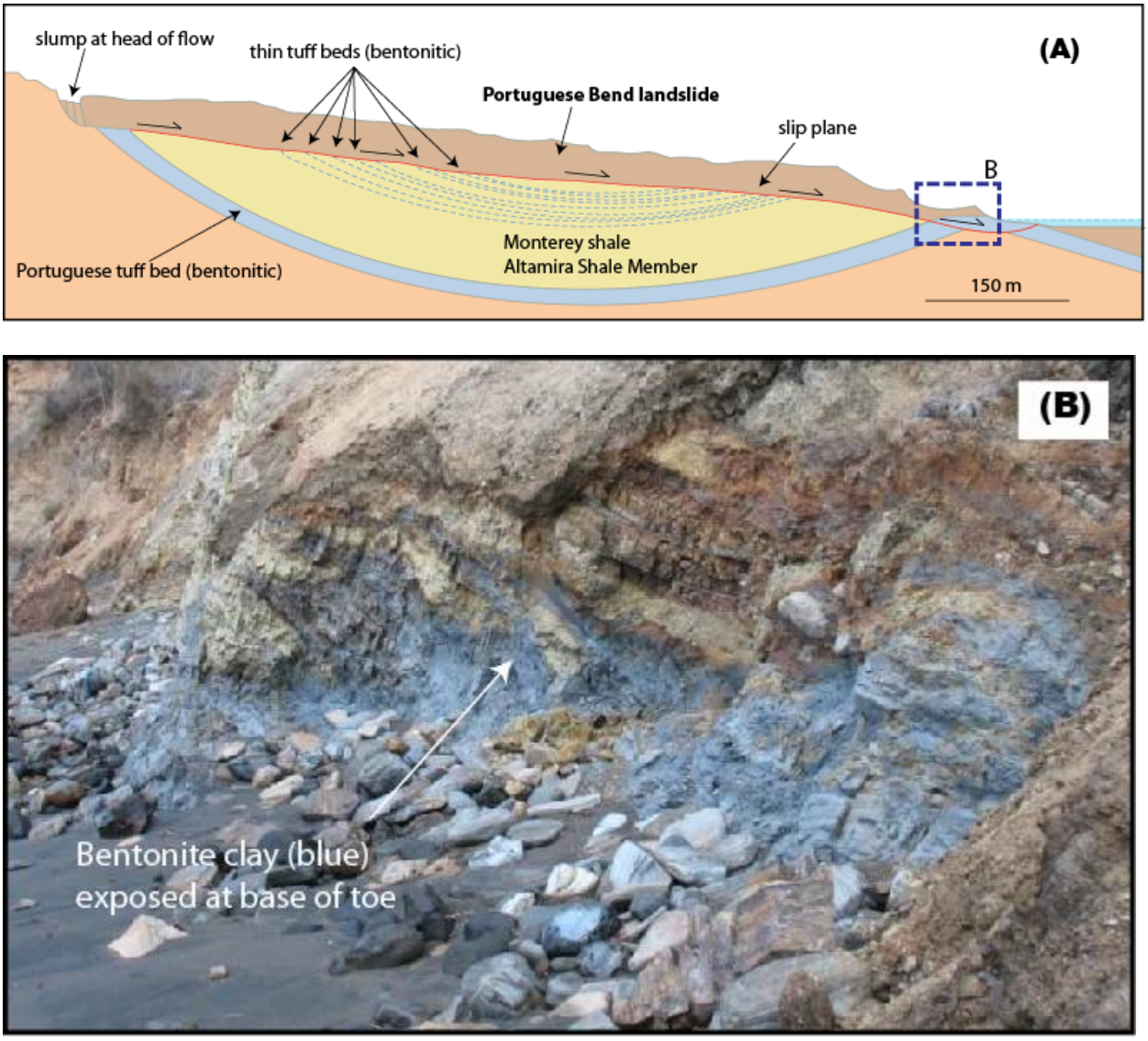

Figure 3.13. **Terrestrial analog: Portuguese Bend landslide.** (A) Schematic cross section of the Portuguese Bend landslide in Palos Verdes, CA, showing features of the slide (after Kerr and Drew, 1969). Note the clay-rich (altered tuff) layers along the slip surface, which experienced a significant loss in shear strength upon absorption of water and lubricated the base of the earthflow during emplacement. This example provides a mechanistic analog for VM landslide outer zone emplacement, whereby seismic shaking induces thixotropic flow and basal lubrication by smectite clay to form earthflow long runout. (B) Bentonite clay (blue) exposed at the base of the Portuguese Bend landslide toe, revealing its contribution to lubricated basal slip (after Douglas, 2011).

in the Mount La Perouse rock avalanche (**Fig. 3.6B**). Also, the slope instabilities required for liquefaction can be obtained even in the absence of pore water through accommodation of the pore pressure by grain-grain interactions (Kolymbas, 1988), though the nonessential contribution of pore fluid in addition to mechanisms of granular flow in VM cannot be excluded.

There are implications for this clay lubricating layer model that are associated with the geologic processes that may generate clay-bearing materials at the base of the trough walls. First, recurring landslide initiation requires a mechanism for constant regeneration of an unstable slope, given that an undisturbed landscape would re-equilibrate over the period of time represented by the range of VM long-runout landslide ages. Due to the observed spatial correlation between VM rotational landslide systems and trough-bounding faults, this is most likely produced by persistent fault activity along VM troughs since its formation. Second, the exact source of the sustained accumulation of clay minerals on the trough floor is uncertain, but processes that may concentrate them there include: (1) erosion of proximal wall rock facies, (2) deposition of sediment from the plateau, and (3) weathering and alteration of pristine grains.

If the first process is involved, within the current understanding of VM geologic history, the smectite in the landslide debris aprons likely originated from a layer in the wall rock. This smectite contributes to floor deposits throughout the canyon as a result of ongoing activity along trough-bounding faults associated with the extensional opening of the canyon.

If the second process plays a role, an implication for the regional environment would be prevalent mass wasting, deposition, and aeolian redistribution of clay-bearing materials. These materials may represent plateau phyllosilicates proposed to have formed by weathering of Noachian bedrock by percolation of meteoric water, with local contribution from fluvial activity and deuteric alteration (Le Deit et al., 2012).

If the third process is at work, there would be implications for Mars climate and surficial conditions. In this case, hydrated silicates would have formed by an aqueous process modifying trough floor material prior to landslide emplacement. This chemical alteration could thus indicate the punctuated participation of surface or near-surface groundwater, or some top-down weathering process (e.g., snow/precipitation, ice) in VM. Alternatively, given the mixture-like spectral signature of the doublet unit and that it has only been observed in floor deposits, the "doublet material" may be a result of the landsliding promoting the mixture of multiple compositional layers (Thollot et al., 2012).

3.7 Conclusions

Morphologic investigation of the underlying mechanisms of transport of landslides in VM, including measurement of the mass-independent basal coefficient of friction and regional slope, suggests basal lubrication is the cause of long runout and extensive lateral spreading. Detailed mapping does not support models involving ice/snow or water-layer lubrication, and our compositional survey indicates that hydrated basal sliding zones are not anomalous in VM. We examined two new models for landslide long-distance transport: self-lubrication of landslide material itself, as a result of exhumation of altered fault-zone rocks, and a lubricating clay layer. The integrated morphologic and spectral analysis of VM long-runout landslide geomorphologic, compositional, and morphometric properties is inconclusive in constraining the first mechanism, but supports the critical role of entrained and fluidized hydrated-silicate-bearing trough-floor deposits in assisting landslide transport by lubricating the basal sliding zone. This facilitates the extensive lateral spreading and long runout of landslide outer zones, as exemplified by emplacement of the Portuguese Bend landslide. The clay lubrication model implies ongoing

activity along VM trough-bounding faults since its opening, prevalent regional redistribution of clay-bearing materials, and potential punctuated participation of surface aqueous processes, in addition to the long-lasting impact of clay minerals on geomorphic processes on Mars into the recent past.

3.8 References

Adams et al. (2009), Salt tectonics and collapse of Hebes Chasma, Valles Marineris, Mars, *Geology*, *37*, 691-694.

Akers et al. (2012), What caused the landslides in Valles Marineris, Mars? (abs), *Lunar Planet. Sci. XLIII*, 1659.

Andrews-Hanna, J. C. (2012a), The formation of Valles Marineris: 1. Tectonic architecture and the relative roles of extension and subsidence, *J. Geophys. Res., 117*, E003953.

Andrews-Hanna, J. C. (2012b), The formation of Valles Marineris: 2. Stress focusing along the buried dichotomy boundary, *J. Geophys. Res., 117*, E003954.

Andrews-Hanna, J. C. (2012c), The formation of Valles Marineris: 3. Trough formation through super-isostasy, stress, sedimentation, and subsidence, *J. Geophys. Res., 117*, E004059.

Anguita et al. (2001), Tharsis dome, Mars: new evidence for Noachian–Hesperian thick-skin and Amazonian thin-skin tectonics, *J. Geophys. Res., 106*, 7577–7589.

Bagnold, R.A. (1956), The flow of cohesionless grains in fluids, *Philosophical Transactions of the Royal Society of London, Series A, Mathematical and Physical Sciences, 249*, 235-297.

Baum et al. (2003), Mechanics of earth flows, In Proceedings of the International Conference FLOWS, Sorrento, Italy.

Barnouin-Jha et al. (2005), Comparing landslides to fluidized crater ejecta on Mars, *J. Geophys. Res., 110,* E04010.

Bibring et al. (2006), Global Mineralogical and Aqueous Mars History Derived from OMEGA/Mars Express Data, *Science, 312,* 400-404.

Bigot-Cormier, F. and D.R. Montgomery (2007), Valles Marineris landslides: Evidence for a strength limit to Martian relief?, *Earth Planet. Sci. Lett., 260,* 179-186.

Blasius et al. (1977), Geology of Valles Marineris: First Analysis of Imaging from the Viking 1 Orbiter Primary Mission, *J. Geophys. Res., 82,* 4067-4091.

Brunetti et al. (2014), Analysis of a new geomorphological inventory of landslides in Valles Marineris, Mars, *Earth Planet. Sci. Lett., 405,* 156-168.

Bulmer, M.H. and B.A. Zimmerman (2005), Reassessing landslide deformation in Ganges Chasma, Mars, *Geophys. Res. Lett., 32,* L06201.

Burns, R.G. (1993), Rates and mechanisms of chemical weathering of ferromagnesian silicate minerals on Mars, *Geochimica et Cosmochimica Acta, 57,* 4555-4574.

Carr, M.H. (1973), Volcanism on Mars, *J. Geophys. Res.*, *78,* 4049-4062.

Christensen et al. (2003), Morphology and composition of the surface of Mars: Mars Odyssey THEMIS Results, *Science, 300,* 2056-2061.

Christensen et al. (2004), The Thermal Emission Imaging System (THEMIS) for the Mars 2001 Odyssey Mission, *Space Sci. Rev., 110,* 85-130.

Clark et al. (1990), Material absorption band depth mapping of imaging spectrometer data using a complete band shape least-squares fit with library reference spectra, In Proceedings of the Second Airborne Visible/Infrared Imaging Spectrometer (AVIRIS) Workshop, 2, 4-5.

Collins, G.S. and H.J. Melosh (2003), Acoustic fluidization and the extraordinary mobility of

sturzstroms, *J. Geophys. Res., 108*, 2473.

Cruden, D.M. and D.J. Varnes (1996), Landslide types and processes, In A.K. Turner and R.L. Schuster (eds.), Landslides: Investigation and Mitigation, pp. 26-75, Special Report 247, National Academy Press, Washington, D.C.

Dahlen, F.A. (1990), Critical taper model of fold-and-thrust belts and accretionary wedges, *Annual Reviews in Earth and Planetary Science, 18*, 55-99.

Davies, T.R. (1982), Spreading of rock avalanche debris by mechanical fluidization, *Rock Mechanics, 15*, 9-24.

Davies, T.R. and M.J. McSaveney (2009), The role of rock fragmentation in the motion of large landslides, *Engineering Geology, 109*, 67-79.

De Blasio, F.V. and A. Elverhøi (2008), A model for frictional melt production beneath large rock avalanches, *J. Geophys. Res., 113*, F02014.

De Blasio, F.V. (2011), Landslides in Valles Marineris (Mars): A possible role of basal lubrication by sub-surface ice, *Planet. Space Sci., 59*, 1384-1392.

Di Toro et al. (2004), Friction falls towards zero in quartz rock as slip velocity approaches seismic rates, *Nature, 427*, 436-439.

Dohm et al. (2001), Ancient drainage basin of the Tharsis region, Mars: Potential source for outflow channel systems and putative oceans or paleolakes, *J. Geophys. Res., 106*, 32943-32958.

Dohm et al. (2009), New evidence for a magmatic influence on the origin of Valles Marineris, Mars, *J. Volcanol. Geotherm. Res., 185*, 12-27.

Douglas, R. (2011), Notes on the Portuguese Bend Landslide, Abalone Cove Landslide Abatement District Misc. Report, City of Rancho Palos Verdes.

Ehlmann et al. (2011), Subsurface water and clay mineral formation on early Mars, *Nature, 479*, 53-60.

Ehlmann et al. (2013), Geochemical consequences of widespread clay mineral formation in Mars' ancient crust, *Space Science Reviews, 174*, 329-364.

Erismann, T.H. (1979), Mechanisms of large landslides, *Rock Mechanics, 12*, 15-46.

Flahaut et al. (2012), Pristine Noachian crust and key geologic transitions in the lower walls of Valles Marineris: Insights into early igneous processes on Mars, *Icarus, 221*, 420-435.

Frey-Martínez et al. (2006), Frontally confined versus frontally emergent submarine landslides: A 3D seismic characterization, *Marine and Petroleum Geology, 23*, 585–604.

Fueten et al. (2005), Structural attitudes of large scale layering in Valles Marineris, Mars, calculated from Mars Orbiter Laser Altimeter data and Mars Orbiter Camera imagery, *Icarus, 175*, 68-77.

Fueten et al. (2008), Stratigraphy and structure of interior layered deposits in west Candor Chasma, Mars, from High Resolution Stereo Camera (HRSC) stereo imagery and derived elevations, *J. Geophys. Res., 113*, E10008.

Golombek, M.P. and R.J. Phillips (2010), Mars tectonics, In T.R. Watters and R.A. Schultz (eds.), Planetary Tectonics, pp. 183-232, Cambridge University Press, New York.

Grindrod, P.M. and N.H. Warner (2014), Erosion rate and previous extent of interior layered deposits on Mars revealed by obstructed landslides, *Geology, 42*, 795–798.

Harrison, K.P. and M.G. Chapman (2008), Evidence for ponding and catastrophic floods in central Valles Marineris, Mars, *Icarus, 198*, 351-364.

Harrison, K.P. and R.E. Grimm (2003), Rheological constraints on Martian landslides, *Icarus, 163*, 347-362.

Highland, L.M., and P. Bobrowsky (2008), The landslide handbook—A guide to understanding landslides, U.S. Geological Survey Circular 1325, Reston, Virginia, 129 p.

Hungr, O. (1995), A model for the runout analysis of rapid flow slides, debris flows, and avalanches, *Can. Geotech. J., 32*, 610-623.

Hungr, O. (2008), Simplified models of spreading flow of dry granular material, *Can. Geotech. J., 45*, 1156-1168.

Hungr, O. and S.G. Evans (2004), Entrainment of debris in rock avalanches: An analysis of a long run-out mechanism, *Geol. Soc. Am. Bull., 116*, 1240–1252.

Hsu, K.J. (1975), Catastrophic debris streams (strurzstroms) generated by rockfalls, *Geol. Soc. Am. Bull., 86*, 129-140.

IAEG (1990), IAEG Commission on landslides, suggested nomenclature for landslides, *Bulletin of the International Association of Engineering Geology, 41,* 13-16.

Iverson, R.M. (1997), The physics of debris flows, *Reviews of geophysics, 35*, 245-296.

Iverson et al. (2011), Positive feedback and momentum growth during debris flow entrainment of wet bed sediment, *Nature Geoscience, 4*, 116-121.

Johnson, B. (1978), Blackhawk landslide, California, USA, *Rockslides and avalanches, 1,* 481-504.

Kerr, P.F. and I.M. Drew (1967), Clay mobility, Portuguese Bend, California, *Short Contributions to California Geology*, Special Report 100, 3-16.

Khaldoun et al. (2009), Quick clay and landslides of clayey soils, *Phys. Rev. Lett., 103*, 188301.

Kolymbas, D. (1988), Behaviour of liquefied sand, *Philosophical Transactions of the Royal Society of London, Series A, Mathematical and Physical Sciences,* 2609-2622.

Le Deit et al. (2012), Extensive surface pedogenic alteration of the Martian Noachian crust

suggested by plateau phyllosilicates around Valles Marineris, *J. Geophys. Res., 117*, E00J05.

Legros, F. (2002), The mobility of long-runout landslides, *Engineering Geology, 63*, 301-331.

Leverington, D.W. (2004), Volcanic rilles, streamlined islands, and the origin of outflow channels on Mars, *J. Geophys. Res., 109*, E10011.

Leverington, D.W. (2009), Reconciling channel formation processes with the nature of elevated outflow systems at Ophir and Aurorae Plana, Mars, *J. Geophys. Res., 114*, E10005.

Lucas, A. and A. Mangeney (2007), Mobility and topographic effects for large Valles Marineris landslides on Mars, *Geophys. Res. Lett., 34*, L10201.

Lucas et al. (2011), Influence of the scar geometry on landslide dynamics and deposits: Application to Martian landslides, *J. Geophys. Res., 116*, E10001.

Lucchitta, B.K. (1978), A Large Landslide on Mars, *Geol. Soc. Am. Bull., 89*, 1601-1609.

Lucchitta, B.K. (1979), Landslides in Valles Marineris, Mars, *J. Geophys. Res., 84*, 8097-8113.

Lucchitta, B.K. (1987), Valles Marineris, Mars: Wet Debris Flows and Ground Ice, *Icarus, 72*, 411-429.

Lucchitta et al. (1994), Topography of Valles Marineris: implications for erosional and structural history, *J. Geophys. Res., 99*, 3783–3798.

MacKay, J.R. (1973), The growth of pingos, western Arctic coast, Canada, *Canadian Journal of Earth Sciences, 10*, 979-1004.

Malin et al. (2007), Context Camera Investigation on board the Mars Reconnaissance Orbiter, *J. Geophys. Res., 112*, E05S04.

Masson, P. (1985), Origin and evolution of Valles Marineris region of Mars, *Adv. Space Res., 5*, 83-92.

McEwen, A.S. (1989), Mobility of large rock avalanches: Evidence from Valles Marineris, Mars, *Geology, 17*, 1111-1114.

McEwen et al. (1999), Voluminous volcanism on early Mars revealed in Valles Marineris, *Nature, 397*, 584-586.

McEwen et al. (2007), Mars Reconnaissance Orbiter's High Resolution Imaging Science Experiment (HiRISE), *J. Geophys. Res., 112*, E05S02.

McKenzie, D., and F. Nimmo (1999), The generation of Martian floods by the melting of ground ice above dykes, *Nature, 397*, 231–233.

McSaveney, M.J. (1978), Sherman Glacier rock avalanche, Alaska, USA, In: Voight, B. (ed.), Rockslides and Avalanches 1, Dev. Geotech. Eng., 14A, S. 197-258.

Mège et al. (2003), Volcanic rifting at Martian grabens, *J. Geophys. Res., 108*, 5044.

Mège, D. and O. Bourgeois (2010), Equatorial glaciations on Mars revealed by gravitational collapse of Valles Marineris wallslopes, *Earth Planet. Sci. Lett., 310*, 182-191.

Mège, D. and P. Masson (1996b), Amounts of crustal stretching in Valles Marineris, Mars, *Planet. Space Sci., 44*, 749-782.

Melosh, H.J. (1979), Acoustic fluidization- A new geologic process, *J. Geophys. Res., 84*, 7513-7520.

Melosh, H.J. (1987), The mechanics of large rock avalanches, *Reviews in Engineering Geology, 7*, 41-50.

Metz et al. (2010), Thin-skinned deformation of sedimentary rocks in Valles Marineris, Mars, *J. Geophys. Res., 115*, E11004.

Montgomery et al. (2009), Continental-scale salt tectonics on Mars and the origin of Valles Marineris and associated outflow channels, *Geol. Soc. Am. Bull., 121*, 117-133.

Murchie et al. (2007), Compact Reconnaissance Imaging Spectrometer for Mars (CRISM) on Mars Reconnaissance Orbiter (MRO), *J. Geophys. Res., 112*, E05S03.

Murchie et al. (2009), A synthesis of Martian aqueous mineralogy after 1 Mars year of observations from the Mars Reconnaissance Orbiter, *J. Geophys. Res., 114*, E2.

Nedell et al. (1987), Origin and evolution of the layered deposits in the Valles Marineris, Mars, *Icarus, 70*, 409-441.

Neuffer, D.P. and R.A. Schultz (2006), Mechanisms of slope failure in Valles Marineris, Mars, *Quarterly J. of Engineering Geology and Hydrogeology*, *39*, 227-240.

Neukum, G. and R. Jaumann (2004), The High Resolution Stereo Camera of Mars Express, In A. Wilson and A. Chicarro (eds.), Mars Express: The Scientific Payload, pp. 17-35, ESA SP-1240, Noordwijk, The Netherlands.

Okubo, C.H. (2010), Structural geology of Amazonian-aged layered sedimentary deposits in southwest Candor Chasma, Mars, *Icarus*, *207*, 210-225.

Paterson, W. S. B. (1994), The physics of glaciers, 480 pp.

Pelkey et al. (2007), CRISM multispectral summary products: Parameterizing mineral diversity on Mars from reflectance, *J. Geophys. Res., 112*, E08S14.

Peulvast et al. (2001), Morphology, evolution and tectonics of Valles Marineris wall slopes (Mars), *Geomorphology, 37*, 329-352.

Peulvast, J.P. and P.L. Masson (1993), Erosion and tectonics in central Valles Marineris (Mars): A new morpho-structural model, *Earth, Moon, and Planets, 61*, 191-217.

Purucker et al. (2000), An altitude-normalized magnetic map of Mars and its interpretation, *Geophys. Res. Lett., 27*, 2449-2452.

Quantin et al. (2004a), Morphology and geometry of Valles Marineris landslides, *Planet. Space*

Sci., 52 , 1011-1022.

Quantin et al. (2004b), Ages of Valles Marineris (Mars) landslides and implications for canyon history, *Icarus, 172*, 555-572.

Reese et al. (2004), Magmatic evolution of impact-induced Martian mantle plumes and the origin of Tharsis, *J. Geophys. Res., 109*, E08009.

Roach et al. (2010a), Diagenetic haematite and sulfate assemblages in Valles Marineris, *Icarus, 207*, 659-674.

Roach et al. (2010b), Hydrated mineral stratigraphy of Ius Chasma, Valles Marineris, *Icarus, 206*, 253-268.

Roche et al. (2011), On the run-out distance of geophysical gravitational flows: Insight from fluidized granular collapse experiments, *Earth Planet. Sci. Lett., 311*, 375-385.

Saffer, D.M. and C. Marone (2003), Comparison of smectite-and illite-rich gouge frictional properties: application to the updip limit of the seismogenic zone along subduction megathrusts, *Earth Planet. Sci. Lett., 215*, 219-235.

Schultz, R.A. (1998), Multiple-process origin of Valles Marineris basins and troughs, Mars, *Planet. Space Sci., 46*, 827-829.

Schultz, R.A. (2002), Stability of rock slopes in Valles Marineris, Mars, *Geophys. Res. Lett, 29*, 1932.

Schultz et al. (2010), Interpretation and analysis of planetary structures, *J. Structural Geol., 32*, 855-875.

Shaller, P.J. (1991), Analysis and implications of large Martian and terrestrial landslides, Ph.D. Thesis, pp.586, Calif. Inst. Tech., Pasadena, California.

Sharp, R.P. (1973), Mars: troughed terrain, *J. Geophys. Res.,78*, 4063-4072.

Shreve, R. L. (1959), Geology and mechanics of the Blackhawk landslide, Lucerne Valley, California, Ph.D. Thesis, Calif. Inst. Tech., Pasadena, California.

Shreve, R. L. (1966), Sherman landslide, Alaska, *Science, 154*, 1639-1643.

Shreve, R. L. (1968), The Blackhawk landslide, *Geol. Soc. Am. Special Papers, 108*, 1-48.

Shreve, R. L. (1968), Leakage and fluidization in air-layer lubricated avalanches, *Geol. Soc. Am. Bull.,* 79, 653-658.

Soare et al. (2005), Possible pingos and a periglacial landscape in northwest Utopia Planitia, *Icarus, 174*, 373-382.

Solomon, S.C. and J.W. Head (1982), Evolution of the Tharsis province of Mars: The importance of heterogeneous lithospheric thickness and volcanic construction, *J. Geophys. Res.,87*, 9755-9774.

Soukhovitskaya, V. and M. Manga (2006), Martian landslides in Valles Marineris: Wet or dry?, *Icarus, 180*, 348-352.

Spencer, J.R. and F.P. Fanale (1990), New models for the origin of Valles Marineris closed depressions, *J. Geophys. Res., 95*, 14301-14313.

Thollot et al. (2012), Most Mars minerals in a nutshell: Various alteration phases formed in a single environment in Noctis Labyrinthus, *J. Geophys. Res.,117*, E11.

Varnes, D.J. (1978), Slope movement types and processes, In R.L. Schuster and R.J. Krizek (eds), Landslides: Analysis and Control, Special Report, Transp. Res. Board, Nat. Acad. Sci. 176. National Academy of Sciences, Washington, DC, 11-33.

Vaniman et al. (2014), Mineralogy of a mudstone at Yellowknife Bay, Gale crater, Mars, *Science, 343*.

Viviano-Beck, C.E. and S.L. Murchie (2014), Hydrothermally altered stratigraphy in the walls of

Valles Marineris (abs), *Lunar Planet. Sci. XLV*, 1963.

Warner et al. (2013), Fill and spill of giant lakes in the eastern Valles Marineris region of Mars, *Geology, 41*, 675-678.

Watkins et al. (2015), Long-runout landslides and the long-lasting effects of early water activity on Mars, *Geology, 43*, 107-110.

Weidinger, J.T. and O. Korup (2009), Frictionite as evidence for a large Late Quaternary rockslide near Kanchenjunga, Sikkim Himalayas, India- Implications for extreme events in mountain relief destruction, *Geomorphology, 103*, 57-65.

Weiss, D.K. and J.W. Head (2013), Formation of double-layered ejecta craters on Mars: A glacial substrate model, *Geophys. Res. Lett., 40*, 3819-3824.

Weiss, D.K. and J.W. Head (2014) Ejecta mobility of layered ejecta craters on Mars: Assessing the influence of snow and ice deposits, *Icarus, 233*, 131-146.

Weitz et al. (2011), Diverse mineralogies in two troughs of Noctis Labyrinthus, Mars, *Geology, 39*, 899-902.

Weitz et al. (2014), Fresh exposures of hydrous Fe-bearing amorphous silicates on Mars, *Geophys. Res. Lett., 41*, 8744-8751.

Weitz et al. (2015), Mixtures of clays and sulfates within deposits in western Melas Chasma, Mars, *Icarus, 251*, 291-314.

Williams et al. (2003), Layering in the wall rock of Valles Marineris: intrusive and extrusive magmatism, *J. Geophys. Res., 30*, 1623.

Witbeck et al. (1991), Geologic map of the Valles Marineris region, Mars, scale 1:2000000, U.S. Geol. Survey Misc. Inv. Series Map I-2010.

Yin, A. (2012a), Structural analysis of the Valles Marineris fault zone: Possible evidence for

large-scale strike-slip faulting on Mars, *Lithosphere, 4*, 286-330.

Yin, A. (2012b), An episodic slab-rollback model for the origin of the Tharsis rise on Mars: Implications for initiation of local plate subduction and final unification of a kinematically linked global plate-tectonic network on Earth, *Lithosphere, 4*, 553-593.

Zhong, S. (2009), Migration of Tharsis volcanism on Mars caused by differential rotation of the lithosphere, *Nature Geoscience, 2*, 19-23.

Zuber et al. (1992), The Mars Observer Laser Altimeter Investigation, *J. Geophys. Res., 97*, 7781-7797.

CHAPTER 4

Emplacement mechanisms and spatiotemporal evolution of the long-runout Quaternary Eureka Valley landslide, Eastern California

4.1 Introduction

As described in Chapter 2, long-runout landslides are large landslides whose deposits are exceptional in that their extent is much larger can be explained by the initial height of their source area (e.g., Hsu, 1975). The extraordinarily long travel distance of long-runout landslide deposits suggests that their extent requires a special mechanism to explain their emplacement. Debate over characterization of this mechanism, specifically whether these landslides flow or slide and the role of water or fluids in their initiation and transport, has occurred over the past several decades (e.g., Hungr, 1995; Melosh, 1987; Shreve, 1968; Hsu, 1975; McSaveney, 1978).

Heim (1882) was the first to hypothesize on the mechanism for producing the low coefficient of friction exhibited by these slides, in its examination of the Elm landslide in Switzerland. Through analysis of first-hand accounts of the event, this study conjectured that the landslide entrained liquefied substrate (also see Hungr and Evans, 2004) and was characterized by internal deformation due to kinetic energy transfer by grain collision, which converted a more or less rectangular block into a sheet of debris that flowed, rather than slid, across the valley floor below.

Subsequent hypotheses focused on the source of interstitial surface or near-surface fluids or volatiles that may have permitted the slides to move as flows. Shreve (1959) invoked a new mechanism to explain the mobilization of the Blackhawk landslide in southern California (and later, the Sherman Glacier landslide in Alaska; Shreve, 1966): a lubricating layer of trapped and

compressed air at the base of the slide mass reduced the friction at the basal contact, facilitating long-distance sliding. Hsu (1975) further characterized Heim's grain-contact notion, in support of the turbulent flow of a dispersion of cohesionless grains in the presence of intergranular fluids. McSaveney (1978) appealed to mechanical fluidization combined with sliding on wet snow as friction-reducing mechanisms in the emplacement of the Sherman Glacier landslide. This investigation suggested that during the original rock fall, the thixotropic, or liquefiable upon stress, debris mass became fluidized and flowed across the glacier surface for several kilometers, melting the snow-covered glacier surface below.

In light of the identification of long-runout landslide deposits on Mars by Lucchitta (1978), which appealed to a basal lubricating layer for emplacement, dry mechanisms of reducing the normal stress between fragments and resulting coefficient of friction during transport were also proposed. Johnson (1978) speculated that Blackhawk landslide runout was facilitated by transport of the landslide mass over a thin layer of mobile, sandy mud. Melosh (1979) proposed acoustic fluidization of long-runout landslides, attributing momentary relief of the static overburden pressure within the rock mass to vibration associated with earthquakes, permitting sliding in the unloaded regions (also see Collins and Melosh, 2003). Erismann (1979) asserted that self-lubrication of large landslides was facilitated by melt generation at the base as a result of high energy concentration in the sliding zone. Davies (1982) also responded to the morphological similarity between terrestrial and extraterrestrial long-runout landslide deposits in its analysis of mechanical fluidization, noting that the mechanism is independent of variable atmospheric and gravitational conditions. More recently, dynamic rock fragmentation was proposed by Davies and McSaveney (2009), attributing the low frictional resistance of large landslides to dispersive pressures due to failure of individual grains.

A key component missing from this body of work is an in-depth geological analysis of a well-preserved and well-exposed long-runout landslide deposit. Detailed characterization of the geomorphology and structure of such a deposit would constrain the hypotheses for mechanisms of long-runout landslide emplacement. Furthermore, it would facilitate understanding of long-runout landslide dynamics on Earth, as well as other planetary surfaces such as the Moon, Mars (e.g., Watkins et al., 2015), and Saturn's moon Iapetus (Singer et al., 2012).

The Eureka Valley (EV) landslide in southeast Eureka Valley, CA presents a unique opportunity for this type of observation. It is positioned just northwest of Death Valley, west of the Last Chance Range, just west of the Eureka Valley Sand Dunes (**Fig. 4.1A**). The landslide deposit is an elongated, lobate sheet estimated to be originally ~1700 m long, ~400 m wide, and maximum ~15 m in height. It trends ~N60W, nearly orthogonal to the Last Chance Range front trend (**Figs. 4.1B and 4.1C**). The EV landslide has been mapped as a Quaternary landslide deposit by Wrucke and Corbett (1990), based on its relationship to alluvial fans in the southeast which imply that it was likely emplaced in the Quaternary (**Fig. 4.1C**). The travel distance of the original EV landslide volume is more extensive than is expected solely from the elevation drop upon slope failure. Thus, we classify the EV landslide as a long-runout landslide, adding to the short list of terrestrial long-runout landslide examples. The evolution of the landslide has not yet been studied in depth despite its scale, the high interest within its geologic setting, and that it provides an extremely well-preserved deposit for investigation of long-runout morphological detail. The aim of this work is to characterize the emplacement processes of the EV landslide through systematic field-based observation, high resolution satellite image and spectral data analysis, and luminescence age dating in order to constrain the contributing factors in long-runout landslide initiation and transport.

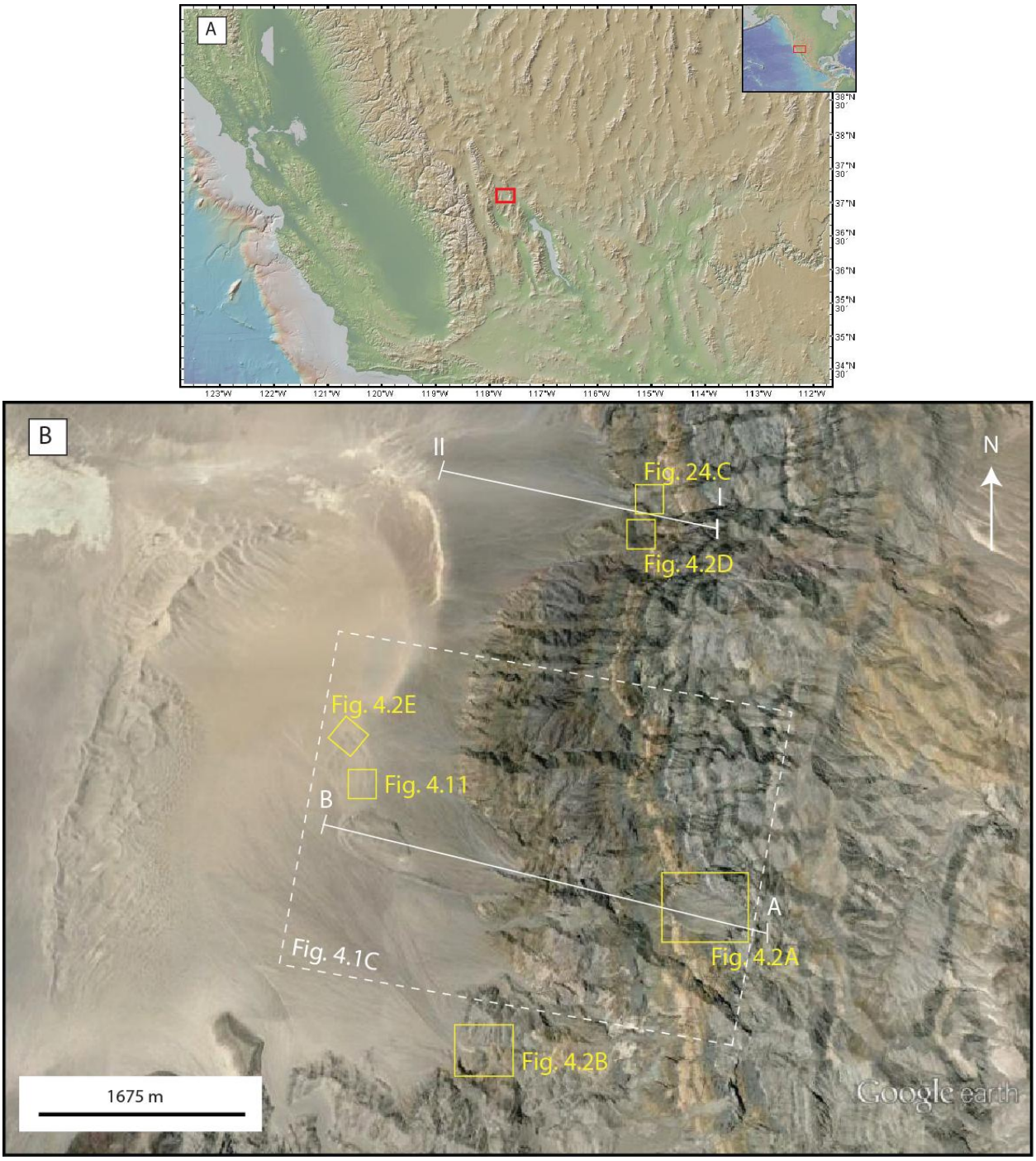

Figure 4.1. (A) Locational context of Eureka Valley in California. (B) Eureka Valley field area, showing the locations of field photographs of the source cliff and the range front (Fig. 4.2), as well as the locations of C, Fig. 4.11, and regional cross-sections (Fig. 4.12).

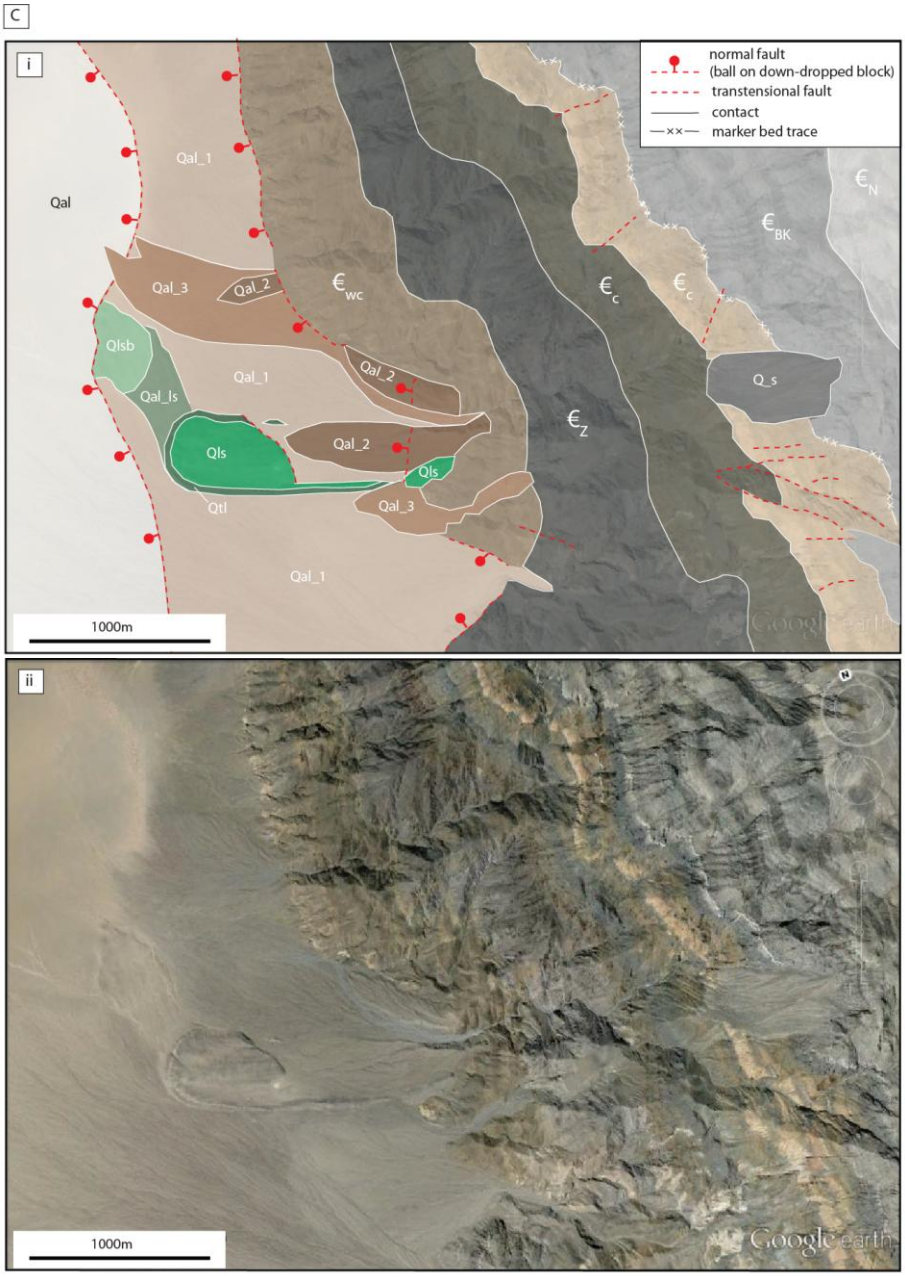

Figure 4.1, cont. (C) (i) Regional map and legend of Eureka Valley landslide and surrounding area. Qal = Quaternary alluvium; Qal_ls = Quaternary alluvium with basalt and limestone clasts; Qls = Quaternary landslide; Qlsb = Quaternary basalt clasts and landslide material; Qtl = Quaternary talus around the landslide rim, within which landslide units are exposed; Q_s = Quaternary source of landslide; Qal_1 = oldest Quaternary alluvium; Qal_2 = middle age Quaternary alluvium; Qal_3 = youngest Quaternary alluvium; $€_{WC}$ = Wood Canyon Formation (Early Cambrian); $€_Z$ = Zabriskie Quartzite (Middle and Early Cambrian); $€_C$ = Carrara Formation (Middle Cambrian); $€_{BK}$ = Bonanza King Formation (Late and Middle Cambrian). (ii) Base Landsat image from Google Earth.

4.1.1 Geologic setting

An understanding of the initial conditions within Eureka Valley is crucial to understanding the origin and emplacement mechanisms of the EV landslide. Eureka Valley itself is an entirely enclosed basin like Deep Springs Valley to the northwest and Death Valley to the southeast. The EV landslide source region (Q_s) is located at ~1800 m elevation at the top of the Last Chance Range western margin, to the east of the landslide, and is mapped as Quaternary talus material by Wrucke and Corbett (1990) (**Fig. 4.1C**). It is readily visible in the cliffside from the valley floor and is a large, gray, striated scarp, which is highly granular and overlies many rock strata (**Fig. 4.2A**). Corbett (1989) mapped the stratigraphy within the source area of the landslide as Upper Cambrian strata, which is classified as the Carrara, Bonanza King, and Nopah Formations. The upper member of the Carrara Formation is characterized by buff to light-orange weathering, and thin- to thick-bedded limestones. The upper contact is gradational with the overlying Bonanza King Formation. The Bonanza King Formation forms distinctively banded cliffs along the crest of the northern Last Chance Range, and is composed of buff or light- to dark-gray weathering, and medium- to thick-bedded dolomite. The contact with the overlying Dunderberg Shale Member of the Nopah Formation is sharp and conformable. This lower Nopah Formation member consists of siltstones, shales and marls. The thickness of the Dunderberg Shale is generally less than 50 m as a consequence of tectonic thinning (Corbett, 1989).

Landslide movement can be traced down the slope from the source region, where remnants of the slide were observed in the cliff, to a canyon southwest of the landslide, where a down-dropped block of Last Chance range-bounding normal faulting had been emplaced. Upon investigation of this down-dropped block, numerous examples of extensive normal faulting were

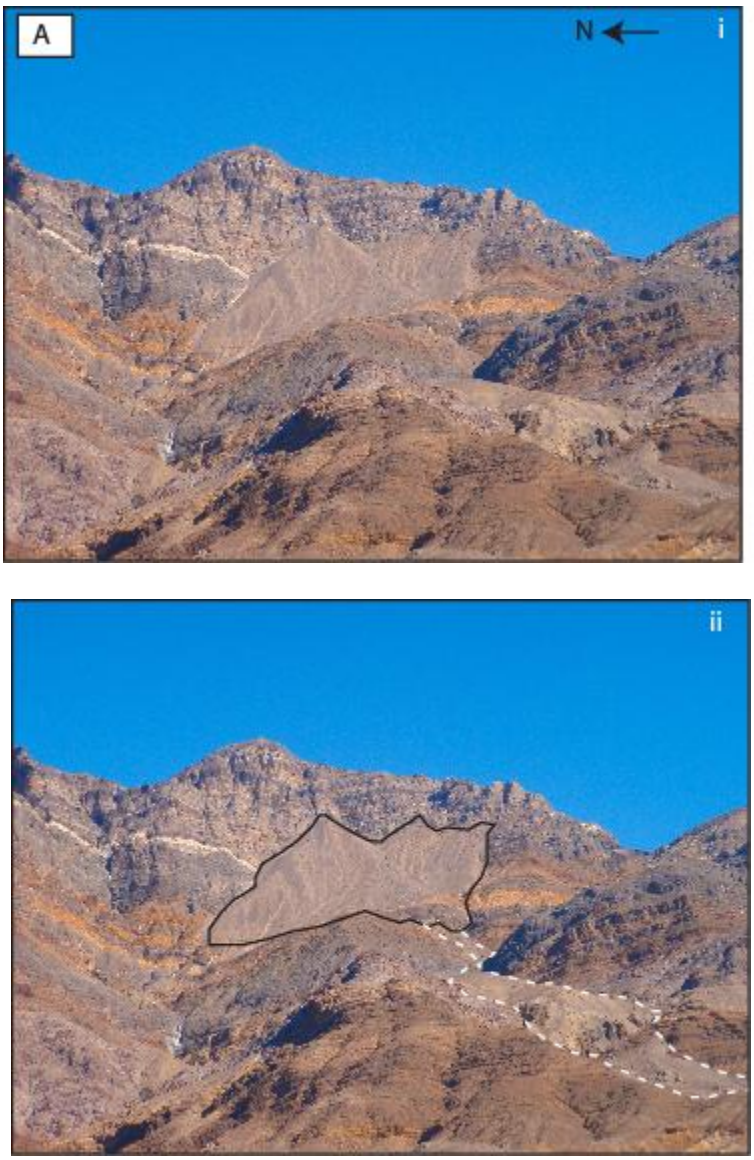

Figure 4.2. (A) Field photograph of interpreted landslide slip surface (solid line) and travel path in the source cliff (dashed line). See Fig. 4.1B for context.

observed (**Fig. 4.2B**). Prevalent range-bounding normal faulting was also observed in a canyon in the adjacent range front north of the landslide (**Figs. 4.2C and 4.2D**). Raised terraces formed as exhumed fans west of the toe of the landslide deposit (**Fig. 4.2E**) and prevalent normal faulting (oriented at ~004/44E, slipping to the west) observed in the range front proximal to the landslide (**Figs. 4.2C and 4.2D**) provide additional evidence of extensive regional range-bounding, range-parallel normal faulting in the vicinity.

Shoreline and mineralogical evidence imply that fluctuating lakes were prevalent in basins in the Death Valley region around the Pleistocene (**Fig. 4.3**; Stoffer, 2004; Blanc and Cleveland, 1961). Based on field data and physiographic relationships between the basins, it has been proposed that Eureka Valley was filled through spillover of the Pleistocene lake recorded in the adjacent Deep Springs Valley (Lustig, 1965; Miller, 1928), supported by mineralogical evidence of a Pliocene saline pluvial lake in Eureka Valley (Knott et al., 2014). In addition, ubiquitous limestone in the Last Chance Range, which bounds Eureka Valley, represents a lacustrine depositional environment in which calcium carbonate likely precipitated from shallow lake water. Also of note are the Eureka Dunes just to the west of the landslide deposit, which are among the tallest in North America and were likely formed by aeolian transport of sand exposed on the valley floor by the desiccation of a paleolake in the valley in the late Pleistocene, similar to that proposed for the nearby Kelso Dunes (e.g., Kocurek and Lancaster, 1999). A shallow lake may have again developed in the Holocene as a result of cooler and wetter conditions (Enzel et al., 1992). These observations indicate that the present-day Eureka Valley floor is the dry bed of a late Pleistocene lake, the remnants of which are found in the valley walls, the alluvial deposits that source from them, and on the floor itself.

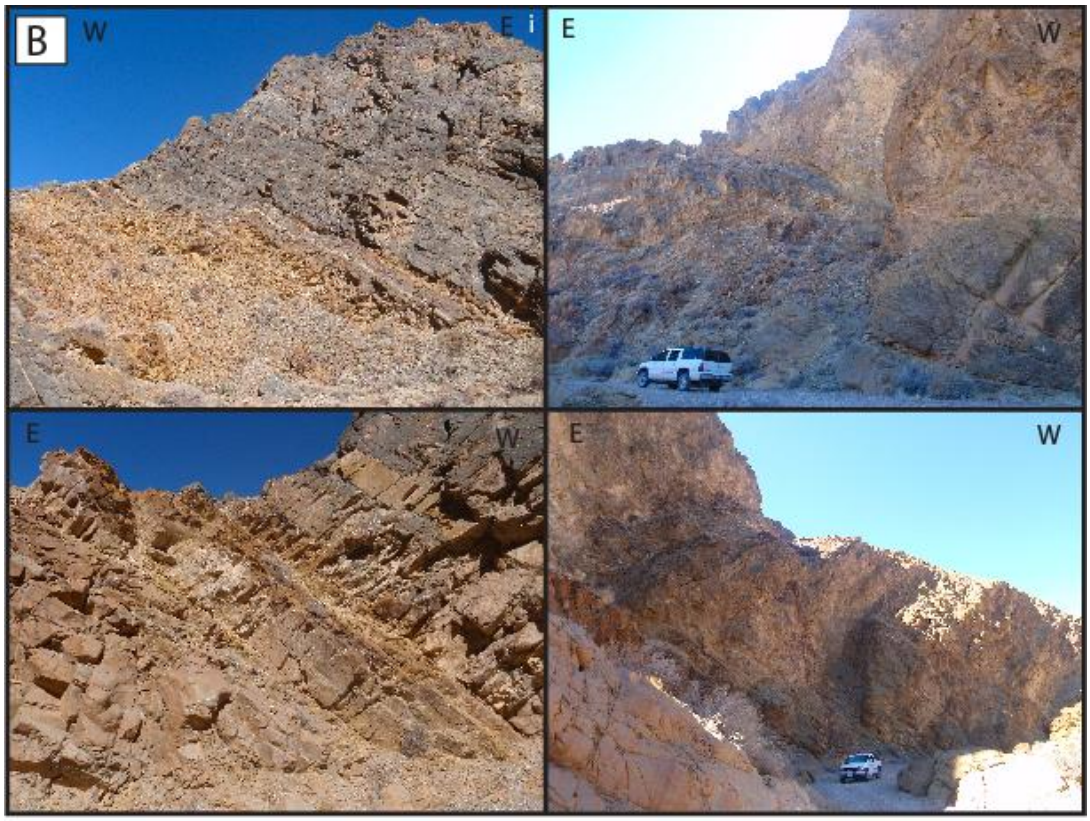
B
W
E
i
E
W
E
W
E
W

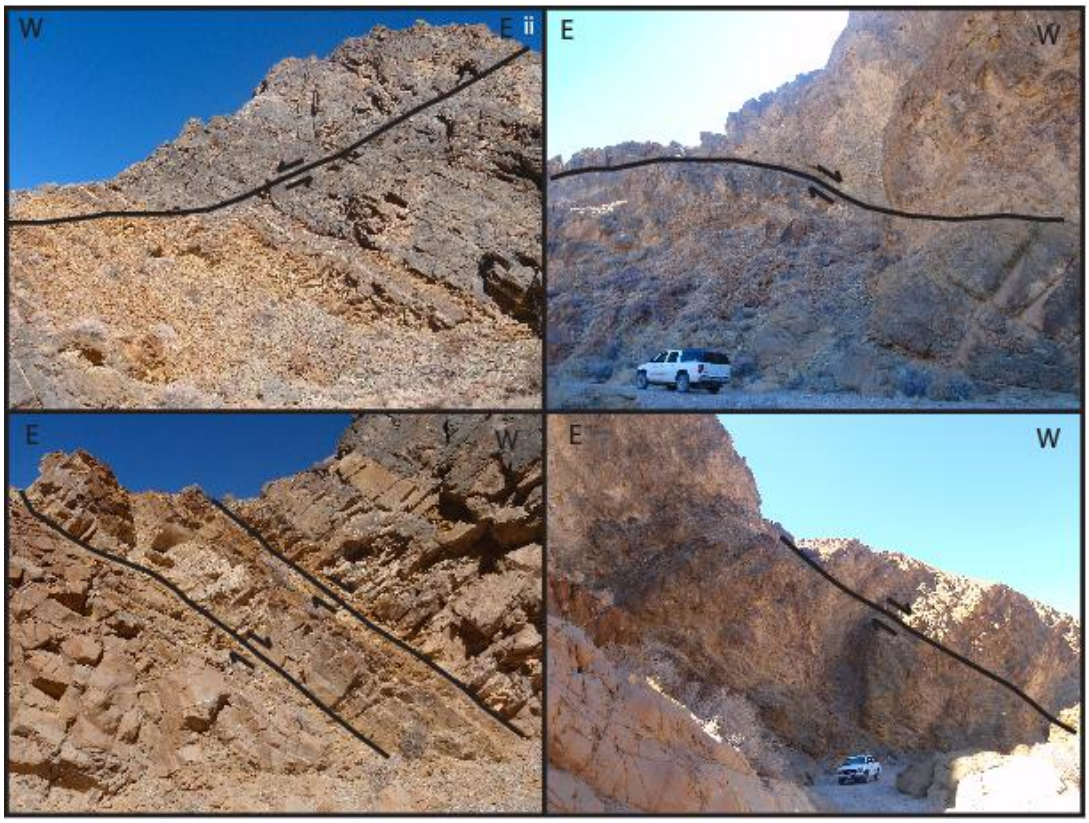
W
E
ii
E
W
E
W
E
W


C
N
S
i


N
S
ii


D
NE
SW
i


NE
SW
ii

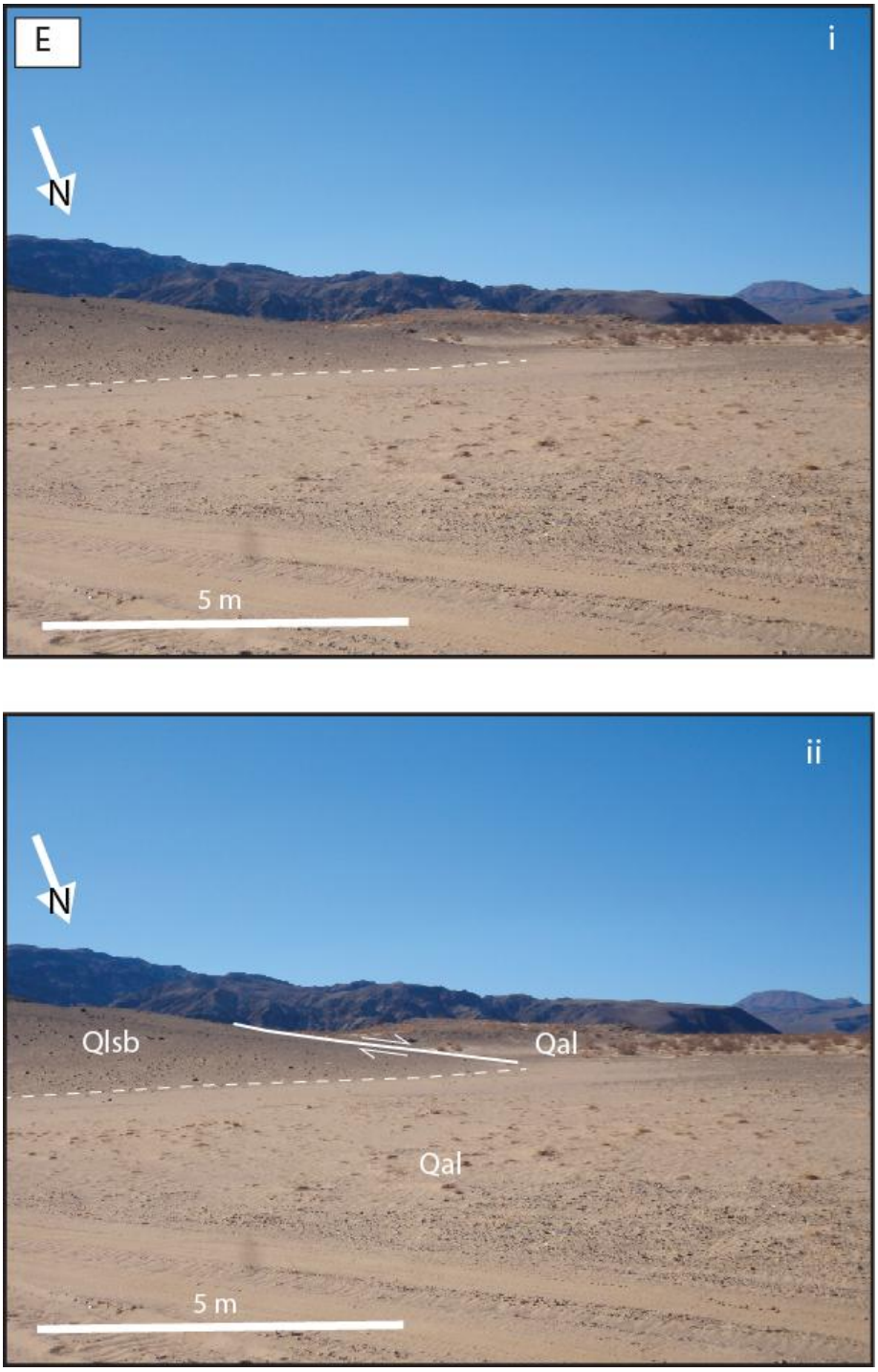

Figure 4.2, cont. (B-E) Field photographs of proximal Last Chance range front, displaying evidence for prevalent regional normal faulting. See Fig. 4.1B for locations.

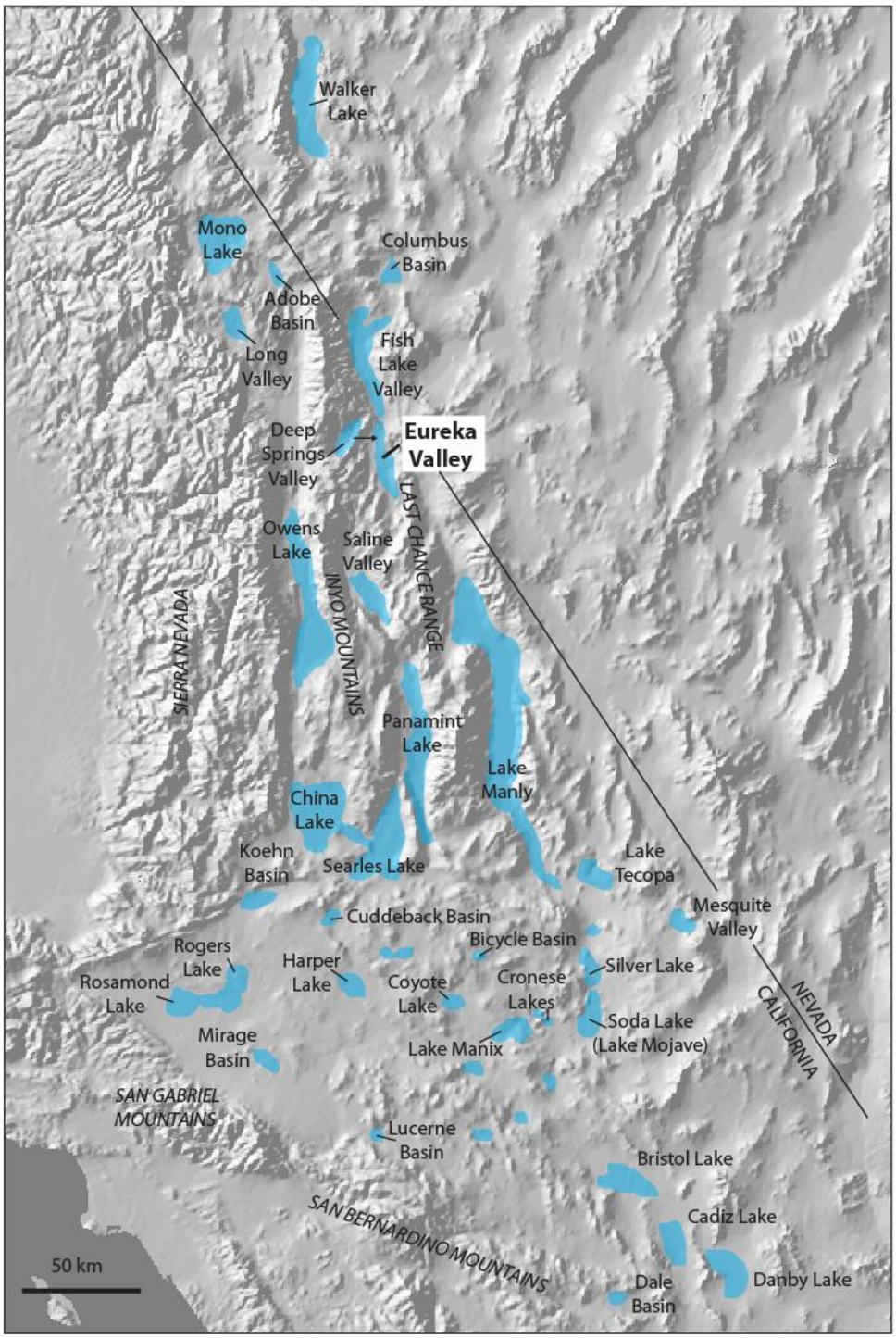

Figure 4.3 .Map of Death Valley region showing the locations and extents of proposed Pleistocene lakes in basins, proposed based on shoreline and mineralogical evidence (base image: USGS Shaded Relief map; after Stoffer, 2004 and Blanc and Cleveland, 1961). Note that one such lake is interpreted to have filled Eureka Valley.

4.2 Data and methods

Three lines of geologic research were pursued in this work in order to investigate EV landslide emplacement mechanisms: (1) systematic mapping of the landslide and surrounding region through a field-based approach, (2) photogeologic analysis of high resolution satellite imagery and spectral data, and (3) age determination of landslide-related units using optically stimulated luminescence (OSL) dating techniques. Geomorphologic features of the EV landslide were compared with those of other terrestrial long-runout examples to examine potential EV landslide emplacement mechanisms.

The first task included detailed study of a representative portion of the landslide's cross-section, as well as a kinematic GPS survey across the southern segment of the landslide, utilized to obtain horizontal and longitudinal profiles of the surface of the landslide deposit. The Trimble kinematic GPS survey system employed by this study consisted of two GPS units with a GPS receiver and a GPS interface/workstation. One unit functioned as the base station, set up at a reasonable distance from the field area and left in a single location. It continuously recorded its position just before, during, and just after the survey made by the roaming station. As part of a Digital Fieldbook Fast Static survey, the roaming station was moved to locations of interest across the landslide surface, where it recorded its precise GPS position for three minutes at each location. The mobility and efficiency of the roaming station results in a decrease in accuracy of location determination as compared to that of the base station, which remains stationary. Post-processing software used the high accuracy of the base station location to increase the accuracy of the roaming station location to less than 1 cm. During the survey taken across the landslide surface, 37 kinematic GPS points were recorded: 10 laterally across the easternmost side of the deposit, 9 laterally across the middle of the easternmost section of the deposit, 5 laterally across

the middle of the western section of the deposit, 7 laterally across the toe of the slide, and 5 longitudinally from the toe towards the head, to the site where erosion of the slide deposit begins. The latitude, longitude, and elevation accuracies of these points are within 1 cm. Lastly, the exposed volume, strike and dip orientation, and GPS location of 12 representative large boulders exposed on the surface of the landslide deposit were measured.

The second task was completed based on analysis of (1) Landsat coverage of the study area through the Google Earth platform, enabling preliminary observation and provisional identification and photogeologic mapping of morphological units and structural features, and (2) ASTER Level 1B (VIS-SWIR) data available from USGS EarthExplorer, from which band ratio images were calculated from diagnostic absorptions in order to illuminate spectral features in the images. Bands used in this study include Band 4 and Band 8, which are equivalent to Landsat bands 5 and 7. These bands cover 1.55-1.75μm and 1.08-2.35μm, respectively, and were selected to distinctively highlight OH vibrations in hydrated materials when ratioed.

The third task was performed through utilization of luminescence methods to reliably estimate the time since single grains of quartz were last exposed to daylight (Rhodes, 2011). A site clear of large, surficial basal clasts was selected for the pit both in order to avoid contribution from mass-wasted sediment not directly sourced from the EV landslide, as well as to facilitate efficacy of OSL dating. Two samples were collected using stainless steel tubes pushed into the vertical face exposed in a pit near the landslide toe. Dose rates were determined for each sample location based on in-situ gamma spectrometry. Standard laboratory sample treatment procedures outlined by Wintle (1997) were followed, including wet sieving, heavy liquid separation, hydrofluoric acid treatment, and mounting on aluminum discs for measurement on the Risø DA-15 automated reader equipped with a single grain laser attachment at the University of Sheffield.

4.3 Results

4.3.1 Surface morphology

Several geomorphologic observations were made in the plan view of the landslide field area in order to investigate the emplacement processes of the landslide. The landslide deposit itself (Qs) exhibits a striking displacement of the eastern half of the original deposit (**Fig. 4.1C**). A large drainage is evident through the alluvium that fills this eastern segment, and an increase in clast size is observed moving upstream in the main channel. A sandy deposit immediately northwest of the landslide (Qal_ls) contains material of predominantly limestone and basalt composition, similar to the landslide deposit and to older basaltic alluvial fan deposits ubiquitous throughout the valley floor. A raised sand bank is discernible within this unit (**Fig. 4.4**). A thicker sandy deposit containing weathered basalt boulders (Qlsb) is also present northwest of the landslide (**Fig. 4.4**).

Alluvial drainage channels on the top surface of the landslide follow normal faults which strike obliquely from the edges, forming a series of observable minor en echelon ridges, shallow troughs, and lineations oblique to the main lateral ridge (**Figs. 4.5A-C**). A braided stream pattern of mid-channel bars and paleochannels was observed along these surficial ridges, though there was no currently active fluvial system. Paleochannel morphologies were observed in the field and satellite imagery of the landslide, including pointed convergences, an increase in clast size on the elevated mid-channel bars as compared to the stream deposits, a high topographic knob at the center of the landslide deposit, and several playa deposits in the southern section, with lighter-colored mud and no discernible clasts. Furthermore, mid-channel bars are cut off diagonally across where the surface of the landslide deposit meets the erosional surface. Also, near the edge of the toe, areas where sections have finer-grained, younger fill than the

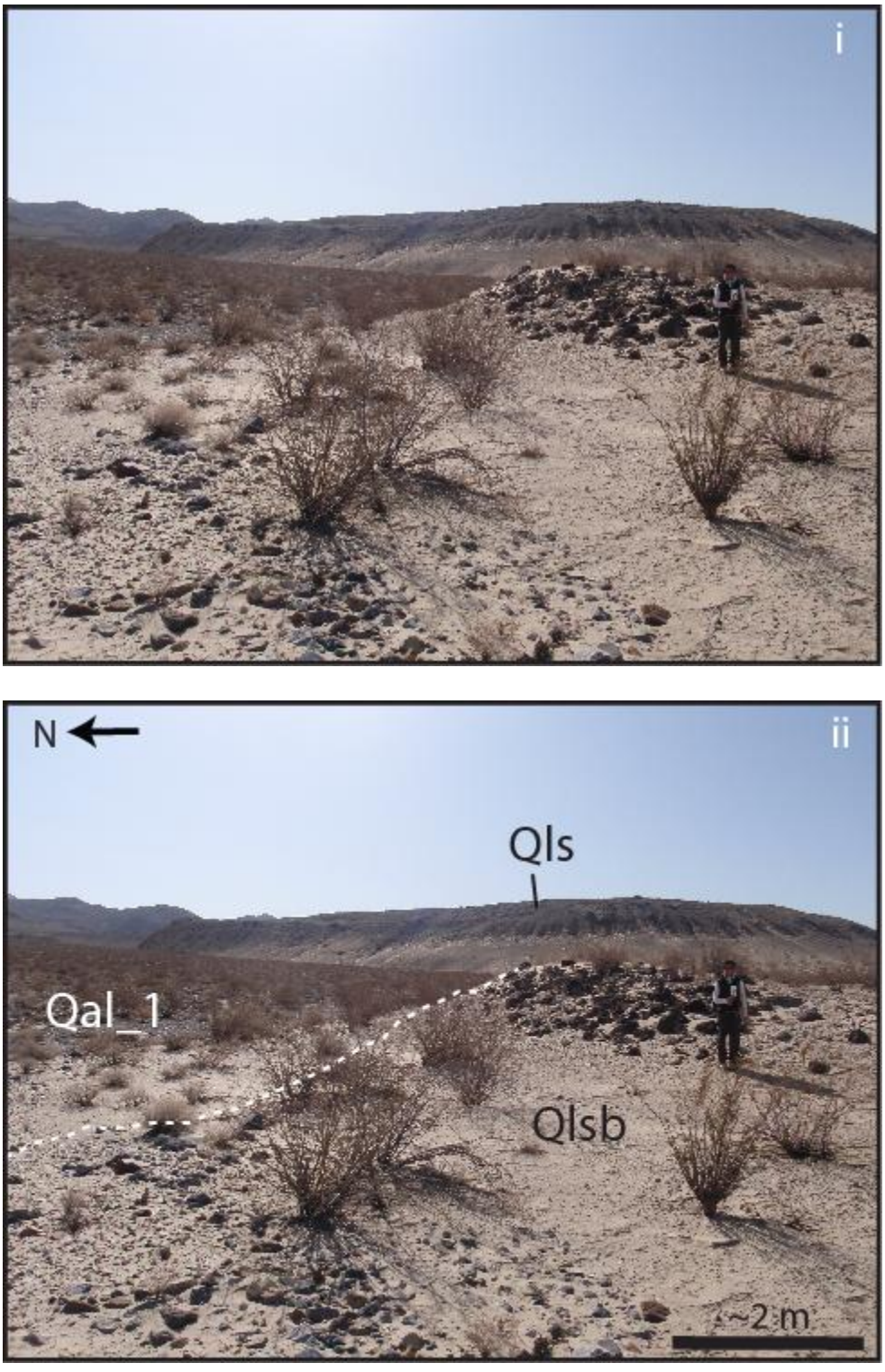

Figure 4.4. Field photograph of thicker sandy unit with limestone clasts and basalt boulders northwest of the landslide toe (Qlsb). A raised sand bank separates this unit from adjacent alluvium.

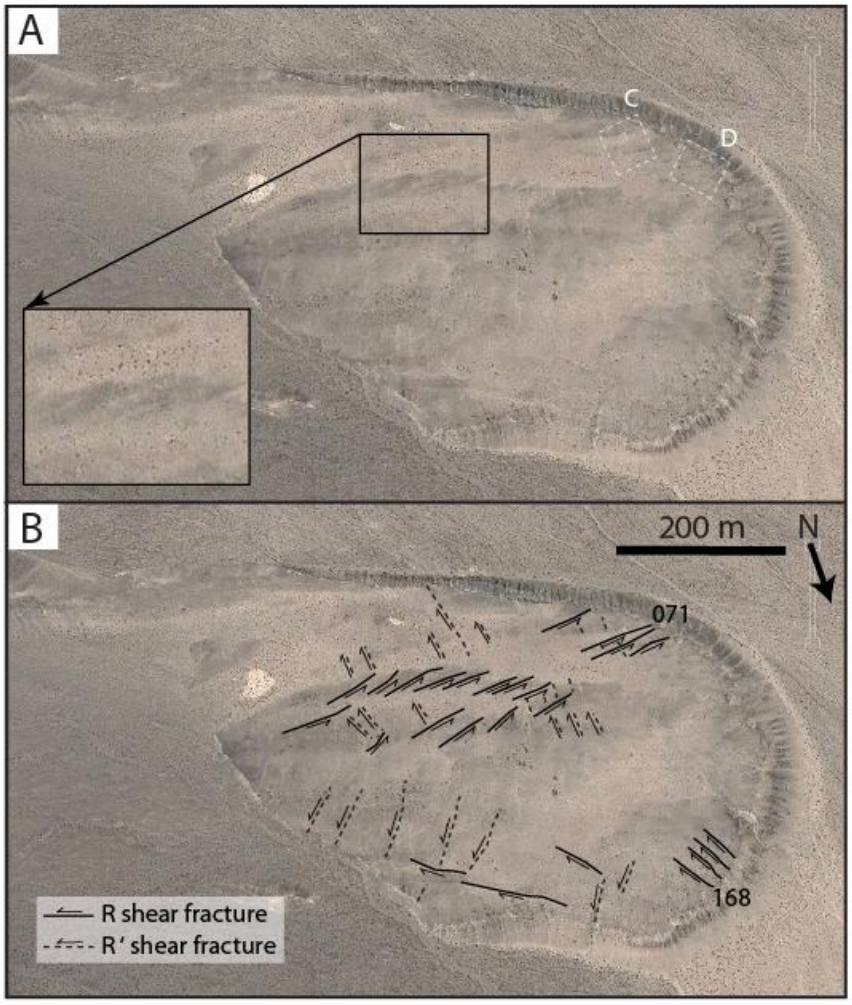

Figure 4.5. (A) Lobate landslide surface, with the locations of field photographs of the surface expressions of 3-D simple shear (C and D). (B) An en echelon fault pattern is oblique from the edges in map view. It is likely generated by a Poiseuille-like flow, accommodating faster motion along the long axis of the landslide sheet. The surface trends of several Riedel shears are included.

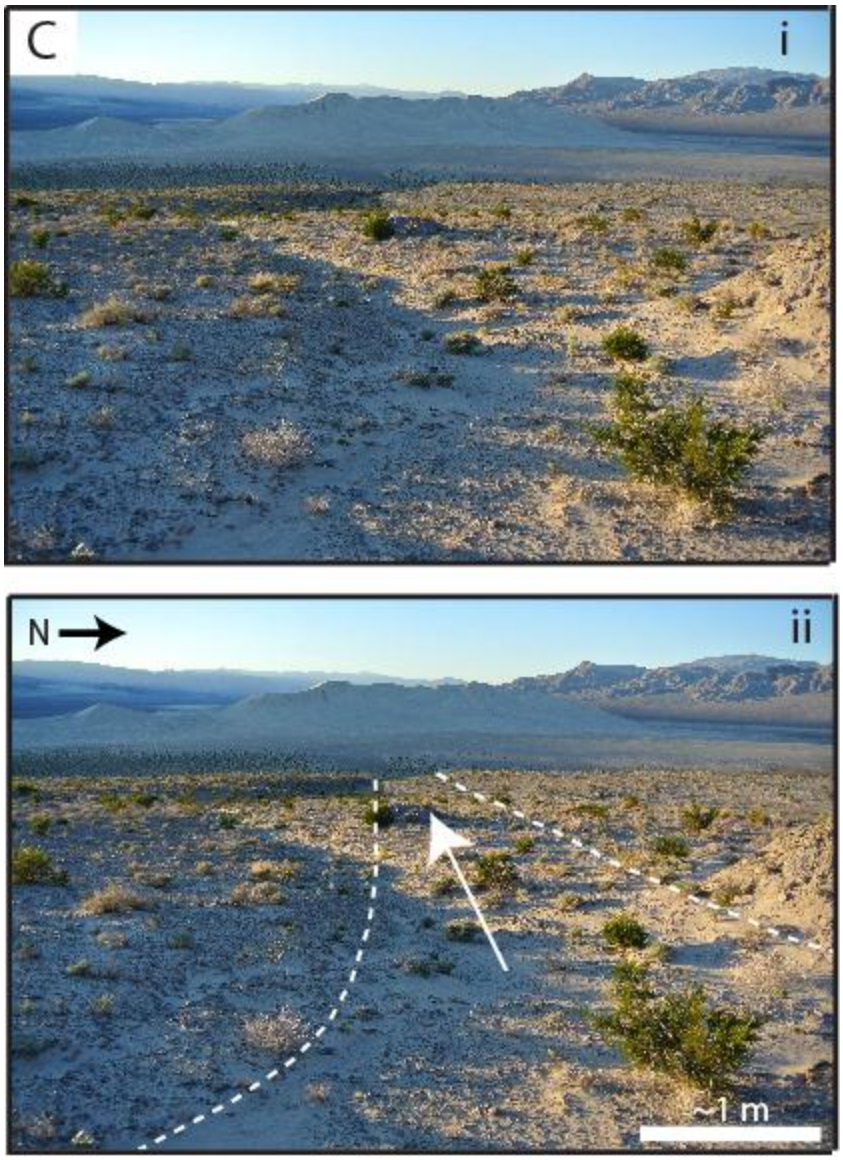

Figure 4.5, cont. (C) Field photograph of a paleochannel and surrounding mid-channel bars in the surficial braided stream network. See A for location.

surrounding coarser-grained, older landslide material were observed (**Fig. 4.5D**). Lastly, measured orientations of 12 representative large, shattered boulders on the top surface of the landslide were all distinct from each other (**Fig. 4.6 and Table 4.1**).

To quantify several of these morphological observations, detailed transverse (**Fig. 4.7A**) and longitudinal (**Fig. 4.7B**) topographic profiles of these stream networks were created based on kinematic GPS surveys taken across the southern half of the landslide surface where the mid-channel bars and paleochannel deposits are especially well-developed. The transverse profile depicts the elevation differences between the mid-channel bars and paleochannels, and the ridges that bound the system of paleochannels and bars. The longitudinal profile displays the current tilt of the landslide from toe to head.

4.3.2 Stratigraphy

A representative stratigraphy of the landslide deposit is evident in the exposed ~16m-high cross-section along the southern face of the landslide (**Fig. 4.8**). The stratigraphy in the landslide deposit is consistent with the regional stratigraphy of the source region (Corbett, 1989), though the units are thinned and broken up (**Fig. 4.8A**).

The lowest, oldest stratigraphic layer in the landslide deposit, Qlsmo, is a mottled limestone with orange veins. It is very poorly sorted, with subrounded to mildly subangular grains. A fine-grained, yellow matrix comprises 25% of the unit. The minimum grain size in the unit is 2x2 mm, the maximum clast size is 50x50 cm, and the median clast size is 5x6 cm. The unit is ~4 m thick (**Fig. 4.8B-D**).

Working up in the landslide deposit section, Qlsc is a limestone with little brown weathering, and some calcite concretions. It is very poorly sorted, with largely subangular grains

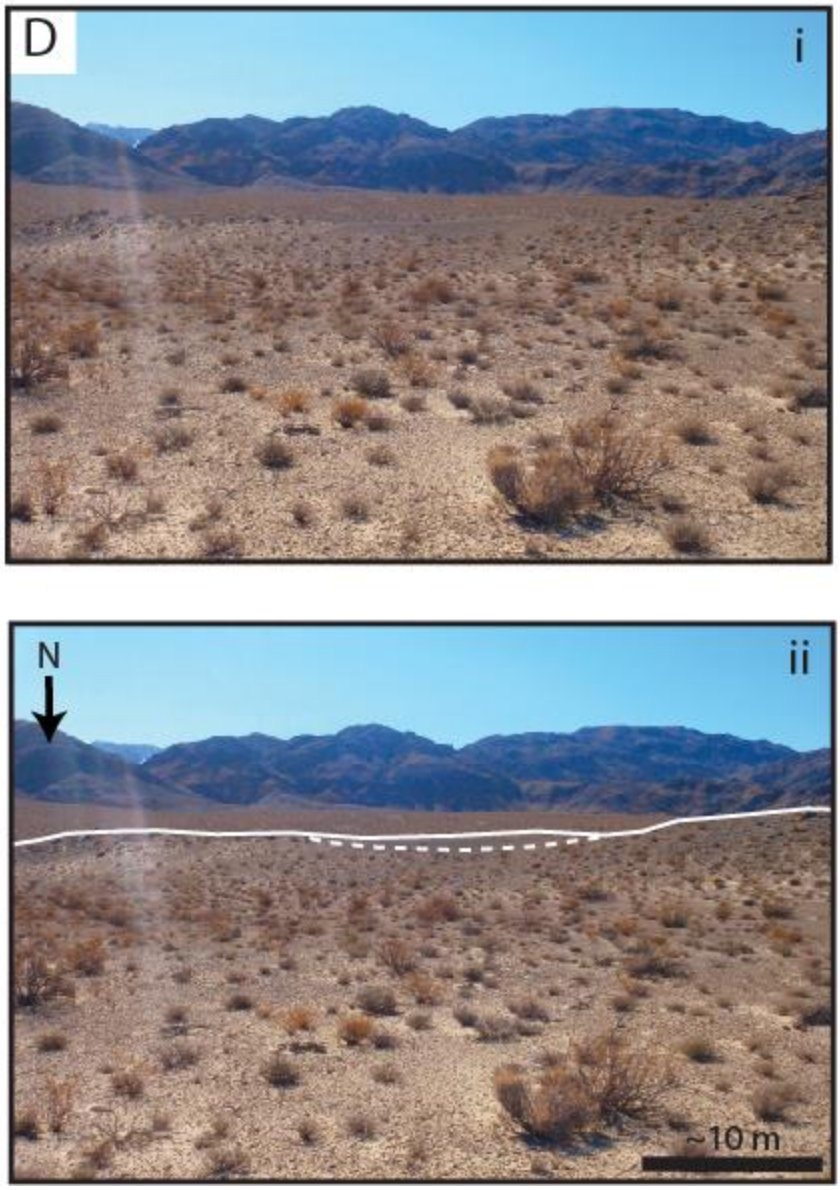

Figure 4.5, cont. (D) Field photograph of a wind gap along the rim of the landslide deposit, filled with fine-grained sediment. See A for location.

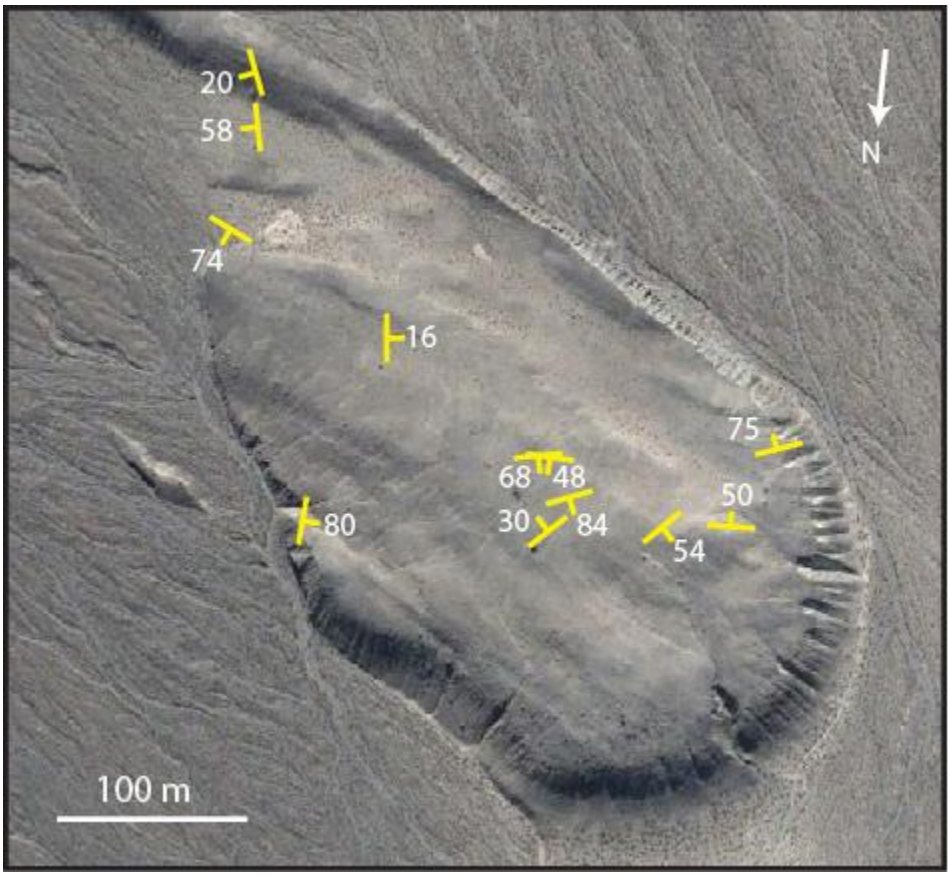

Figure 4.6. Mapped boulder locations and orientations on the surface. Note the chaotic arrangement of boulder emplacement, with no preferred orientation. See Table 4.1 for boulder measurements.

	Latitude	Longitude	Height (cm)	Width (cm)	Exposed Depth (cm)	Composition	Orientation
B1	N 37°4’26.0”	W 117°38’46.1”	204	150	123	Banded limestone	141/74N
B2	N 37°4’22.8”	W 117°38’46.4”	335	277	50	Banded limestone	174/58E
B3	N 37°4’21.3”	W 117°38’45.9”	320	400	192	Massive limestone	164/20E
B4	N 37°4’28.3”	W 117°38’52.4”	415	248	136	Massive limestone with large calcite veins	000/16W
B5	N 37°4’34.0”	W 117°38’51.2”	455	404	140	Massive, weathered limestone with calcite	010/80W
B6	N 37°4’32.8”	W 117°38’59.4”	765	500	333	Banded limestone with 83cm wide marble vein	052/36S
B7	N 37°4’32.4”	W 117°38’59.7”	596	347	180	Banded limestone, marble vein	074/84N
B8	N 37°4’31.4”	W 117°38’58.4”	406	264	184	Massive, dark limestone with thin calcite veins	084/68N
B9	N 37°4’31.4”	W 117°38’58.5”	324	259	136	Massive limestone with calcite veins; more heavily jointed	098/48NE
B10	N 37°4’37.04”	W 117°38’32.4”	506	296	234	Weathered marble	051/54N
B11	N 37°4’31.6”	W 117°39’09.0”	393	197	103	Massive limestone with weathering texture	094/50S
B12	N 37°4’30.2”	W 117°39’07.5”	586	337	114	Banded limestone	076/75S

Table 4.1. Table of measurements of boulders exposed on the landslide surface.

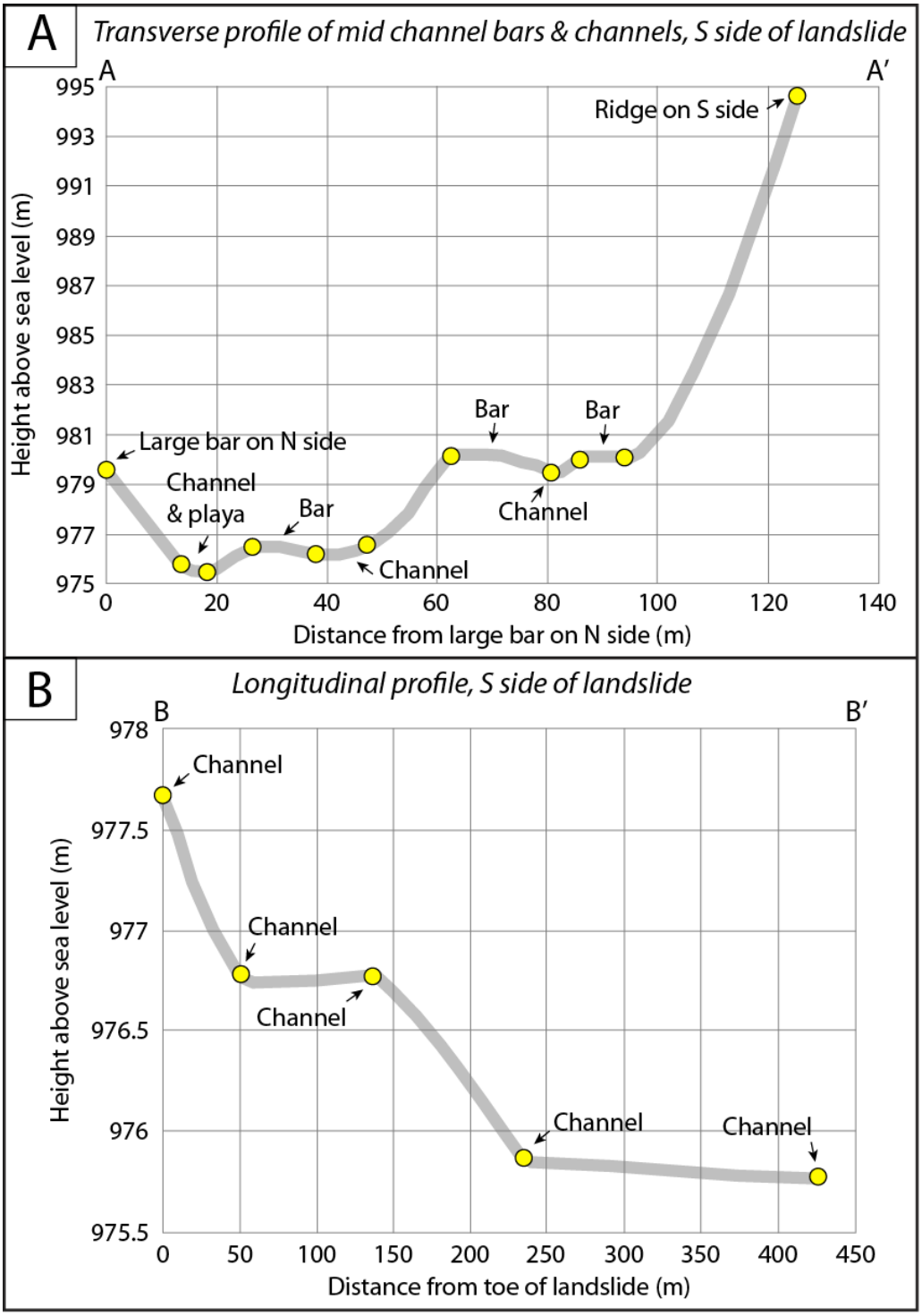

Figure 4.7. (A) Transverse kinematic GPS profile across surface of landslide deposit. (B) Longitudinal kinematic GPS profile across surface of landslide deposit.

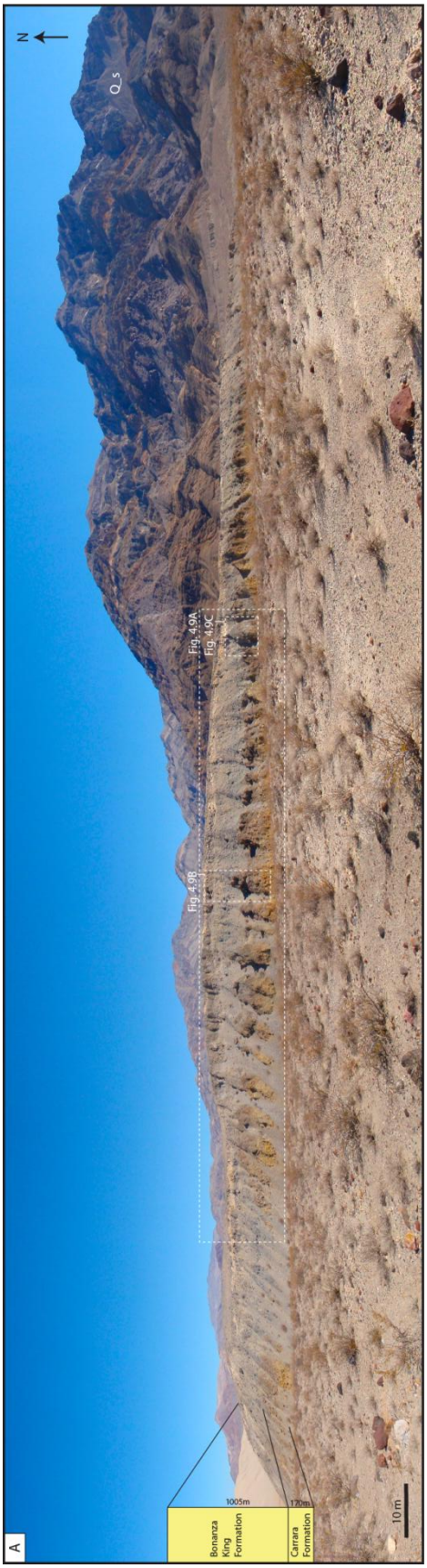

Figure 4.8. (A) Southern cross-section of the landslide deposit showing the thinning of the units from the source region to the emplaced deposit, resulting from extreme stretching upon transport. The locations of field

photographs of layers offset by Riedel shears (Fig. 4.9) are shown.

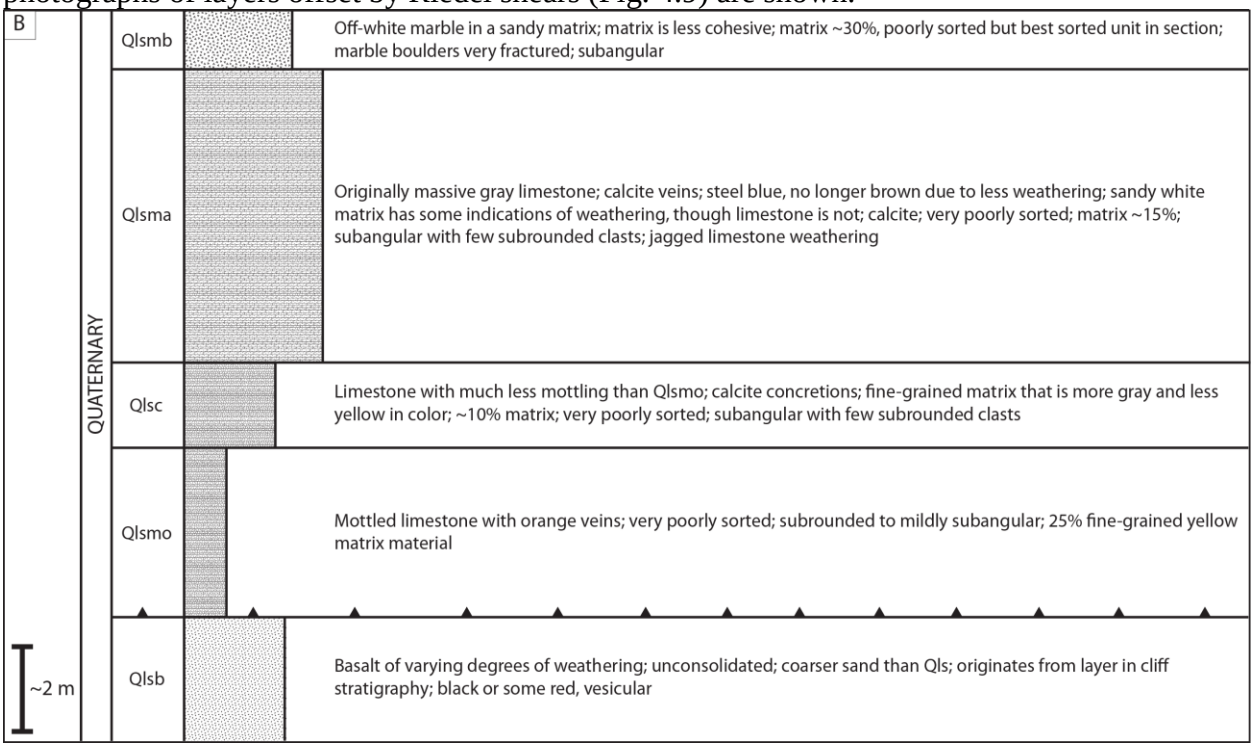

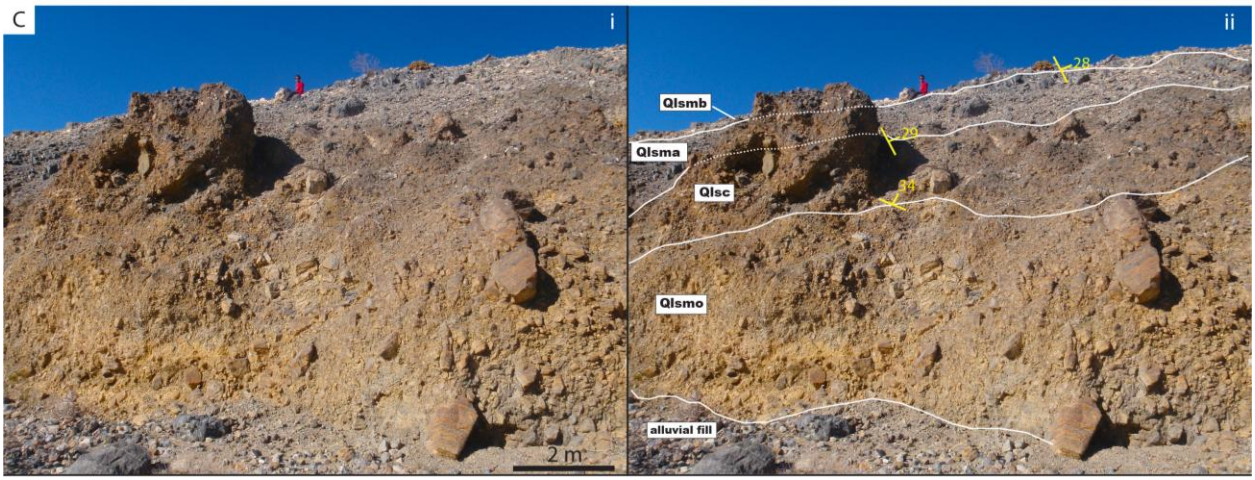

Figure 4.8, cont. (B) Stratigraphic column of mechanical stratigraphy within the landslide deposit, in which the original source region stratigraphy is preserved. (C) Representative stratigraphy of the landslide deposit, upon which the stratigraphic column is based.

and some subrounded grains. A fine-grained, grayish-yellow matrix comprises 10% of the unit. The minimum grain size in the unit is 4x4 mm, the maximum clast size is 43x22 cm, and the median clast size is 7x13 cm. Layers within this unit are offset. The unit is ~7 m thick (**Figs. 4.8B, 4.8C and 4.8E**).

Qlsma is an unweathered gray limestone with calcite veins. It has no remnants of the brown weathering feature, though there is some pink/peach coloration. It is very poorly sorted, with largely subangular grains and some subrounded grains. A lighter, sandier white fine-grained matrix comprises 15% of the unit. The matrix contains some weathering and calcite. The minimum grain size in the unit is 7x3 mm, the maximum clast size is 74x92 cm, and the median clast size is 14x9 cm. The unit is ~6-8 m thick (**Figs. 4.8B, 4.8C and 4.8F**).

The uppermost stratigraphic layer in the landslide deposit, Qlsmb, is off-white marble in a sandy matrix. The marble boulders are heavily fractured. The constituent pieces of these boulders are loosely fitted together in a 3-D jigsaw puzzle. The unit is poorly sorted, but is the best sorted of all the landslide deposit units. The marble is subangular. The matrix is less cohesive than that of the units below it, and comprises 30% of the unit. The minimum grain size in the unit is 15x10 mm, the maximum clast size is 70x30 cm, and the median clast size is 12x9 cm. The unit is ~1.5 m thick (**Figs. 4.8B, 4.8C and 4.8G**). Each of the layered breccia units are offset ~5-7m by normal faults that terminate upward at the Qlsmb unit (**Fig. 4.9**).

4.3.3 Spectral composition

An ASTER 4:8 band ratio image, illuminating hydrated materials in the study area, clearly shows multiple, alternating hydrated layers in the landslide source cliff, and two of these thin, bright layers intersect the landslide breakaway scarp (Q_s) (**Fig. 4.10**). These layers are also

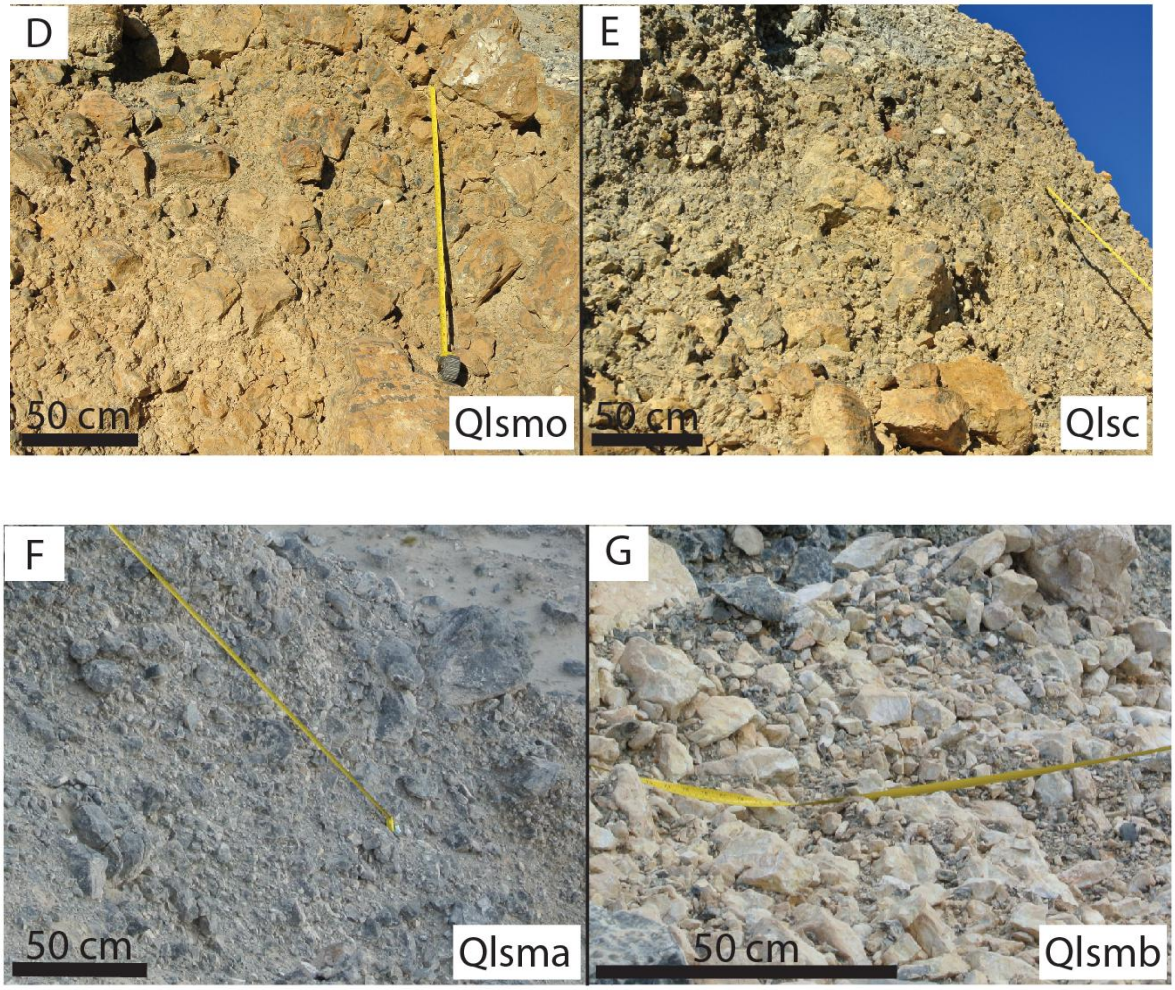

Figure 4.8, cont. (D) Field photograph of unit Qlsmo, mottled limestone with orange veins. (E) Field photograph of unit Qlsc, limestone with less mottling. (F) Field photograph of unit Qlsma, massive limestone. (G) Field photograph of unit Qlsmb, fractured marble.

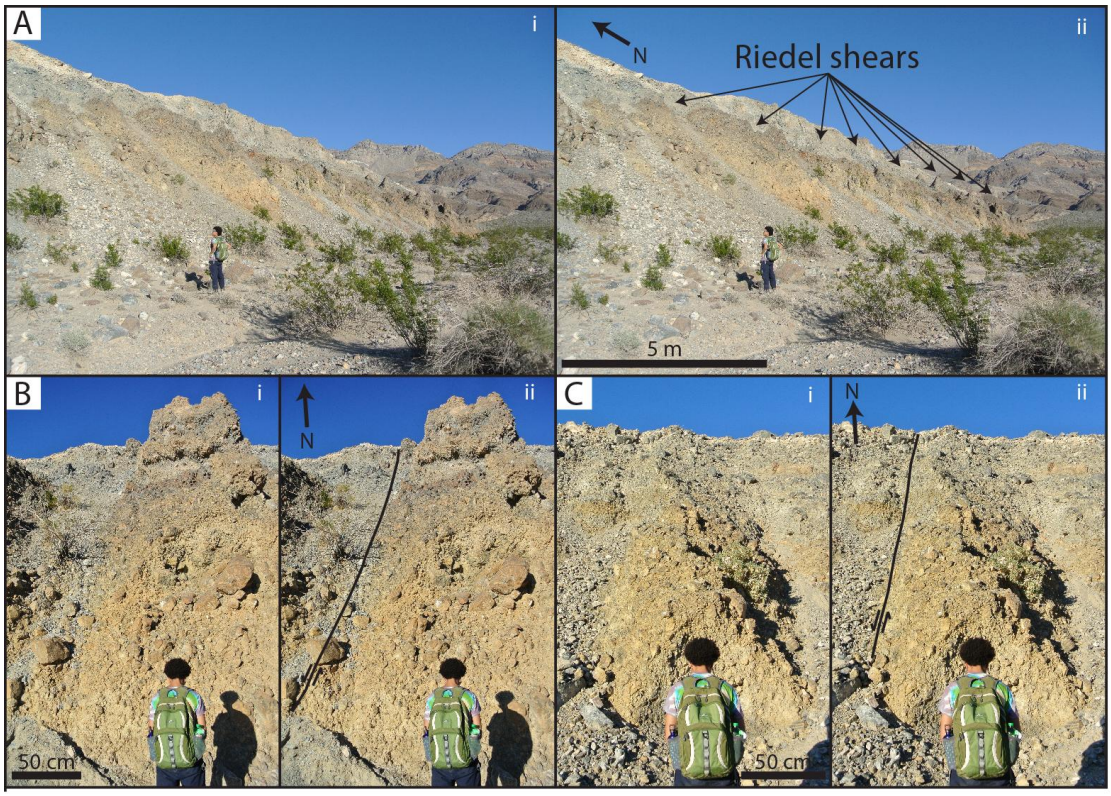

Figure 4.9. Field photographs within the cross-section, displaying Riedel shears and offset stratigraphic layers. See Fig. 4.8A for locations.

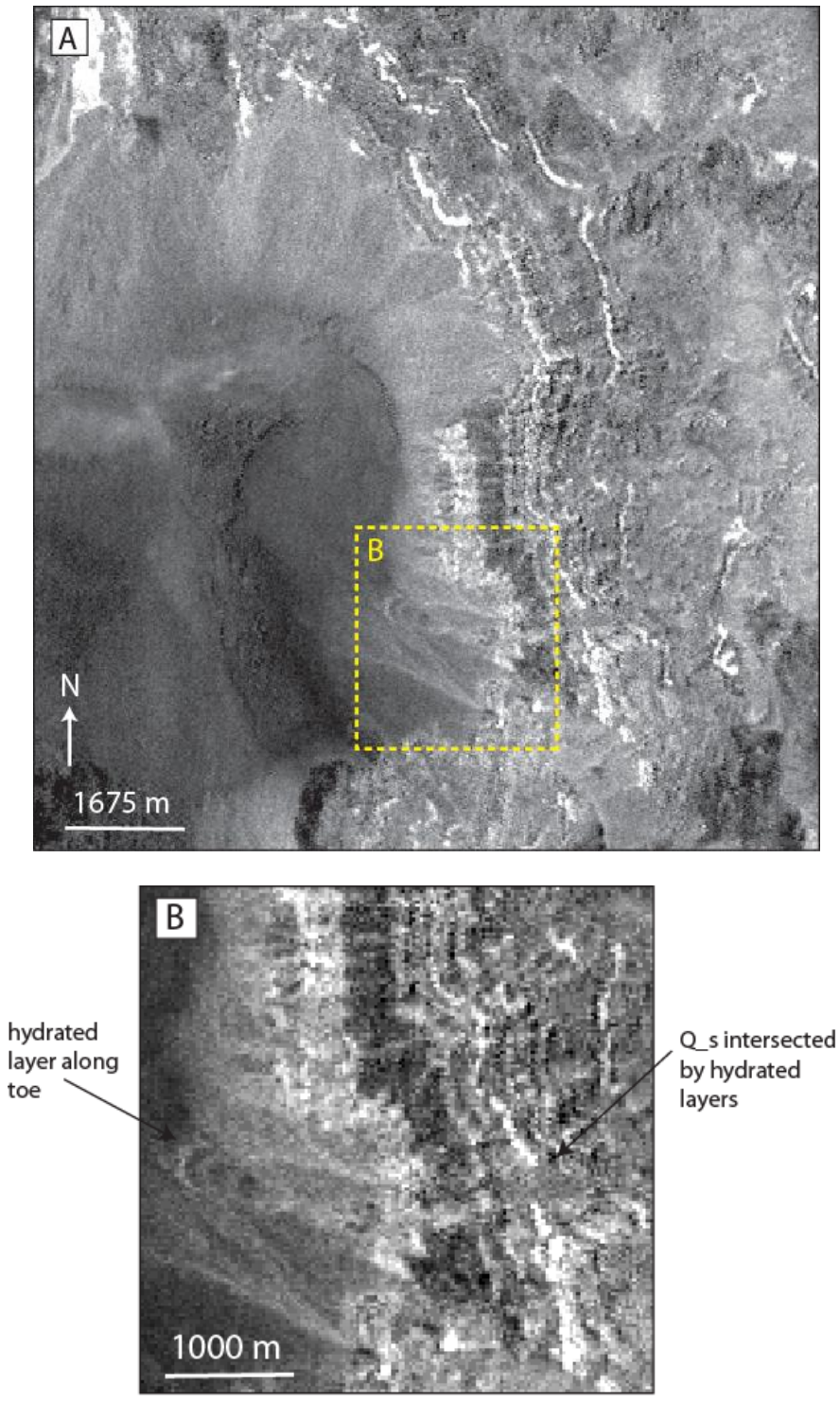

Figure 4.10. (A) ASTER 4:8 band ratio image, illuminating hydrated materials in the Last Chance Range and EV landslide vicinity. (B) Zoom-in displaying the intersection of hydrated layers in the landslide source cliff with the landslide breakaway scarp (Q_s), and a hydrated layer along the toe which mimics its shape, in contrast to the unhydrated surface of the landslide deposit.

lightest in natural color. The distinct outline of a hydrated layer in a horseshoe-shape is visible along the toe of the landslide deposit. This layer is significantly brighter than the top surface of the landslide deposit, which appears to be unhydrated both in the band ratio image and in visual field investigation. Alluvial fans in the vicinity of the slide express a subdued hydration signature, while the region which corresponds to the Eureka Dunes to the west is substantially darker in the image, implying a lack of hydration in the dune sands.

4.3.4 Age

A pit was dug into the Qal_ls unit in order to constrain the age of an EV-landslide-related unit through OSL dating. The stratigraphy within the pit consisted of coarse alluvial sand at the base, 51.5 cm below the surface, a Qlsmb marble gravel unit beginning 47 cm below the surface, and finer alluvial sand from a depth of 30.5 cm up to the surface (**Fig. 4.11**).

The first sample analyzed was taken from the finer sand unit of Qal_ls. The majority of the grains in this sample combine to give an equivalent dose of 30.6 +/- 1.0 Gy. Given a dose rate of 4.1 mGy/yr, this corresponds to a preliminary age of 9465 +/- 380 yr BP (with 1 sigma uncertainty). The second sample analyzed was taken from the coarser sand unit at the base of the pit. The grains in this sample combine to give an equivalent dose of 30.1 +/- 0.9 Gy. Given a dose rate of 4.8 mGy/yr, this corresponds to a preliminary age of 8275 +/- 300 yr BP. This age corroborates the reliability of that of the upper sand sample in that it is moderately older, as their stratigraphic relationship would predict.

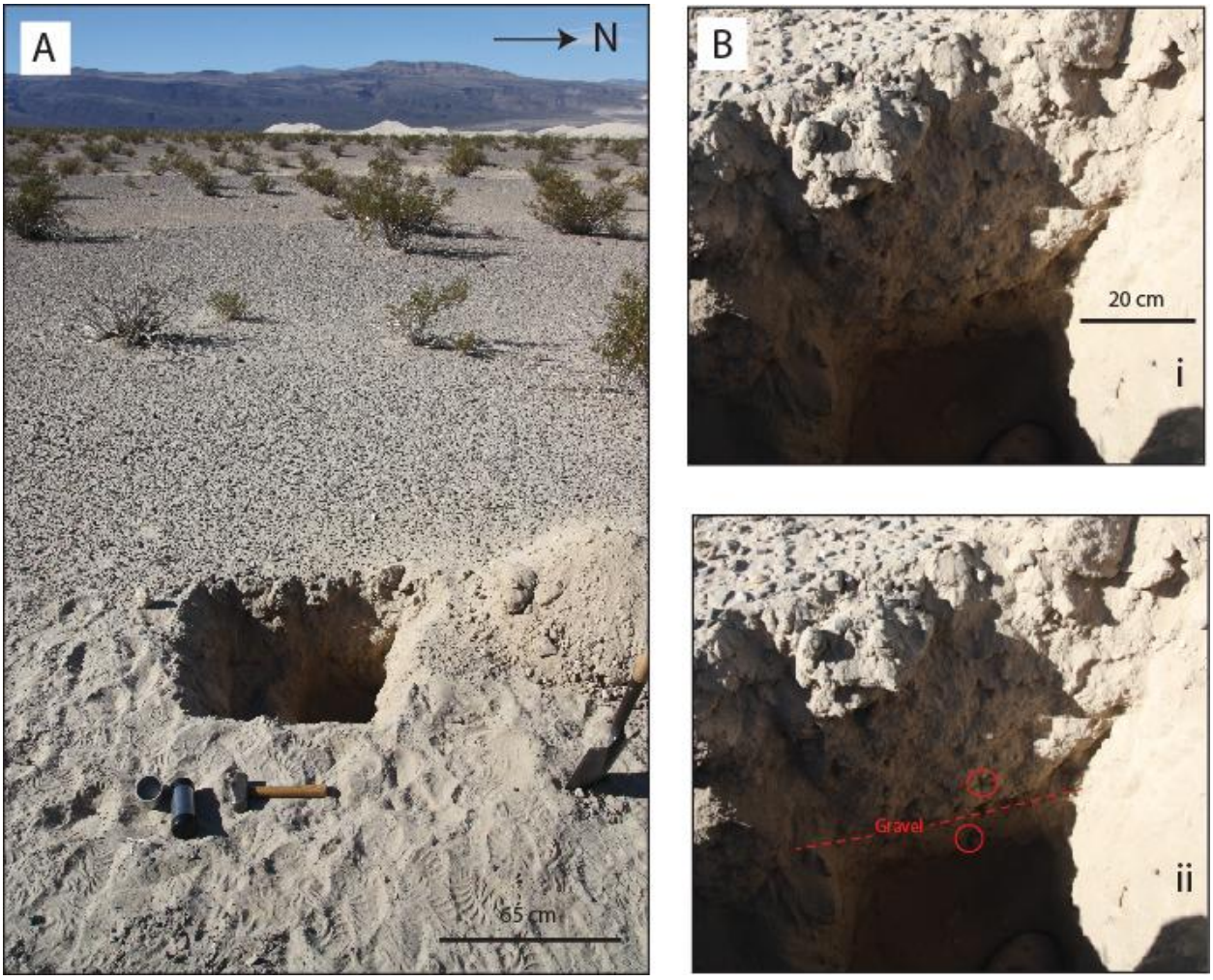

Figure 4.11. (A) Field photograph of pit dug into Qal_ls unit for OSL dating. See Fig. 4.1B for location. (B) View inside the pit of sample locations (red circles) and stratigraphic context.

4.4 Discussion

4.4.1 Initiation

According to the Mohr-Coulomb fracture criterion, landslides initiate when downslope shear strength exceeds the internal strength of the materials composing the slope. Prevalent range-bounding normal faulting provides a mechanism for creating the force imbalance required for slope failure (**Fig. 4.12A**). The EV landslide is interpreted to have been triggered by seismic activity along normal fractures of a paleolandslide scarp with similar orientation to the closely-spaced normal faults of the Last Chance Range west margin source cliff, as evidenced in canyons in the vicinity (**Fig. 4.12B**). A reactivated cliff normal fracture became the basal detachment along which the EV landslide was initiated and mobilized after breaking away from the source region (**Fig. 4.13**).

Observed bedding orientation in the source region orthogonal to the landslide slip direction implies that EV landslide initiation was not controlled by bedding or foliation, as is often the case (Cruden and Varnes, 1996). Instead, slip on the EV landslide was likely controlled by fault-generated fracture, whereby regional normal faulting in the cliff created a plane of weakness, leading to slope failure. Failure likely occurred during a seismic event and/or a period of heavy rainfall. The latter is supported by the significant amount of channel reworking in the eroded region of the original slide deposit and on the modified slide surface.

4.4.2 3-D simple shear model

Based on the characteristic geometric relationships expressed in the southern cross-section of the landslide, we interpret the landslide deposit as an extensional duplex structure (**Fig. 4.14A**). The sole normal fault of the landslide, interpreted to be underneath the landslide

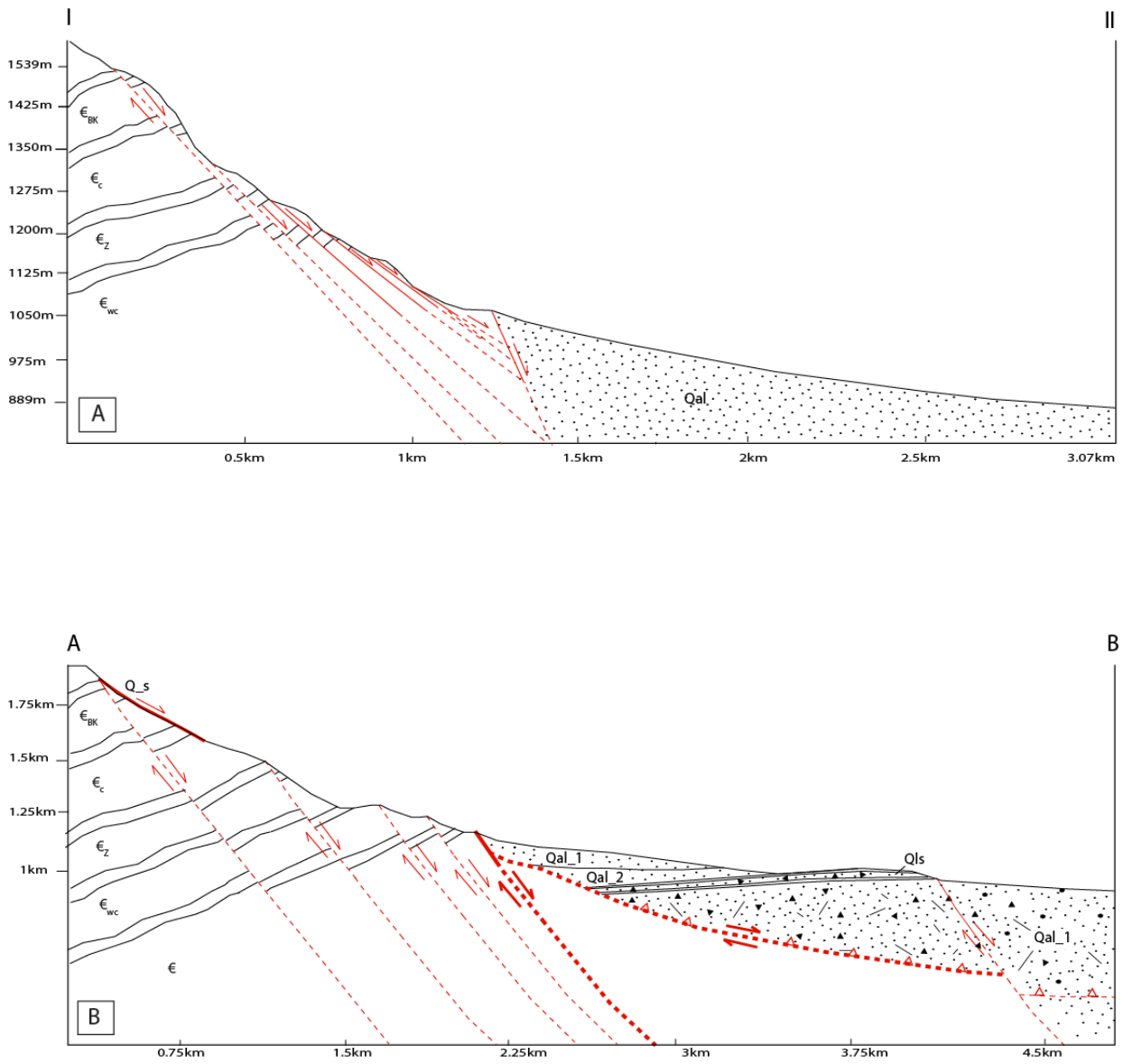

Figure 4.12. (A) Regional cross-section interpreted from field data across the range front, through the landslide, and up to the source region, with topographic profile derived from Landsat data (see Fig. 4.1 for location). (B) Regional cross-section interpreted from field data across the range front adjacent to the landslide path, with topographic profile derived from Landsat data (see Fig. 4.1 for location).

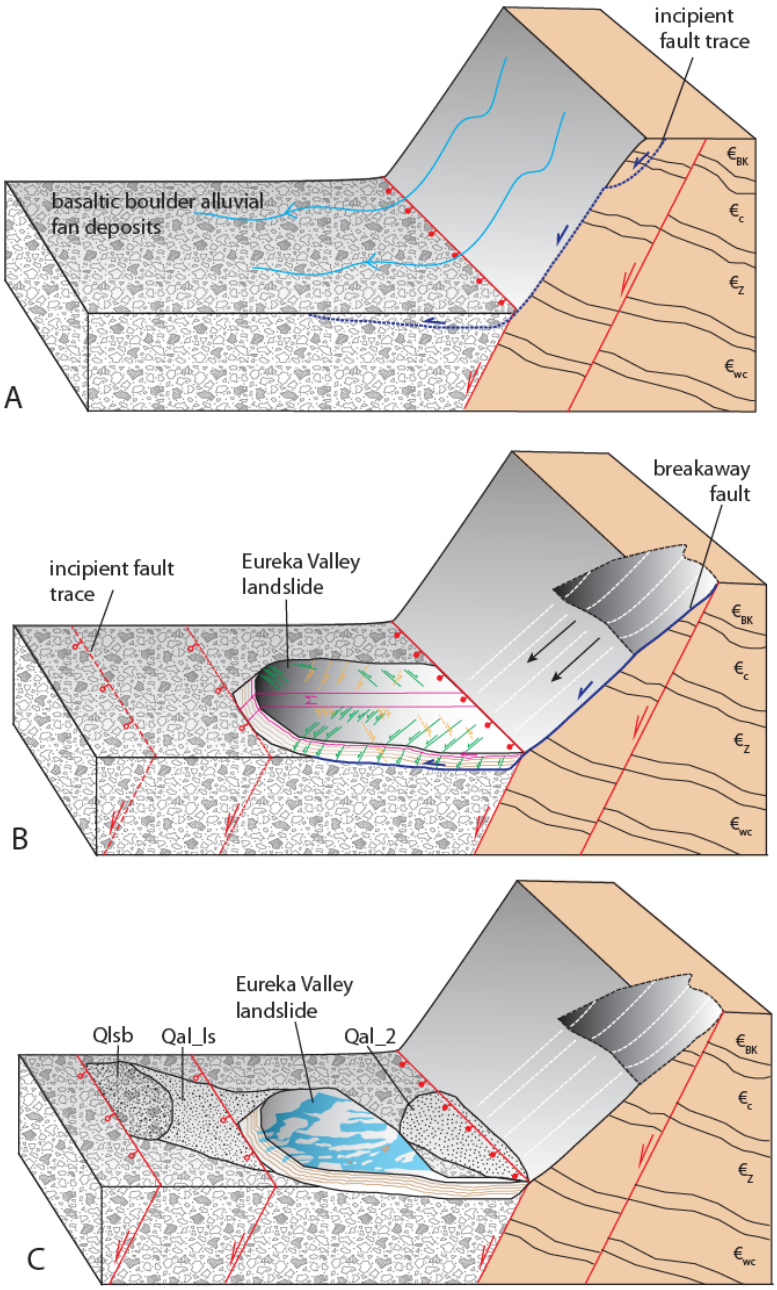

Figure 4.13. (A) Interpreted pre-landsliding structural context for Last Chance Range and valley floor, including an incipient fault in the cliff along a paleolandslide scarp and fluvial activity forming fan deposits. (B) The EV landslide was initiated along the reactivated fault-generated fracture, likely following a seismic triggering event and/or a very wet season. (C) Following its emplacement, the EV landslide deposit was modified by fluvial activity, forming a braided stream network on the surface. Talus sediment eroded off the top of the landslide surface accumulated northwest of the landslide (Qal_ls). The block underneath the landslide was then rotated back towards the Last Chance Range, shutting off the fluvial system. Incomplete resurfacing eroded a portion of the landslide, which was transported and deposited downstream (Qlsb).

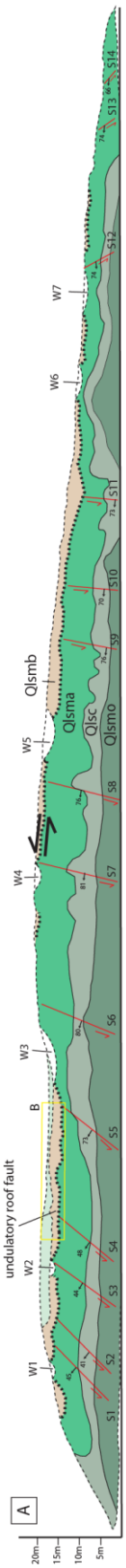

Figure 4.14. (A) Interpreted 3-D simple shear model, where normal faults in cross-section view are Riedel shears that accommodate top-west landslide transport via layer-parallel simple shear. Normal faults terminate upward at an undulatory roof detachment surface, characteristic of an extensional duplex system. Riedel shears are labeled with an "S", and wind gaps are labeled with a "W". Landslide deposit units are also labeled (see Fig. 4.8).

and thus not observable on the surface, was the landslide slip surface. The thin Qlsmb top unit may be original tectonic breccia, formed as a result of range-bounding normal fault activity, as evidenced by its joints and fractures. It thus consists of superposed tectonic and mechanical stratigraphy, and is interpreted as the mullion roof fault contact and as a landslide slip surface (**Fig. 4.14B**). The normal faults that offset the layered breccia units in between the paired faults terminate upward at the flat detachment surface. The thinning of each unit while their original stratigraphic position is maintained, is interpreted to be a result of extreme stretching due to penetrative normal faulting during transport (**Fig. 4.8A**).

We interpret that the west-dipping normal faults, their en echelon surficial pattern, and a superposed, stretched mechanical stratigraphy all contribute to a single 3-D simple shear model. In this model, the normal faults visible in cross-section view are Riedel (synthetic) shears that accommodate top-west EV landslide transport via layer-parallel strike-slip simple shear (Sylvester, 1988) (**Figs. 4.13, 4.14A and 4.14C**). Moreover, the oblique, en echelon fault pattern visible in map view was likely generated by Poiseuille-like flow (Yin and Taylor, 2011), characterized by two parallel shear zones with opposite senses of shear accommodating faster motion along the long axis of the EV landslide sheet (**Figs. 4.13 and 4.5**). In this surficial plane, the south side of the landslide was subject to left-lateral shear, while the north side was subject to right-lateral shear. The orientations of lineations mapped on the surface are consistent with the expected orientations of Riedel and Riedel prime shear structures (Sylvester, 1988). In the cross-sectional plane, flow of the landslide and friction along the base created a left-lateral shear system (**Figs. 4.13 and 4.14A**). In the third plane, shear thinned the landslide layers (**Fig. 4.8A**). This flow created pressure that pushed the levees to the side, resulting in the lobate spoon shape of the deposit observed.

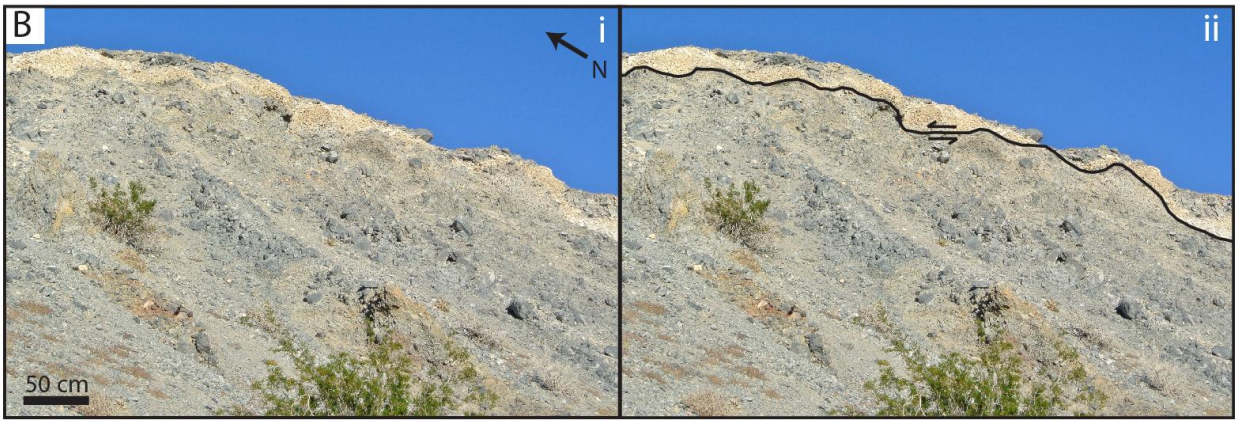

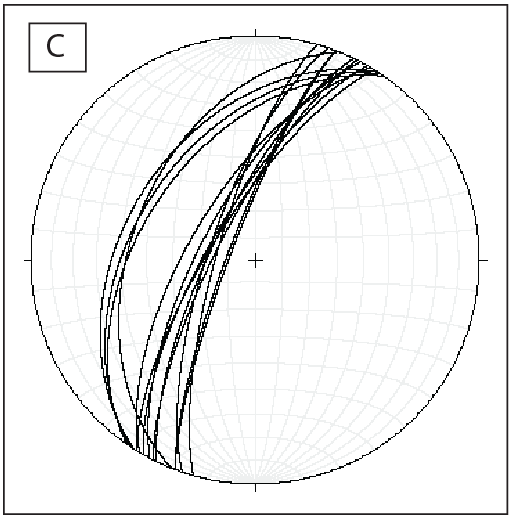

Figure 4.14, cont. (B) Field photograph of undulatory roof fault. See A for location. (C) Stereoplot of Riedel shear planes expressed in the southern cross-section of the landslide, illustrating their parallel orientation.

4.4.3 Transport mechanism

Our geomorphological observations of the EV landslide are in discordance with several previously proposed long-runout landslide emplacement mechanisms. The morphology of the EV landslide indicates that its long-distance transport was not facilitated by an air-layer cushion. The primary evidence for this inference is that features with very similar morphology are observed on planetary surfaces devoid of a detectable atmosphere (e.g., Singer et al., 2012), as the presence of an atmosphere is required by this model. In-depth analysis of EV landslide units also precludes lubricated transport as a result of melt generation, as compelling evidence of fused or transformed rock indicative of extremely high energy concentration in the sliding zone is not observed. Lastly, emplacement of the EV landslide through lubrication by ice or snow is also untenable based on a lack of morphologic features related to the presence of ice or snow preserved on the Eureka Valley floor. Two plausible models for EV landslide emplacement remain: lubrication by soft/weak materials and subaqueous emplacement.

i. Clay-lubricated transport

Of the models for EV landslide transport proposed in this work, we interpret lubrication of the landslide mass by hydrated clay materials within the landslide base as the most likely mechanism. While no direct evidence of basal clays was observed, two main lines of observational evidence support this model: (1) the preserved internal stratigraphy and structure of the landslide deposit and (2) the possible identification of hydrated materials at the base of the landslide in the remote sensing data.

The form, stratigraphy, and internal structure of the main debris lobe of the EV landslide are indicative of fluidization of the landslide mass. Mechanical fluidization is the fundamentally

three-dimensional process (Erismann, 1979) by which a high energy input to a solid mass of loose debris causes rebounding collisions between individual grains, so that they become separated and the mass dilates as a result of unidirectional basal shear. The internal friction is thereby reduced, and the mass may flow, spreading out under gravity and retaining forward motion (McSaveney, 1978; Davies, 1982). The initial high energy may source from earthquake vibrations (McSaveney, 1978), or from the relative velocity between the base of a high speed debris mass, resulting from its fall from elevation, and the underlying stationary ground (Davies, 1982). The well-preserved features of the EV landslide deposit suggest that it reached a sufficiently high energy level to begin to flow, thinning and spreading the mass before it came to a halt.

The EV landslide is interpreted to have translated as a sheet, retaining its internal stratigraphy, although the internal shaking energy was transferred to the fracturing of the rocks within the landslide deposit. The original stratigraphy observed in the cliff is preserved within the layers of the landslide deposit. That is, the sequential order of units present in the rock mass prior to its fall from the cliff was retained (**Fig. 4.8A**). This translational motion is shared by the Elm (Heim, 1882), and Sherman (McSaveney, 1978) landslides, and is likely caused by fluidization, as granular flow would produce a lack of slip at the base due to locally high basal shear precluding entrainment and mixing between lithological layers in the debris (Davies, 1982). In addition, the observed brecciation of the original stratigraphy is likely created through intense internal deformation throughout the deposit as a result of shaking upon emplacement (**Fig. 4.8**). Substantial preservation of the original source region stratigraphy with highly broken-up layers is consistent with a mechanical stratigraphy created by shearing of the landslide as it was transported. Within the landslide deposit, a relative fining downwards of median grain size

and increasing roundedness towards the base is observed (**Fig. 4.8**), also consistent with more rounded and smaller clasts at the base of the section having experienced higher and more uniform strain. The observed universal decrease in thickness of the units in the landslide deposit as compared to their thicknesses in the landslide source region is another expected geomorphological consequence of significant internal deformation. This stretching and thinning of the crust result from longitudinal strain and resultant penetrative normal faulting within the deforming debris mass.

The accumulation of several large, shattered boulders exposed at the surface of the deposit, observed in other long-runout landslide deposits as well as the EV landslide (Shreve, 1968; **Fig. 4.6**), may be explained within a fluidization model by the fact that dispersive pressure on a clast increases with clast size. Hence, large clasts will tend to be preferentially forced into the region of lowest shear at the surface (Davies, 1982). Additionally, there is no correlation between the distance of these boulders from the source area and their exposed volumes, which indicates a relatively chaotic, flow-dominated emplacement of the landslide whereby shattered rocks were carried for long distances on the surface of the flow without their constituent pieces becoming widely separated (**Fig. 4.15;** Davies, 1982).

Perhaps the most compelling piece of geologic evidence in support of a fluidization model for emplacement is the internal structure of EV landslide. A fluidized mass, like a liquid, normally displays indications of appreciable deformation within its entire volume (Johnson, 1978; Erismann, 1979), including ubiquitous closely-spaced joints and steeply-dipping faults. We interpret the 3-D simple shear preserved within the EV landslide deposit as evidence of such deformation. The pervasive network of Riedel shears indicates prevalent zones of high shear throughout the deposit, necessary consequences of fluidization. Deformation is also exhibited in

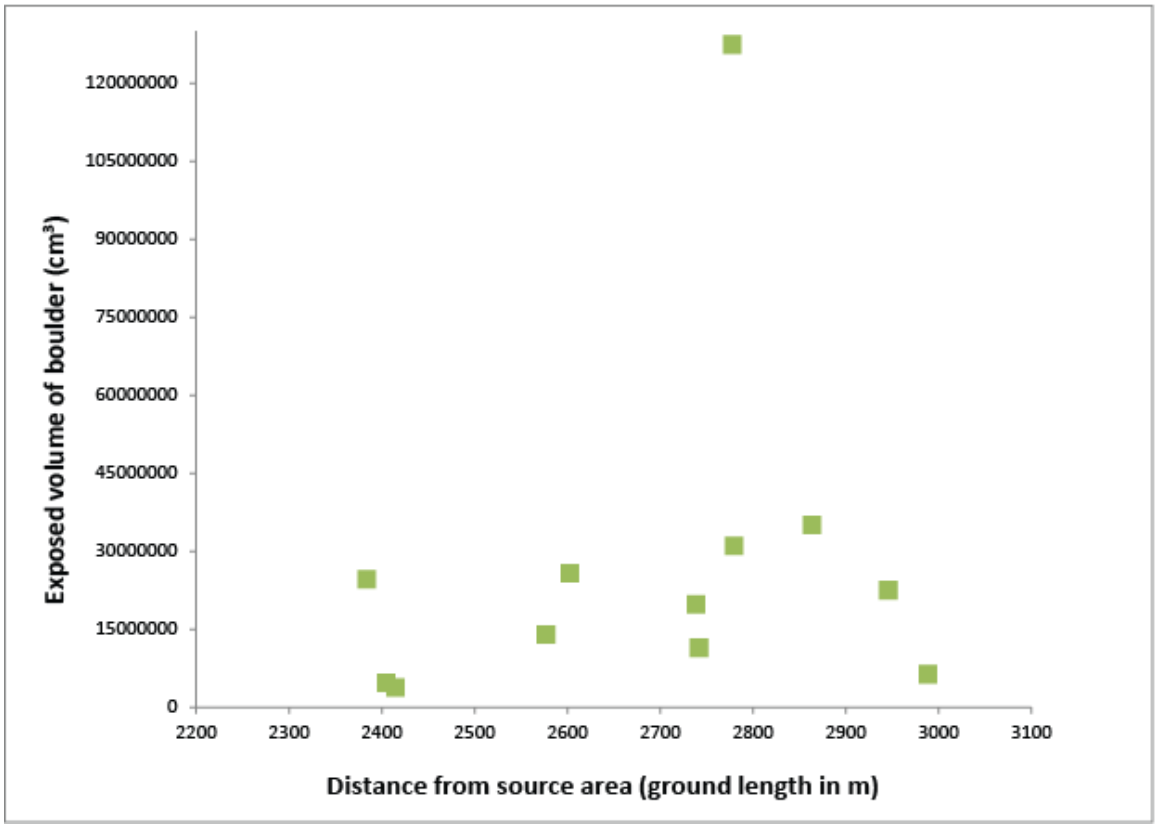

Figure 4.15. Plot of boulder volume compared with distance from the source region. Note that no significant correlation can be deduced.

the presence of the large boulders, shattered during or subsequent to landslide initiation. The 3-D jigsaw puzzle effect exhibited by such boulders was originally recognized as an indication of internal deformation in the Blackhawk landslide (Shreve, 1968). Erratic orientations of these boulders is indicative of a significant amount of reworking of the EV landslide due to shaking as it was translated down the slope from the source area, through the narrowing and widening of the channel. In the absence of intense internal deformation, the orientation of boulders near the head would be expected to be in the same orientation as the bedding in the source cliff, which is not observed (**Fig. 4.6 and Table 4.1**).

Additionally, in the case the of the Sherman landslide, the pervasively fractured nature of the Shattered Peak source rock facilitated initiation and thixotropic flow of the debris mass, particularly following violent ground motion during the Great Alaska Earthquake of 1964. We interpret the EV landslide to have been similarly triggered by major shaking related to Last Chance Range-bounding fault earthquake activity (see section 4.1). This would have imparted sufficient energy to the landslide mass to cause dilation and subsequent fluidization.

The second line of observational evidence of fluidization of the landslide mass is the identification of likely hydrated materials at the base of the landslide, which suggest that the presence of clays contained in the fluidized basal unit may have contributed to lubrication of the landslide mass and facilitated the transport of the main EV landslide deposit to its current extent. The lack of hydrated signature from rocks of the same bulk composition elsewhere in the slide deposit where they are not obstructed by more recent alluvial features, the lack of hydrated signature from the sand on either side of the Eureka Dunes, and the horseshoe shape of the hydration detection which precisely mimics that of the landslide toe around which it is draped, imply that this signature is most likely from an exposure of the base of the landslide rather than

sediment related to regional aeolian or fluvial activity, or due to variation in topography or illumination angle.

One indication that the hydration observed at the toe of the landslide corresponds to clay-bearing materials is the correlation between hydrated signatures in the cliff and source units lightest in color. Also, based on the preservation of the source stratigraphy in the landslide deposit, these layers correspond to the bottommost landslide unit, Qlsmo, and the topmost landslide unit, Qlsmb, which have the highest percentages of matrix material. Both of these observations suggest that though these units are dominantly comprised of limestone, they have higher clay content than the other cliff and landslide units. Further, the former of these units, Qlsmo, is at the base of the landslide, and has the smallest median clast size of the landslide units, consistent with fluidization of basal clay-bearing material.

An additional indication of the contribution of clays to the observed hydrated signature at the base of the toe is the ability of clays to lubricate landslides to produce long-distance transport. The low frictional strength of clay weakens and facilitates slip of clay-bearing materials, making it an ideal lubricant (see chapter 2; Watkins et al., 2015). Heim's ratio, H/L, where H is the elevation drop of the landslide and L is the distance of landslide runout, is a reasonable estimate for coefficient of friction (see chapter 2; Heim, 1882). Calculated for EV landslide, it yields a coefficient of friction of 0.27, as compared to ~0.7 for limestone (Byerlee, 1978). This low value is consistent with those determined for clays under high normal stress (Saffer and Marone, 2003), such as that exerted at the EV landslide base.

A similar process of clay lubrication of long-runout landslides has been proposed for examples in Valles Marineris, Mars, whereby clay-bearing trough-floor deposits are entrained in the basal sliding zone (Watkins et al., 2015), and for Blackhawk landslide, whereby highly

mobile mud derived from the overlying sandstone forms a basal sliding layer (Johnson, 1978). This transport mechanism for Blackhawk landslide is similarly supported by an ASTER 4:8 band ratio image, displaying a hydrated layer in the source breakaway scarp of the slide, as well as the outline of a lubricating layer along the base of the slide down to the toe (**Fig. 4.16**), suggesting the participation of clays in self-lubrication of the fluidized landslide mass. Because the EV landslide base is not exposed at the surface, however, it is not certain whether lake bed materials were entrained at the base or if the landslide was self-lubricated by its basal materials.

ii. Subaqueous emplacement

An alternate hypothesis for the long-distance transport of the EV landslide is subaqueous emplacement. Several morphological features exhibited by the EV landslide deposit are remarkably similar to those of subaqueous landslide deposits. Because deposit morphology can provide insight into the mechanism of emplacement, these similarities may support this model, pointing to the participation of water in emplacement.

First, the mobility of the EV landslide requires a mechanism of reducing the basal coefficient of friction. Subaqueous landslides exhibit extraordinarily long runout distances compared to subaerial landslides of the same volume, as well as low frictional resistance, indicative of the effect of water on lubricating and enhancing the flow (De Blasio et al., 2006; Mazzanti and De Blasio, 2010). In this way, the involvement of a thin water layer in landslide transport (i.e., hydroplaning; Mohrig et al., 1998) would sufficiently reduce the friction at the bed, thus facilitating long runout.

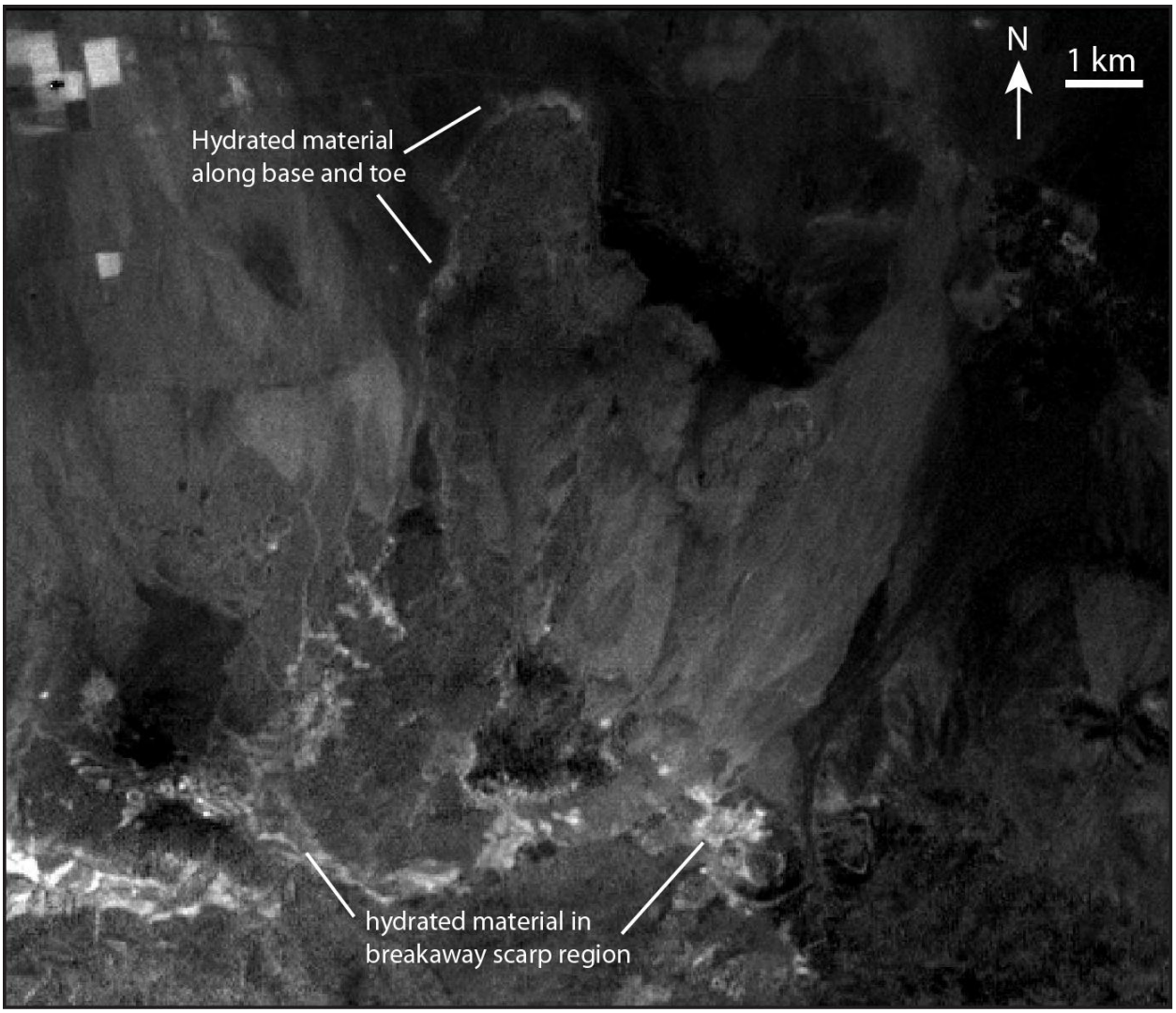

Figure 4.16. ASTER 4:8 band ratio image of Blackhawk landslide, displaying hydrated layers in the breakaway scarp and along the base and toe of the slide. This contribution of hydrated materials is similar to that of the EV landslide (see Fig. 4.10), supporting the proposed participation of lubricating clays in landslide transport.

In addition, Mazzanti and De Blasio (2010) describes a horseshoe-shaped morphology typical of subaqueous and coastal landslide deposits. These deposits exhibit perfectly semi-circular rims that are higher than the rear part **(Fig. 4.17).** They suggest that this morphology is formed as a result of the interaction between the water and the moving mass during landslide emplacement, which is affected by both drag and lift forces. The front drag force operates parallel and in opposition to the direction of movement, acts on the frontal area of the body, and is therefore strongly dependent on the object form. Conversely, the lift force is normal to the direction of travel and to the drag force. At high velocities, the lift force could become greater than the pressure load exerted by the mass (De Blasio et al., 2006) and thus the frontal part of the mass is lifted up. Mazzanti and De Blasio (2010) proposes that "flip-back" of the landslide rim as a result of lifting of the frontal part of the flow in combination with significantly increased front drag could explain the horseshoe-shape of subaqueous landslide deposits, given that in an unconfined and flat area, the landslide mass moves radially from the source with a maximum velocity in the flow direction and decreasing velocities in the direction of spreading (see Fig. 4.5).

The last morphological characteristic of subaqueous landslides is a high degree of internal deformation as a result of initiation by some disturbance, commonly earthquake shaking (Keefer, 1984; Hutchinson, 1986). The resulting loading can generate high excess pressures in the pore fluid, which lead to a sudden and significant loss of shear strength and a correspondingly high mobility of the moving debris, even on very gentle slopes (Hutchinson, 1986).

The similarities between each of these morphologic features characteristic of subaqueous landslides and those observed in the EV landslide deposit suggest that it is plausible that

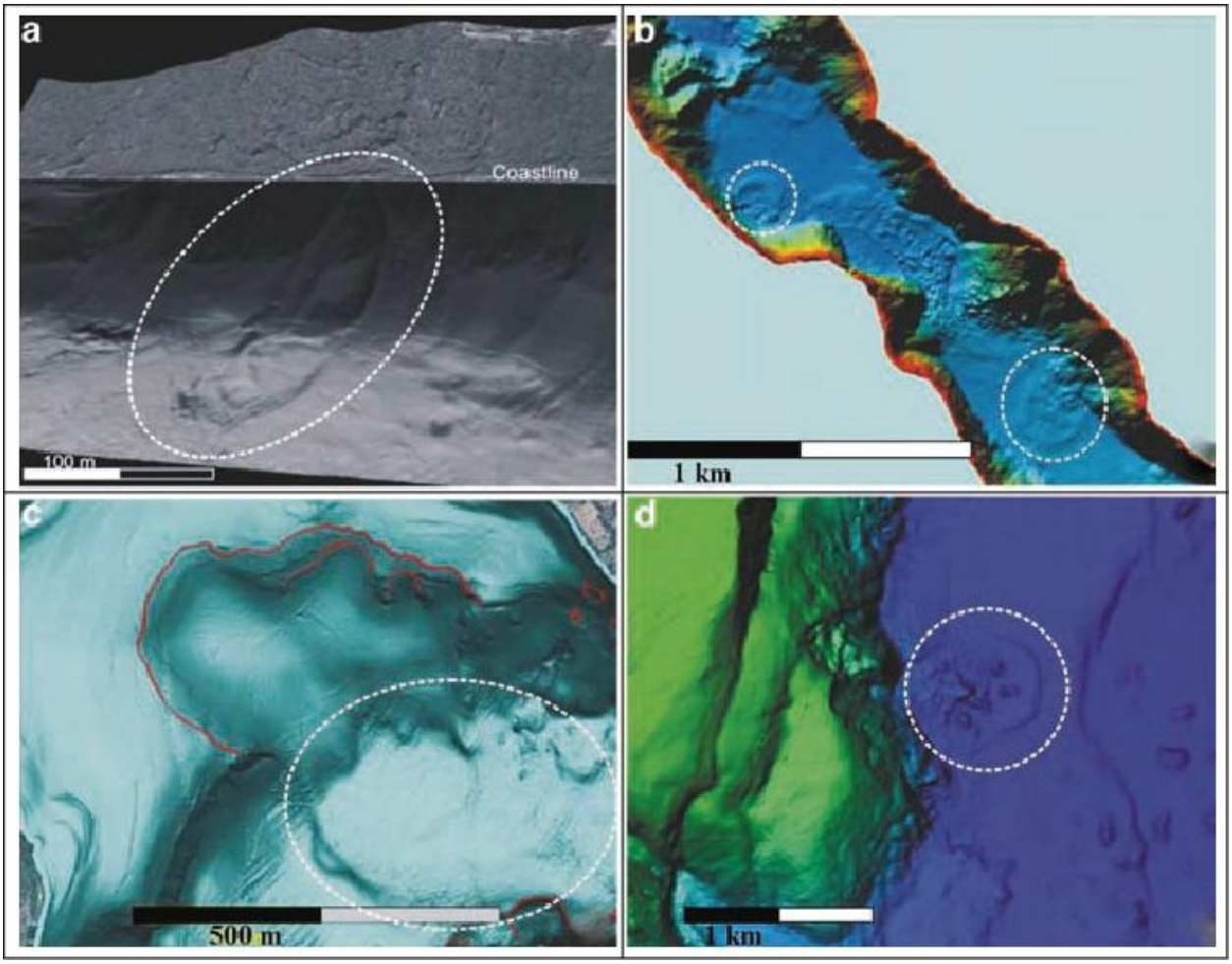

Figure 4.17. Horseshoe-shaped deposits at: (a-c) Albano Lake (Italy); (b) Tafjord (Norway); (d) Lake Tahoe (USA) (figure from Mazzanti and De Blasio, 2010). Horseshoe-shaped deposits are enclosed in dotted white ellipses. The EV landslide deposit shares this morphologic characteristic, suggesting it may have a similar emplacement mechanism.

following subaerial initiation, the EV landslide was emplaced into a subaqueous environment, lubricating the base and facilitating long runout.

4.4.4 Modification

The observations made in this work lead to the interpretation that after the landslide was originally emplaced, the landslide surface was modified by stream deposits, which flowed down the mountain slope and produced the braided stream network along the incised Riedel and Riedel prime shears (**Fig. 4.18**). Wind gaps observed around the landslide toe edge, some of which are partially in-filled (**Fig. 4.5D**), are evidence of active fluvial modification on the top surface of the landslide, indicating a longitudinal water flow direction. The large topographic knob on the landslide surface is additional evidence of fluvial incision, formed as the braided stream system created ridges and islands of high topography as a result of cut banks. Kinematic GPS data analyses sustain this hypothesis at centimeter-scale accuracy (**Fig. 4.7**). Talus sediment eroded off the top of the landslide surface by this fluvial activity accumulated northwest of the landslide as a result of the prevailing wind direction, forming Qal_ls.

Activity along a range-bounding normal fault is then interpreted to have caused rotation of the block on which the landslide deposit is situated, tilting the deposit back towards the Last Chance Range source (**Fig. 4.13**). This is evidenced in the longitudinal profile of the landslide (**Fig. 4.7B**). As the block was rotated back, lowering the head area of the landslide in elevation, it is likely that the surface fluvial system was shut off because the streams could not flow upslope to overtop the toe of the slide. Paleochannels (shaded blue in **Fig. 4.18)** and mid-channel bars (shaded grey in **Fig. 4.18**) were likely cut off by the erosional surface defining the hinge of downward tilting of the landslide. The playa deposits (shaded brown in **Fig. 4.18**) on the

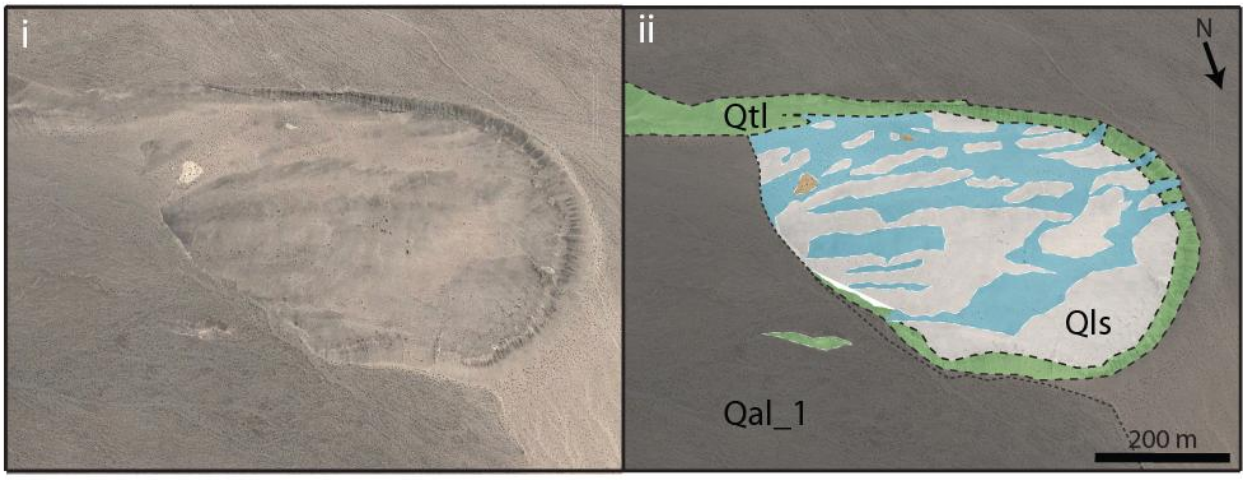

Figure 4.18. Modified landslide surface, with mapped braided stream network interpreted to be preserved following the shut-off of a surficial fluvial system as a result of rotation of the landslide block. Blue corresponds to paleochannels, gray shaded regions are mid-channel bars, and orange corresponds to playa deposits.

landslide surface were likely formed from ponding of recent rainwater as a result of the current tilt of the landslide.

Part of the landslide deposit was subsequently eroded and separated from the rest of the landslide deposit body, and was transported downstream where it was deposited on top of a previously emplaced unit of basaltic alluvial fan deposits (**Fig. 4.19**). This displaced mass likely followed the path of a large, recent drainage down the regional slope to be deposited as unit Qlsb in its current location west of and near to the toe of the landslide. The recent drainage may have been diverted since the deposition of Qlsb, but it indicates the process and rough direction that the paleostream would have taken to deposit Qlsb. It is evident that the basalt field predates the movement of the landslide body downstream, because as the stream carried the material down, it cut the observed sand bank in the basalt field. Down the channel, the stream crossed over and mixed with the basalt field that was already emplaced, depositing Qlsb. The increase in clast size upstream is consistent with the notion that as the landslide material moved downstream, it was broken up into the smaller clast sizes observed in Qlsb. This unit is thicker than the sandy deposit just northwest of the landslide and is raised many meters off the floor of the valley because it is composed of both the older basalt unit as well as the landslide deposit on top. The limestone and basalt composition of Qlsb is also consistent with the limestone being deposited from the eroded landslide, as well as the basalt originating from source rock in the cliff. The valley resulting from this incomplete resurfacing was subsequently filled with erosive alluvium (Qal_1), producing a buttress unconformity.

Within the subaqueous emplacement model, some tilting of the landslide deposit would have originally occurred as a result of flip-back of the rim due to frontal lifting and drag during emplacement. The fluvial features observed on the surface are interpreted to have formed

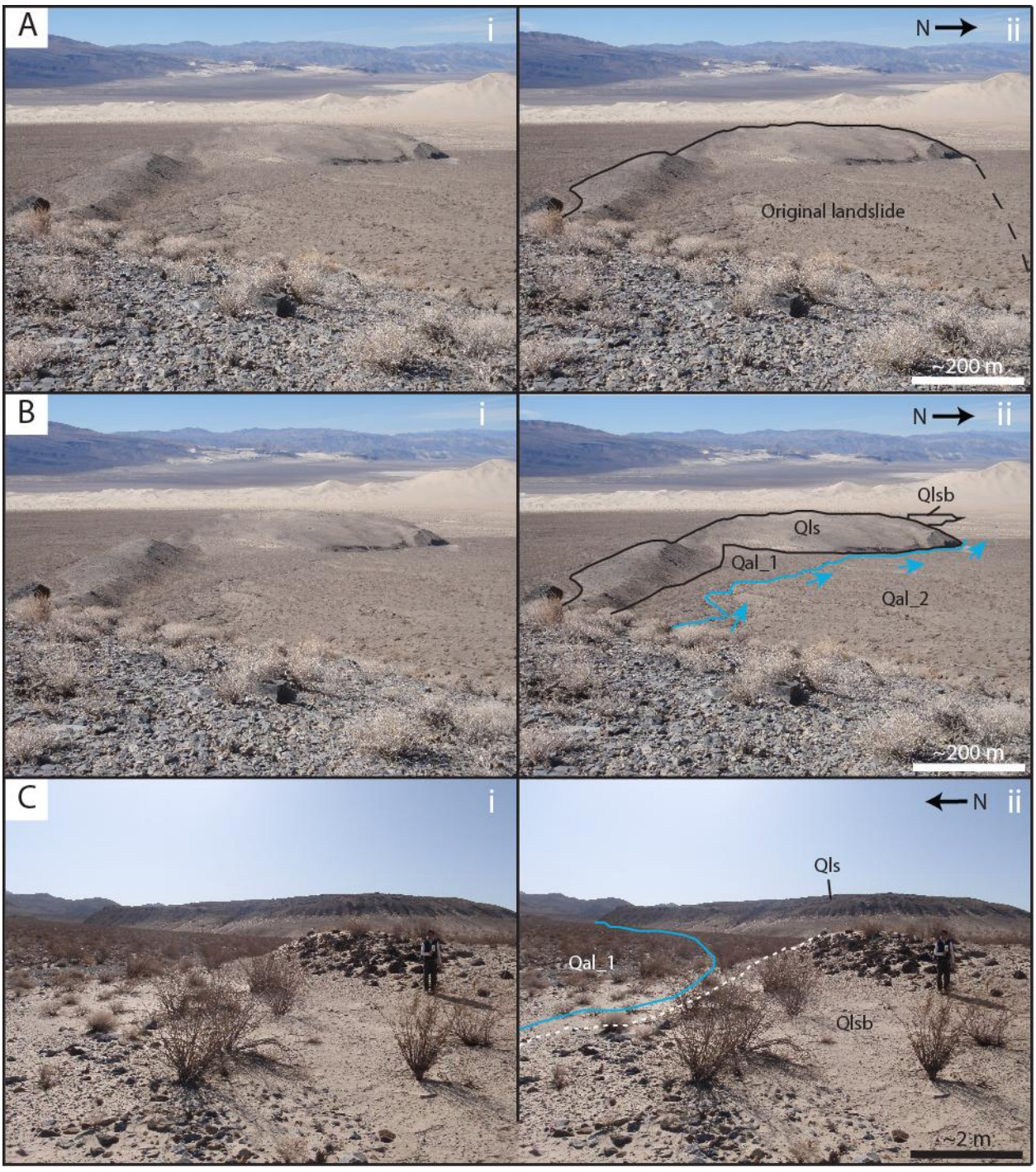

Figure 4.19. (A) Field photograph with interpreted original extent of landslide deposit on the valley floor. (B) Current extent of the landslide deposit, showing a recent drainage indicative of the rough transport path of the eroded section of the landslide. (C) Unit Qlsb northwest of the landslide toe, where the displaced mass is interpreted to have been deposited on top of a preexisting basalt field.

following the desiccation of the lake as a result of regional climate cycles. Subsequent rotation of the landslide block and the resulting shut-off of surficial fluvial activity are interpreted to have then formed the observed N-S erosional surface, playa deposits, and wind gaps. Stretching of the landslide toe may have resulted from higher frontal velocities due to front lubrication by a water layer, which could have led to segmentation and partitioning of the landslide mass (De Blasio et al., 2006; Locat and Lee, 2002) and contributed to the displacement of the portion of the landslide interpreted to have been deposited downstream as Qlsb.

4.4.5 Age

The sample ages determined in this work are interpreted to provide a minimum age of emplacement of the EV landslide. Qal_ls is interpreted to have formed through the deposition of talus material eroded off the top of the landslide during post-emplacement fluvial modification of the deposit, represented by Qlsmb marble clasts in the unit, and the deposition of alluvial material originating from the source cliff during a separate landsliding event, represented by fragmented basalt in the unit. The sand in the unit was likely deposited by continuous, prevalent aeolian activity in the valley (as most notably indicated by the Eureka Dunes). Stratigraphic relationships require that the two sand units from which the samples were derived must have been deposited before and after the marble gravel unit, respectively. The Qlsmb gravel unit is interpreted to have been deposited prior to tilting of the EV landslide block, at which point fluvial activity was shut off and water could not have overtopped the landslide toe in order to deposit the talus material. Aeolian transport of the cm-scale clasts is unlikely. In this way, though the amount of time between landslide emplacement and the shut off of surficial fluvial activity is unknown, stratigraphic relationships and dating of the upper sand sample produces the early to

mid Holocene as a reasonable minimum age for EV landslide emplacement and a maximum age for post-emplacement rotation of the landslide deposit (**Fig. 4.20A**).

This minimum emplacement age provides a constraint on EV landslide initiation and emplacement mechanisms. It is consistent with timing of dated regional normal faulting (e.g., Bacon et al., 2005), corroborating the notion proposed in this work that EV landslide initiation was fault-controlled.

In addition, this early to mid Holocene minimum emplacement age supports the subaqueous model for EV landslide emplacement. Within this model, landslide emplacement would have occurred earlier than in the subaerial model, because sufficient time after its emplacement would be required to dry out the lake prior to tilting and fluvial modification in order to form the fluvial features observed on the surface of the deposit (**Fig. 4.20B**). Regardless of the lack of constraint on the duration of desiccation, the presence of ephemeral lakes in Eureka Valley into the Holocene is temporally consistent with the subaqueous emplacement of the EV landslide in the early Holocene at minimum. In this way, the subaqueous model for EV landslide emplacement implies cooler, wetter climatic conditions within Eureka Valley in the Quaternary.

4.5 Conclusions

Integrated field, photogeologic, spectral, and dating investigation of the geomorphology of the extremely well-preserved EV landslide deposit has permitted constraint of its origin, emplacement, and modification processes. It is a translational landslide, characterized by the preservation of the original stratigraphy, sourced in the Upper Cambrian strata of the Last Chance Range, and initiated as a result of fault-generated fracture. It was most likely transported

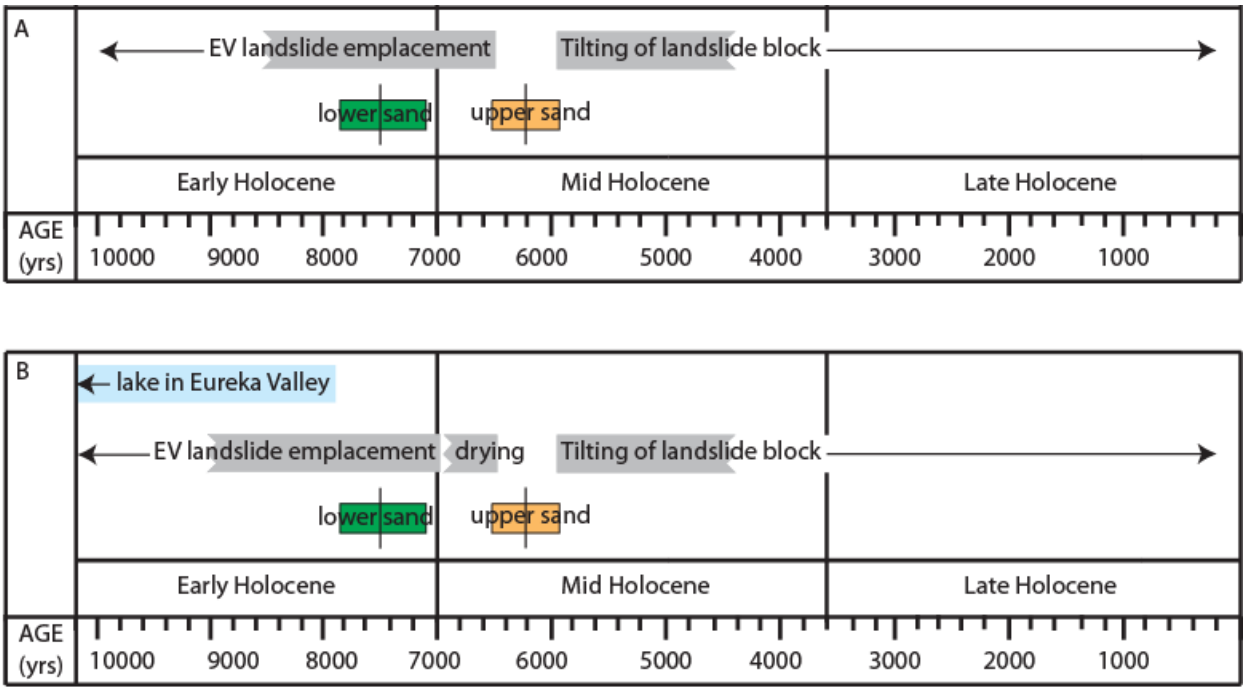

Figure 4.20. (A) Summary timeline of events related to EV landslide emplacement, based on unit ages and field interpretations within the self-lubrication model. The early to mid Holocene age of the upper sand sample constrains a minimum age for EV landslide emplacement and a maximum age for post-emplacement rotation of the landslide deposit. (B) Summary timeline of events related to EV landslide emplacement, based on environmental context within the valley, unit ages, and field interpretations within a subaqueous emplacement model.

by lubrication of the fluidized landslide mass through the presence of basal clays, though subaqueous emplacement is also tenable, and it experienced intense 3-D simple shear internal deformation during transport. Following emplacement, the EV landslide was subjected to fluvial modification and rotation of the landslide deposit. Determination of the age of the EV landslide has provided a minimum emplacement age and a maximum age of post-emplacement rotation of mid to early Holocene.

This detailed geomorphological characterization of features related to long-distance transport may be applied to other long-runout landslides with similar morphologies, including those on other planetary surfaces, providing continued insight not only into the evolution of Earth's surface, but the geologic history of other planetary bodies as well. In addition, a long-debated question in landslide dynamics is the potential involvement of water as a mechanism of long-distance transport of long-runout landslides. The interpretation that EV landslide transport does not require the participation of intergranular fluid implies that long-runout landslide deposits on other planetary surfaces also do not necessitate the presence of water or other fluids for emplacement and may instead be the result of granular flow, though subaqueous emplacement of the EV landslide would have implications for cooler, wetter Quaternary climatic conditions within Eureka Valley.

4.6 References

Bacon, S.N., Jayko, A.S., J.P. McGeehin (2005), Holocene and latest Pleistocene oblique dextral faulting on the southern Inyo Mountains fault, Owens Lake Basin, California, *Bulletin of the Seismological Society of America, 95*, 2472-2485.

Blanc, R.P. and G.B. Cleveland (1961), Pleistocene lakes of southeastern California, Mineral Information Services, Division of Mines, State of California, 14.

Byerlee, J. (1978), Friction of rocks, *Pure and Applied Geophysics, 116*, 615–626.

Collins, G.S. and H.J. Melosh (2003), Acoustic fluidization and the extraordinary mobility of Sturzstroms, *J. Geophys. Res., 108*, 2473.

Corbett, K.P. (1989), Structural geology of the Last Chance thrust system, east-central California [Ph.D. thesis], Los Angeles, University of California, 245 p.

Cruden, D.M. and D.J. Varnes (1996), Landslide types and processes, In A.K. Turner and R.L. Schuster (eds.), Landslides: Investigation and Mitigation, pp. 26-75, Special Report 247, National Academy Press, Washington, D.C.

Davies, T.R. (1982), Spreading of rock avalanche debris by mechanical fluidization, *Rock Mechanics, 15*, 9-24.

Davies, T.R. and M.J. McSaveney (2009), The role of rock fragmentation in the motion of large landslides, *Engineering Geology, 109*, 67-79.

De Blasio et al. (2006), Understanding the high mobility of subaqueous debris flows, *Norwegian Journal of Geology, 86*, 275-284.

De Blasio, F.V., Engvik, L.E., Elverhøi, A. (2006), Sliding of outrunner blocks from submarine landslides, *Geophysical Research Letters, 33*, L06614.

Enzel et al. (1992), Short-duration Holocene lakes in the Mojave River drainage basin, Southern California, *Quaternary Research, 38*, 60-73.

Erismann, T.H. (1979), Mechanisms of large landslides, *Rock Mechanics, 12*, 15-46.

Heim, A. (1882), Der Bergsturz von Elm, 2, *Z. Dtsh. Geol. Ges., 34*, 74-115.

Hsu, K. J. (1975), Catastrophic debris streams (sturzstroms) generated by rockfalls, *Geological Society of America Bulletin, 86,* 129-140.

Hungr, O. (1995), A model for the runout analysis of rapid flow slides, debris flows, and Avalanches, *Can. Geotech. J., 32*, 610-623.

Hungr, O. and S.G. Evans (2004), Entrainment of debris in rock avalanches: An analysis of a long run-out mechanism, *Geol. Soc. Am. Bull., 116*, 1240–1252.

Hutchinson, J.N. (1986), A sliding-consolidation model for flow slides, *Can. Geotech. J., 23*, 115-126.

Johnson, B. (1978), Blackhawk landslide, California, USA, *Rockslides and avalanches, 1*, 481-504.

Keefer, D.K. (1984), Landslides caused by earthquakes, *Geological Society of America Bulletin, 95*, 406–421.

Knott et al. (2014), Late Neogene geology of the Last Chance Range: Implications for paleohydrology of the Death Valley area, eastern California (abs), Geological Society of America Annual Meeting, no. 149-2.

Kocurek, G. and N. Lancaster (1999), Aeolian system sediment state: theory and Mojave Desert Kelso dune field example, *Sedimentology, 46*, 505-515.

Locat, J. and H.J. Lee (2002), Submarine landslides: advances and challenges, *Can. Geotech. J., 39*, 193–212.

Lucchitta, B. K. (1978), A large landslide on Mars, *Geological Society of America Bulletin, 89*, 1601-1609.

Lustig, L.K. (1965), Clastic sedimentation in Deep Springs Valley California, Geological Survey Professional Paper 352-F, In Erosion and Sedimentation in a Semiarid Environment, 131-192.

Mazzanti, P. and F. V. De Blasio (2010), Peculiar morphologies of subaqueous landslide deposits and their relationship to flow dynamics, In D.C. Mosher et al. (eds.), Submarine Mass Movements and Their Consequences, Advances in Natural and Technological Hazards Research, 28, 141-151, Springer Netherlands.

McSaveney, M. J. (1978), Sherman Glacier rock avalanche, Alaska, USA, In Voight, B. (ed.), Rockslides and Avalanches 1, Dev. Geotech. Eng., 14A, S. 197-258.

Melosh, H. J. (1979), Acoustic fluidization: A new geologic process?, *Journal of Geophysical Research Letters, 84*, 7513-7520.

Melosh, H.J. (1987), The mechanics of large rock avalanches, *Reviews in Engineering Geology, 7*, 41-50.

Miller, W.J. (1928), Geology of Deep Spring Valley, California, *The Journal of Geology, 36*, 510-525.

Mohrig et al. (1998), Hydroplaning of subaqueous debris flows, *Geological Society of America Bulletin, 110*, 387–394.

Rhodes, E. J. (2011), Optically stimulated luminescence dating of sediments over the past 200,000 years, *Annual Review of Earth and Planetary Sciences, 39*, 461-488.

Saffer, D.M. and C. Marone (2003), Comparison of smectite-and illite-rich gouge frictional properties: application to the updip limit of the seismogenic zone along subduction megathrusts, *Earth Planet. Sci. Lett., 215*, 219-235.

Shreve, R. L. (1959), Geology and mechanics of the Blackhawk landslide, Lucerne Valley,

California, Ph.D. Thesis, Calif. Inst. Tech., Pasadena, California.

Shreve, R. L. (1966), Sherman landslide, Alaska, *Science, 154*, 1639-1643.

Shreve, R.L. (1968), Leakage and Fluidization in Air-Layer Lubricated Avalanches, *Geological Society of America Bulletin, 79*, 653-658.

Singer, K.N., McKinnon, W.B., Schenk, P.M., Moore, J.M. (2012), Massive ice avalanches on Iapetus mobilized by friction reduction during flash heating, *Nature Geoscience, 5*, 574-578.

Stoffer, P. (2004), Changing climates and ancient lakes, In Desert Landforms and Surface Processes in the Mojave National Preserve and Vicinity: Open-File Report 2004-1007, U.S. Geological Survey, U.S. Department of the Interior.

Sylvester, A.G. (1988), Strike-slip faults, *Geological Society of America Bulletin, 100*, 1666-1703.

Watkins, J., Ehlmann, B., Yin, A. (2015), Long-runout landslides and the long-lasting effects of early water activity on Mars, *Geology, 43*, 107-110.

Wintle, A. G. (1997), Luminescence dating: laboratory procedures and protocols, *Radiation Measurements, 27*, 769-817.

Wrucke, C.T. and K.P. Corbett (1990), Geologic map of the Last Chance quadrangle, California and Nevada: U.S. Geological Survey Open-File Report OF-90-6470A, scale 1:62,500.

Yin, A. and Taylor, M.H. (2011), Mechanics of V-shaped conjugate strike-slip faults and the corresponding continuum mode of continental deformation, *Geological Society of America Bulletin, 123*, 1798-1821.

CHAPTER 5

Structurally controlled subsurface fluid flow as a mechanism for the formation of recurring slope lineae

5.1 Introduction

Ongoing monitoring of high-resolution images of the present-day surface of Mars has permitted identification and consistent observation of the activity of recurring slope lineae (RSL). RSL are seasonal, narrow (0.5 to 5 m), low albedo features up to a few hundred meters in length that originate at the base of cliff-forming bedrock outcrops and extend downward on steep (25° to 40°), equator- and west-facing, mid-latitude and equatorial rocky slopes of Mars (**Fig. 5.1**) (McEwen et al., 2011; McEwen et al., 2014). They exhibit progressive growth in the downslope direction during warm seasons, anastomosing around topographic obstacles, and fade during cold seasons, implying a temperature dependence (**Fig. 5.2**) (McEwen et al., 2011; 2014; Ojha et al., 2014). The geologic environments associated with slopes containing RSL are diverse, yet all appear to be sites marked by significant geological activity, including "fresh" impact craters, active mass wasting sites, massifs, spurs and ridges (Chojnacki et al., 2014; Ojha et al., 2014; McEwen et al., 2011).

The mechanisms of RSL formation have been highly debated since their discovery in 2011. Formation has been largely attributed to the seepage and downslope transport of water-based liquid through permeable regolith near the surface. Seepage of this liquid is interpreted to wet and thus darken the RSL surface, and evaporate once seasonal flow ceases (e.g., McEwen et al., 2011; Chevrier and Rivera-Valentin, 2012; Levy, 2012). While pure water has been invoked (Stillman et al., 2014; Grimm et al., 2014), it is highly unstable in present-day Mars surface

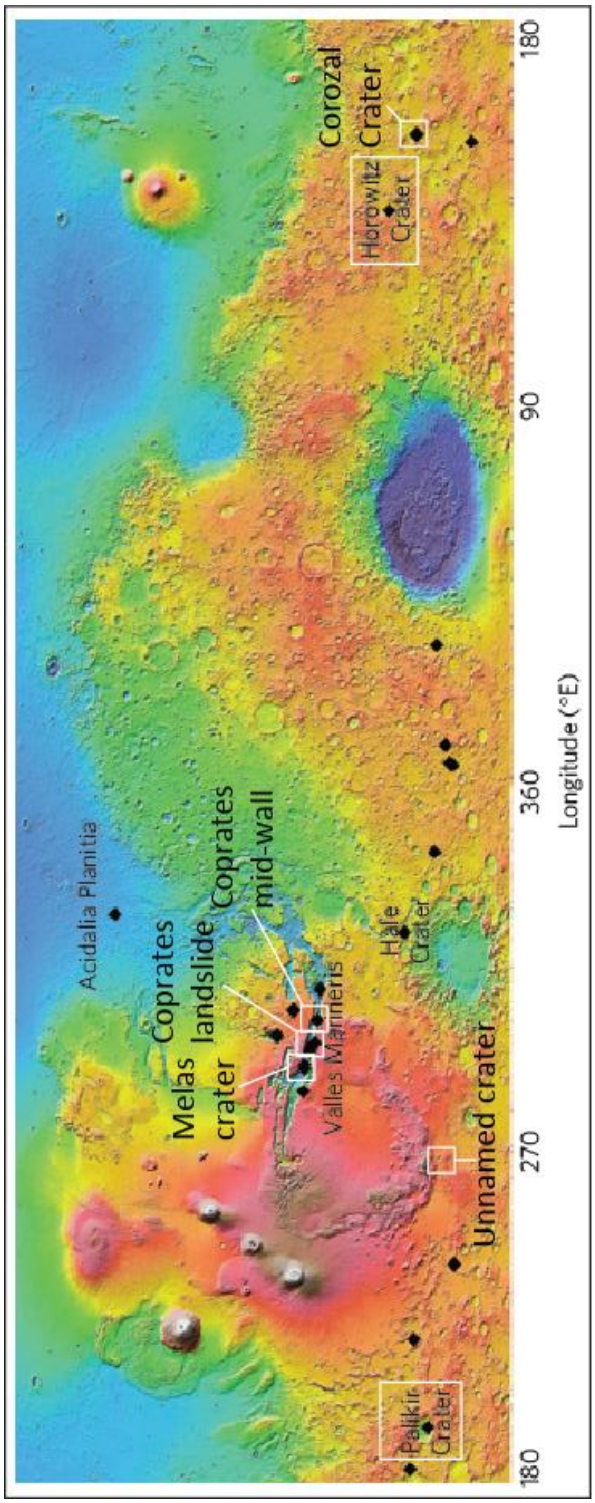

Figure 5.1. Global distribution of confirmed recurring slope lineae (RSL) sites (black diamonds) on MOLA altimetry (modified from McEwen et al., 2014). Locations of study areas are also shown (white boxes).

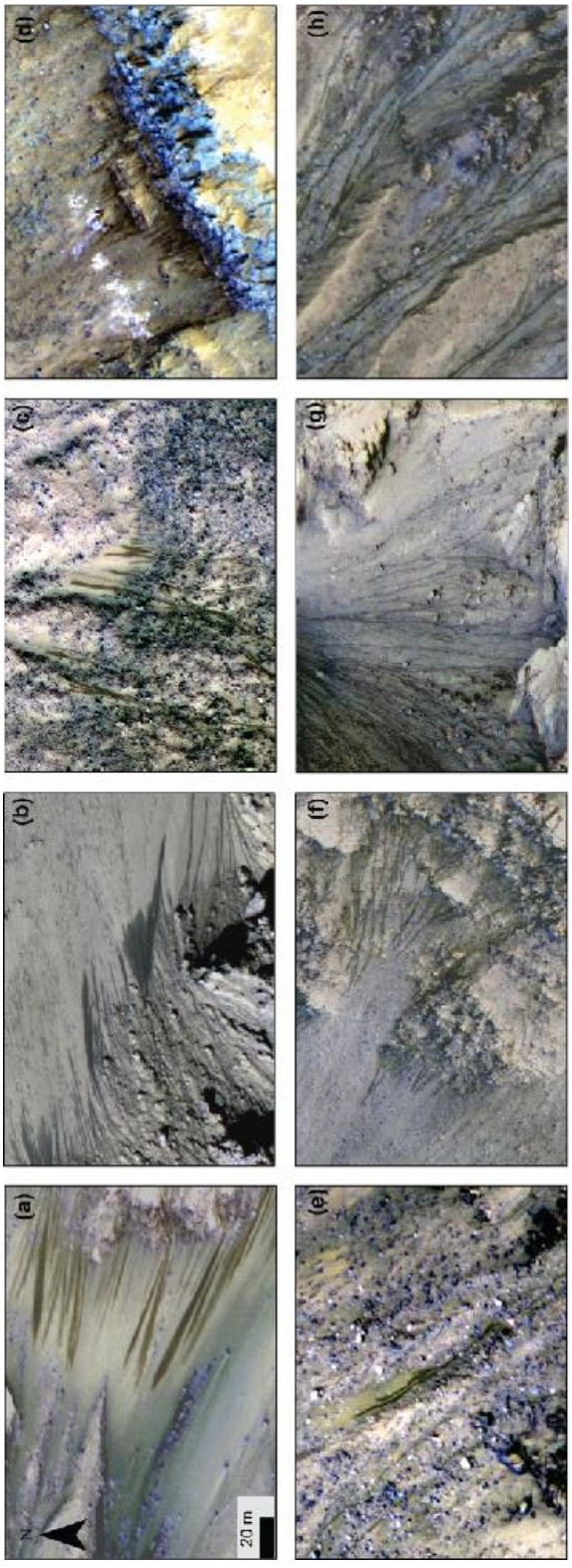

Figure 5.2. HiRISE images displaying characteristic morphology of RSL features, including their narrow width, low albedo, meter-scale length, and diversion around topographic obstacles downslope (downhill direction is along the elongated path of RSL): (a) ESP_022689_1380, (b) PSP_005787_1475, (c) ESP_013835_1330, (d) PSP_006261_1410, (e) ESP_014288_1315, (f) PSP_005524_1470, (g) PSP_005646_1360, (h) ESP_022973_1335. Images have been manually stretched (figure from Ojha et al., 2014).

conditions. Salt can significantly lower the freezing temperature and evaporation rates, increasing the stability of salt-bearing (briny) water (Chevrier and Rivera-Valentin, 2012). However, the source of the putative water, and an active recharge mechanism to maintain this source over even short geological timescales, are not currently understood (McEwen et al., 2014; Ojha et al., 2014; Chevrier and Rivera-Valentin, 2012). Current hypotheses for the source of the putative liquid include surface absorption of atmospheric water vapor by hygroscopic salts (deliquescence) (Chevrier and Rivera-Valentin, 2010; Grimm et al., 2014), near-surface groundwater or thawed regional ice layers that create sufficient hydraulic head to initiate and maintain fluid flow to the surface (McEwen et al., 2014; McEwen et al., 2011), and deeper subsurface brines (McEwen et al., 2014) and freshwater flows (Stillman et al., 2014). In contrast, dry mass wasting formation mechanisms have also been explored, whereby granular flow of low albedo materials triggered by seasonally high winds or dust devils darkens the slope surface. However, the dry models do not adequately explain the incremental growth aspect of these features, nor their latitude-dependence (McEwen et al., 2011).

The existing efforts in constraining RSL formation mechanism(s) are limited by the lack of detailed characterization of the geologic settings of RSL source regions. Thus, key questions such as whether RSL source regions in varying geologic contexts share distinguishing characteristics and whether RSL formation is controlled by discontinuities in the source rock remain uncertain. Here, we address this issue by conducting detailed geologic mapping of spatial relationships between RSL source regions and their surrounding regions using high-resolution HiRISE (High Resolution Science Imaging Experiment) images obtained by MRO (Mars Reconnaissance Orbiter) (McEwen et al., 2007) in combination with topographic data from the Mars Orbiter Laser Altimeter (MOLA) on the MGS spacecraft (Zuber et al., 1992).

Understanding of the geologic context for RSL source regions will enable constraint on RSL formation mechanisms and provide insight into the hydrological cycle and the potential presence of habitable conditions on the present-day Martian surface.

5.2 Data and methods

5.2.1 Data

HiRISE acquires very high resolution (up to 25 cm/pixel) imagery, useful in analyzing very detailed structural and morphologic relationships and features (McEwen et al., 2007). Orthorectified HiRISE images were utilized for photogeologic mapping to facilitate co-alignment with high resolution digital terrain models (DTMs) created from HiRISE stereo pairs and MOLA elevation data (**Table 5.1**)**.** HiRISE orthoimages with a grid spacing of 0.25 m, 0.5 m, 1.0 m, or 2.0 m, denoted by convention with an A, B, or C, respectively, in the product name following the source observation ID, were selected for investigation within this study in order to adequately resolve small-scale RSL-related features. The HiRISE Reduced Data Record (RDR) images of two locations, Corozal crater and the unnamed crater, were used instead of the orthoimage because distortions in the DTM prevented co-alignment. Images ~6 m/pixel in resolution from the context camera (CTX) (Malin et al., 2007) also onboard MRO were also examined for analysis of regional context.

5.2.2 Mapping methods

Continued survey and monitoring of HiRISE images has led to a total of 13 fully confirmed RSL sites in the southern mid-latitudes, 1 in a northern mid-latitude, and 12 in the

Site	HiRISE image number	DTM image number
Coprates mid-wall	ESP_029318_1650_RED_A_01_ORTHO	DTEEC_025441_1650_027973_1650_A01
Coprates landslide scarp	ESP_020879_1670_RED_B_01_ORTHO	DTEED_020879_1670_021657_1670_A01
Palikir crater	ESP_022689_1380_RED_A_01_ORTHO	DTEEC_005943_1380_011428_1380_A01
Horowitz crater	PSP_005787_1475_RED_A_01_ORTHO	DTEEC_021689_1475_020832_1475_A01
Corozal crater	PSP_006261_1410_RED	
Melas crater	ESP_031059_1685_RED_A_01_ORTHO	DTEEC_027802_1685_028501_1685_A01
Unnamed crater	ESP_023016_1345_RED	

Table 5.1. HiRISE and DTM image numbers by site analyzed in this chapter.

tropics, including several in Valles Marineris (McEwen et al., 2014; Ojha et al., 2014). A confirmed site is defined as one in which RSL are observed to grow incrementally during a warm season, fade or completely disappear in colder seasons, and recur in multiple Mars years (Ojha et al., 2014). Of these, six sites were selected for this study, representing each of the geologic environments found to be conducive to RSL formation: Palikir crater and Corozal crater (southern mid-latitude craters), Horowitz crater (central uplift crater), Melas Chasma crater (equatorial crater on canyon floor), Coprates Chasma landslide scarp (equatorial landslide within canyon), and Coprates Chasma mid-wall (equatorial canyon wall). Multiple HiRISE observations have been made at each of these locations over the course of monitoring of RSL activity. Images taken during a season in which RSL were observed to be the most active were selected for analysis. One site which exhibits favorable conditions for RSL formation (e.g., southern mid-latitude location, equator-facing slopes within a crater), but in which RSL are not observed, was also selected (unnamed crater).

HiRISE orthoimages were selected and run through a spatial information rectification application (courtesy Hare, USGS) before detailed mapping of RSL and their spatial relationships with surrounding geologic features was completed directly on HiRISE orthoimages in an ArcGIS framework. In order to minimize bias, RSL features were mapped separately from geologic context and then were overlain together on the orthoimage. The orthoimages were overlain on the high resolution DTMs in a 3-D ArcScene framework for 3-D perspective.

Geologic mapping at three sites, Palikir crater, Corozal crater, and the unnamed crater, included identification of RSL source regions, the geologic units comprising the surface slope, and structural discontinuities, including faults, fractures, and joints. The contextual geologic settings of Horowitz crater and the Coprates landslide scarp were also mapped, including

geologic units and structural features. At Horowitz crater, the Melas Chasma crater, the Coprates mid-wall, and the Coprates landslide scarp sites, mapping focused on the identification of RSL source regions and fractures. Systematic, double-blind quantification and characterization of correlation and intersecting relationships between RSL source regions and mapped fractures was completed at each of the RSL sites.

Geologic units were defined and characterized based on variable textures observed in the orthoimage. Fractures were identified by terrestrial morphological expressions, including truncation and offset of marker beds, sub-parallel linear features and risers bounding rocky outcrops, drainage path convergence at fracture traces, sharp ridge crests with steep collapse slopes, and triangular facets (**Fig. 5.3**). Most structural discontinuities identified in this study are classified as joints based on their observed displacement to length ratio; definitive faults with resolvable displacement are few (Okubo and McEwen, 2007). DTMs were utilized in order to rotate the topography and observe the fracture planes in the along-strike direction, in order to establish a sense of offset, orientation, and dip direction. Observed fractures were assigned a classification based on type and level of confidence. To increase the viability of the results, only fractures within the "identity and existence (reasonably) certain", and "location accurate" or "location approximate" classifications were mapped and included in the study. RSL source regions were defined as the approximate location of where the feature begins to resolve on the slope, though the features may actually source from higher up and be obscured by overlying bedrock (**Fig. 5.4**). In order to quantify the correlation between RSL source regions and fractures in each location, buffer zones were defined surrounding the outlines of the source regions at distances that reasonably bracket the width of the damage zone (~10% of fracture length (Faulkner and Rutter, 2001)), characterized by increased permeability (Caine et al., 1996), and

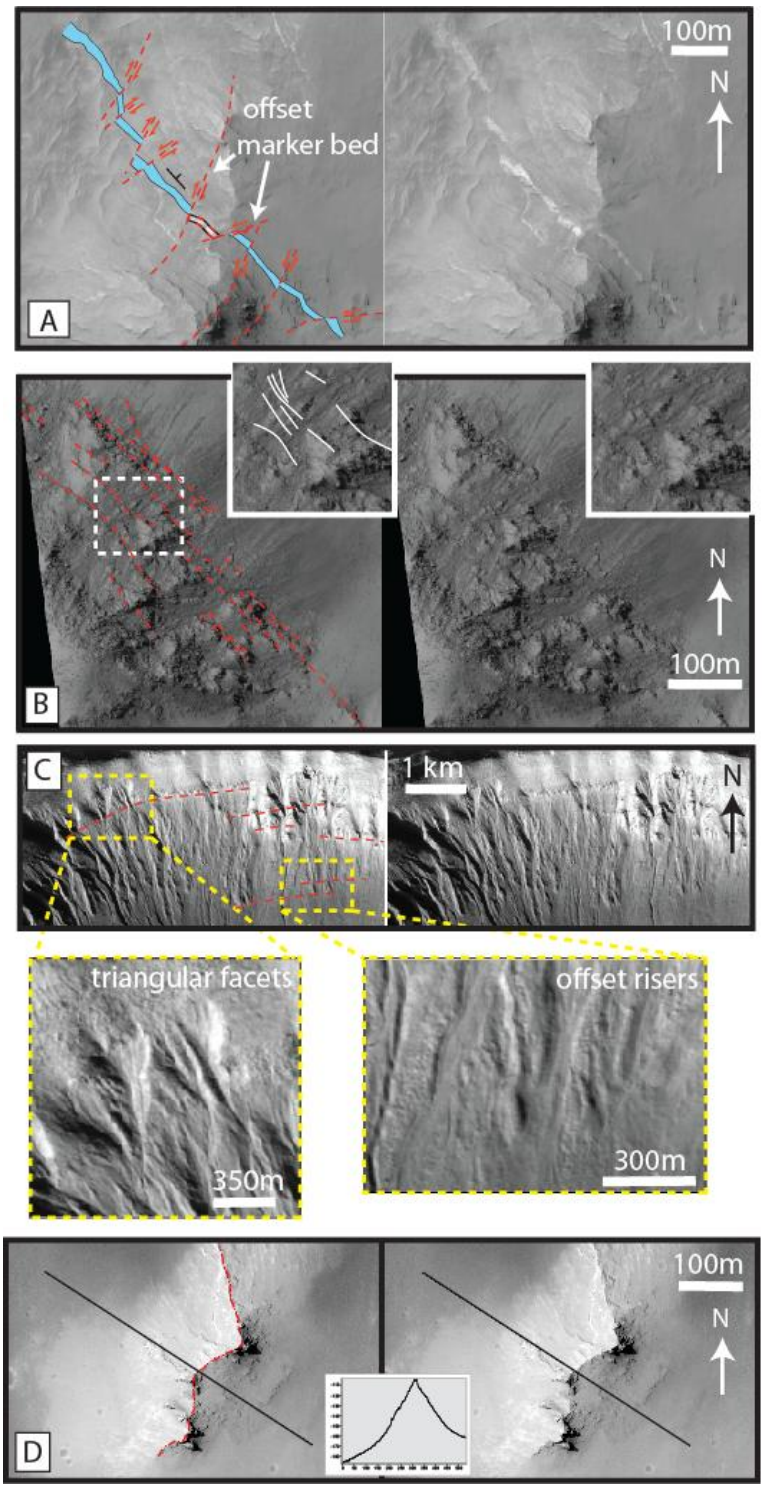

Figure 5.3. Examples of fracture morphological expressions used for identification, including (A) truncation and offset of marker beds, (B) sub-parallel linear features bounding rocky outcrops (Horowitz crater- HiRISE image PSP_005787_1475), (C) triangular facets and offset risers (Palikir crater- CTX image B18_016808_1378_XI_42S157W), and (D) sharp ridge crests with steep collapse slopes (Horowitz crater- PSP_005787_1475).

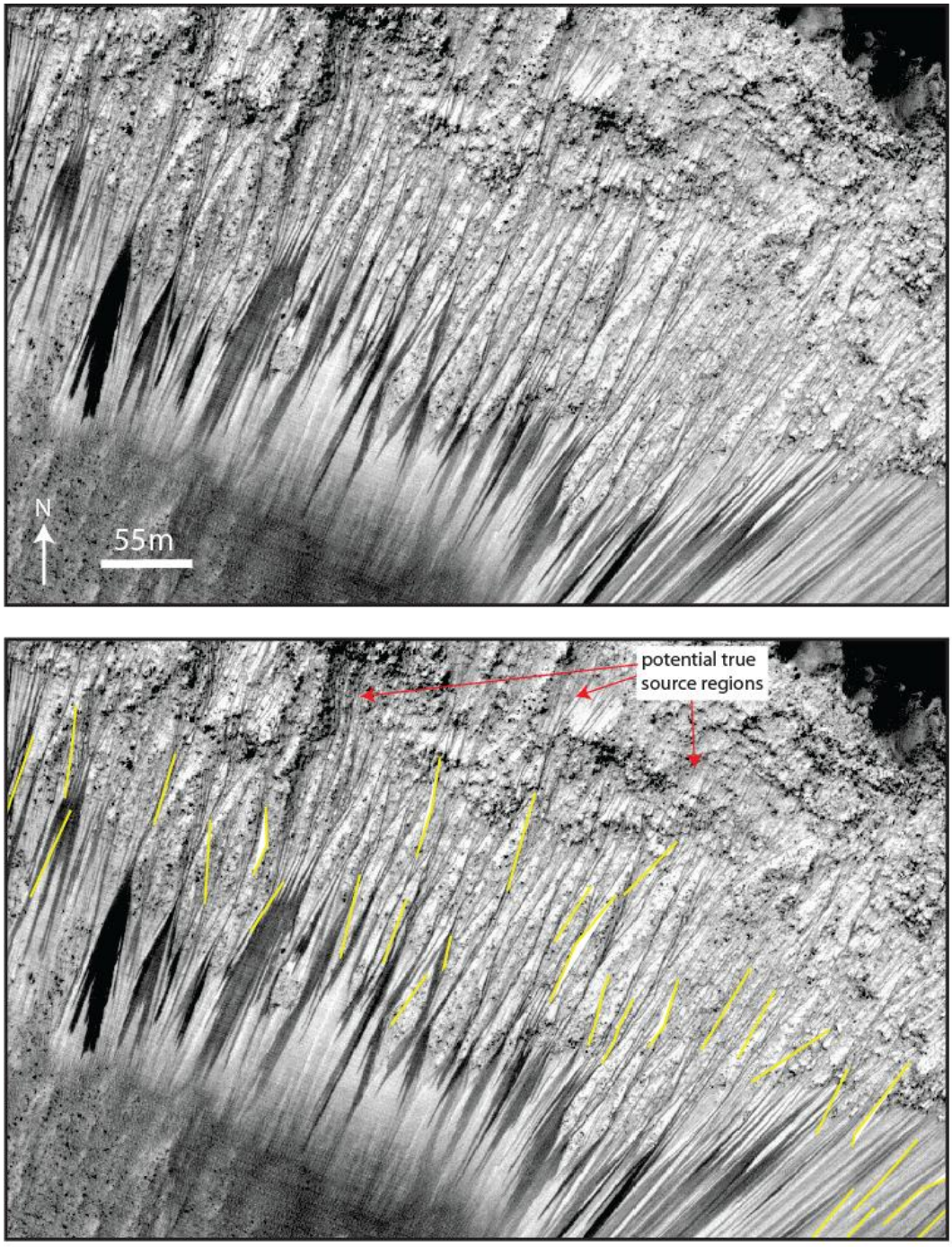

Figure 5.4. Example of RSL source regions within the bedrock as defined in this study (yellow), though the features may actually source from higher up in the bedrock (Melas Chasma crater-HiRISE image ESP_031059_1685). Image has been manually stretched.

account for observational error in source region identification. The percentage of buffer zones intersected by a fault was then calculated at each site. Fundamental GIS operations, including slope, slope aspect, and solar radiation calculation, were then performed with the ArcGIS geoprocessing toolbox on the orthoimages of the Coprates landslide and Coprates mid-wall sites, with mapped features overlain on the maps to investigate whether any correlations exist.

5.3 Results

In order to constrain the distinguishing characteristics of RSL source regions, the RSL-bearing slopes of Palikir and Corozal craters were mapped in detail. In both locations, RSL exhibit a common association with a highly-incised rocky unit (dark blue in **Figs. 5.5A and 5.5B**). A prevalence of fractures in series is observed in these layers in confirmed RSL geologic settings in both southern mid-latitude and equatorial sites (red in **Figs. 5.5A and 5.5B**). RSL are also associated with mass wasting features in several investigated locations, including in Palikir and Corozal craters (**Figs. 5.5A and 5.5B**), a large slump in the Melas Chasma crater, and several slump deposits along the Coprates landslide scarp. The unnamed crater location with no RSL, despite favorable conditions for formation, exhibits a distinct lack of fractures, only observed in a single layer, and an absence of the highly incised rocky unit (**Fig. 5.5C**). While this lack of observable faulting could be the result of a lack of exposure of features on the surface, as faulting would be expected to occur during the impact process, it represents an end-member scenario which a formation mechanism must also explain.

Across all the RSL sites examined, a distinct, reproducible spatial correlation is observed between RSL source regions and fault-related morphology indicative of multiple styles of brittle deformation, including strike-slip, normal, and fractures (**Fig. 5.6**). Of the 92 total RSL mapped

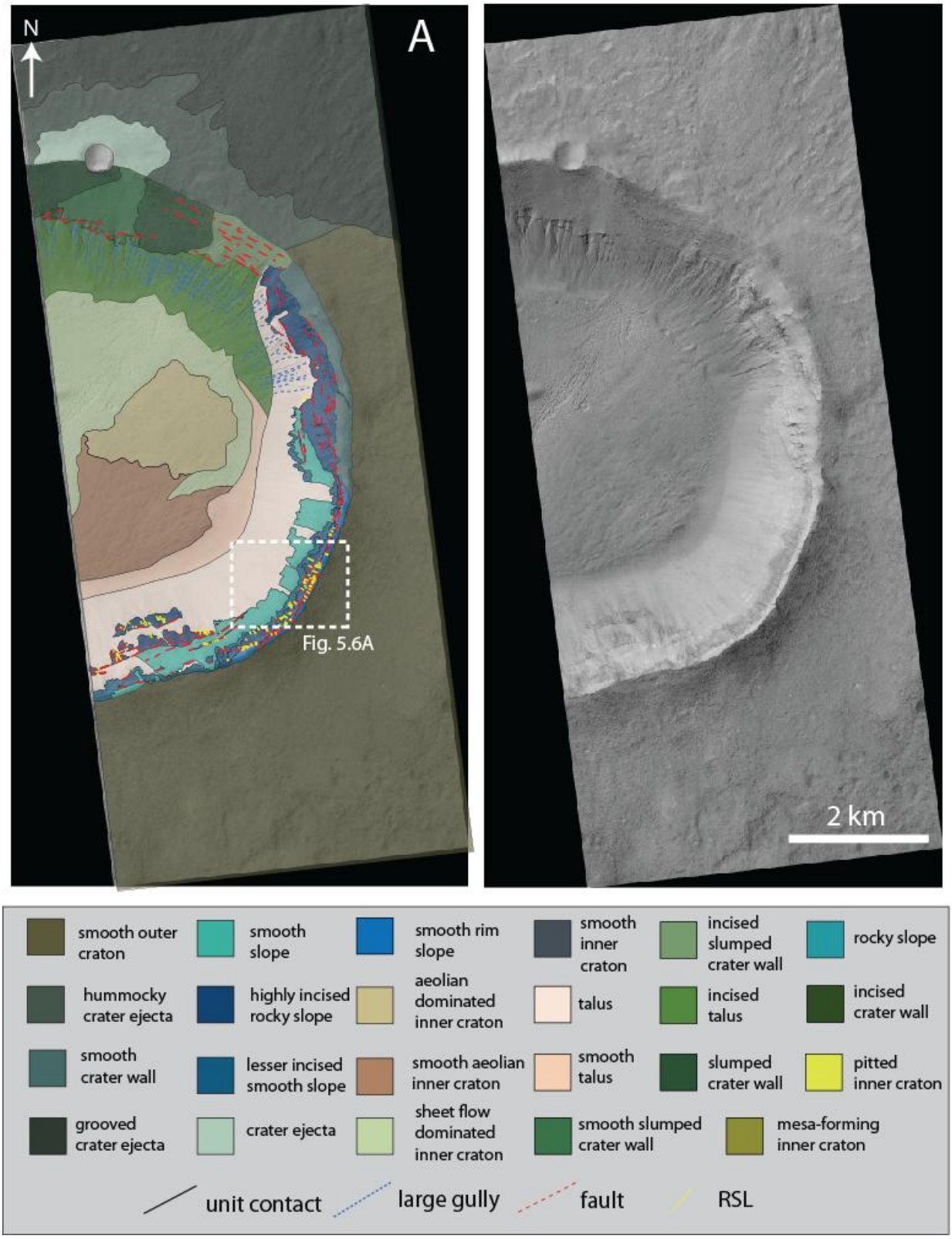

Figure 5.5. (A) Geologic map of Corozal crater RSL site, with the location of Fig. 5.6A.

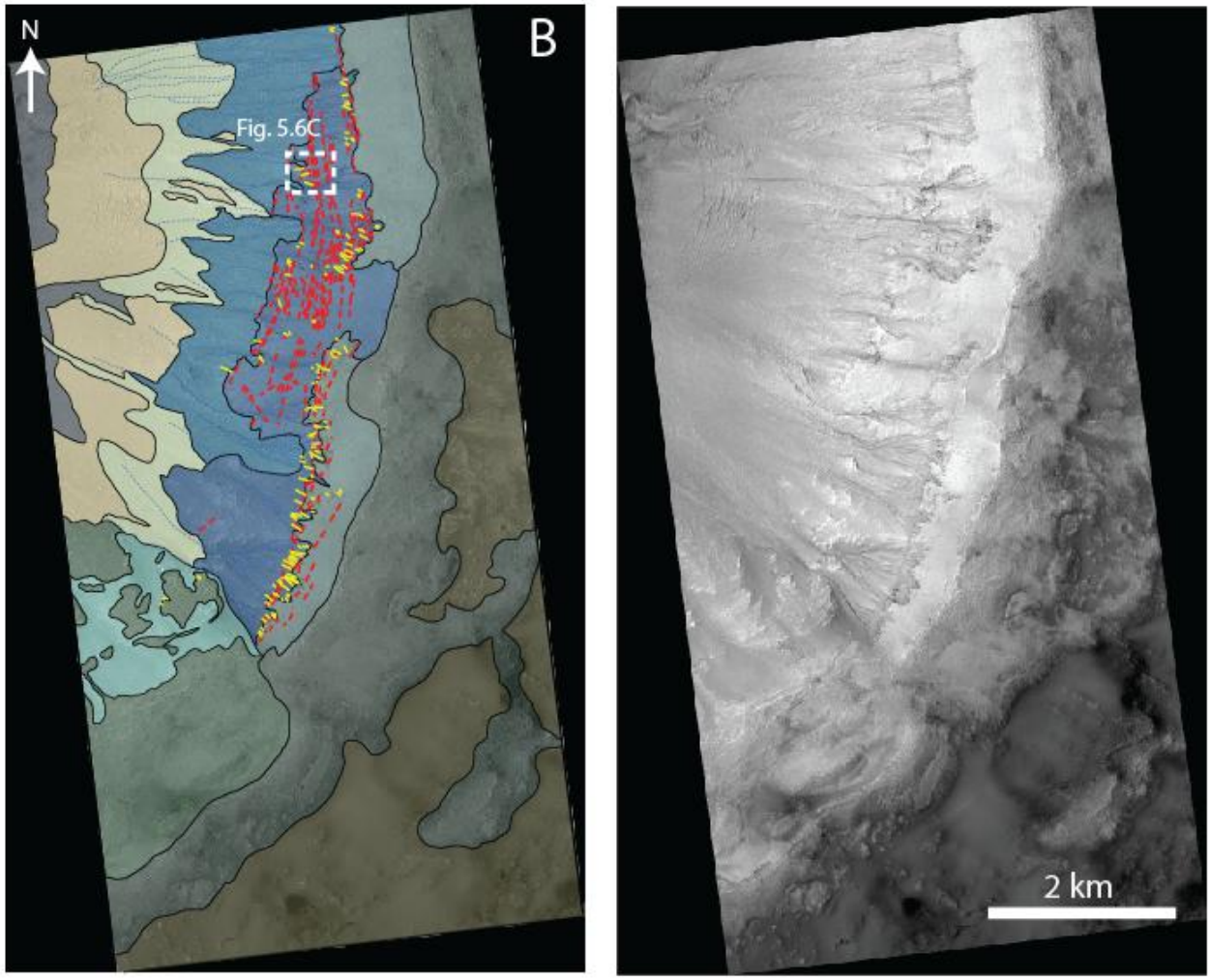

Figure 5.5, cont. (B) Geologic map of Palikir crater RSL site, with the location of Fig. 5.6C. Colors and units correspond to those mapped in A, defined in legend. Note the common association between the highly-incised rocky unit (dark blue), RSL source regions (yellow), and fractures (red). Mass wasting features are also present in each location.

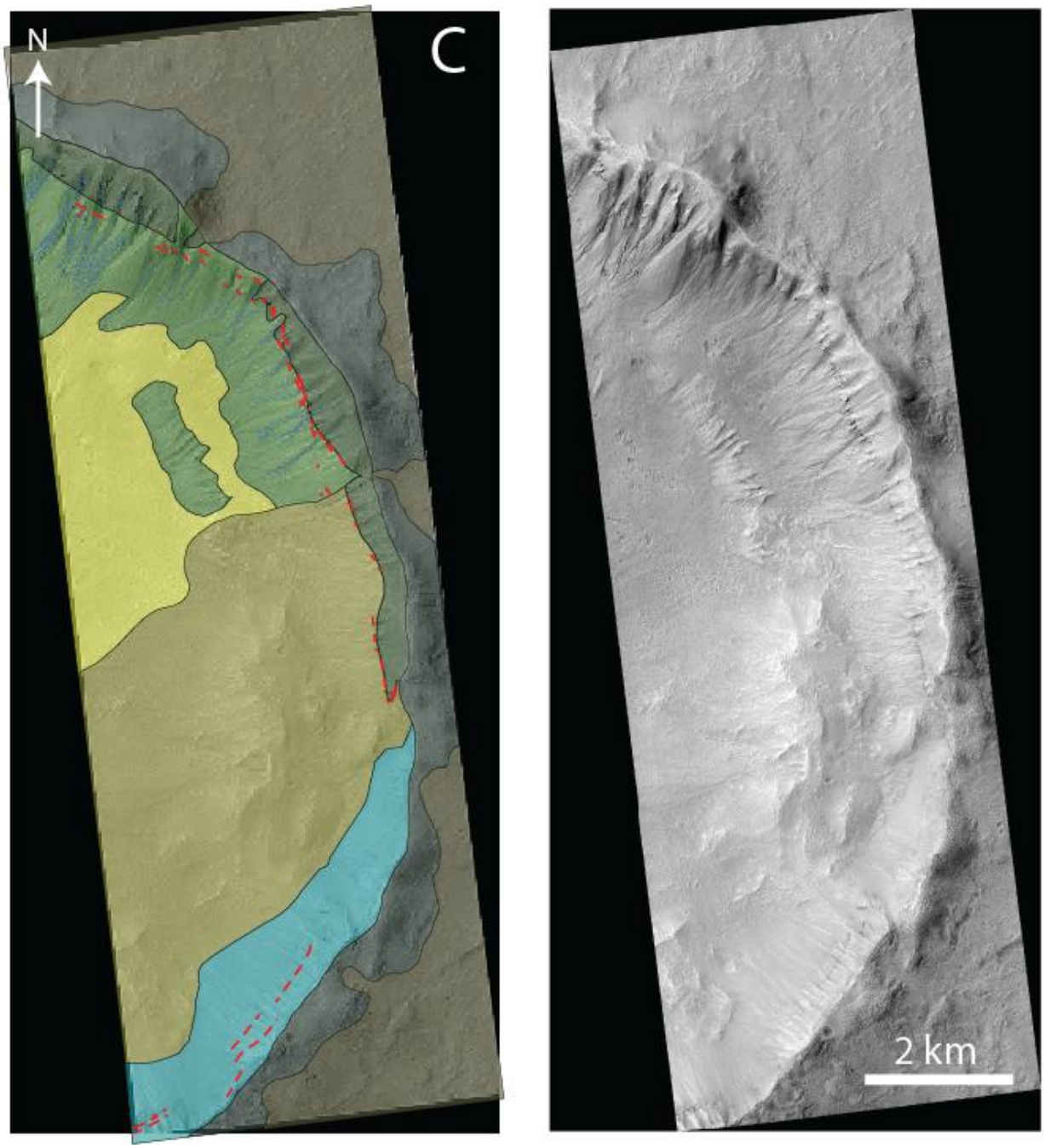

Figure 5.5, cont. (C) Geologic map of unnamed crater with no RSL. Colors and units correspond to those mapped in A. Note the paucity of fractures and the absence of the highly incised rocky unit.

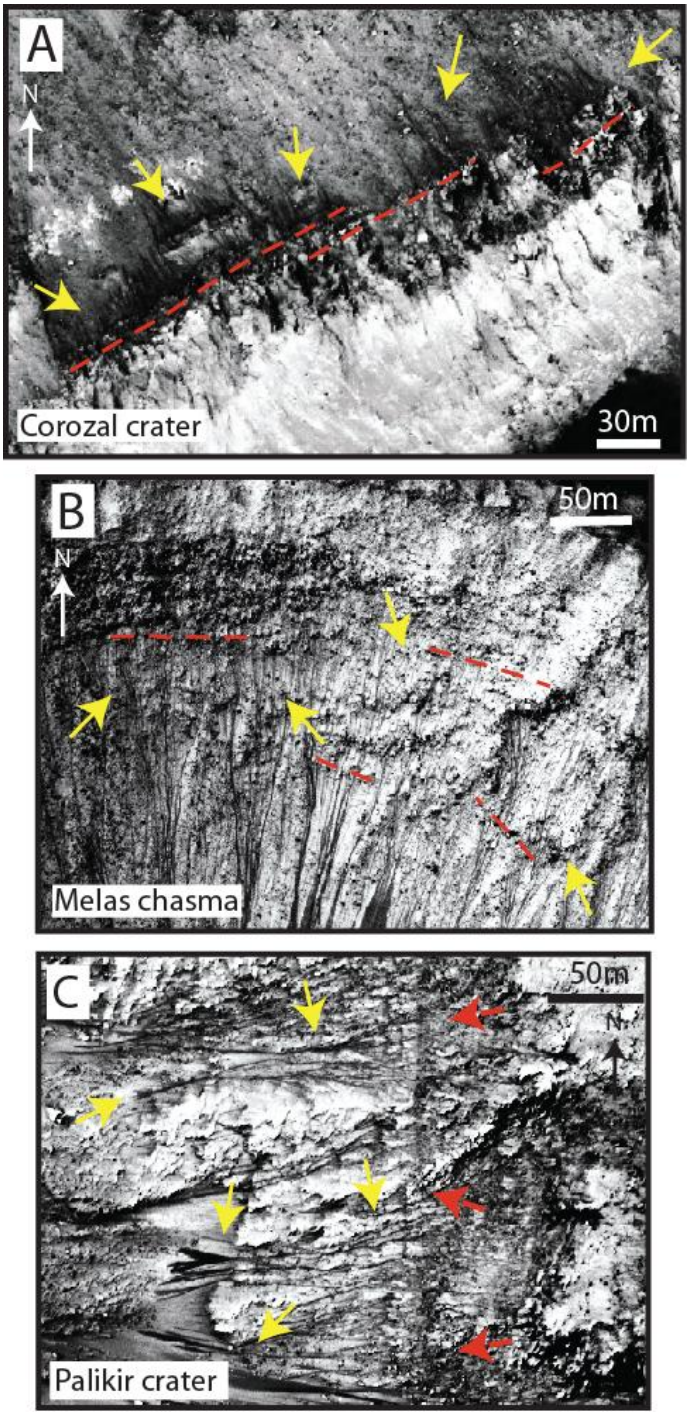

Figure 5.6. Stretched zoom-ins of example RSL source regions in (A) Corozal crater (HiRISE image PSP_006261_1410), (B) Melas Chasma crater (ESP_031059_1685), and (C) Palikir crater (ESP_022689_1380). Yellow arrows show RSL locations; red lines and arrows indicate spatially correlated fault traces. Images have been manually stretched.

in Palikir crater, 90% of buffer zones around RSL source regions intersect a fracture within 50 m (**Figs. 5.7A and 5.7B**). Of the 139 total RSL mapped in Corozal crater, 81% of RSL source regions are within 50 m of a fracture (**Fig. 5.7C**). Of the 1068 total RSL mapped in Horowitz crater, 78% of RSL source regions are within 100 m of a fracture (**Figs. 5.7D and 5.7E**). The thousands of RSL at this site are exhibited over numerous slopes, and the features are often not distinct, increasing the difficulty of pinpointing their exact origin. Because of this, this calculation involves more possible error than other sites we examined. Also, in order to understand which topographic features within the crater were likely expressions of an adjacent impact-induced fracture, a central uplift formation model based on analysis of analog Haughton crater in northern Canada by Osinski and Spray (2005) was extrapolated to frame that expected for this site (**Fig. 5.8**). Of the 49 total RSL mapped in Melas Chasma crater, 96% of RSL source regions are within 10 m of a fracture (**Figs. 5.7F and 5.7G**). Of the 43 total RSL mapped on the Coprates landslide scarp, 19% of RSL source regions are within 100 m of a distinct fracture (**Figs. 5.7H and 5.7I**). However, the entire breakaway scarp along which all the RSL in this location are found is fundamentally the exposed surface expression of a large normal fault. In addition, the prominent RSL average transport direction based on mapping of RSL stream order spatially correlates strongly to the (independently mapped) locations of more recent slump deposits with more fluidized morphology (As1(N)) (**Fig. 5.9**). Of the 207 total RSL mapped on the Coprates mid-wall, 89% of RSL source regions are within 100 m of a fracture (**Figs. 5.7J and 5.7K**). In this location, true source regions are often obscured by talus materials, increasing the error associated with this correlation. Each of these percentages represent a conservative minimum correlation, given that true RSL source regions compared to those mapped may often be higher up in the bedrock where faulting is most prevalent (see **Fig. 5.4**).

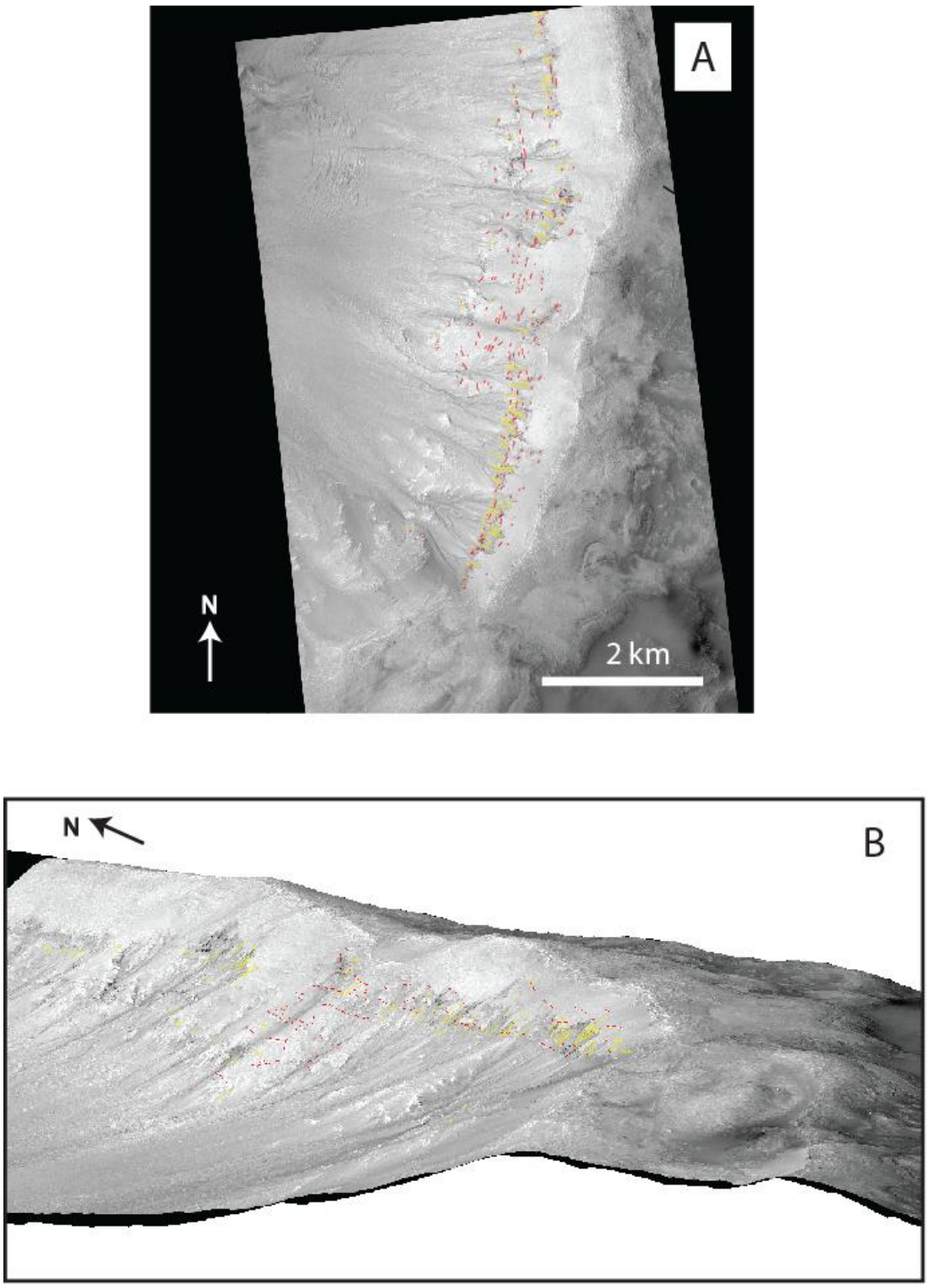

Figure 5.7. (A) Map of RSL source regions (yellow) and fractures (red) in Palikir crater. (B) 3-D rendering of Palikir crater map.

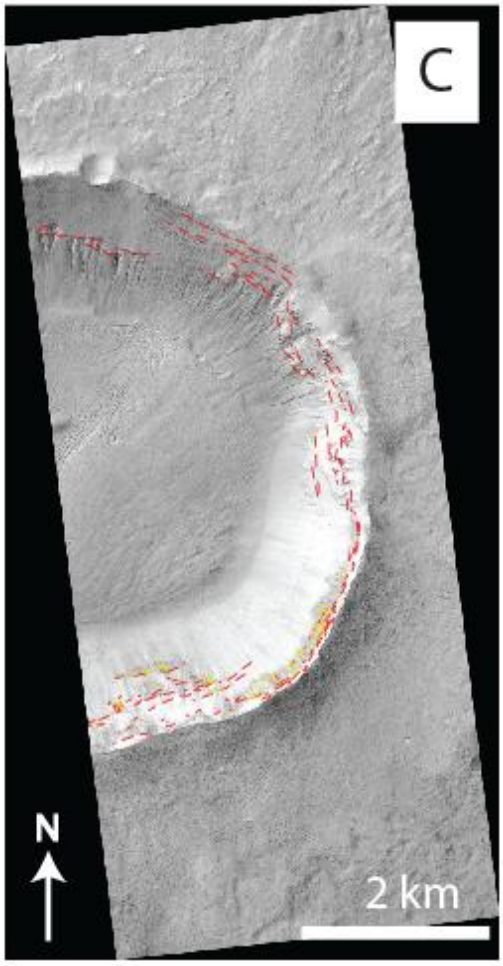

Figure 5.7, cont. (C) Map of RSL source regions and fractures in Corozal crater.

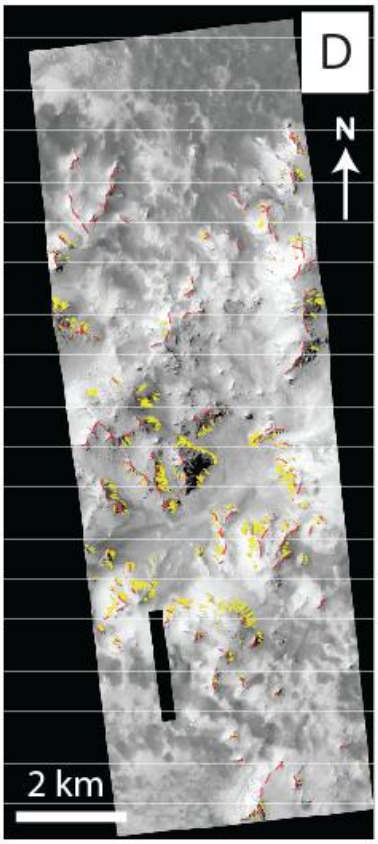

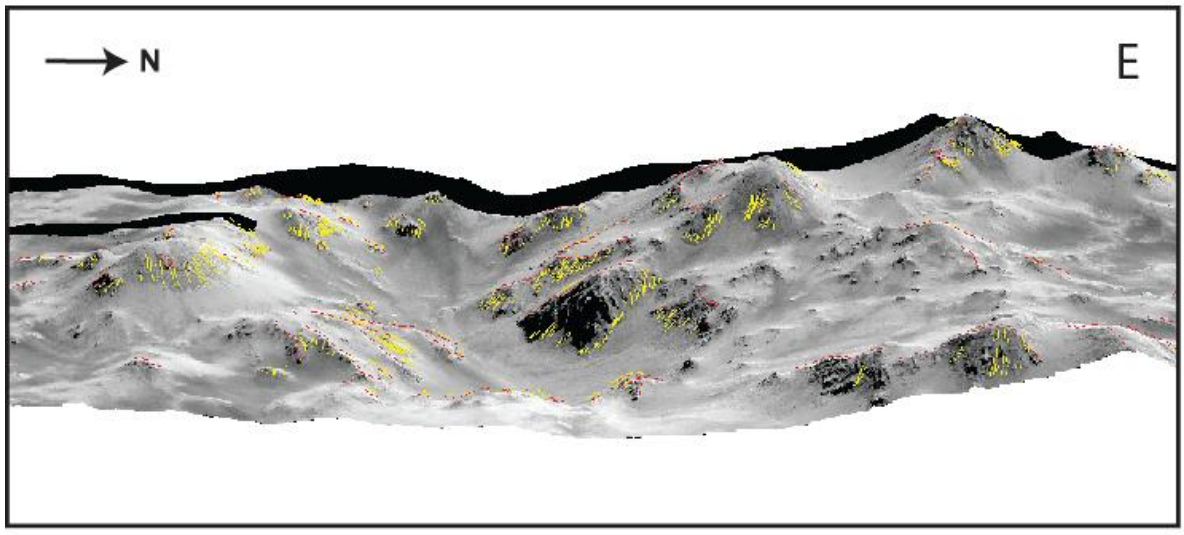

Figure 5.7, cont. (D) Map of RSL source regions and fractures in Horowitz crater. (E) 3-D rendering of Horowitz crater map.

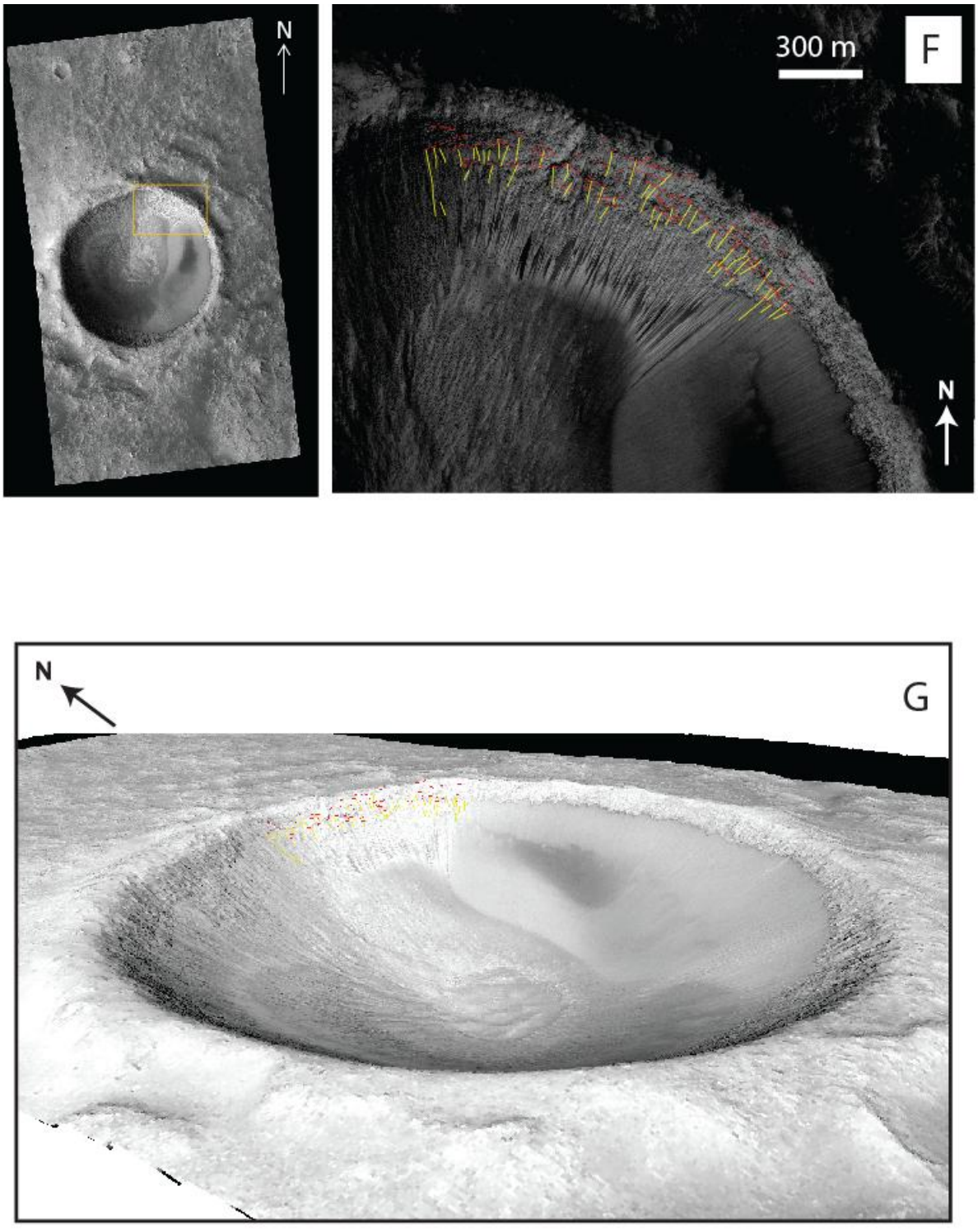

Figure 5.7, cont. (F) Map of RSL source regions and fractures in Melas Chasma crater; location within crater shown on left. (G) 3-D rendering of Melas Chasma crater map.

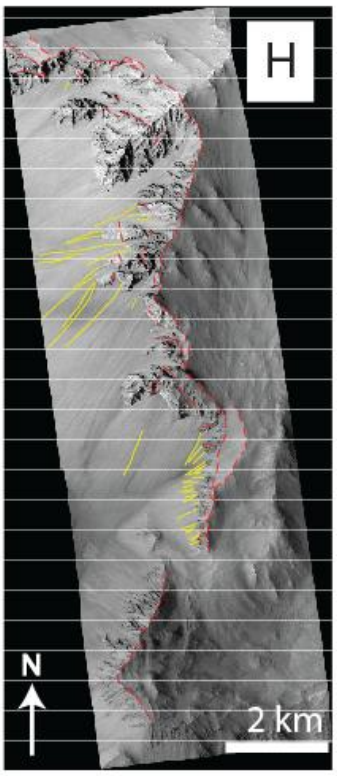

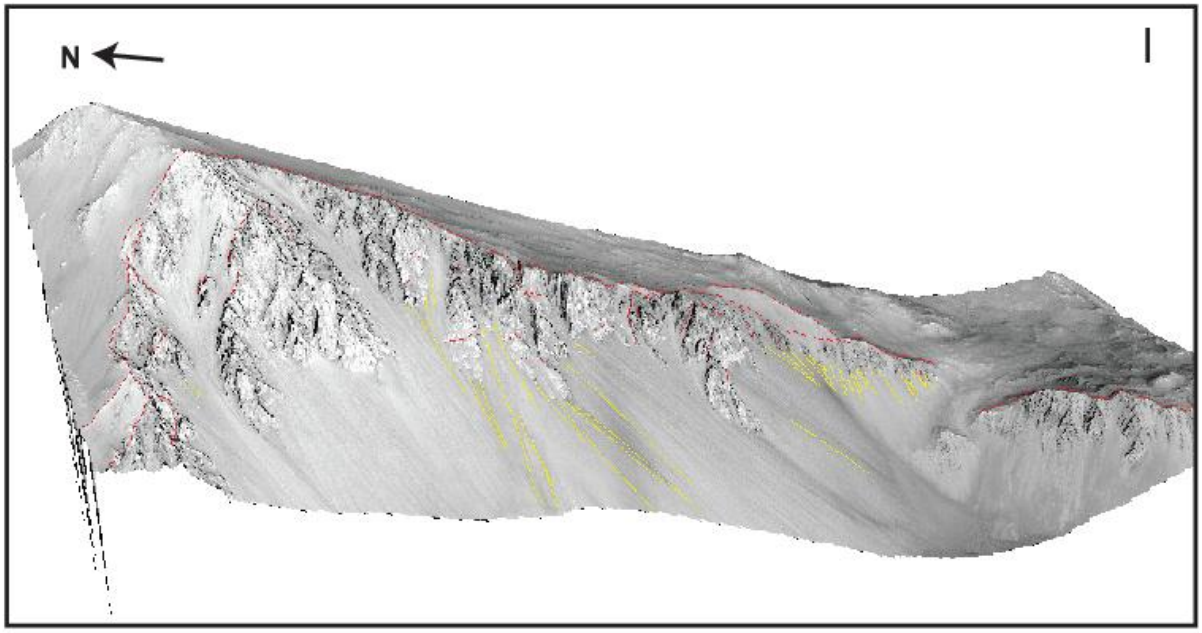

Figure 5.7, cont. (H) Map of RSL source regions and fractures on the Coprates landslide scarp. (I) 3-D rendering of Coprates landslide map. Note that the breakaway scarp along which all the RSL in this location are found is the surface expression of a large normal fault.

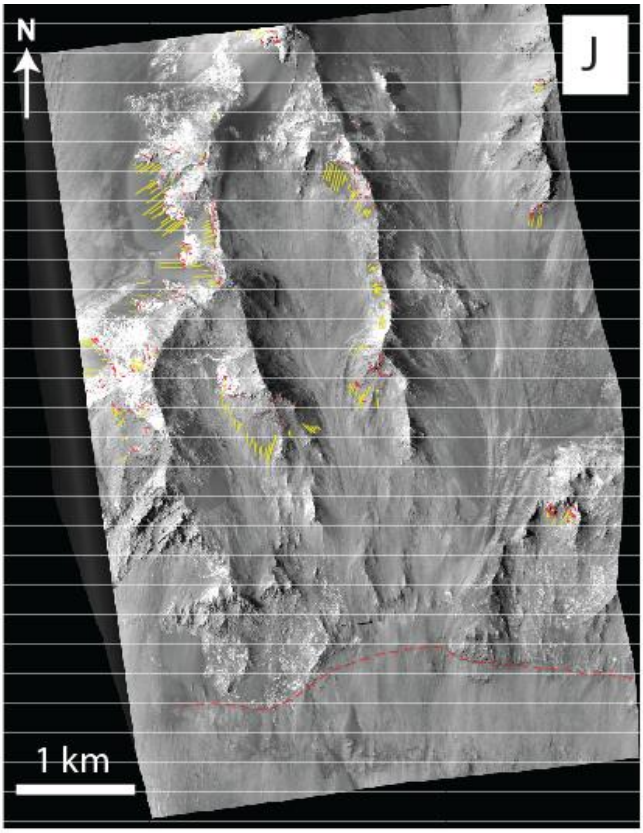

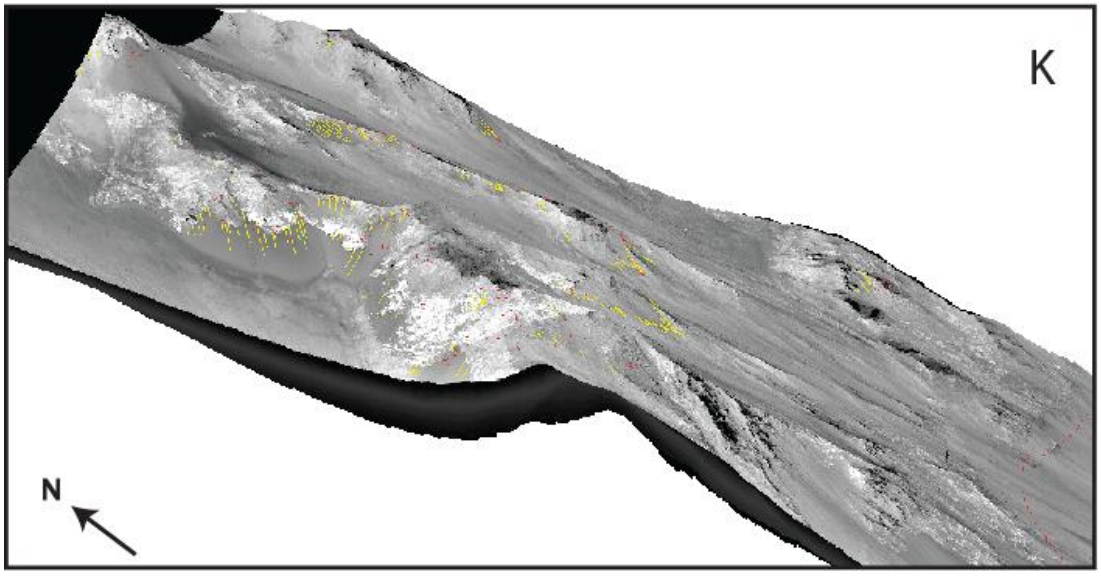

Figure 5.7, cont. (J) Map of RSL source regions and fractures on the Coprates mid-wall. (K) 3-D rendering of Coprates mid-wall map.

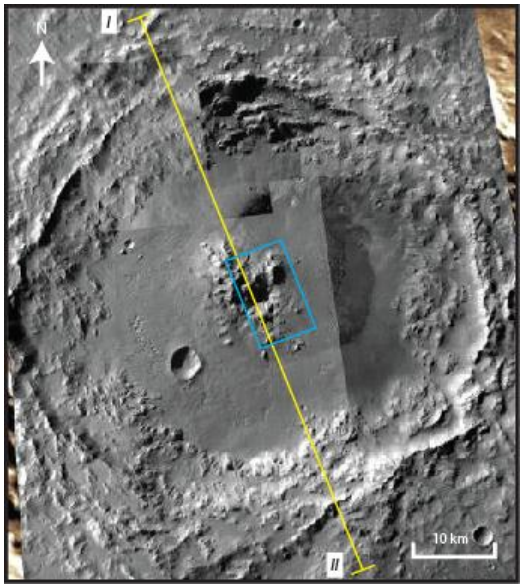

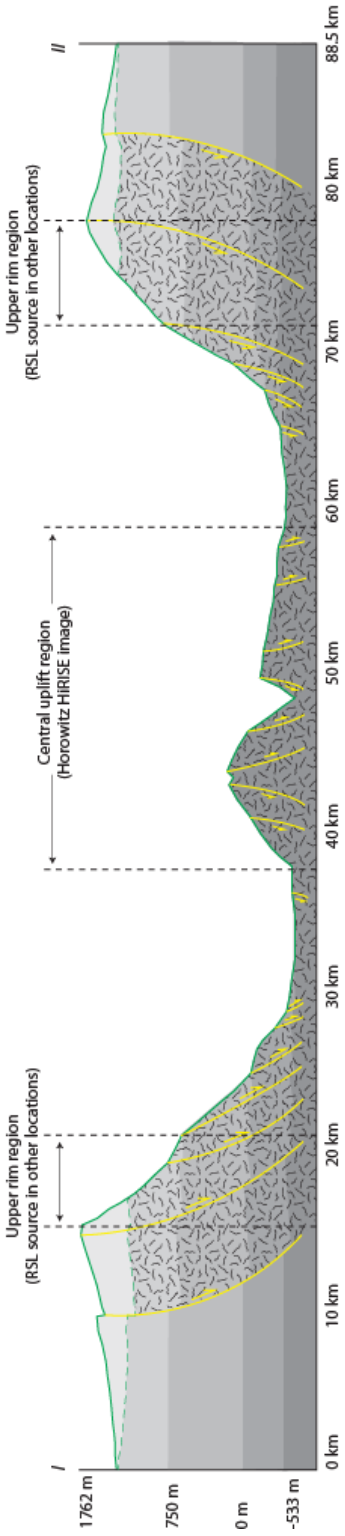

Figure 5.8. Central uplift formation model for Haughton crater (Canada) extrapolated to frame expected topographic expressions of fracture in Horowitz crater (cross section location shown left).

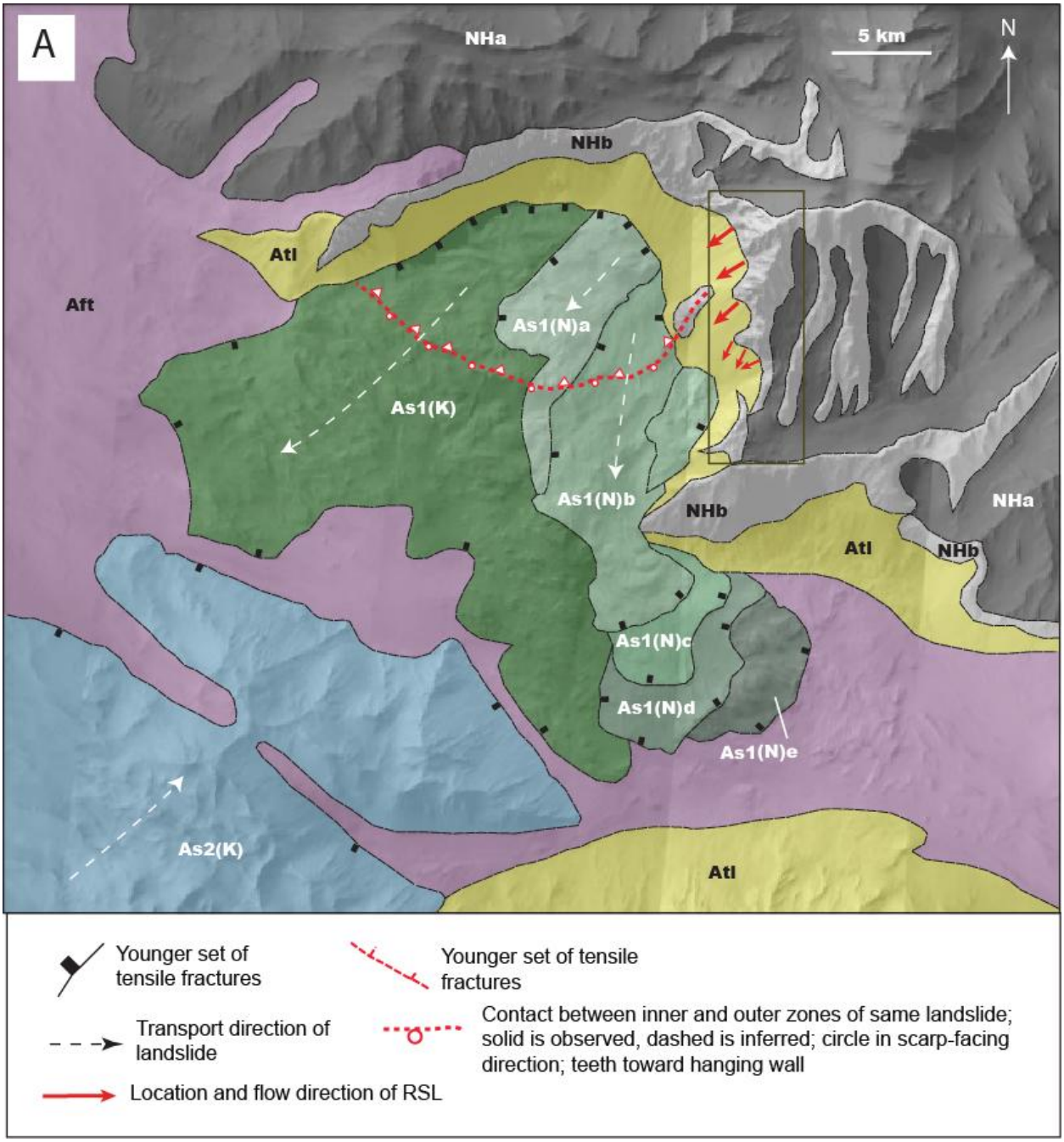

Figure 5.9. (A) Geologic context map of the Coprates landslide scarp, displaying deposits of several mass wasting events along the same slope and direction throughout the Amazonian, including the location of HiRISE image ESP_020879_1670 in B and in which RSL source regions and fractures were mapped in Figs. 5.7H and 5.7 I.

Figure 5.9, cont. Unmarked THEMIS mosaic mapped above.

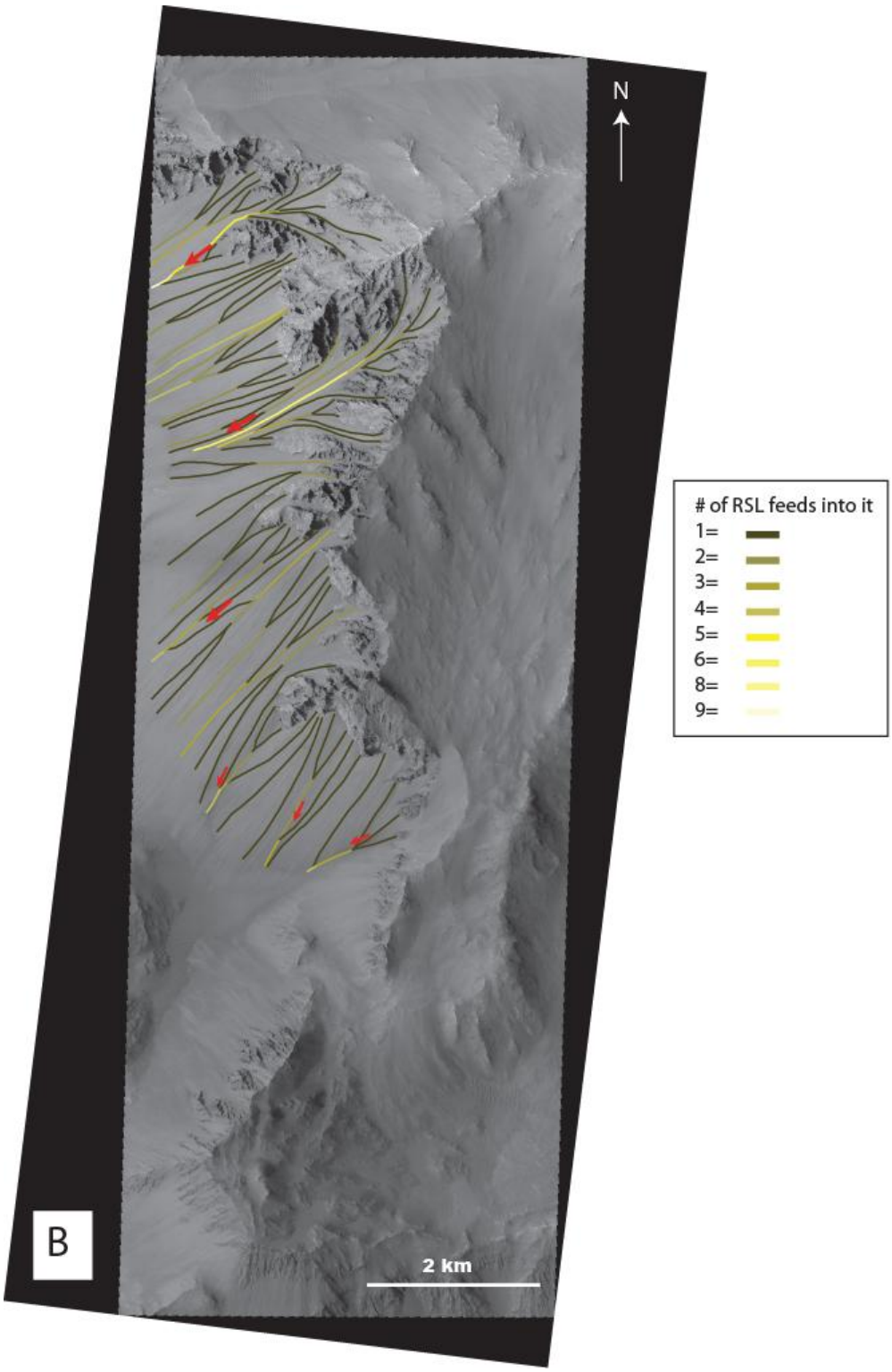

Figure 5.9, cont. (B) Interpreted combined average transport direction of RSL (red arrow) based on mapping of RSL stream order.

The slope maps of both the Coprates mid-wall and Coprates landslide sites, calculated with the ArcGIS geoprocessing toolbox, confirm that RSL are highly spatially correlated with very steep slopes (red regions in **Fig. 5.10**). Geoprocessed slope aspect maps of both sites also confirm that RSL are associated with blue-shaded slopes, corresponding to a west-facing orientation (**Fig. 5.11**). A significant correlation also exists between RSL source regions and slopes with low solar radiation in both locations (blue regions in **Fig. 5.12**).

5.4 Discussion

The main observation of this work is the fundamental, spatially reproducible geologic relationship between RSL source regions and fractures. Significant correlation between RSL source regions and steep, incised, west-facing slopes with low solar radiation and prevalent mass wasting is also observed. These observations suggest preexisting structural inhomogeneities may play a key role in RSL formation, most likely by providing pathways for groundwater migration. Below we discuss how fractures can facilitate groundwater flow, and how such a mechanism can also reproduce the seasonal- and temperature-dependence of RSL formation within each geologic setting analyzed.

5.4.1 Unsaturated groundwater flow

Flow (flux of water) in porous media is governed by the fundamental hydrogeological principle given by Darcy's Law:

$$\boldsymbol{q} = \frac{\boldsymbol{Q}}{\boldsymbol{A}} = -\boldsymbol{k}\boldsymbol{\nabla}\boldsymbol{h} \qquad (1)$$

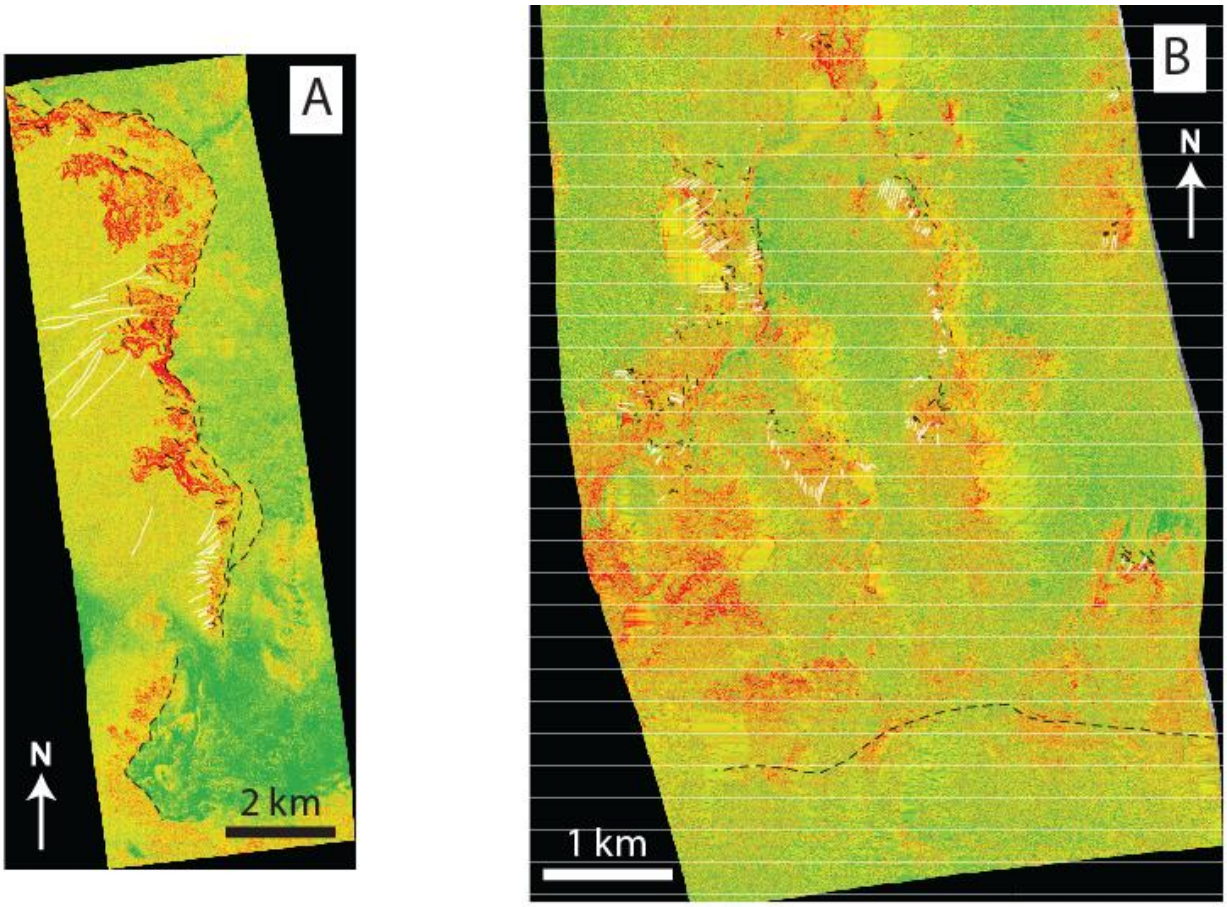

Figure 5.10. Slope maps of (A) Coprates landslide scarp and (B) Coprates mid-wall as calculated with the ArcGIS geoprocessing toolbox. Steep slopes are represented by warmer colors (red); shallower slopes are represented by cooler colors (green). Mapped RSL source regions are overlain in white; mapped fractures are in black. Note the spatial correlation between RSL source regions and very steep slopes.

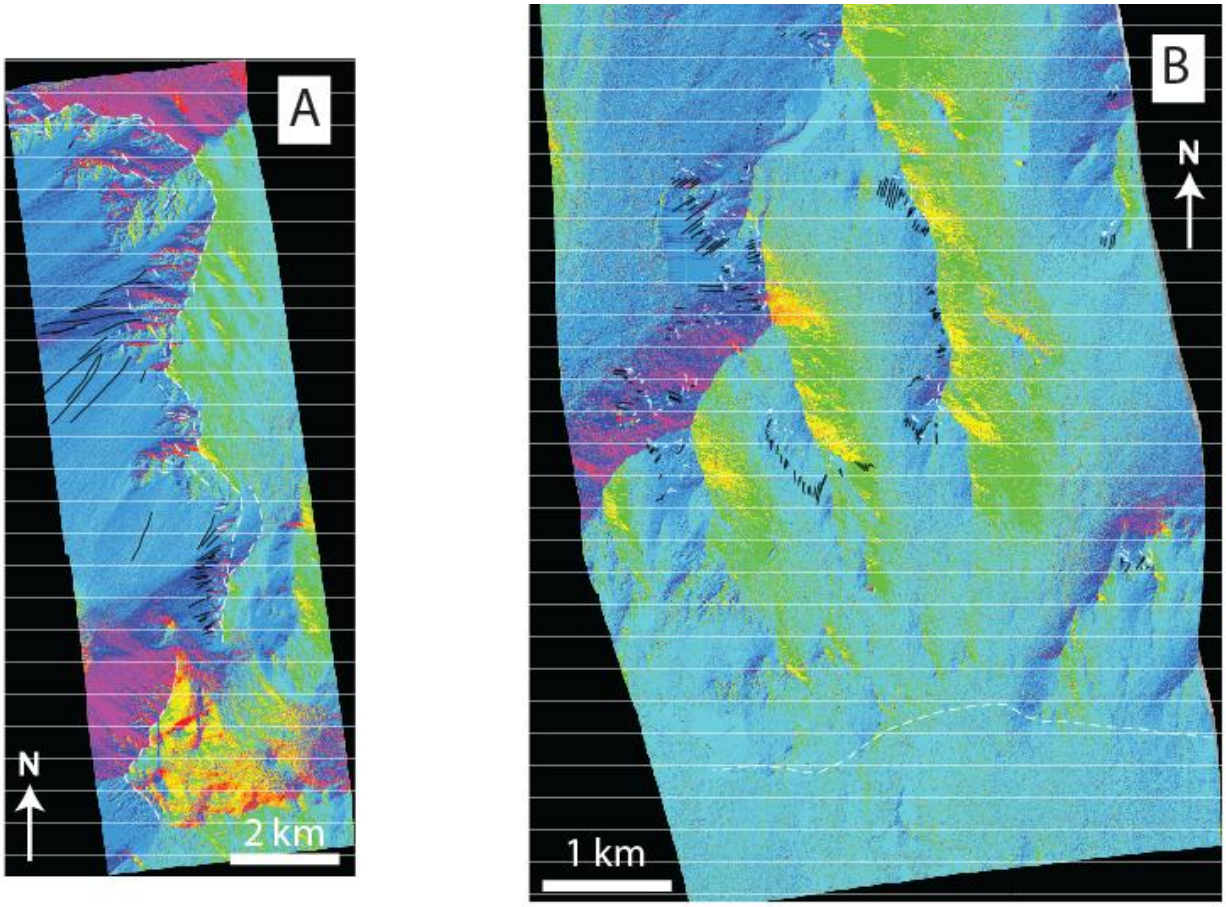

Figure 5.11. Geoprocessed slope aspect maps of (A) Coprates landslide scarp and (B) Coprates mid-wall. North-facing slopes are red, northeast are orange, yellow are east, southeast are green, south are cyan, southwest are light blue, west are blue, and northwest are magenta. Mapped RSL source regions are overlain in black; mapped fractures are in white. Note the correlation between RSL and west-facing slopes.

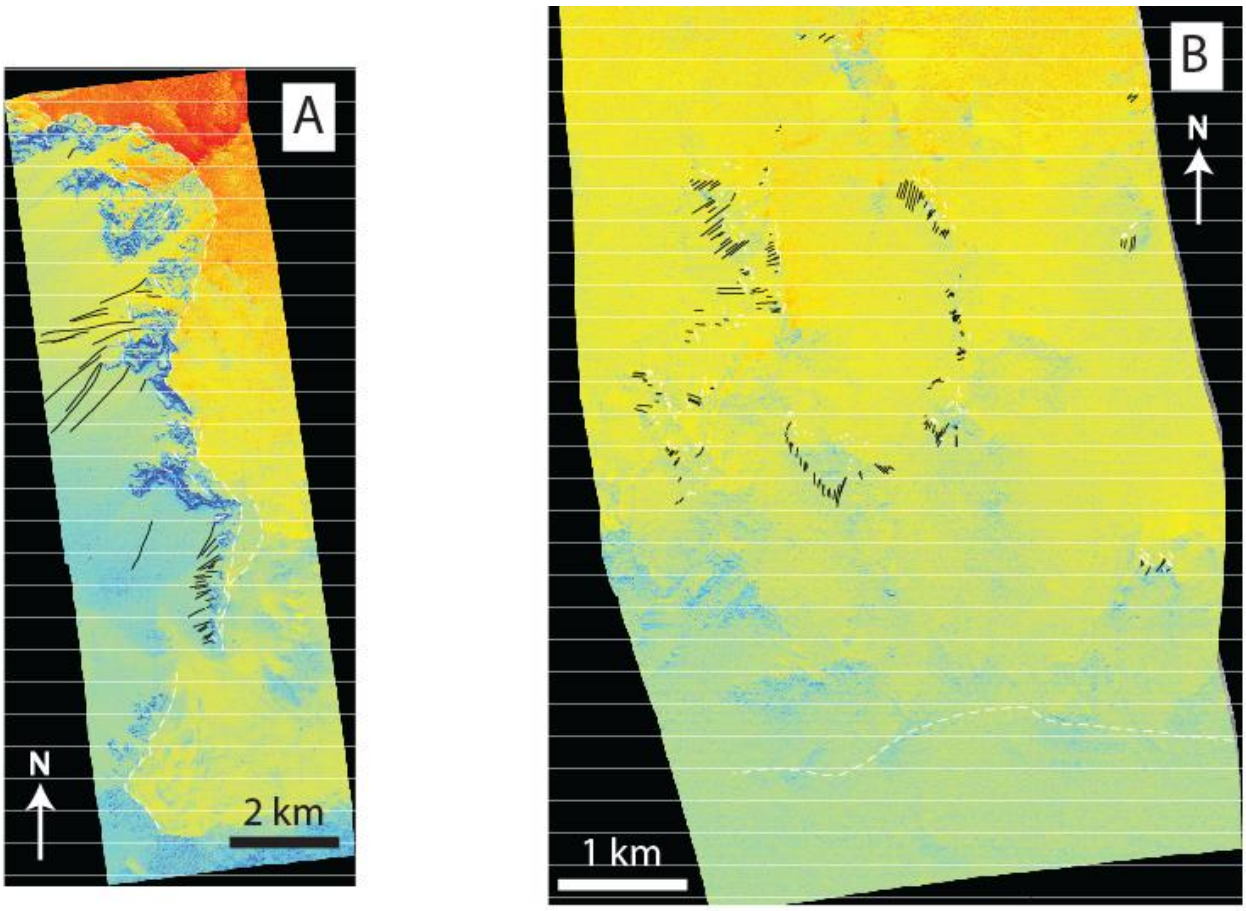

Figure 5.12. Geoprocessed solar radiation maps of (A) Coprates landslide scarp and (B) Coprates mid-wall. High solar radiation is represented by warmer colors (red) and low solar radiation is represented by cooler colors (blue). Mapped RSL source regions are overlain in black; mapped fractures are in white. Note the correlation between RSL source regions and slopes with low solar radiation.

where q is the Darcy flux (or specific discharge), Q is volumetric flow, A is cross-sectional area of flow, k is the coefficient of permeability, and the last term is the gradient in piezometric head over flow distance, given by:

$$\boldsymbol{h} = \frac{\boldsymbol{p}}{\boldsymbol{\rho_w g}} + \boldsymbol{z} \qquad (2)$$

where p is gauge pressure, which is the pressure above atmospheric pressure, ρ_w is density of liquid water, g is gravitational acceleration, and z is elevation above a datum. The first term in Equation 2 is the matric head term, and the second term is the gravity drainage term acting downward. In general q can be a three-dimensional quantity, but unsaturated flow, i.e., between the land surface and the saturated zone at some depth beneath the surface, is mainly in the z-direction (vertical) only. As such, the relevant Darcy flux is given by:

$$\boldsymbol{q_z} = -\boldsymbol{k_z}\left(\frac{\boldsymbol{\partial h}}{\boldsymbol{\partial t}}\right) \qquad (3)$$

This principle is critical because it sets out the specific conditions and determining factors for which subsurface fluid could reach the surface, constraining the feasibility of potential hydrological mechanisms. The key relationship is that the flow is proportional to both the permeability k and to the gradient in hydraulic head $\frac{\partial h}{\partial t}$. The hydraulic gradient is controlled by the pressure exerted at a given depth by the weight of the overlying rocks. Spatial gradients in h are what drive flow, where in particular water will flow from areas of higher h to areas of lower h. If the matric head gradient is negative, it acts against gravity, and if it is large in magnitude, it may overcome the gravity term so that flow will be upward. On Earth, unsaturated flow occurs in the low permeability rocks (often clays) between a confined aquifer and the land surface. When the groundwater in the confined aquifer is under sufficient pressure to force the water level to rise above the depth of the aquifer (that is, negative and sufficiently large matric head gradient),

it is defined as an artesian aquifer (**Fig. 5.13**). Recharge of these artesian aquifers is orographic-driven, occurring when the water table at its recharge zone is at a higher elevation than where the water reaches the surface.

As flow is also dependent on permeability (Equation 3), water that moves through artesian aquifers is discharged upward through areas of increased permeability in the overlying confining bed. The coefficient of permeability of bedrock materials depends not only on intrinsic properties of the material such as grain size, shape, sorting, compaction, etc., but also on the degree of fracturing. Penetrative fracturing renders permeable otherwise impervious confining rock, allowing water to escape upwards. Brittle fault zones can act as conduits, enhancing flow to the surface in the vertical direction through a network of subsidiary structures (e.g., minor faults and fractures) in the damage zone which yield high porosity and permeability (Caine et al., 1996; Faulkner and Rutter, 2001) (**Fig. 5.14**). Fluid flow is commonly associated with fault traces on Earth, forming springs, streams, waterfalls, and sag ponds. In faulted areas, water under high gauge pressure in artesian aquifers can rise above the aquifer, up fractures to the surface.

5.4.2 Fracture-controlled brine flow RSL formation model

The consistent correlation between fractures and RSL source regions observed in each of the RSL sites analyzed in this work best fits the application of Darcy's law to unsaturated flow through structural access to a briny artesian aquifer below the melting isotherm less than a few hundred meters from the surface (Mellon and Phillips, 2001).

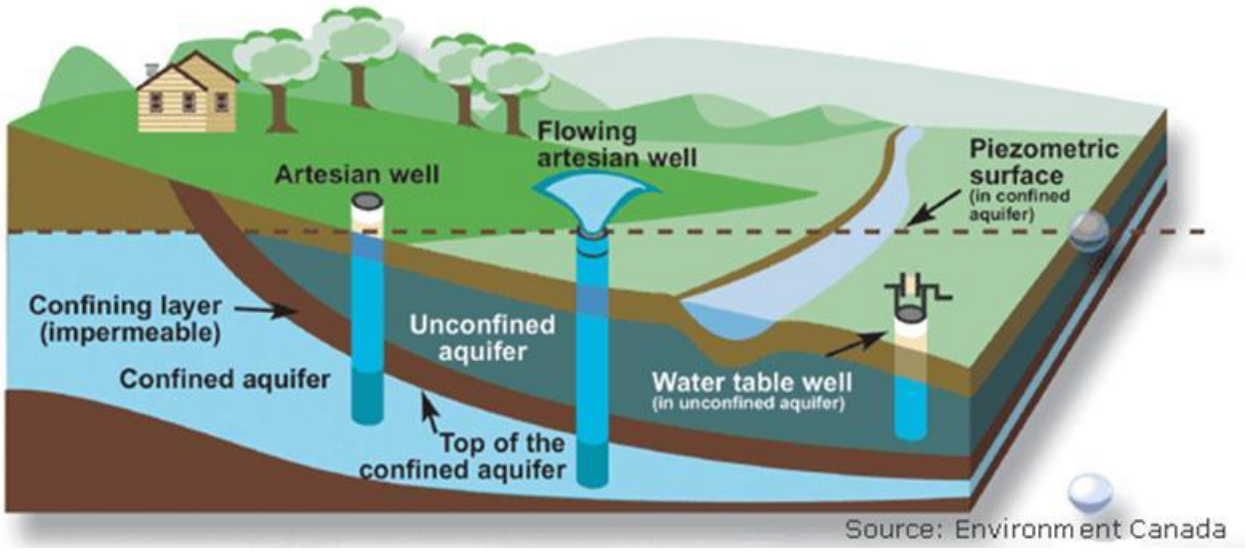

Figure 5.13. Schematic of artesian aquifer on Earth, with confining, impermeable layer overlying a confined aquifer, accessed by artesian wells and recharged upslope.

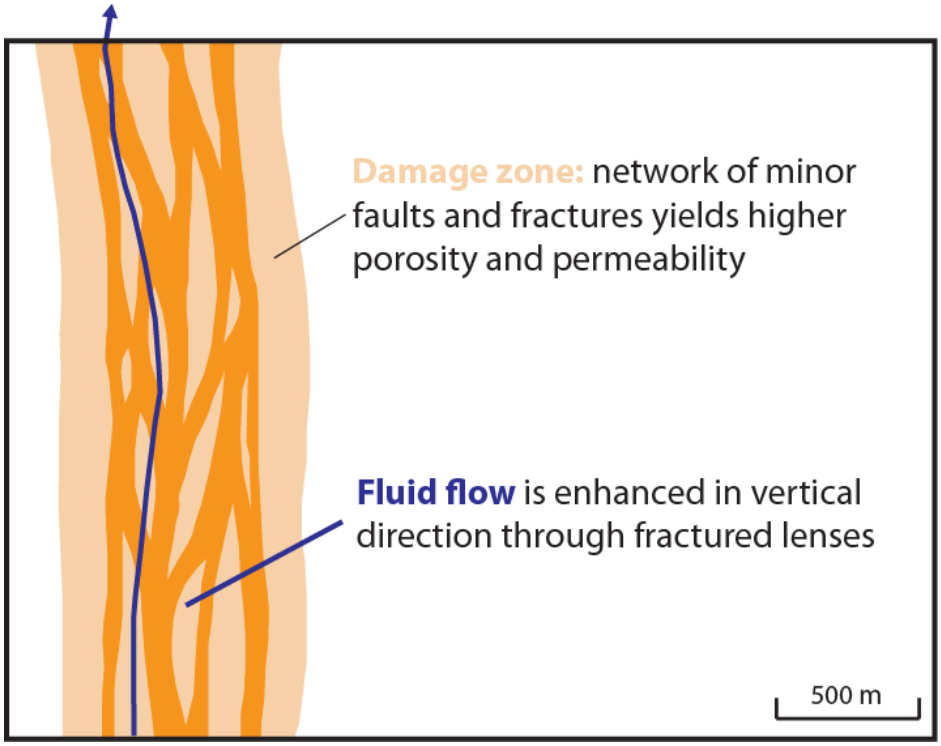

Figure 5.14. Schematic cross section through a vertical fault zone (Carboneras in southeast Spain; after Faulkner and Rutter, 2001). Brittle fault zones can act as conduits for flow to the surface in the vertical direction through a network of subsidiary structures (e.g., minor faults and fractures) in the damage zone which yield high porosity and permeability.

i. Model for crater sites

For the crater RSL locations, we propose that in warm seasons, thawed brine enters the exposed edge of an aquifer at high elevation and percolates downward through interconnected pore spaces, mimicking the topography. Overlying basalt forms an impermeable layer, creating a confined, artesian aquifer at a depth corresponding to sufficient pressure for upward flow and sufficient geothermal heating for melt. Conduit damage zone fractures through the confining layer of basalt, developed from the aquifer to the surface as a result of impact-related stresses, facilitate vertical migration of thawed brine to the surface as routes of increased permeability, forming RSL (**Fig. 5.15**). Equator-facing slopes, such as the ones on which RSL form (see **Figs. 5.11 and 5.12**) have been determined to experience maximum diurnal variations in surface temperatures high enough to allow various salt-ice mixtures to melt, even at depth (Chevrier and Rivera-Valentin, 2012; Ojha et al., 2014; McEwen et al., 2014). Within this model, the steep nature of these RSL-forming slopes (see **Fig. 5.10**) is an expression of unsaturated upward Darcy flow in the characteristically vertical direction. In addition, the series of fractures observed at each of the sites represents a more extensive damage zone of increased permeability for groundwater to exploit. In this way, the observed geologic setting of southern mid-latitude craters, whereby RSL source regions are correlated with fractures near the rim and within the central peak, is consistent with this model (**Fig. 5.15**). Locations where RSL might otherwise be expected but are not observed can also be explained within this model, in scenarios where fractures either reach the surface above the piezometric surface (**Fig. 5.16A**) or do not reach the confined aquifer (**Fig. 5.16B**). As previously mentioned, features formed by this mechanism at these sites may also be obscured from detection. Recharge of a confined aquifer could occur at

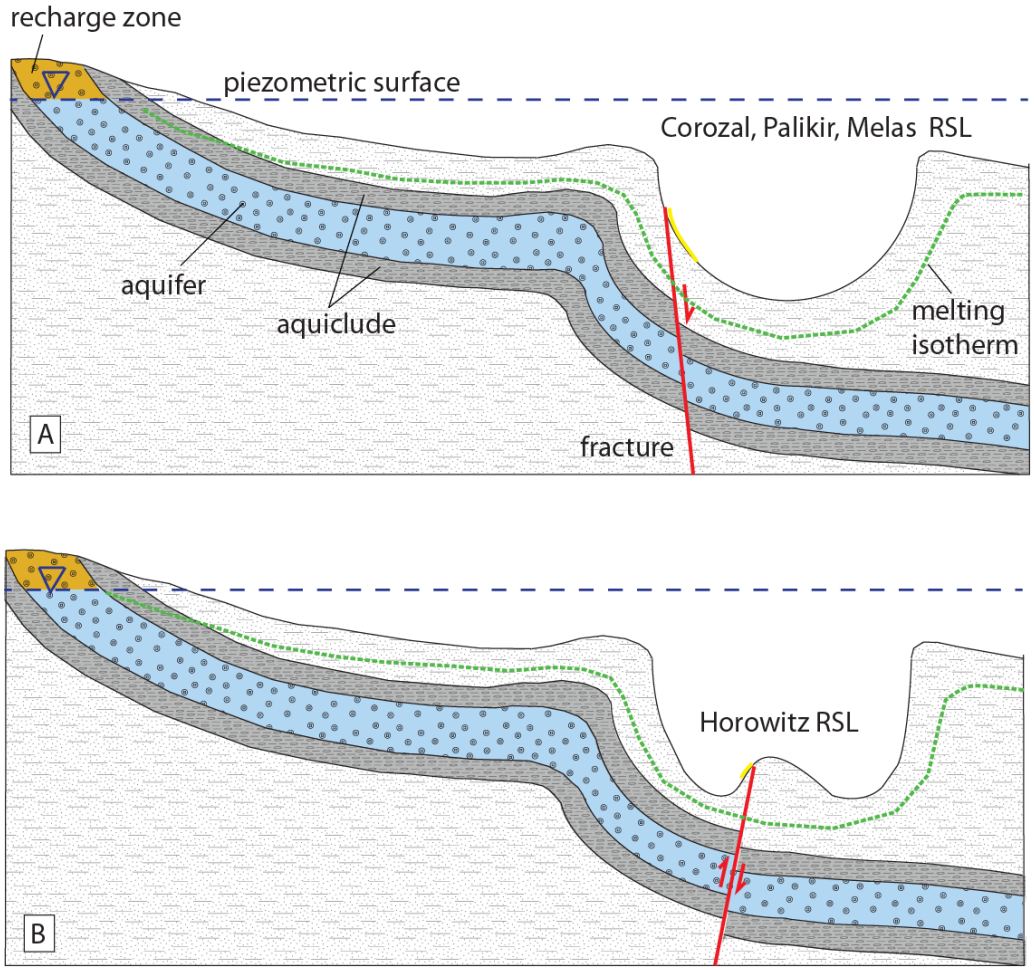

Figure 5.15. Fracture-controlled brine flow model for RSL formation at (A) Palikir, Corozal, and Melas Chasma craters, and (B) Horowitz crater, whereby conduit damage zone fractures through the basalt confining layer facilitate vertical migration of thawed brine from an artesian aquifer to the surface as routes of increased permeability.

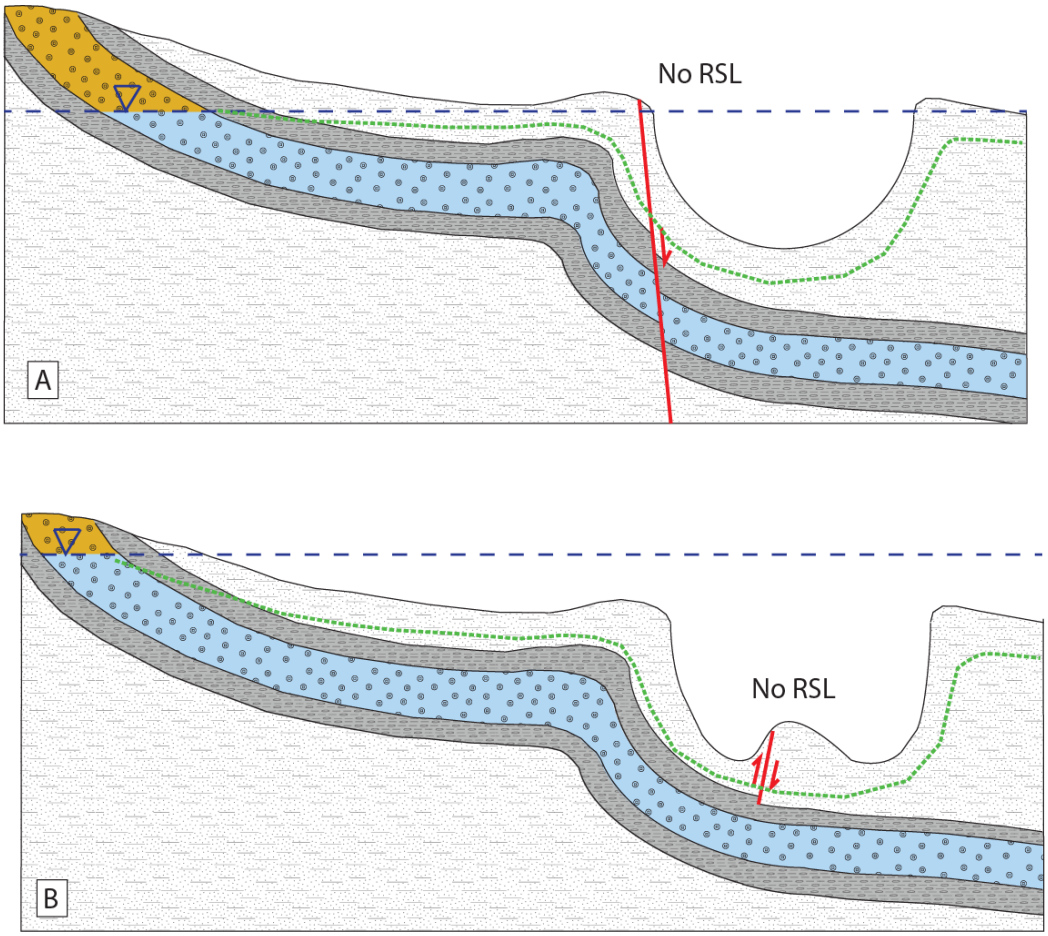

Figure 5.16. Examples of how a lack of RSL could be observed on the crater surface within the fracture-controlled flow model: (A) Fractures reach the surface above the water table, and (B) Fractures do not reach the confined aquifer.

times of extreme warming such as high obliquity, increasing thawing of briny ice at the surface in the recharge zone.

ii. Model for equatorial wall sites

Despite that equatorial canyon wall settings are positive relief topographic features, as opposed to the negative relief crater sites, fracture-controlled flow is a tenable formation mechanism of RSL at these locations as well. Within the model described in section (i), brine thawed in warm seasons enters the exposed edge of an aquifer at a distant topographic high and percolates downward through interconnected pore spaces, following the topography of the canyon. In the lowest region of the canyon, as evidenced by the regional slope (**Fig. 5.17A)**, brines under high gauge pressure in the artesian aquifer at the melting isotherm utilize conduit damage zone fractures related to trough-bounding tectonic activity (e.g., Lucchitta, 1979; Schultz, 1998; Yin, 2012) to migrate to the surface and form equatorial RSL (**Fig. 5.17B**). In this case, the spatial distribution of RSL locations within Valles Marineris, largely limited to the easternmost regions, may be correlated with variations in elevation of the piezometric surface or variations in thickness of the confining layer of the aquifer.

The observed correlation between RSL source regions and mass wasting features, including landslide scarps and slumps, is consistent with this model (**Fig. 5.17B**). Geologic context of the Coprates landslide scarp reveals representation of three periods of potentially fluidized deposition: (1) Amazonian slump (age based on cross-cutting relations with crater-counted estimates of Quantin et al., 2004), (2) late Amazonian flows, and (3) present-day RSL, and suggests that the direction and slope of the main slump were largely preserved through the present (**Fig. 5.9**). This implies that at present, as in the past, mass wasting and fluid flow follow

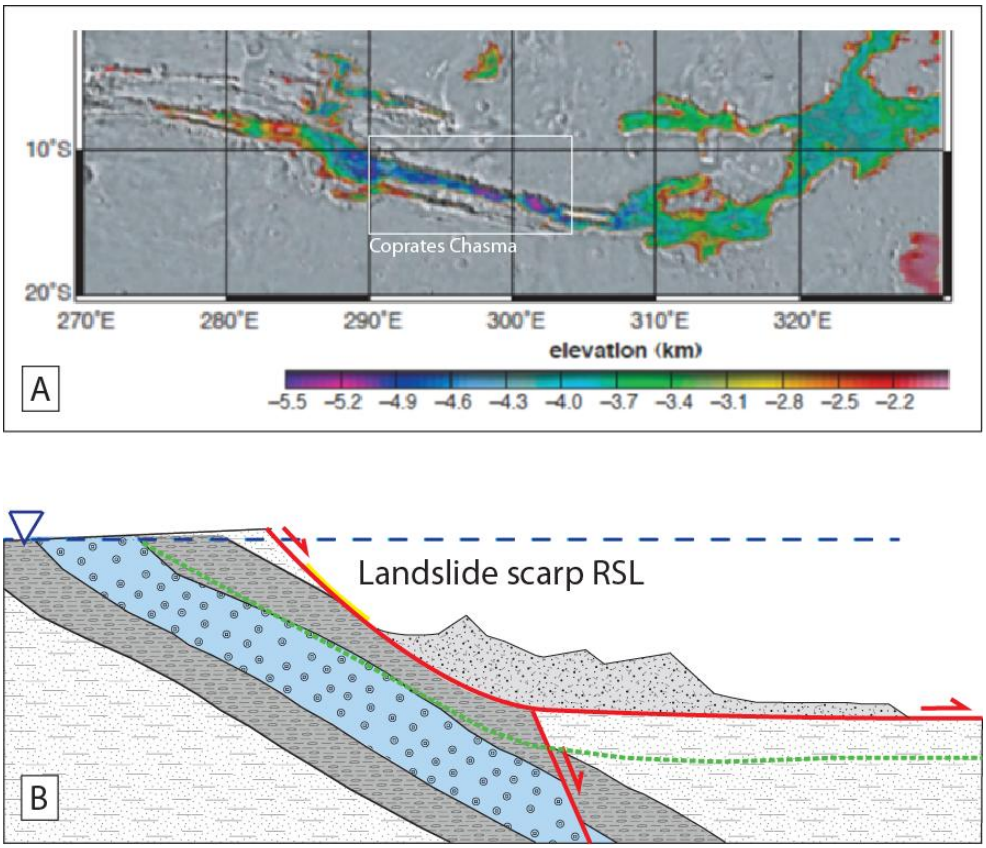

Figure 5.17. (A) MOLA elevation map within the floor of Valles Marineris, displaying the decrease in regional slope to the east which renders Coprates Chasma, where most of the equatorial RSL sites are found, the lowermost region in the canyon (white box). All areas in gray have elevations above -1.9 km, including the canyon rim, whose height remains relatively consistent at ~3 km. (B) Fracture-controlled brine flow model for RSL formation at equatorial wall sites, shown at a landslide scarp site. Brines under high pressure in the artesian aquifer utilize conduit damage zone fractures related to trough-bounding tectonic activity to migrate to the surface.

the local gradient created by the landslide breakaway fault. In this way, tectonic activity that originally formed RSL-generating surfaces facilitates RSL formation in those locations by permitting groundwater flow to the surface through faults.

Alternatively, given that equatorial RSL sites can exhibit somewhat different behavior (Chojnacki et al., 2014), it may be expected that a subset of RSL locations within specific geologic settings may be controlled by a slightly different mechanism. In these cases, near-surface thawed brines could plausibly be involved in RSL formation rather than accessing a confined aquifer. One such mechanism may employ fractures as regions of high permeability, facilitating seepage of near-surface thawed brines. Another potential candidate is low-permeability-fracture-controlled flow from a perched aquifer, where near-surface thawed brine is trapped on a relatively shallow aquiclude. However, perched aquifers are rare and not widely distributed on Earth, and their localized nature would require an unknown recharge mechanism. These possibilities exemplify the limitations of the current database of RSL locations, and can be tested by future studies as identification, monitoring, and confirmation of the global distribution of RSL continues.

iii. Examples of fluid flow near fault traces

Conduits along impact-generated and graben-related preexisting fractures and joints have been previously identified as a mechanism for subsurface fluid migration both on Earth and on Mars. In its analysis of Haughton crater on Devon Island in northern Canada, Osinski et al. (2005) identify exposed zones of intense, impact-generated fault systems around a highly fractured rim and central uplift, which acted as pathways for subsequent fluid migration, and are indicated by

pervasive calcite vein networks lining these highly fractured zones. Fault trace ridges in Valles Marineris, in locations in the vicinity of equatorial RSL sites (**Fig. 5.18**), were associated with a subsurface groundwater aquifer by Treiman (2008). In addition, Okubo and McEwen (2007) proposed fluid flow along preexisting fractures and joints as a mechanism for subsurface fluid migration in layered deposits in western Candor Chasma. Lastly, propagation of fluid-filled fractures from a deep confined aquifer to the surface was proposed as the initiation mechanism of the catastrophic outflow-channel forming floods just east of Valles Marineris by Andrews-Hanna and Phillips (2007). These studies demonstrate the applicability of the proposed fracture-controlled flow model to RSL locations, and emphasize the importance of fracture permeability in the Martian crust.

5.5 Conclusions and implications

Detailed mapping and quantification of RSL-bearing geologic contexts reveals a distinct spatial correlation between RSL source regions and fractures in all RSL geologic environments. These observations support the key role of unsaturated Darcy flow upward along preexisting fractures in facilitating RSL formation. This fracture-controlled flow model indicates that an atmospheric water vapor source for RSL is not required. Further, the proposed model implicates widespread, sustained subsurface brines in regions where RSL form, at variable depths across latitudes. This implication suggests that subsurface brines may be involved in the formation processes of other surface slope features on Mars with which RSL are associated, including landslides, channels, fans, and gullies, which may represent gradational features of RSL, and points to potentially habitable conditions on present-day Mars.

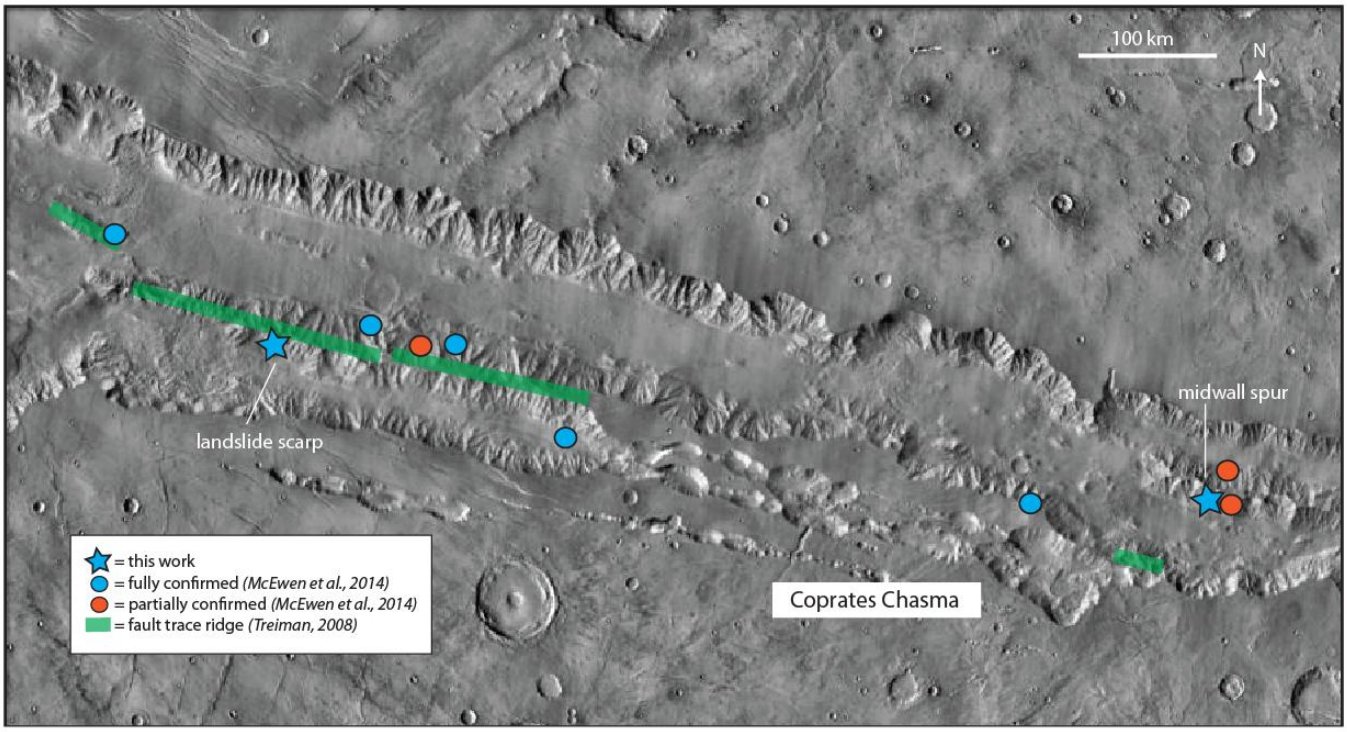

Figure 5.18. Distribution of RSL sites in Coprates Chasma, including partially confirmed sites; sites analyzed in this study are marked with stars. Also mapped are the locations of fault trace ridges associated with a subsurface groundwater aquifer (Treiman, 2008; green) in the vicinity.

5.6 References

Andrews-Hanna, J.C. and R.J. Phillips (2007), Hydrological modeling of outflow channels and chaos regions on Mars, *J. Geophys. Res., 112*, E08001.

Caine, J.S., Evans, J.P., Forster, C.B. (1996), Fault zone architecture and permeability structure, *Geology, 24*, 1025-1028.

Chevrier, V.F. and E.G. Rivera-Valentin (2012), Formation of recurring slope lineae by liquid brines on present-day Mars, *Geophys. Res. Lett., 39*, L21202.

Chojnacki et al. (2014), Geologic context of recurring slope lineae in Coprates Chasma (abs), *Lunar Planet. Sci. XLV*, 2701.

Faulkner, D.R. and E.H. Rutter (2001), Can the maintenance of overpressured fluids in large strike-slip fault zones explain their apparent weakness?, *Geology, 29*, 503-506.

Grimm, R.E., Harrison, K.P., Stillman, D.E. (2014), Water budgets of martian recurring slope lineae, *Icarus, 233*, 316-327.

Levy, J. (2012), Hydrological characteristics of recurrent slope lineae on Mars: Evidence for liquid flow through regolith and comparisons with Antarctic terrestrial analogs, *Icarus, 219*, 1-4.

Lucchitta, B.K. (1979), Landslides in Valles Marineris, Mars, *J. Geophys. Res., 84*, 8097-8113.

Mellon, M.T. and R.J. Phillips, (2001), Recent gullies on Mars and the source of liquid water, *J. Geophys. Res., 106*, 23165-23179.

McEwen et al. (2007), Mars Reconnaissance Orbiter's High Resolution Imaging Science Experiment (HiRISE), *J. Geophys. Res.,112*, E05S02.

McEwen et al. (2011), Seasonal flows on warm Martian slopes, *Science, 333*, 740-743.

McEwen et al. (2014), Recurring slope lineae in equatorial regions of Mars, *Nat. Geosci., 7*, 53-

58.

Ojha et al. (2014), HiRISE observations of Recurring Slope Lineae (RSL) during southern summer on Mars, *Icarus, 231*, 365-376.

Okubo, C.H. and A.S. McEwen (2007), Fracture-controlled paleo-fluid flow in Candor Chasma, Mars, *Science, 315*, 983-985.

Osinski, G.R. and J.G. Spray (2005), Tectonics of complex crater formation as revealed by the Haughton impact structure, Devon Island, Canadian High Arctic, *Meteoritics & Planetary Science, 40*, 1813-1834.

Osinski et al. (2005) Geological overview and cratering model for the Haughton impact structure, Devon Island, Canadian High Arctic, *Meteoritics & Planetary Science, 40*, 1759-1776.

Quantin et al. (2004), Ages of Valles Marineris (Mars) landslides and implications for canyon history, *Icarus, 172*, 555-572.

Schultz, R.A. (1998), Multiple-process origin of Valles Marineris basins and troughs, Mars, *Planet. Space Sci., 46*, 827-829.

Stillman et al. (2014), New observations of southern mid-latitude recurring slope lineae (RSL) imply formation by freshwater subsurface flows, *Icarus, 233*, 328-341.

Treiman, A.H. (2008), Ancient groundwater flow in the Valles Marineris on Mars inferred from fault trace ridges, *Nat. Geosci., 1*, 181-183.

Yin, A. (2012), Structural analysis of the Valles Marineris fault zone: Possible evidence for large-scale strike-slip faulting on Mars, *Lithosphere, 4*, 286-330.

Zuber et al. (1992), The Mars Observer Laser Altimeter Investigation, *J. Geophys. Res., 97*, 7781-7797.

CHAPTER 6

Concluding remarks

6.1 Conclusions and implications

In this dissertation, I have contributed substantially to the study of aqueous and tectonic processes on planetary surfaces by constraining the role of water, hydrated materials, and tectonic activity in the emplacement mechanisms of long-runout landslides on Mars and an analog on Earth, and the formation mechanisms of hillslope geomorphic features on Mars. Through this multi-disciplinary, comparative analysis, I have demonstrated the importance of the interaction between tectonics and water on both planets throughout geologic time.

This interaction in ancient geologic time is exemplified by our investigation of long-runout landslides on Mars in the second and third chapters, in which we apply the fundamental principles that govern mass wasting, outlined in the introduction in the first chapter, in order to constrain their emplacement mechanisms in Valles Marineris. In the second chapter, based on image and spectral analysis of a well-exposed example in Ius Chasma, we introduce a clay lubrication model of VM long-runout landslide transport which involves slope failure related to tectonic activity along trough-bounding faults and lubricated sliding of entrained clay-bearing trough-floor materials. The third chapter describes the results of the application of this model on a regional scale. We concluded that a distinct correlation of transport distance, lateral spreading, and low, mass-independent basal coefficient of friction with the presence of hydrated silicates in the basal sliding zones exists within VM landslides. The hydrated silicates in the basal sliding zone in turn are spatially related to hydrated-silicate-bearing trough-floor deposits in VM. These results favor lubrication through the presence of liquefied, entrained hydrated-silicate-bearing

trough-floor deposits in the basal sliding zones as the transport mechanism of VM landslides. Within this model, outer deposits of VM landslides resemble clay-assisted long-runout terrestrial earthflows.

The interaction between tectonics and water in the recent geologic past is elucidated by our examination of a long-runout landslide in Eureka Valley, CA in the fourth chapter, in which we report the findings of integrated field, photogeologic, spectral, and luminescence dating analysis of the geomorphology of the well-preserved EV landslide deposit. We determine that the landslide was initiated as a result of fault-generated fracture, likely transported by lubrication through the presence of basal clays, and that it was subjected to intense 3-D simple shear internal deformation during transport and fluvial modification following emplacement. A minimum EV landslide emplacement age and a maximum age of post-emplacement rotation of mid to early Holocene was deduced.

Aqueous and tectonic interaction in the present-day is represented by our study of recurring slope lineae on Mars in the fifth chapter, in which we characterize and quantify RSL-bearing geologic contexts in order to constrain their formation mechanisms. We establish a distinct spatial correlation between RSL source regions and fractures, supporting the key role of fluid flow along preexisting fractures in facilitating RSL formation.

The conclusions described in this dissertation have implications for the climatic, aqueous, tectonic, and surface conditions of Mars, Earth, and other planetary surfaces. Our proposed clay-lubrication model for long-runout landslide transport in Valles Marineris implies that landslide occurrence since 3.5 Ga has been independent of changing climate conditions. This new understanding also indicates that clay minerals, generated as a result of water-rock interactions in the Noachian and Hesperian (4.1–3.3 Ga), exert a long-lasting influence on

geomorphic processes that shape the surface of the planet into the recent past. The accumulation of hydrated silicates on the trough floor for participation in episodic, sustained landslide activity throughout the canyon's history implies ongoing faulting along VM troughs since its formation, prevalent mass wasting, deposition, and aeolian redistribution of clay-bearing materials, and/or punctuated aqueous alteration on the surface of Mars prior to VM landslide emplacement.

The basal lubrication model we proposed for the emplacement of the EV landslide does not require the participation of intergranular fluid, implying that long-runout landslide deposits on other planetary surfaces also do not necessitate the presence of fluids for emplacement. This analog study therefore supports the conclusions of the landslide studies on Mars in the second and third chapters, and suggests that granular flow of lubricating hydrated material may be a reasonable resolution to the debate over the involvement of water as a mechanism of long-distance landslide transport. In this way, long-runout landslides may serve as a proxy for hydrated materials on the surfaces of rocky bodies throughout the solar system, explaining the lack of longitudinally-grooved long-runout landslides on solar system bodies, such as Earth's moon (Lucchitta, 1978), that lack hydrated minerals. In addition, the potential subaqueous emplacement of the EV landslide would have implications for cooler, wetter conditions within Eureka Valley during the Quaternary than the current arid conditions.

The fracture-controlled flow model we proposed for the formation of RSL implies that an atmospheric water vapor source for RSL is not required, and that subsurface brines are widespread at variable depths across regions in which RSL form. This suggests that subsurface brines may be involved in formation processes of other RSL-associated slope features on Mars, including landslides, channels, fans, and gullies, and signifies potentially habitable conditions on present-day Mars.

The formation models proposed in this dissertation provide tenable mechanisms that make specific predictions which can be tested in subsequent analyses. Future work to further constrain the interaction between aqueous and tectonic processes on planetary surfaces enabled by this contribution include exploration of whether the clay-lubrication model can viably be applied to other long-runout landslides on Mars (e.g., flanks of Olympus Mons; McGovern, 2009) and on Earth (e.g., Socompa volcanic debris avalanche; Davies et al., 2010), establishment of the maximum age of the EV landslide in order to fully bracket its emplacement and distinguish between the two remaining hypotheses for its transport mechanism, and application of the fault-controlled flow model to all RSL sites, including to the regional topography and subsurface thermal environment, as orbital and even rover data acquisition continues.

6.2 References

Davies, T., McSaveney, M., Kelfoun, K. (2010), Runout of the Socompa volcanic debris avalanche, Chile: a mechanical explanation for low basal shear resistance, *Bulletin of Volcanology, 72,* 933-944.

Lucchitta, B.K. (1978), A large landslide on Mars, *GSA Bulletin,* 89, 1601-1609.

McGovern, P.J. and J.K. Morgan (2009), Volcanic spreading and lateral variations in the structure of Olympus Mons, Mars, *Geology, 37,* 139-142.